Biomechanical computer models provide novel insights into musculoskeletal function by overcoming technical and ethical barriers faced by experimental techniques. Current macroscopic, continuum-mechanical skeletal muscle models, however, neglect certain aspects of motor-unit physiology and thus oversimplify muscle function. This Ph.D. thesis deals with methods to enrich such models with microstructurally derived motor-unit information. By doing so, contraction dynamics and joint-kinematics can be predicted, for the first time, as a combination of individual motor-unit -activity, -properties, and (three-dimensional) -anatomy. Such a model uncovers unique relationships between neuromuscular physiology and muscle function, for example, the role of motor-unit remodelling (typically occurring during ageing and neuromuscular disorders) on joint-function. This integrated neuro-musculoskeletal modelling approach can be applied to better understand phenomena such as fatigue and be used to inform medical interventions by predicting surgery outcomes or aiding movement rehabilitation protocols related to trauma, neuromuscular disorders, or ageing.

Harnoor Saini

ISBN 978-3-946412-07-6

H. Saini

Modelling the Functional Heterogeneity of Skeletal Muscles

CBM-08 (2021)

Modelling the Functional Heterogeneity of Skeletal Muscles: Enriching Continuum-Mechanical Models on a Motor-Unit Level

Harnoor Deep Singh Saini

vorgelegt an der
Universität Stuttgart

Modelling the Functional Heterogeneity of Skeletal Muscles: Enriching Continuum-Mechanical Models on a Motor-Unit Level

Von der Fakultät Bau- und Umweltingenieurwissenschaften
der Universität Stuttgart zur Erlangung der Würde
eines Doktor-Ingenieurs (Dr.-Ing.)
genehmigte Abhandlung

Vorgelegt von

Harnoor Deep Singh Saini

aus

Ogbomosho

Hauptberichter:	Prof. Oliver Röhrle, Ph.D.
1. Mitberichter:	Prof. Leo K. Cheng
2. Mitberichter:	Prof. Dr. Dr. Bernd Lapatki

Tag der mündlichen Prüfung: 22 April 2021

Institut für Modellierung und Simulation Biomechanischer Systeme
der Universität Stuttgart

2021

Report No.: CBM-08
Institute for Modelling and Simulation of Biomechanical Systems
Chair of Continuum Biomechanics and Mechanobiology
University of Stuttgart, Germany, 2021

Editor:
Prof. O. Röhrle, Ph.D.

Institute for Modelling and Simulation of Biomechanical Systems
Chair of Continuum Biomechanics and Mechanobiology
University of Stuttgart
Pfaffenwaldring 5a
70569 Stuttgart, Germany

ISBN 978-3-946412-07-6
(D93 – Dissertation, Universität Stuttgart)

Declaration of originality

Hiermit erkläre ich, dass ich die vorliegende Arbeit selbstständig verfasst habe, dass ich keine anderen als die angegebenen Quellen benutzt und alle wörtlich oder sinngemäß aus anderen Werken übernommen Aussagen als solche gekennzeichnet habe, dass die eingereichte Arbeit weder vollständig noch in wesentlichen Teilen Gegenstand eines anderen Prüfungsverfahrens gewesen ist, dass ich die Arbeit weder vollständig noch in Teilen bereits veröffentlicht habe und dass das elektronische Exemplar mit den anderen Exemplaren übereinstimmt.

I hereby declare that I have written the present work independently, that I have not used any sources other than those specified and that all statements taken verbatim or meaningfully from other works have been marked as such, that the submitted work has not been completely or partially the subject of another examination procedure, that I have not published the work either completely or in part, and that the electronic copy coincides exactly with the other copies.

Harnoor Deep Singh Saini
Stuttgart, June 2021

Acknowledgements

This thesis is a culmination of nearly four years of work at the Institute of Modelling and Simulation of Biomechanical Systems at the University of Stuttgart. Far from being a solitary endevaour, it was made possible by the generous contributions of various people. While others remain unnamed, their role in this work has not been forgotten. In particular, I wish to thank the following:

The Deutsche Forschungsgemeinschaft for funding my work as part of the Soft Tissue Robotics international research training group (GRK 2198). I hope my research contributions can live up to the wonderful opportunity that has been provided me.

My supervisors, Professor Oliver Röhrle and Professor Leo Cheng, for their insights, guidance, goodwill, and for gently prodding me when I needed it. Oliver—although I wandered out of academia, first after my bachelors, and then after my masters, I eventually returned to the world of biomechanics each time. Thank you for fostering my interest in this field, and for the opportunities and journey so far. Leo—thank you for creating an amiable atmosphere during my research stays at the Auckland Bioengineering Institute and for many illuminating discussions.

The Continuum Biomechanics and Mechanobiology group, for creating a warm and lively research environment, where inspiration was just a cup of coffee away. In particular; Andreas for always lending a helpful hand; Christian, for uncovering theoretical intricacies; Thomas, for the lively discussions on physiology; and Leonardo, for guiding me when I strayed too far into the world of experiments.

My friends and family, near and far, who have made this journey that much more enjoyable. In particular: Sangeeta, Gagan, Sophie, Camilo, Dominik, Giada, Riccardo, and Birsha. My wife's family, who have been a source of warmth and joy, in particular: Gabriella, Piotr, Beate, Damian, Joanna, and Stefan. My parents, Jatinder Saini and Rajinder Saini, for kindling my love of engineering, and for their sacrifices, love, and support. My sister, brother and their families, for making trips back to New Zealand filled with love and laughter.

My daughter Valerie and my son Vincent, for cheering me up after a long day of research by simply being so cute … and for saving me from having to set my alarm in the mornings! My wife, Maria, for the thousand little things she did that kept me going. For her infectious enthusiasm for life. For taking care of the kids while I spent long days (and nights) in front of the computer. For her love, advice, patience, encouragement, and for keeping me sane when I needed it the most.

Above all, God, for His inexhaustible grace. So, with the psalmist I can exclaim *"Praise the Lord! O give thanks to the Lord, for he is good; for his steadfast love endures for ever!"*—Psalm 106:1.

Contents

Deutsche Zusammenfassung **xi**

Abstract **xvii**

Nomenclature **xxiii**

1 Introduction **1**
1.1 Motivation . . . 1
1.2 State-of-the-art . . . 3
1.2.1 Continuum-mechanical modelling of skeletal muscles . . . 3
1.2.2 Functional heterogeneity of skeletal muscles . . . 5
1.2.3 Measurement and modelling of motor-unit anatomy . . . 6
1.3 Research Goals . . . 10
1.4 Prototype Masticatory System Model and Case-Studies . . . 11
1.5 Outline . . . 13
1.6 List of Publications . . . 14

2 Physiological Background of the Neuro-Musculoskeletal System **15**
2.1 The Musculotendon Complex and Muscle Contraction . . . 15
2.1.1 Connective tissues . . . 16
2.1.2 Sarcomeres and excitation-contraction coupling . . . 16
2.1.3 Muscle fibres . . . 17
2.2 The Neuromuscular System . . . 21
2.2.1 The motor-unit . . . 21
2.2.2 Recruitment of motor-units . . . 22

3 Theoretical Framework of the Mechanical Problem **25**
3.1 Continuum Mechanics . . . 25
3.1.1 Kinematic relations . . . 26
3.1.2 Deformation and strain measures . . . 28
3.1.3 Rate of deformation . . . 30
3.1.4 Stress measures . . . 30
3.1.5 Balance relations . . . 32
3.1.6 Objectivity . . . 35
3.1.7 Initial boundary value problem . . . 36
3.2 Finite Element Method . . . 37
3.2.1 Principle of virtual work . . . 37
3.2.2 Spatial discretisation and approximate solution . . . 38
3.2.3 Numerical solvers . . . 40

3.3 Contact Mechanics . . . 41
3.3.1 Tangential contact . . . 43
3.3.2 Weak formulation of the contact problem . . . 44

4 Constitutive Modelling of the Musculoskeletal System 45
4.1 Hyperelasticity . . . 46
4.1.1 Incompressibility and quasi-incompressibility . . . 48
4.1.2 Isotropy . . . 49
4.1.3 Transverse isotropy . . . 49
4.2 Musculotendon Complex . . . 50
4.2.1 Isotropic response . . . 51
4.2.2 Anisotropic-passive response . . . 52
4.2.3 Anisotropic-active response . . . 53
4.2.4 Accounting for motor-unit anatomy and activity . . . 53
4.2.5 Musculotendon complex . . . 54
4.3 Other Soft Tissues and Bones . . . 55
4.4 Material Characterisation . . . 55
4.4.1 Non-active musculotendon complex behaviour . . . 56
4.4.2 Active muscle behaviour . . . 58
4.4.3 Overview and parameter variations . . . 59

5 Modelling Motor-Unit Activity and Anatomy 63
5.1 Motor-Unit Activity . . . 64
5.1.1 Motor-neuron pool recruitment . . . 65
5.1.2 Motor-unit contractile response . . . 66
5.1.3 Motor-unit activity: model characterisation . . . 68
5.2 Reconstructing Skeletal Muscle Microstructure . . . 74
5.2.1 Fibre orientation interpolation . . . 74
5.2.2 Seed-point surface generation and fibre-scaffold tracking . . . 75
5.2.3 Case-studies . . . 78
5.3 Motor-Unit Anatomy in Three-Dimensional Skeletal Muscle Models . . . 81
5.3.1 Motor-unit size . . . 81
5.3.2 Motor-unit territory location and overlap . . . 82
5.3.3 Motor-unit territory shape . . . 83
5.3.4 Fibre distribution metric . . . 85
5.3.5 Motor-unit anatomy: model characterisation . . . 85
5.4 Discussion . . . 92
5.4.1 Motor-unit activity . . . 92
5.4.2 Reconstruction of microstructure . . . 92
5.4.3 Motor-unit territory anatomy models . . . 93
5.4.4 Plausibility of motor-unit territories . . . 94

6 Integrating the Neural and Skeletal Muscle Models 97
6.1 Homogenising Motor-Unit Territories . . . 97
6.2 Muscle Activity Decomposition: Assumption on Action-Potential Propagation 99
6.2.1 Methods . . . 100
6.2.2 Results . . . 100

6.3 Implementing the Neuro-Musculoskeletal Model . . . 102
6.3.1 Pre-computing neural information in MATLAB . . . 102
6.3.2 Integrated neuromuscular model in Abaqus/Explicit . . . 104
6.3.3 Incompressibility and element types . . . 108
6.3.4 Convergence of element types . . . 109
6.4 Demonstration of the Integrated Model . . . 112
6.4.1 Methods . . . 112
6.4.2 Results . . . 113
6.5 Discussion . . . 116
6.5.1 Modelling limitations . . . 116
6.5.2 Accuracy of incompressibility . . . 119
6.5.3 Element choice . . . 119
6.5.4 Demonstration of the integrated model . . . 119

7 A Prototype Integrated Neuro-Musculoskeletal Model 121
7.1 The Masticatory System . . . 122
7.1.1 Other soft tissues and bones . . . 122
7.1.2 Masseters . . . 122
7.2 Modelling the Masticatory System . . . 124
7.2.1 Geometry and meshing . . . 125
7.2.2 Masseter architecture and motor-unit pool . . . 127
7.2.3 Constitutive modelling and characterisation . . . 130
7.3 The Influence of Masseter Motor-Units on Bite Force . . . 131
7.3.1 Methods . . . 133
7.3.2 Results . . . 134
7.4 Discussion . . . 140
7.4.1 Motor-unit anatomy . . . 140
7.4.2 Modelling limitations . . . 141
7.4.3 Comparison to constant-activity model . . . 142

8 Case-Studies Using the Masticatory System Model 145
8.1 Compartmental Activity of Masseters and Bite Force . . . 145
8.1.1 Methods . . . 146
8.1.2 Results . . . 148
8.1.3 Discussion . . . 151
8.1.4 Conclusion . . . 152
8.2 Compartmental Activity and Intramuscular Pressure in the Masseters . . . 152
8.2.1 Methods . . . 153
8.2.2 Results . . . 154
8.2.3 Discussion . . . 154
8.2.4 Conclusion . . . 156
8.3 Determining Motor-Unit Twitch Properties in the Masticatory System . . . 156
8.3.1 Methods . . . 156
8.3.2 Results . . . 158
8.3.3 Discussions . . . 159
8.3.4 Conclusion . . . 161

9 Extended Case Study: Ageing and Disorders **163**
9.1 Modelling Denervation and Reinnervation . . . 164
9.2 Changes in Bite Force during Ageing and Disease . . . 167
9.2.1 Methods . . . 167
9.2.2 Results . . . 168
9.3 Discussion . . . 170

10 Discussion and Outlook **173**
10.1 General Limitations and Proposed Solutions . . . 174
10.1.1 Limited scope . . . 174
10.1.2 Number of motor-units and mesh size . . . 175
10.2 General Findings and Implications . . . 176
10.2.1 Implications for traditional macroscopic models . . . 176
10.2.2 Implications for multiscale models . . . 177
10.2.3 Implications for other models . . . 177
10.3 Conclusion and Outlook . . . 178
10.3.1 Decoding experimental data . . . 178
10.3.2 Augmenting control of human-machine-interaction devices . . . 178
10.3.3 Improving motor-output predictions during fatigue . . . 179
10.3.4 Improving applicability of the neuro-musculoskeletal model . . . 180
10.3.5 Virtual test-bed for medical interventions . . . 181
10.3.6 Concluding remarks . . . 181

Appendices **183**

A Occlusal boundary conditions **183**
A.1 Methods . . . 184
A.2 Results . . . 185
A.3 Discussion . . . 186
A.4 Conclusion . . . 187

B Simulated Motor-Unit Territories **189**

Bibliography **195**

Released Report Series **223**

List of Figures

1.1 Learning to stand and walk . . . 1
1.2 Muscle biopsies for healthy (young and old) and pathological muscles . . . 8
1.3 Motor-unit anatomical shapes obtained by Magnetic Resonance Imaging . . . 9

2.1 Simplified myofibril and sarcomere structure . . . 17
2.2 Hierarchical structure of skeletal muscle . . . 18
2.3 Force-length relationship of sarcomeres and force-velocity relationship of muscle fibres . . . 19
2.4 Motor-unit twitch response . . . 22

3.1 Kinematic setting of a continuum body . . . 27
3.2 Kinematic setting of continuum bodies in contact . . . 42

4.1 Penalty strain-energy function enforcing the incompressibility constraint . . . 52
4.2 Predicted passive-muscle and -tendon responses compared to experimental values . . . 59
4.3 Active force-length relationship and influence of muscle volume fraction parameter . . . 60
4.4 Effect of muscle specific material parameters on overall muscle stress response 60
4.5 Overall stress response of the skeletal muscle . . . 61

5.1 Workflow to compute motor-unit anatomy and activity . . . 64
5.2 Motor-neuron pool recruitment behaviour . . . 70
5.3 Motor-neuron pool properties . . . 71
5.4 The spread of normalised peak twitch forces and times-to-peak in the motor-unit pool . . . 72
5.5 Motor-unit activity in response to sustained stimulation at fixed frequencies . 73
5.6 Muscle activity computed as the weighted sum of individual motor-unit activity 73
5.7 Biceps brachii microstructure reconstruction case-study . . . 79
5.8 Lateral pterygoid microstructure reconstruction case-study . . . 80
5.9 Masseter microstructure reconstruction case-study . . . 80
5.10 Schematic of select motor-unit territory distribution parameters . . . 83
5.11 Fibre distributions generated by varying R and D . . . 88
5.12 Territory boundaries generated by varying R and D . . . 89
5.13 Fibre distributions generated by varying ΔR and ΔD . . . 90
5.14 Territory boundaries generated by varying ΔR and ΔD . . . 90
5.15 Relationship between motor-unit anatomy and fibre dispersion and territory size 91
5.16 Relationship between fibre dispersion and territory area . . . 91

6.1 Multiscale neuromuscular simulation architecture and activation for action-potential comparisons . . . 101

6.2 Snapshots of multiscale simulation with and without action-potential propagation 101
6.3 Reaction force for both models with and without action-potential propagation 103
6.4 Accuracy of incompressible behaviour and effect on computational time . . . 109
6.5 Idealised geometry for element type convergence analysis 110
6.6 Convergence of different element types under mesh refinement—passive behaviour 111
6.7 Convergence of different element types under mesh refinement—active behaviour 111
6.8 Homogenisation of motor-unit territories 114
6.9 Comparison of motor-output between motor-unit driven and constant-activity models 115
6.10 Comparison of stress distribution between motor-unit driven and constant-activity models 115
6.11 Dependence of motor-unit anatomy with innervation-ratio 118

7.1 Skeletal muscles of the masticatory system 123
7.2 Schematic of the prototype masticatory model 127
7.3 Finite-element mesh of the prototype masticatory model 128
7.4 Meta-unit territory distribution in the left masseter simulation model 131
7.5 Activation protocols for the maximal case for the motor-unit driven and constant-activity models 134
7.6 Maximum bite force magnitude development for the motor-unit driven and constant-activity models 135
7.7 Maximum bite force orientation development for the motor-unit driven and constant-activity models 136
7.8 Snapshot of intramuscular pressure distribution in the right masseter during sub-maximal contraction 136
7.9 Evolution of stress in the masseters during the maximal contraction simulation for the motor-unit driven model 138
7.10 Spread of contraction in the masseter cross-section during the maximal contraction simulation for the motor-unit driven model 139

8.1 Activation protocol for the sub-maximal case for the motor-unit driven model 146
8.2 Variation in bite forces with changing meta-unit anatomy 148
8.3 Variation in bite force angles with changing meta-unit anatomy 149
8.4 Variation of peak force magnitude with fibre dispersion 150
8.5 Correlations of active and passive compartmental pressures with bite force . . 155
8.6 Relative error in twitch force components 158
8.7 Linearly summed and compound-twitch forces 159
8.8 Comparisons of motor-output between various twitch simulations 160

9.1 Evolution of fibre distribution during denervation/reinnervation cycles 166
9.2 Fibre distributions of the right masseter after cycles of denervation/reinnervation 169
9.3 Influence of ageing and pathology on bite force 170

A.1 Occlusal load case models 184
A.2 Stress distribution in the molar and mandible in the sagittal plane for various occlusal loads 186

B.1 Meta-unit territory distribution ID 1 in the left masseter simulation model . . 190
B.2 Meta-unit territory distribution ID 3 in the left masseter simulation model . . 190
B.3 Meta-unit territory distribution ID 4 in the left masseter simulation model . . 191
B.4 Meta-unit territory distribution ID 5 in the left masseter simulation model . . 191
B.5 Meta-unit territory distribution ID 6 in the left masseter simulation model . . 192
B.6 Meta-unit territory distribution ID 7 in the left masseter simulation model . . 192
B.7 Meta-unit territory distribution ID 8 in the left masseter simulation model . . 193
B.8 Meta-unit territory distribution ID 9 in the left masseter simulation model . . 193
B.9 Meta-unit territory distribution ID 10 in the left masseter simulation model . . 194

List of Tables

1.1 Motor-unit territory sizes in animals and humans 7

2.1 Structural information for select muscles 16

4.1 Summary of material properties for the musculotendon complex 58

5.1 Parameters characterising a generic human muscle α-motor-neuron pool . . . 69
5.2 Reference values for the rate coefficients determining the cross-bridge kinetics 71
5.3 Overview of muscles for the seed-point generation algorithm case-study . . . 78
5.4 Parameter variations for innervation pattern generation 86

6.1 Element types available in `Abaqus/Explicit` 109

7.1 Mesh details of the prototype masticatory model 126
7.2 Material properties in finite element model of the masticatory system 132

8.1 Motor-unit anatomy parameters for the meta-unit territory distribution variations in the masseter 147
8.2 Experimental and simulated motor-unit territory sizes in the human masseter 149
8.3 Sensitivity of bite force to masseter meta-unit anatomical variations 150

9.1 Cyclic denervation/reinnervation parameters for the idealised geometry . . . 165
9.2 Fibre distribution statistics at the end of the denervation/reinnervation cycles 166
9.3 Cyclic denervation/reinnervation parameters and fibre distribution statistics in the masseter model 168
9.4 Influence of ageing and pathology on peak bite force 168

A.1 Summary of muscle weights, scaling factors and unit vectors for implicit muscles 185

B.1 Masseter motor-unit territory statistics for various distributions 189

Deutsche Zusammenfassung

Motoreinheiten sind die Bausteine der im Skelettmuskel und umfassen alle Fasern, die von einem einzigen Motorneuron innerviert werden. Die Skelettmuskulatur wiederum besteht je nach Muskel aus einigen wenigen bis mehreren hundert Motoreinheiten. Die Fasern der Motoreinheit sind oft auf bestimmte Weise innerhalb des Muskels verteilt und nehmen Teilbereiche seiner Querschnittsfläche ein. Die selektive Rekrutierung der Motoreinheiten ist die Grundlage der funktionellen Heterogenität der Skelettmuskulatur. So sind zum Beispiel die Fasern im tiefen Bereich des Kaumuskels bei der Kieferretraktion aktiver, während die oberflächlichen Fasern bei der Kieferhebung und -protrusion aktiver sind. Hinzu kommt, dass die besondere Anordnung der Fasern einer Motoreinheit in einem Muskel (Motoreinheitsanatomie) im Erwachsenenalter nicht fixiert bleibt. Stattdessen wird die Motoreinheitsanatomie während des gesunden Alterns allmählich und bei neuromuskulären Erkrankungen wie Amyotropher Lateralsklerose (ALS), Cerebral Palsy und Parkinson-Krankheit schneller umgestaltet. Daher ist die Berücksichtigung der Anatomie und Aktivität der Motoreinheit für ein tieferes Verständnis der gesunden und pathologischen Funktion des Skeletmuskelsystems von größter Bedeutung.

Biomechanische Modelle können Einsichten und Daten liefern, die mit experimentellen Techniken praktisch und/oder ethisch nicht erreichbar sind. Modernste dreidimensionale Modelle des neuromuskulären Systems lassen sich in zwei große Kategorien einteilen: makroskopische und mehrskalige Modelle. Die enorme physiologische Detailgenauigkeit, die durch mehrskalige Modelle zur Verfügung steht, geht auf Kosten der Einfachheit der Modelle und der Rechengeschwindigkeit. Diese Modelle werden daher häufig für Analysen auf Mikro- und/oder Gewebeebene verwendet. Andererseits gilt für moderne makroskopische Modelle, die auf Gliedmaßen- oder Gelenkebene verwendet werden, dass Motoreinheiten gleichmäßig im Muskel verteilt sind. Daher sind bestehende Modellierungsansätze entweder zu "herangezoomt" und damit für funktionelle Untersuchungen an der Gliedmaßenskala unpraktisch, oder sie nehmen eine zu globale Sichtweise ein und berücksichtigen nicht die funktionelle Heterogenität der Muskeln.

Ziel dieser Arbeit ist es, diese Einschränkungen durch die Entwicklung einer neuartigen Methode zu überwinden, die bestimmte Aspekte der beiden bestehenden Ansätze kombiniert. Die Muskelaktivität ist, analog zu den Multiskalenmodellen, mikrostrukturell begründet, wenn auch mit einer gröberen Auflösung. Im Gegensatz zu diesen Modellen werden die Bereiche mit Motoreinheiten (Motoreinheitsterritorien) jedoch nicht auf einer Pro-Faser-Basis, sondern gemittelt dargestellt, was über ein Homogenisierungsverfahren berechnet wird. Jede Motoreinheit wird dann mit ihrem eigenen Aktivitätsimpuls angesprochen, wodurch die (räumlich und zeitlich) granulare Natur der Muskelkontraktion erfasst werden kann. Die Berechnung der räumlichen Verteilung, Aktivität und Homogenisierung der Motoreinheiten erfolgt während einer Offlinephase. Dadurch gibt es analog zu makroskopischen Modellen, keine Notwendigkeit mehr, einzelne Fasern während der Laufzeit zu berücksichtigen. Da die (homogenisierte) neuronale Information vorberechnet wird, ist der Berechnungsaufwand des vorgestellten

Motoreinheit-getriebenen Modellierungsansatzes während der Laufzeit minimal im Vergleich zu makroskopischen Status-quo-Modellen. Dies ermöglicht erstmals die dreidimensionale Untersuchung der Beziehung zwischen den individuellen Eigenschaften, Aktivitäten und Anatomie von Motoreinheiten und der motorische Gesamtleistung eines anatomisch realistischen, kontinuumsmechanischen Modells des Bewegungsapparats im Gelenk- oder Gliedmaßenskala.

Modellierung dreidimensionaler Motoreinheiten

Eine der größten Herausforderungen bei diesem Ansatz ist die Definition von anatomisch realistischen, dreidimensionalen Motoreinheitsterritorien. Motoreinheitsterritorien beim Menschen zeigen zwar eine enorme Vielfalt zwischen Muskeln und Individuen, weisen jedoch einige Schlüsselmerkmale auf: sie sind lokal auf Unterregionen des Muskels beschränkt, sie überschneiden sich mit mehreren anderen Territorien, und bestimmte Motoreinheitstypen können bevorzugt in bestimmten Muskelquerschnittsflächen lokalisiert. Bestehende Methoden zur Verteilung von Motoreinheiten verwenden bisher entweder idealisierte Muskelgeometrien, eine vereinfachte Motoreinheitsanatomie oder beides. Darüber hinaus unterscheiden diese Methoden in der Regel nicht zwischen junger, alter und pathologischer Motoreinheitsanatomie.

Um diesen Einschränkungen zu begegnen, wird ein neuartiger Algorithmus zur Konstruktion der Motoreinheitsanatomie entwickelt. Vor der Erzeugung der Motoreinheitsanatomie werden die Muskelfasern in der dreidimensionalen Muskelgeometrie rekonstruiert. Der Algorithmus innerviert dann die virtuellen Muskelfasern, um eine Referenz- oder gesunde Motoreinheitsanatomie zu bilden. Dies geschieht iterativ pro Motoreinheit: Zunächst wird eine zentrale Faser in Bezug auf einen manuell festgelegten Referenzpunkt identifiziert. Danach werden die peripheren Fasern innerviert, nun in Bezug auf die zentrale Faser (der gegebenen Motoreinheit). Der Innervationsalgorithmus wird iterativ fortgesetzt, bis alle virtuellen Fasern innerviert sind. Die Anatomie der Motoreinheit ist durch Abstände gekennzeichnet, die die Suchräume für die zentralen und peripheren Fasern bestimmen. Die Referenzmotoreinheitsanatomie kann einem zyklischen Prozess der Denervation und teilweisen oder vollständigen Reinnervation unterworfen werden, um sich einer gealterten oder ungeordneten Motoreinheitsanatomie anzunähern. Durch die Steuerung von Parametern wie der Häufigkeit des Absterbens der α-Motorneuronen und der Wachstumsrate der Motoneuron-Sprossen, wird eine Vielzahl umgebauter Motoreinheiten, einschließlich Atrophie, erstellt.

Eine gewisse Einschränkung der Abstände zwischen den zentralen und peripheren Muskelfasern und die optionale Anwendung von Zyklen der Denervation/Reinnervation ermöglicht die Rekonstuktion einer Vielzahl anatomisch realistischer, gesunder oder pathologischer, Motoreinheitsterritorien. Die Motoreinheitsanatomie wird dann mittels einer statistischen Methode homogenisiert, um Motoreinheitsterritorien in dreidimensionalen, anatomisch realistischen Muskelmodellen zu generieren. Die räumliche Beschreibungen von Motoreinheitsterritorien werden mit individueller Motoreinheitsaktivität zur Verwendung mit einer kontinuumsmechanischen konstitutiven Beziehung der Skelettmuskulatur kombiniert.

Prototyp eines neuro-muskuloskelettalen Modells

Der integrierte neuromuskuläre Ansatz wird mit einem Prototypmodell des Kausystems demonstriert. Dieses Modell umfasste den Unterkiefer, den rechten Molaren, die linken und rechten Kiefergelenke (Fossae, Gelenkscheiben & Kondylen) und die Kasumuskeln. Die molare Okklus-

alfläche, die Fossae und der Muskelursprung (am Jochbogen) sind im Raum fixiert. Während der Kontraktion der Kaumuskeln übertragen sie über die Muskelansätze Kraft auf den Unterkiefer. Die Kraft ist dann teilweise auf die Kiefergelenke und den Molar verteilt, wodurch ein statischer Biss simuliert wird. Die Kaumuskeln werden mit jeweils 50 *Meta-Einheiten* (die jeweils aus einer Untermenge von Motoreinheiten bestehen) bestückt. Das Ausmaß der Überlappung der Meta-Einheiten und ihre Positionen innerhalb des Kaumuskels werden anhand von Literaturdaten ermittelt.

Zuerst wird das Prototyp-Modell mit dem Status-Quo-Modellierungsansatz verglichen. Im zweiten Schritt wird eine Reihe von Fallstudien durchgeführt, um das Potenzial des integrierten Modellierungsansatzes aufzuzeigen, wie zum Beispiel der Kalibrierung von experimentellen Messtechniken. In den folgenden Unterabschnitten wird zunächst der Modellvergleich behandelt, dann wird jede der (vier) Fallstudien beschrieben.

Einfluss der Kaumuskelmotoreinheiten auf die Beißkraft

Biomechanische Simulationen des Kausystems können einzigartige Einblicke in die Kaumuskelfunktion und die Entwicklung der Okklusionskraft liefern. Die meisten Modelle vernachlässigen jedoch die funktionelle Heterogenität der Kaumuskulatur, indem sie von gleichmäßig verteilten Motoreinheiten in der Kaumuskulatur ausgehen. Das Prototypmodell wird verwendet, um den Einfluss dieser Annahme auf die Bisskraft zu untersuchen.

Durch die sequentielle Rekrutierung der Motoreinheiten des Kaumuskels wird die regionale Kontraktion simuliert, die vom anterioren tiefen Kopf der Kaumuskeln nach außen verläuft. Die resultierende (maximale) Beißkraft wird mit einem Status-quo-Modell verglichen, bei dem die Kaumuskeln durch eine äquivalente, räumlich konstante Aktivität gleichmäßig rekrutiert werden.

Bei einer durchschnittlichen Kaumuskelaktivität von 50 % unterschied sich die Größe der Beißkraft bei einigen Kraftkomponenten um bis zu 40 %. Dabei unterschied sich die vorhergesagte *Richtung* der Beißkraft beider Modelle während des Beißprozesses. Zum Beispiel war der Kraftvektor im Prototypmodell zunächst kraniodorsal ausgerichtet und es erfolgte eine Umorientierung nach kranioventral nachdem die oberflächlichen Motoreinheiten des Kaumuskels aktiviert wurden. Im Status-quo-Modell wurde keine solche Richtungsumkehrung beobachtet. Sowohl Größe als auch Richtung der Beißkraft konvergierten zwischen den beiden Modellen oberhalb von etwa 70 % der Kaumuskelaktivierung.

Der intramuskuläre Druck im Kaumuskel wird ebenfalls zwischen den beiden Modellen verglichen. Bei einer 20 % Aktivierung zeigte das Prototypmodell ausgeprägte Regionen mit hohem (−0,1 MPa) und niedrigem Druck, die den kontrahierenden beziehungsweise inaktiven Kaumuskel-Regionen entsprachen. Das Status-quo-Modell zeigte dagegen keine solchen Extreme in der Druckverteilung und stattdessen war der Druck normal um einen Mittelwert (−0,06 MPa) verteilt.

Diese Ergebnisse deuten darauf hin, dass die Modellierung Motoreinheiten die motorischen Leistung des Kaumuskels und die Beißkraft für niedrige bis mittlere Kontraktionen stark beeinflusst. Dies kann zu besseren Vorhersagen während des Kauens und anderer submaximaler Kauaufgaben, zum Beispiel Bruxismus, führen. Allgemeiner gesagt zeigen die Ergebnisse, dass die räumlich-zeitliche Modellierung der Motoreinheiten in komplexen Muskeln, die an submaximalen Aufgaben beteiligt sind, für das Verständnis ihrer motorischen Leistung von entscheidender Bedeutung ist.

Sensitivitätsanalyse der Beißkraft als Funktion der Motoreinheitsanatomie

Die Anatomie der Motoreinheit variiert zwischen Muskeln und Individuen und ihre selektive Rekrutierung führt zu Variationen in der motorischen Leistung. Um die Auswirkungen der Motoreinheitsanatomie-Variation auf die motorischen Leistung zu quantifizieren, werden mehrere Prototypmodelle erstellt, jedes mit einer einzigartigen Motoreinheitsanatomie. Ein submaximaler Biss wird durch die sequentielle Rekrutierung von 34 von 50 der Motoreinheiten durchgeführt, was einer durchschnittlichen 20 % Aktivität entspricht.

Zwei Arten von Variationen (insgesamt 10) der Motoreinheitsanatomien werden verwendet: Variation der Überlappung und der Position von Motoreinheitsterritorien. Die resultierenden (10) Spitzenwerte der Beißkraft hatten einen Mittelwert von 146 N $\pm$ 7 N in einem Kraftbereich von 26 N. Die Kraftrichtung wurde stärker beeinflusst, wobei der Winkel in der horizontalen Ebene einen Mittelwert von $-78° \pm 34°$ und einen Bereich von 122° hatte.

Die Position des Motoreinheitsterritoriums hatte einen größeren Einfluss auf die Beißkraft als die Überlappung der Motoreinheitsfasern, was weitgehend auf die Veränderungen der Hebelverhältnisse der Motoreinheit zurückzuführen ist. Dies deutet darauf hin, dass aus funktioneller Sicht experimentelle Daten über die mittlere Lage des Motoreinheitsterritoriums und nicht über die individuelle Verteilungen der Fasern der Motoreinheit ausreichen könnten, um das Motoreinheitsanatomiemodell zu charakterisieren.

Bereichsaufgelöste Aktivität und intramuskulärer Druck

Intramuskulärer Druck kann zur Ableitung von Muskelaktivität verwendet werden, da der lokale Flüssigkeitsdruck im Muskel mit der Kontraktion des Muskels zunimmt. Während submaximaler Kontraktionen bleiben jedoch einige Muskelbereiche inaktiv. Diese passiven Regionen erfahren aufgrund der lateralen Kraftübertragung über das Bindegewebe ebenfalls Druckveränderungen. Dabei ist es unklar, inwieweit der Druck in diesen (passiven) Bereichen dazu dienen kann, die Gelenkkraft vorherzusagen.

Dies wird untersucht, indem die Drücke in den aktiven und passiven Bereichen der Kasumuskeln während einer submaximalen Beißsimulation mit der Beißkraft verglichen wird. Der Druck im Kaumuskel wird auf der Grundlage der (mittleren) Aktivität der Region entweder als aktiv oder passiv klassifiziert und mit der Beißkraft über die gesamte Dauer des submaximalen Bisses korreliert.

Im Allgemeinen korrelierten die Drücke in den aktiven Kompartimenten gut mit der Beißkraft, mit einem mittleren Spearman Korrelationskoeffizienten von $r = 0{,}86 \pm 0{,}13$. Die Drücke in den passiven Regionen korrelierten beide weniger stark mit einem mittleren Koeffizienten von $r = 0{,}78 \pm 0{,}22$ und zeigten eine Links- oder Negativschiefe, was darauf hindeutet, dass eine größere Streuung der weniger korrelierten Drücke in den passiven Regionen auftrat.

Dies bedeutet, dass die Verwendung anatomischer Informationen zur Platzierung des intramuskulären Druckkatheters in der Nähe der aktiven Kompartimente seine Vorhersagefähigkeit bei submaximalen Kontraktionen verbessern würde.

Bestimmen der Zuckungseigenschaften der Motoreinheit

Die Identifizierung der individuellen Eigenschaften von Motoreinheiten ist entscheidend für das Verständnis von Muskelkontraktionen. Ansätze wie Spike-triggered-averaging oder neuere faltungsbasierte Methoden können verwendet werden, um Kontraktionseigenschaften

einzelner Motoreinheiten in vivo zu ermitteln. Solche Methoden messen typischerweise (i) die Kontraktionskraft an einem biomechanisch mit dem Muskel verbundenen Punkt und (ii) gehen davon aus, dass die Kontraktionskräfte der einzelnen Motoreinheiten linear aufsummiert werden können, um die Muskelkraft zu erhalten. Um den Einfluss des Messpunktes zu untersuchen, werden ausgewählte Motoreinheiten im Kaumuskel des Prototypmodells stimuliert. Dabei wird die Bisskraft gemessen und die Spannung am Kaumuskelansatz am Jochbogen bestimmt, welche die wahre Muskelkraft darstellt. Das lineare Modell der Muskelkraft wird überprüft, indem zunächst eine Gruppe von Motoreinheiten separat stimuliert und ihre einzelnen Kraftantworten arithmetisch summiert werden. Die gleiche Gruppe von Motoreinheiten wird dann gleichzeitig stimuliert, um die Kraftantwort des gesamten Systems zu erhalten.

Die am Zahn gemessene maximale Kraft unterscheidet sich im allgemeinen Fall von der am Muskel gemessenen Kraft, wobei größere Unterschiede bei größeren Motoreinheiten auftreten: Die Abweichung beträgt etwa 10 % für die Motoreinheit 10 (von 50) und 29 % für die Motoreinheit 40. Die vom linearen Modell vorhergesagten Muskelkräfte lagen ebenfalls unter der vom dreidimensionalen Modell vorhergesagten Muskelkraft. Dabei wächst die Diskrepanz zwischen beiden Modellen mit der Anzahl der aktiven Motoreinheiten; so ist die simulierte Muskelkraft bei vier gleichzeitig aktiven Motoreinheiten um 31 % höher als im linearen Modell. Dies bedeutet, dass erstens die Umverteilung der Spannung innerhalb des Muskels und der dentalen Strukturen (Unterkiefer, parodontales Ligament usw.) zu einer geringeren Kraft am Messpunkt (Molaren) führt als am Muskelursprung. Zweitens lösen die kombinierten Twitches im Vergleich zur linearen Summation der Scherkräfte eine geringere Scherspannung im Muskel aus, was zeigt, dass das lineare Modell die tatsächliche Muskelkraft unterschätzt.

Strukturelle Veränderungen während des Alterns und neuromuskuläre Störungen

Die Veränderungen in der neuromuskulären und muskuloskelettalen Struktur und Funktion, die während des gesunden Alterns und bei neuromuskulären Störungen auftreten, sind komplex, voneinander abhängig und mit experimentellen Techniken schwer zu isolieren. Es bleibt unklar, inwieweit allein die Umgestaltung der Motoreinheitsanatomie die motorische Leistung während des Alterns und bei neuromuskuläre Störungen verändert.

Zu diesem Zweck wird das Prototypmodell verwendet, indem einzelne gesunde, gealterte und kranke Modelle erzeugt werden, die jeweils einen unterschiedlichen Grad an Umbau und Atrophie der Motoreinheit aufweisen. Das heißt, die Rekrutierung, die Zuckungen, die querschnittsspezifische Stärke und die Geometrien des Muskels usw. werden konstant gehalten und nur die Anatomie der Motoreinheiten wird verändert. Die Kasumuskeln werden maximal rekrutiert und die resultierende Beißkraft verglichen.

Der Beißkraftverlust war größer als der Prozentsatz der atrophierten Fasern, zum Beispiel führten 38 % atrophierte Fasern zu einem Spitzenkraftverlust von 51 % verglichen mit gesunden Kasumuskeln. Die *Richtung* der Bisskraft hingegen wurde erst beeinflusst, wenn die Atrophie 50 % überschritt. Selbst wenn die für die Kontraktion verantwortliche Eigenschaften des Muskels unverändert bliebe, reichte die Atrophie der Muskeln allein nicht aus, um den gesamten Kraftverlust zu erklären, und hatte einen nichtlinearen Einfluss auf die Bissrichtung.

Das bedeutet, dass die Veränderungen in der Anatomie der Motoreinheit und ihre Auswirkungen auf die Muskelfunktion, zum Beispiel Veränderungen der Hebelverhältnisse oder der allgemeinen Muskelkontraktionsdynamik, bei der Untersuchung des Kraftverlustes während des Alterns und neuromuskulärer Störungen berücksichtigt werden sollten.

Schlussfolgerung und Ausblick

Der in dieser Arbeit entwickelte Modellierungsansatz ermöglicht zum ersten Mal die Untersuchung der Aktivität und Anatomie einzelner Motoreinheiten im Kontext eines dreidimensionalen, anatomisch realistischen muskuloskelettalen Modells auf der Gelenk- und Extremitätenskala.

Obwohl bestimmte mikrostrukturelle Merkmale idealisiert wurden, und trotz des hier auf Kasumuskeln begrenzten Anwendungsfalls, zeigten das Prototypenmodell und die Proof-of-Concept Untersuchungen das Potenzial dieser integrierten neuro-muskuloskelettalen Umgebung. Durch die Modellierung der lokal aufgelösten Aktivierung der Muskeln wurde die motorische Leistung, in Form von intramuskulärem Druck und Gelenkmoment, stark beeinflusst. Unterschiede in der motorischen Leistung wirkten sich am deutlichsten auf niedrige bis mittlere Muskelkontraktionen aus, was darauf hindeutet, dass Untersuchungen von Aufgaben wie der Bewahrung einer gesunden Körperhaltung und alltäglichen Bewegungen von solchen Modellen profitieren können.

Mechanisch basierte experimentelle Techniken, zum Beispiel Messung des intramuskulären Drucks, Ultraschall, Tensiomyographie, Mechanomyographie und hoch-aufgelöste-Kraftmyographie, profitieren ebenfalls von den Fähigkeiten des vorgestellten motoreinheitsgetriebenen Modellierungsansatzes. Der Grund dafür ist, dass das integrierte Modell gleichzeitig die Beziehungen zwischen der Motoreinheitsaktivität, lokalen strukturellen Veränderungen der Muskeln und der globalen motorischen Leistung aufzeigt. Darüber hinaus könnte die Anwendung des Modells auf der Extremitätenskala auch die Kontrollstrategien für Geräte mit Mensch-Maschine-Schnittstelle, wie zum Beispiel angetriebene Prothesen und -Orthesen, verbessern.

Die vorhergesagte motorische Leistung im Prototypmodell hängt, anders als bei Status-Quo Modellen, stark von einem zunehmenden Clustergrad der Motoreinheitsfasern ab. Ein solches Clustering tritt zusätzlich zur Atrophie allmählich während des gesunden Alterns und schneller bei neuromuskulären Störungen auf. Angesichts der alternden Weltbevölkerung könnte die Berücksichtigung der lokalen Aktivität der Muskeln zunehmend an Bedeutung gewinnen. Mit Blick auf die Zukunft könnten solche Modelle helfen, Phänomene wie Ermüdung zu verstehen und für medizinische Eingriffe, zum Beispiel der Vorhersage von Operationsergebnissen oder der Planung von Bewegungs-Rehabilitationsprotokollen im Zusammenhang mit Trauma, neuromuskulären Störungen oder des Alterns, genutzt werden.

Abstract

Motor-units are the building blocks of force in skeletal muscle and comprise all fibres that are innervated by a single motor-neuron. Skeletal muscles are, in turn, composed of a few to several hundred motor-units, depending on the muscle. The fibres of a motor-unit are often distributed uniquely, and occupy subregions of a muscle's cross-sectional area. The selective recruitment of motor-units is the basis of functional heterogeneity in skeletal muscles. For example, fibres in the deep region of the masseter are more vigorously activated during jaw retraction, and the same is true for superficial fibres during jaw elevation and protrusion. Additionally, the particular arrangement of a motor-unit's fibres in a muscle (motor-unit anatomy) does not remain fixed in adulthood. Instead, motor-unit anatomy is remodelled gradually during healthy ageing, and more rapidly during neuromuscular disorders such as amyotrophic lateral sclerosis (ALS), cerebral palsy, and Parkinson's disease. Therefore, the consideration of motor-unit anatomy and activity is paramount to a deeper understanding of healthy and pathological musculoskeletal system function.

Biomechanical models can provide insights and data that are not practically and/or ethically obtainable via experimental techniques. State-of-the-art, three-dimensional models of the neuromuscular system fall into two broad categories—macroscopic and multiscale. The tremendous physiological detail afforded by multiscale models comes at the cost of model simplicity and computational speed. These models are thus often applied to micro and/or tissue-scale analyses. On the other hand, state-of-the-art macroscopic models, while being used at the limb- and joint-scale, treat motor-units as being uniformly distributed in the muscle. Therefore, existing modelling approaches are either too "zoomed-in" and thus impractical for functional investigations at the limb-scale, or they take too global a view and do not account for the functional heterogeneity of muscles.

This thesis aims to overcome these limitations by developing a novel method which combines certain aspects of the two existing approaches. Muscle activity is microstructurally based, analogous to multiscale models, albeit at a coarser resolution. In contrast to these models, however, the motor-unit territories are not represented on a per-fibre basis, but rather represented in an averaged sense, computed via a homogenisation procedure. Each motor-unit is then supplied with its own activity, thus capturing the (spatially and temporally) granular nature of muscle contraction. The computation of the motor-unit distribution, and activity, as well as the homogenisation procedure occurs during an offline phase. This means that, analogous to macroscopic models, individual fibres are no longer required during run-time. Since the (homogenised) neural information is pre-computed, the computational cost incurred by the proposed modelling approach during run-time is minimal in comparison to status-quo macroscopic models. This allows, for the first time, three-dimensional investigations of the relationship between individual motor-unit-properties, -activities, and -anatomy, and motor-output of an anatomically realistic, continuum-mechanical musculoskeletal system model at the joint- or limb-scale.

Modelling Three-Dimensional Motor-Units

One of the major challenges to this approach is the definition of anatomically realistic, three-dimensional motor-unit territories. Human motor-unit territories, while showing enormous variety between muscles and individuals, have some key characteristics: they are locally confined to sub-regions of the muscle, they overlap with multiple other territories, and certain types of motor-units may be preferentially located in certain regions of the muscle cross-sectional area. Existing methods to distribute motor-units have till now either idealised muscle geometries or simplified motor-unit anatomy, or both. Furthermore, these methods typically do not differentiate between young, aged, and pathological motor-unit anatomy.

To address these limitations, a novel algorithm to construct motor-unit anatomy is developed, including the ability to generate healthy and pathological states. Prior to the generation of motor-unit anatomy, muscle fibres are reconstructed in the three-dimensional muscle geometry. The algorithm then innervates the virtual muscle fibres to form a reference or healthy motor-unit anatomy. This is done iteratively per motor-unit: First, a central fibre is identified in relation to a manually specified reference point. Second, peripheral fibres are innervated, now in relation to the central fibre (of the given motor-unit). The innervation algorithm continues iteratively until all virtual fibres are innervated. Motor-unit anatomy is characterised by distances governing the search spaces for the central and peripheral fibres. The reference motor-unit anatomy may be subjected to a cyclic process of denervation and partial or complete reinnervation, to approximate aged or disordered motor-unit anatomy.

By controlling parameters such as the frequency of motor-neuron death and the rate of motor-neuron sprout growth, a variety of motor-unit remodelling, including atrophy, is achieved. By placing certain restrictions on the distances between the central, and peripheral muscle fibres, and optionally applying cycles of denervation/reinnervation, a wide variety of anatomically realistic, healthy, or pathological, motor-unit territories is possible. The motor-unit anatomy is then homogenised via a statistical method to generate motor-unit territories in three-dimensional, anatomically realistic muscle models. The spatial descriptions of motor-unit territories are combined with individual motor-unit activities for use with a continuum-mechanical constitutive relation of skeletal muscle.

Prototype Neuro-Musculoskeletal Model

The integrated neuromuscular method is demonstrated with a prototype model of the masticatory system. This model comprises the mandible, right molar, left and right temporomandibular joints (fossae, articular discs & condyles) and masseters. The molar occlusal surface, fossae and origin of the masseter (at the zygomatich arch) are fixed in space. When the masseters contract, they transmit force to the mandible via the attachment areas. The contractile force is then routed partly to the temporomandibular joints and partly to the molar, thus simulating a static bite. Each of the left and right masseter is populated by 50 *meta*-units (a meta-unit represents a subset of motor-units). The amount of motor-unit overlap and their positions within the masseter are informed by literature data.

First, the prototype model is compared to the status-quo modelling approach. Second, a series of case-studies are carried out (with the prototype model) to highlight the potential of the integrated modelling approach, for example, to aid the calibration of experimental techniques. In the following subsections, first the modelling comparison is covered, then each of the (four) case-studies are described.

The influence of masseter motor-units on bite force

Biomechanical simulations of the masticatory system can provide unique insights into masticatory muscle function and occlusal force development. Most models, however, assume uniformly distributed motor-units in the masticatory muscles and thereby neglect their functional heterogeneity. The prototype model is used to investigate the influence of this assumption on bite force.

By sequentially recruiting masseter motor-units, regional contraction, progressing outward from anterior deep head, is simulated. The resulting (maximal) bite force is compared to a status-quo model; where the masseters are recruited uniformly by an equivalent, spatially-constant activity. At an averaged 50 % masseter activity, the bite force magnitude differed up to 40 % in some components. The bite force *direction* differed drastically between the two models during the bite process. For example, in the prototype model, the force vector was initially directed cranio-posteriorly and was reoriented cranio-anteriorly as the superficial motor-units of the masseter became active. No such reversal was observed in the status-quo model. Both bite force magnitude and direction converged between the two models above about 70 % masseter activation.

Intramuscular pressure in the masseter is also compared between the two models. At 20 % activation, the prototype model exhibited distinct regions of high (−0.1 MPa) and low pressure, corresponding to the contracting and inactive masseter regions, respectively. The status-quo model, in contrast, did not show such extremes in pressure difference and instead pressure was normally distributed about a mean value (−0.06 MPa).

These results imply that modelling motor-units strongly influences masseter motor-output and bite force for low to medium contractions. This may lead to better predictions during mastication and other sub-maximal masticatory processes, for example, bruxism. More generally, the results highlight that spatio-temporal modelling of motor-units in complex muscles, involved in sub-maximal tasks is vital in understanding their motor-output.

Sensitivity of motor-output to motor-unit anatomy

Motor-unit anatomy varies between muscles and individuals and their selective recruitment leads to variations in motor-output. To quantify the impact of motor-unit variation on motor-output, several prototype models, each with unique motor-unit anatomy, are created. A sub-maximal bite is performed by sequentially recruiting 34 of 50 of each masseters's motor-units, corresponding to an averaged 20 % activity.

Two types of variations (totalling 10) of the motor-unit anatomies are taken: variation of the *overlap* and *positions* of the motor-unit territories. The resulting (10) peak bite force magnitudes had a mean of 146 N$\pm$7 N and a range of 26 N. Force direction was affected to a greater degree, with the angle in the horizontal plane having a mean of −78°$\pm$34° and a range of 122° across all 10 variations.

The position of the motor-unit territory had a greater influence on bite force than the overlap of motor-unit fibres, which is largely due to the changes in motor-unit mechanical advantage. This suggests that from a functional perspective, experimental data of mean territory location, rather than individual motor-unit fibre distributions, may be sufficient to characterise the motor-unit anatomy model.

Regional activity and intramuscular pressure

Intramuscular pressure can be used to infer muscle activity, since local fluid pressure in the muscle increases as the muscle contracts. During sub-maximal contractions, however, some muscle regions remain inactive. These passive regions, due to lateral force transmission via connective tissues, also experience changes in pressure. The degree to which pressure in these (passive) regions can predict joint force is not well understood. This is investigated by comparing pressures in the active and passive regions of the masseters to the bite force during a sub-maximal bite simulation. Pressures in the masseter are classified as either active or passive based on the (mean) activity of the region, and are correlated with the bite force over the entire duration of the sub-maximal bite.

In general, pressures in the active regions correlated well with the bite force, with a mean Spearman correlation coefficient of $r = 0.86 \pm 0.13$. Pressures in the passive regions correlated less strongly, with a mean coefficient of $r = 0.78 \pm 0.22$, and showed a left or negative skew. This indicates that a larger spread of less-correlated pressures occurred in the passive regions.

This implies that using anatomical information to place the intramuscular pressure sensor near the active regions would improve its predictive ability during sub-maximal contractions.

Determining motor-unit twitch properties

Identification of individual motor-unit properties is crucial in understanding muscle contractile behaviour. Approaches such as spike-triggered-averaging or more recent, convolutional techniques can be used to attain twitch properties in vivo. These methods typically (i) measure twitch force at some point biomechanically linked to the muscle and (ii) assume that individual motor-unit twitch forces can be linearly summed to give muscle force. To investigate discrepancies in measurement location, selected motor-units in the masseter of the prototype masticatory model are stimulated, and twitch force measured at the molar and over the masseter origin at the zygomatic arch (the later representing the true twitch force). Linear summation of twitch forces is investigated by first, individually stimulating a set of motor-units and arithmetically summing their twitch responses (linear model). The same set of motor-units are then stimulated simultaneously to obtain the so-called compound twitch.

The twitch forces measured at the tooth underpredicted the twitch forces measured at the muscle, with larger differences (in peak twitch force) arising for larger motor-units: approximately 10 % deviation for motor-unit 10 (of 50) increasing to 29 % for motor-unit 40. The linear model underpredicted twitch force, with the discrepancy increasing with the number of co-contracting motor-units; the compound twitch for four co-contracting motor-units was 31 % higher than the linearly summed counterpart.

This implies that, first, stress redistribution within the muscle and dental structures (mandible, periodontal ligament, etc.) results in a lower twitch force at the measurement point (molar) than at the muscle origin. Second, the compound twitches elicit lower shear stress in the muscle, compared to linear summation of shear, showing that the linear twitch model underpredicts true muscle force output.

Structural and functional changes during ageing and neuromuscular disorders

The changes in the neuromuscular and musculoskeletal structure and function that occur during healthy ageing and neuromuscular disorders are complex, interconnected, and difficult to isolate

with experimental techniques. The extent to which the remodelling of motor-unit anatomy alone alters motor-output during ageing and neuromuscular disorders remains unclear.

The prototype model is used to this end; by generating individual healthy, aged, and diseased models, each with varying degrees of motor-unit remodelling and atrophy. That is, the recruitment, twitch, specific-strength, geometries, etc. are kept constant and only motor-unit anatomy is altered. The masseters in each model are maximally recruited and the resulting bite force is compared.

Bite force loss was greater than the percentage of atrophied fibres, for example, 38 % atrophied fibres resulted in a peak force loss of 51 % compared to the healthy masseters. Bite force *direction* on the other hand was only affected once atrophy exceeded 50 %. Even if the muscle properties responsible for contraction remained unchanged, atrophy of muscles alone was not sufficient to explain all force loss, and had a non-linear effect on bite force direction.

This implies that the alterations in motor-unit anatomy and their impact on muscle function, for example, causing changes in mechanical advantage or overall muscle contraction dynamics, should be considered when investigating force loss during ageing and neuromuscular disorders.

Conclusion and Outlook

The modelling approach developed in this thesis, for the first time, enables the investigation of the activity and anatomy of individual motor-units in the context of a three-dimensional, anatomically realistic musculoskeletal model at the joint- and limb-scale.

Although certain microstructural features were idealised, and although the use-case was limited to the masticatory system, the prototype model and proof-of-concept studies demonstrated the potential of this integrated neuro-musculoskeletal environment. By modelling regional activity of muscles, motor-output was strongly influenced, including intramuscular pressure, shear stress, and joint-torque. Differences in motor-output were manifest at low to medium muscle contractions the most, which suggests that investigations of tasks such as posture maintenance and day-to-day movements would benefit from such models.

Mechanically based experimental techniques such as intramuscular pressure, ultrasound, tensiomyography, mechanomyography, and high-density force-myography can also benefit from the capabilities of the motor-unit driven modelling approach presented. This is because the integrated model simultaneously reveals the relationships between motor-unit activity, local structural changes in muscle, and global motor-output. Furthermore, application of such a model to the limb-scale could also inform control strategies for human-machine-interface devices such as powered-prostheses and -orthoses.

The predicted motor-output in the prototype model, unlike in the status quo model, depends strongly on the degree of clustering of the motor-unit fibres. Such clustering, in addition to atrophy, occurs gradually during healthy ageing and more rapidly during neuromuscular disorders. Given the ageing world-wide population, the consideration of heterogeneous muscle activity via the behaviour of individual motor-units may become increasingly relevant. With an eye towards the future, such models may help understand phenomena such as fatigue and be used to inform medical interventions, for example, by predicting surgery outcomes or planning movement-rehabilitation protocols related to trauma, neuromuscular disorders or ageing.

Nomenclature

General conventions

$(\cdot)^{\mathrm{g}}$	Global coordinate-system
$(\cdot)^{\mathrm{E}}$	Reference coordinate-system
$(\cdot)^{\mathrm{e}}$	Local coordinate-system
$(\cdot)^{\mathrm{M}}$	Muscle parameter
$(\cdot)^{\mathrm{T}}$	Tendon parameter
$(\cdot)^{\mathrm{MTC}}$	Musculotendon parameter
$\dot{(\cdot)} = D(\cdot)/Dt$	Material time derivative
$\breve{(\cdot)}$	Meta-unit parameter
$\det(\cdot)$	Determinant
$\mathrm{Grad}(\cdot)$	Gradient with respect to the reference configuration
$\mathrm{grad}(\cdot)$	Gradient with respect to the current configuration
$\mathrm{Div}(\cdot)$	Divergence with respect to the reference configuration
$\mathrm{div}(\cdot)$	Divergence with respect to the current configuration
$\mathrm{tr}(\cdot) = \boldsymbol{I} \cdot (\cdot)$	Trace operator

Scalars

	Solid mechanics theory	
t	Time	[s]
$\mathcal{B}_0$	Continuum body in the reference configuration ($t = 0$)	
$\mathcal{B}$	Continuum body in the current configuration ($t > 0$)	
$\mathcal{P}$	Particle in $\mathcal{B}$	
$\partial\mathcal{B}_0$	Surface of $\mathcal{B}_0$	
$\partial\mathcal{B}$	Surface of $\mathcal{B}$	
J	Jacobian	
ρ_0	Density in the reference configuration	[g/cm^3]
ρ	Density in the current configuration	[g/cm^3]
$\mathcal{P}_{\mathrm{ext}}$	External power	[J/s]
$\mathcal{P}_{\mathrm{def}}$	Stress power	[J/s]
$\mathcal{K}$	Kinetic energy	[J]

	Musculotendon constitutive law	
Ψ	Internal (strain) energy	[N/mm^2]
E	Young's modulus	[N/mm^2]
ν	Poisson's ratio	
α_{M}	Muscle activity	
λ	Muscle stretch	
λ_{opt}	Optimal muscle stretch	
P_{max}	Maximum isometric specific-strength	[N/mm^2]
$c_{1,2}$	Isotropic material parameters	[N/mm^2]
$c_{3,5}$	Anisotropic-passive material parameters	[N/mm^2]
$c_{4,6}$	Anisotropic-passive material parameters	
c	Incompressibility penalty parameter	[N/mm^2]
f_{l}	Force-length relationship	
$w_{\text{asc,dsc}}$	Anisotropic-active material parameters	
$v_{\text{asc,dsc}}$	Anisotropic-active material parameters	
γ_{M}	Muscle volume fraction	
	Motor-unit activity models	
E	Excitatory drive	
IR_i	Innervation-ratio of motor-unit i	
R_i	Recruitment threshold of motor-unit i	
F_i	Firing rate of motor-unit i	[Hz]
$\tilde{V}_{\text{M}}$	Membrane voltage	
$\tilde{r}$	Calcium concentration	
A_{1-2}	Pre- and post cross-bridge power stroke states	
α_i	Activity of motor-unit i	
	Motor-unit anatomy models	
N_{MU}	Number of motor-units	
N_{FO}	Number of fibre-scaffolds/seed-points	
Λ_{s} & Λ_{f}	Microstructure spacing perpendicular and along fibres	[mm]
R & D	Peripheral and central fibre-scaffold search radii	[mm]
ΔR & ΔD	Increments for R and D	[mm]
λ_{1-3}	Distance skewness factors	
κ	Discrete distribution of motor-unit i	
$\hat{\kappa}$	Homogenised distribution of motor-unit i	
	Ageing & neuromuscular disorder model	
T	Large time span, i.e, $>> t$	
f_{denir}	Frequency of denervation event	[1/T]

n_{denir}	Number of motor-units denervated per denervation event	
$\rho^{\text{I}}_{\text{denir}}$	Probability to denervate type-I motor-units	
t_{dorm}	Dormant time periods before atrophy	[T]
g^{II}_{r} & g^{I}_{r}	Motor-neuron sprout growth rate for type-I & -II motor-units	[mm/T]

Vectors

	Solid mechanics theory	
$\boldsymbol{X}$	Position vector in the reference configuration	[mm]
$\boldsymbol{x}$	Position vector in the current configuration	[mm]
$\boldsymbol{\xi}_0$	Gauß point in the reference configuration	[mm]
$\boldsymbol{\xi}$	Gauß point in the current configuration	[mm]
$\boldsymbol{u}$	Displacement	[mm]
$\boldsymbol{a}_0$	Fibre direction in the reference configuration	
$\boldsymbol{a}$	Fibre direction in the current configuration	
	Motor-unit anatomy models	
$\boldsymbol{c}_{\text{MUT}}$	Motor-unit territory global reference point	[mm]
$\boldsymbol{c}_i$	Motor-unit territory i central reference point	[mm]
$\boldsymbol{s}_k$	Seed-points/virtual neuromuscular junction of fibre-scaffold k	[mm]
$\mathbf{q}$	Stencil for neighbouring seed-points	[mm]
$\mathbf{v}_{1-3}$	Distance skewness axes	

Second-order tensors

	Solid mechanics theory	
$\boldsymbol{I}$	Identity	
$\boldsymbol{F}$	Deformation gradient	
$\boldsymbol{R}$	Rotation	
$\boldsymbol{U}$	Right (material) stretch	
$\boldsymbol{v}$	Left (spatial) stretch	
$\boldsymbol{C}$	Right Cauchy-Green (Green) deformation	
$\boldsymbol{b}$	Left Cauchy-Green (Finger) deformation	
$\boldsymbol{l}$	Velocity gradient	[1/s]
$\boldsymbol{d}$	Rate of deformation	[1/s]
$\boldsymbol{w}$	Rate of rotation	[1/s]
$\boldsymbol{E}$	Green-Lagrange strain	
$\boldsymbol{A}$	Euler-Almansi strain	
$\boldsymbol{\epsilon}$	Small strain	
$\boldsymbol{\sigma}$	Cauchy stress	[N/mm^2]

$\boldsymbol{\sigma}_{\mathrm{D}}$	Deviatoric Cauchy stress	[N/mm^2]
σ_{IMP}	Hydrostatic Cauchy stress	[N/mm^2]
$\boldsymbol{\tau}$	Kirchhoff stress	[N/mm^2]
$\boldsymbol{S}$	First Piola-Kirchhoff stress	[N/mm^2]
$\boldsymbol{P}$	Second Piola-Kirchhoff stress	[N/mm^2]

Sets

	Motor-unit anatomy models
$\mathcal{D}$	Motor-neuron discharge times
$\mathcal{S}$	Seed-points
$\mathcal{F}$	Fibre-scaffold points
$\mathcal{T}_{\mathrm{c}}$	Empty seed-points for central fibre-scaffold search
$\mathcal{T}_{\mathrm{p}}$	Empty seed-points for peripheral fibre-scaffold search

1 Introduction

1.1 Motivation

Figure 1.1: *Movement is a vital part of life. Before we can even talk, we learn to crawl, stand, walk and begin to explore the world (starting with the living-room).*

Our bodies are made to move. Sensory information is integrated in the brain and ultimately governs the actions of the motor system. Although we consciously plan, decide, and are aware of our movements, they seem to be carried out automatically. In other words, not much thought is typically given to the particular intensity and duration of muscle contractions that are required to carry out day-to-day tasks. Rather, these details are handled by the neuromuscular system, where motor-neurons recruit and coordinate muscles in the particular way best suited for a given movement.

The basic functional element of force production in the neuromuscular system is the motor-unit, which consists of all muscle fibres that are innervated by a single motor-neuron (Sherrington, 1929). The force exerted by a muscle depends on the number of motor-units recruited together with the rate of their stimulation (Adrian et al., 1929). As increasing force is demanded of a muscle, a larger number of motor-units are recruited, and their firing rate increases accordingly. Recruitment occurs in order of increasing motor-unit twitch force, referred to as the size-principle (Henneman, 1957) and is so-called because motor-units that produce a larger force tend to comprise more fibres.

Not only do motor-units vary in size, but their fibres are arranged in distinct patterns in a muscle, referred to as motor-unit anatomy or territory. The selective recruitment of motor-units therefore alters the temporal *and* spatial contractile behaviour of muscle. This phenomenon, sometimes called the functional heterogeneity or task-specificity of muscle, means that the nervous system is able to modulate muscle function to meet the varying demands placed on the musculoskeletal system. For example, muscles may contribute differently to different movement tasks by varying their line of action (Herring et al., 1979; Loeb, 1985). This is but one example of the tight linkage between neuromuscular anatomy, activity, and musculoskeletal system function. In an early investigation of skeletal muscle functional heterogeneity, Herring et al. (1979) stated that *"[t]he usual assumptions made about muscles for biomechanical analysis*

such as uniform contraction and constant line of action, are inappropriate for complex muscles [...]".

Motor-unit anatomy, furthermore, does not remain fixed in adulthood. During ageing, motor-units undergo successive cycles of denervation and reinnervation, which leads to both motor-unit fibre clustering and muscle fibre atrophy due to motor-unit loss (e.g. Morris, 1969; Lexell et al., 1988). These changes occur more rapidly and/or to a greater extent during neuromuscular disorders, such as amyotrophic lateral sclerosis (ALS) (Morris, 1969), Charcot-Marie-Tooth disease (Lester et al., 1983) or cerebral palsy (Rose et al., 1998). Therefore, to understand the changes in motor-output during healthy ageing and neuromuscular pathologies, the remodelling of motor-units and its impact on the functional heterogeneity of muscles needs to be taken into account.

Experiments can offer crucial insights into the interplay of motor-unit anatomy, activity, and muscle function. They are, however, faced with certain technical and ethical barriers that limit the type and fidelity of data obtained. In humans, non-invasive techniques such as electromyography, ultrasound, and intramuscular pressure (Floyd et al., 1950; Sejersted et al., 1984; Rutherford et al., 1992), are typically used to infer muscle activity indirectly. The calibration and validation of these techniques is challenging since the neural activity that drives motor-output is typically not known.

Biomechanical models of the musculoskeletal system can be used to augment experimental techniques. Although idealised, these models provide a transparent environment to investigate the relationships between neural-inputs and motor-outputs. These models can be used either to predict movements based on neural activity (forward-dynamics) or to compute neural activities for given movements (inverse-dynamics). So-called Hill-type muscle models typically represent muscles as one-dimensional segments and scale muscle contractile force along a predefined line-of-action (e.g. Zajac, 1989; Delp, 1990). Since these models are computationally inexpensive, they are typically used for multi-muscle, limb, or whole-body movement analysis.

Alternatively, continuum-mechanical macroscopic models treat the muscle as a volumetric, three-dimensional structure and can therefore capture the geometrical and structural features of muscle contraction, e.g., evolving fibre length, pennation angles and contact with other tissues (Johansson et al., 2000; Fernandez et al., 2005), which cannot be taken into account by the Hill-type models due to their oversimplification of muscle anatomy. Despite the detailed structural modelling within macroscopic continuum-mechanical models, a wide practise is to recruit all regions of the muscle simultaneously. In other words, the entire muscle receives the same (time varying) activation. The shortcomings of assuming uniform spatial recruitment is that the functional heterogeneity of skeletal muscles, due to selective recruitment of spatially distinct motor-units, cannot be taken into account.

Another approach to continuum-mechanical skeletal muscle models is the multiscale approach. In multiscale models, individual contractile filaments, sarcomeres, and fibres in the muscle are modelled and thus local muscle contraction is simulated with tremendous detail (e.g. Röhrle et al., 2008). This comes, however, at the cost of model simplicity and computational speed. Therefore, these models are limited to idealised geometries and/or isolated muscle geometries. That is, an anatomically realistic, multiscale model, at the joint-scale, i.e., interacting with surrounding tissues and bones, remains elusive.

The main drawbacks of existing three-dimensional skeletal models for investigating the functional heterogeneity of muscles is that multiscale models are restricted, due to practical reasons, to tissue-level analyses and macroscopic models oversimplify neuromuscular physiology

and thus treat the muscle as a single contractile unit. These models, therefore, are limited in their ability to reveal neuromuscular structure-functional relationships. For example, cerebral palsy causes, in addition to altered neuromuscular-tissue properties and recruitment strategies, changes at the motor-unit anatomical level (Rose et al., 1998). These complex and interrelated alternations typically lead to pathological gait, which often treated via tendon length alteration (e.g. Rutz et al., 2011). Considering these factors simultaneously—alterations in musculotendon structure, neural activity, and motor-unit anatomy—would lead to a more realistic "virtual surgery" and aid in pre-surgical planning. Therefore, to gain a deeper understanding of healthy and pathological limb movement and skeletal muscle motor-output, both neural and muscular systems need to be considered in an integrated sense, at the joint-scale.

This thesis aims to overcome limitations of existing macroscopic and multiscale approaches by developing a model that can both be used at the joint- and limb-scale, with multiple-muscles, and is able to capture the functional heterogeneity of skeletal muscles by modelling anatomically realistic motor-units in three-dimensions. This is done by combining the macroscopic descriptions of muscle structure with neuromuscular information, i.e., motor-unit anatomy and activity, derived from the microscale. By doing so, individual motor-unit activity and anatomy can be linked to overall joint function and limb movement.

In the following, first, the state-of-the-art of continuum-mechanical modelling, experimental evidence of skeletal muscle functional heterogeneity, and the anatomical basis of functional heterogeneity, i.e., motor-unit anatomy, is covered in Section 1.2. Second, the research goals are summarised in Section 1.3. To meet these research goals, a prototype model of the masticatory system is developed and used to perform case studies. The prototype model, and brief introductions to the case studies are given in Section 1.4. Finally, an outline of the thesis is given in Section 1.5

1.2 State-of-the-art

1.2.1 Continuum-mechanical modelling of skeletal muscles

Most (volumetric) biomechanical skeletal muscle models include mechanisms to: activate the muscle via some parameter α_{M}, direct this active stress $\boldsymbol{S}_{\mathrm{active}}$ within the volume according to the arrangement of muscle fibres, and incorporate hallmark muscle properties such as the force-length f_{l} and force-velocity f_{v} relationships (Hill, 1938; Gordon et al., 1966; Zajac, 1989). A generic formula for active stress may be written as

$$\boldsymbol{S}_{\mathrm{active}} \leftarrow \alpha_{\mathrm{M}}\, P_{\mathrm{max}}\, f_{\mathrm{l}}\, f_{\mathrm{v}},$$

where P_{max} is a material parameter (typically in N/mm^2) that scales the magnitude of the active stress. The arrow represents some process which maps the scalar magnitude of the active stress to a three-dimensional stress state, represented by a second-order tensor. The main approaches to do so are discussed below. Additionally, a muscle also passively resists deformation, one method—the so-called active-stress approach[1]—additively splits this contribution, i.e.,

$$\boldsymbol{S}_{\mathrm{muscle}} = \boldsymbol{S}_{\mathrm{passive}} + \boldsymbol{S}_{\mathrm{active}}.$$

[1] An alternative method is the active-strain approach, which uses a multiplicative split of the deformation tensor (e.g. Ambrosi et al., 2012; Hernández-Gascón et al., 2013).

The ways in which each behaviour is derived are plentiful and can be broadly split into two classes—microscopic (multiscale) and macroscopic. In the former approach, the interaction of individual sarcomere filaments are typically modelled, with the relevant electrical and chemical triggers governing their activity (e.g. Röhrle et al., 2008; Röhrle et al., 2012; Heidlauf et al., 2014). For example, the stress of a certain sarcomere at location $\boldsymbol{X}$ in the muscle can be computed via Ca^{2+} concentrations, which can then be normalised to compute muscle activity at the same location, i.e., $\alpha_{\text{M}} \leftarrow \alpha_{\text{M}}(t, \boldsymbol{x})$. The properties of muscle contraction are implicit in the micromechanical interactions of the filaments, for example, the force-length relationship arises naturally due to changes in overlap between the thick and thin filaments. The mapping of (one-dimensional) fibre stresses to the volumetric stress tensor occurs via a homogenisation step, mapping $\boldsymbol{S}_{\text{active}} \leftarrow S_{\text{active}}$ and the geometrical representation of individual fibres ensures that the active stress is directed appropriately within the muscle.

The incredible physiological detail afforded by multiscale models allows precise investigations of the relationships between the microstructure, biochemical/physical-processes and macroscopic muscle contraction and force production (e.g. Heidlauf et al., 2014; Röhrle et al., 2016; Heidlauf et al., 2017). Furthermore, the multi-physics nature of some multiscale models allows the modelling of electrophysiological behaviour of contracting muscles (Mordhorst et al., 2014; Mordhorst et al., 2015). However, this level of physiological fidelity comes at the cost of model-complexity and computational time. To achieve acceptable run-times, these models are typically combined with specialised solution techniques and/or software, e.g., model-order-reduction (Mordhorst et al., 2017) or highly parallel computation (Bradley et al., 2018a; Bradley et al., 2018b; Maier et al., 2019). Even then, such models are typically restricted to idealised geometries (e.g. Mordhorst et al., 2017) and, at best, isolated muscles (e.g. Röhrle et al., 2012; Maier et al., 2019).

Macroscopic models, forgo muscle microstructure and instead describe skeletal muscle behaviour and structure in a homogenised sense. Individual fibres are replaced with a fibre orientation *field*, which describes local variations in muscle anatomy and directs the active stress within the muscle volume. This means that the active stress is not directed by fibre geometry but via a so-called structural tensor, i.e., $\boldsymbol{S}_{\text{active}} \leftarrow S_{\text{active}}\, \boldsymbol{M}$, where $\boldsymbol{M}$ contains the fibre direction information. The deformation of fibres is represented via fibre stretch λ, which is computed from the deformation of the continuum bulk. Muscle behaviour is then captured by lumped phenomenological models acting on λ, for example, the force-length relationship can be defined directly as a function of fibre-stretch $f_l \leftarrow f_l(\lambda)$ (Zajac, 1989).

By doing so, macroscopic models trade physiological accuracy for model simplicity and computational speed, enabling these models to overcome limitations that are typical of more complex and computationally demanding multiscale models. This has lead to the use of macroscopic models at the limb and joint-scale, often involving multiple muscles, and contact between surrounding tissues. For example; forward dynamics simulations of 2-muscle systems to predict static bite force (Weickenmeier et al., 2017) and dynamic movement of the arm (Röhrle et al., 2017); the passive deformation of 11 muscles embedded in soft tissues of the lower-limb stump during contact with a prosthetic (Ramasamy et al., 2018); up to 20 muscle pairs in the face to mimic facial expressions, including interactions with surrounding bones and soft tissues (Wu et al., 2014); or more recently, 23 muscles spanning the shoulder joint, coupled with inverse-dynamics, to compute muscle activities during upper-arm movements (Péan et al., 2019).

Since the microstructural basis of activity is removed, fibres can no longer be grouped

into spatially distinct motor-units and thus muscle activity is applied uniformly throughout the muscle: Gielen et al. (2000), Johansson et al. (2000), Lemos et al. (2001), Oomens et al. (2003), Blemker et al. (2005b), Fernandez et al. (2005), Röhrle et al. (2007), Wu et al. (2014), Fan et al. (2017), Röhrle et al. (2017), Weickenmeier et al. (2017), Ramasamy et al. (2018) and Péan et al. (2019). Status-quo macroscopic muscle models justify the application of a spatially-constant activity by assuming that motor-units are uniformly distributed in the muscle, i.e., $\alpha_{\mathrm{M}} \leftarrow \alpha_{\mathrm{M}}(t) \; \forall \, \boldsymbol{X}$. Such an approach, however, fails to address the ability of the neuromuscular system to alter (regional) skeletal muscle motor-output by selectively recruiting motor-units, which is detrimental to modelling the functional heterogeneity of muscles.

1.2.2 Functional heterogeneity of skeletal muscles

Functional heterogeneity (Herring et al., 1979) refers to the regional variety of a muscle's motor-output. The neuromuscular basis for this is either the recruitment of anatomical neuromuscular compartments (English et al., 1981; Segal, 1992), where muscle compartments are innervated by "private nerve branches". Alternatively, selective recruitment of neighbouring motor-units may occur, leading to regional contraction (e.g. Schindler et al., 2014). Other terms, such as "selective activation", "inhomogeneous activation", "task-dependence/specificity" and "functionally complex" (e.g. Pratt et al., 1991; Holtermann et al., 2005; Holtermann et al., 2009; Miyamoto et al., 2012) are also used to describe the same phenomenon. Some detailed examples are presented below.

Blanksma et al. (1990) used fine-wire electrodes to measure activity in different regions of the temporalis and found that, apart from the anterior regions, the muscle showed alterations in activity in response to changes in bite force direction. Phanachet et al. (2003) used fine-wire electrodes to record electromyography signals of single motor-units at various locations in lateral pterygoid. They found that 14 % of motor-units were specialised to one task. Similarly, Schindler et al. (2014) used fine-wire electrodes in the masseter and found that about half (46 %) of the investigated motor-units were specialised to one task. These findings, among those of Blanksma et al. (1995), Turkawski et al. (1998), Murray et al. (1999), Phanachet et al. (2003), Schindler et al. (2005), Ogawa et al. (2006) and Guzmán-Venegas et al. (2015), reveal the tremendous functional heterogeneity of the masticatory muscles.

Besides the masticatory muscles, other examples of functionally heterogeneous muscles are numerous, for example: biceps brachii (ter Haar Romeny et al., 1984; Pérot et al., 1996; Holtermann et al., 2005), trapezius (Holtermann et al., 2009), rectus femoris (Miyamoto et al., 2012), and triceps surae (Staudenmann et al., 2009; Wakeling, 2009; Csapo et al., 2015).

While the focus till now has been on force production and movement, the functional heterogeneity of muscles also manifests itself in other aspects of motor-output. For example, consider the fluid pressure within muscles, or intramuscular pressure. From a purely mechanical perspective, regional contraction would increase pressure locally due to the law of Laplace (Basford, 2002). These regional pressure variations lead to variations in muscle blood perfusion and may act to mitigate fatigue during sub-maximal sustained contractions (canines—Ameredes et al. (1997); humans—Sjøgaard et al. (1986) and Sjøgaard et al. (1988)).

These experimental observations, among others, highlight the weakness in modelling the muscle as a uniformly contracting unit. Perhaps status-quo macroscopic muscle models can capture muscle contributions to joint-torque and movement in some averaged sense, but the subtleties of regional contraction due to motor-unit activity and anatomy are lost. For

example, in the aforementioned simulation of the shoulder joint (Péan et al., 2019), although the trapezius model is divided into four separate muscles (according to its anatomical subdivisions (e.g. Holtermann et al., 2009)); this may still oversimplify its behaviour. This is because there is evidence that even within a subdivision of the trapezius, selective motor-unit recruitment leads to task-specificity (e.g. Jensen et al., 1997; Samani et al., 2010). Or, consider the static bite force simulation (Weickenmeier et al., 2017), which treats the masseter as a single contracting unit and does not account for the functional heterogeneity of the masseter (e.g. Schindler et al., 2005; Ogawa et al., 2006; Schindler et al., 2014).

1.2.3 Measurement and modelling of motor-unit anatomy

The basis of functional heterogeneity in skeletal muscles is the selective recruitment of motor-units. This section deals, in turn, with the historic development to state-of-the-art of experimental techniques to measure motor-unit anatomy before addressing status-quo computational approaches to model motor-unit anatomy.

Experimental measurement of motor-unit anatomy

The measurement of motor-unit anatomy or motor-unit territories can be broadly classified into direct and indirect methods. Former methods, such as histochemical staining, operate on muscle tissue itself and the latter use biosignals to infer territory location. The typical features that characterise a motor-unit territory are: (two-dimensional) size or (one-dimensional) span, fibre arrangement or density, and position relative to the muscle cross-sectional area or thickness. For example, in various mammals the masseters occupy relatively small fractional muscle cross-sectional area: 4.5–19.6 % compared to limb muscles: 6–76 % (Table 1.1). Furthermore, since motor-units comprise a single fibre-type, often, the distribution of fibre-types can be used as a marker for motor-unit territory location.

Direct methods involve whole muscle cross-sections (animal studies) and muscle biopsies (human studies). Animal studies apply electrical stimulation of an α-motor-neuron axon, together with histochemical staining (glycogen depletion) to identify individual fibres of a motor-unit. Since this is performed manually, only a few motor-units are typically measured per study. The first study to use histochemical staining to investigate motor-unit territory (rat tibialis anterior) was by Edström et al. (1968), who reported motor-unit territories covering 12–26 % of muscle's cross-sectional area. This confirmed the prevailing theory at the time (via indirect methods), that motor-unit territories occupy subregions of a muscle's cross-sectional area and that fibres of different motor-units are found next to each other, i.e., motor-unit territories overlap. Similarly, Burke et al. (1973) reconstructed type-FR and -FF motor-unit territories in a cat's gastrocnemius at various cross-sections along the muscle and found that motor-unit territories are confined to the muscle cross-sectional area and that *"it seems likely that at least* 40–50 *muscle units share any one region within the medial muscle"*.

Bodine-Fowler et al. (1990) formalised the concept of a motor-unit territory boundary by *"connecting outlying fibres by straight lines to form the smallest convex area containing all of the motor-unit fibres"*, which enabled quantitative analysis of fibre distribution within a motor-unit territory. The dispersion of fibres was investigated by computing the local variance in fibre count (density) and revealed that 6 out of 7 motor-unit territories had a fibre distribution different from random. Additionally, their investigations also supported the local confinement of motor-unit territories to subregions of the muscle's cross-sectional area—covering 41–76 %

and 8–22 % of muscle cross-sectional area for soleus and tibialis anterior, respectively. Reports of these and other similar studies on motor-unit territory size are summarised in Table 1.1.

Furthermore, by analysing inter-fibre distances, Bodine-Fowler et al. (1990) quantitatively revealed the existence of "holes" within the fibre distributions, suggesting regions of high and low fibre density within a motor-unit territory. The non-uniform distribution of fibres within a territory may be a remnant of neuromuscular development (e.g. Pfeiffer et al., 1985; Dahm et al., 1988) (cited in Monti et al. (2001)) due to pruning of initially multiply innervated muscle fibres.

An important aspect of the structural changes in skeletal muscles during healthy ageing and neuromuscular disorders is the remodelling of motor-unit anatomy. These investigations are typically performed on biopsies of human muscle, and since a muscle biopsy is devoid of intact α-motor-neuron axons, fibre-type distribution stands in as an indicator of motor-unit territories. The remodelling of motor-units occurs mainly via cycles of denervation and partial or complete reinnervation, leading to both atrophy of some fibres and the clustering of others, during ageing (e.g. Morris, 1969; Lexell et al., 1988) and neuromuscular disorders (e.g. McComas et al., 1973; Lester et al., 1983; Kelly et al., 2018) (Figure 1.2).

Several methods have been proposed to quantify these structural changes, for example, by measuring changes in fibre-type distributions (e.g. Morris, 1969; Johnson et al., 1973b; Lester et al., 1983; Lexell et al., 1988; Lexell et al., 1991). Among these, is the co-dispersion index

Table 1.1: *Motor-unit territory sizes in animals and humans. The method to determine motor-unit territory (MUT) size are GD: glycogen depletion and iEMG, sEMG and HDEMG for needle, surface and high-density surface electromyography, respectively.* † *combined with simulated results.*

			MUT area/%-CSA		
Species	Method	Muscle	Min.	Max.	Source
Rat	GD	soleus	25	75	Kugelberg et al. (1970)
		tibialis anterior	12	26	
		tibialis anterior	6	21	Larsson et al. (1991)
		med. gastrocnemius	8	18	Kanda et al. (1992)
Cat	GD	soleus	41	76	Bodine et al. (1988)
		tibialis anterior	8	22	
Pig	GD	masseter	5	10	Herring et al. (1991)
Rabbit	GD	masseter	4.5	19.6	Kwa et al. (1995b)
			MUT length/mm		
Human	sEMG	vastus medialis	†12	†65	Gallina et al. (2015)
	iEMG	genioglossus	3	14	Luu et al. (2017)
	iEMG	masseter	0.3	19	McMillan et al. (1991)
	iEMG		0.4	13.1	Tonndorf et al. (1994)
	iEMG		0.7	8.6	van Dijk et al. (2016)
	HDEMG		1.2	7.9	Lapatki et al. (2019)

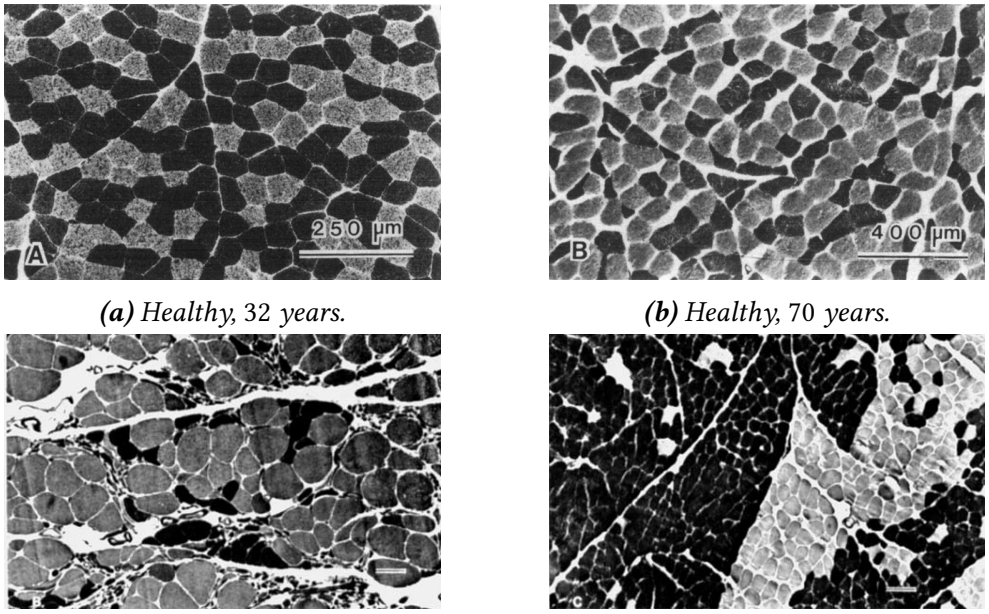

(a) *Healthy,* 32 *years.*

(b) *Healthy,* 70 *years.*

(c) *Amyotrophic lateral sclerosis.*

(d) *Charcot-Marie-Tooth disease.*

Figure 1.2: *Muscle biopsies for healthy (young and old) muscles in (a) and (b) from the vastus lateralus. Pathological muscle biopsies are shown in (c) and (d), the muscle is unspecified, and the scale bar (bottom-right) is* 100 µm. *Type-I fibres are lightly stained and type-II fibres are heavily stained. (a) and (b) reproduced, with permission, from (Lexell et al., 1988) and (c) and (d) from (Lester et al., 1983).*

proposed by Lester et al. (1983), which describes the clustering of fibre-types within a region of muscle cross-sectional area. Segregation of fibre-types yields larger co-dispersion index values, e.g., $+0.27$ and $+0.74$ for amyotrophic lateral sclerosis and Charcot-Marie-Tooth disease, respectively (Figures 1.2c and 1.2d).

Non-invasive techniques such as medical imaging (magnetic resonance imaging or ultrasound) and electromyography (scanning-, needle-, or surface-electromyography), trade in specificity for coverage. That is, a larger number of motor-unit territories can be uncovered, but they are described by their average position in the muscle rather than their individual fibre distributions.

Since motor-unit territory contraction is coupled with electrical activity due to excitation-contraction coupling, electromyography techniques can be used to locate active motor-unit territories indirectly. Early investigations involved intramuscular electrodes together with scanning electromyography techniques, where the electrode is guided through the muscle cross-section and changes in measured potential used to demarcate the active motor-unit territory (e.g. Buchthal et al., 1959). Other studies using scanning electromyography to investigate motor-unit anatomy followed, such as those of McMillan et al. (1991) and Tonndorf et al. (1994).

Today, electromyography remains a popular technique to determine motor-unit anatomy in humans. Needle electromyography, either in a scanning or multi-electrode variant, reveals large numbers of motor-unit territory in human muscles, for example, 30 in the genioglossus (Luu et al., 2017) or 160 in the masseters (van Dijk et al., 2016). Advances in non-invasive, surface electromyography, together with advanced post-processing techniques have remarkably become just as effective as invasive methods in uncovering motor-unit territories: 55 in the medial gastrocnemius (Vieira et al., 2011), 77 in the vastus medialis (Gallina et al., 2015) or 190

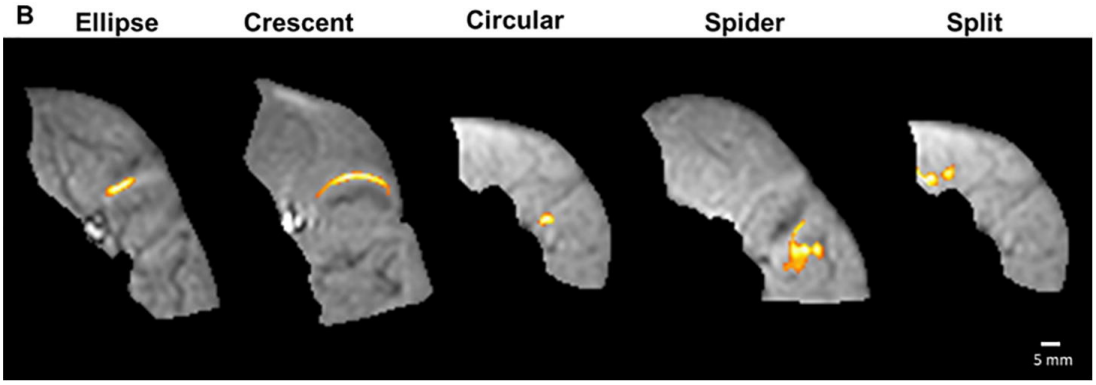

Figure 1.3: *Motor-unit anatomy shapes obtained by Magnetic Resonance Imaging from Birkbeck et al. (2020). Licensed under CC BY 4.0.*[2]

in the masseters (Lapatki et al., 2019) (Table 1.1).

Additionally, medical imaging techniques are also employed to obtain a more detailed picture of motor-unit territories in human muscle. These techniques measure (local) deformations during muscle contraction. While some techniques identify *regions* of local contraction, others are able to demarcate individual motor-unit territories. Deffieux et al. (2008) use high frame rate (up to 2.5 kHz) ultrasound to highlight areas of contractions in the biceps brachii based on tissue velocity. Csapo et al. (2015) were also able to identify regional motor-unit "task groups" using velocity-encoded magnetic resonance imaging in the triceps surae muscle group.

More recently, Rohlén et al. (2020) use high frame rate, high resolution ultrasound to demarcate individual territories in a 4×4 cm cross-section of the biceps brachii. Birkbeck et al. (2020) combined magnetic resonance imaging with external stimulation to image individual motor-unit territories with incredible detail (Figure 1.3).
From the literature, the characteristics of mammalian motor-unit anatomy can be summarised as:

- Territories occupy localised regions within the muscle; some motor-units can occupy up to 75 % of the cross-sectional area.
- Territories overlap with each other, i.e., fibres of 10-50 motor-units can be found within a region of the muscle.
- Fibres within a territory seem to be arranged in sub-clusters separated by "holes" containing relatively few motor-unit fibres.
- Territory shapes are often highly irregular.

In addition to these characteristics, certain muscles show preferential locations of motor-unit types within the muscle cross-sectional area. For example, in the tibialis anterior, where larger motor-units are found to be preferentially located deep in the muscle (Henriksson-Larsén et al., 1985; Mesin et al., 2010) or in the masseter, where higher fractions of smaller motor-units are found posteriorly in the deep head (humans—Eriksson et al. (1983) and Tonndorf et al. (1994); other mammals—Herring et al. (1979) and Turkawski et al. (1998)). However, this seems to vary between muscles and recent studies have challenged these findings, e.g., for the masseter (van Dijk et al., 2016; Lapatki et al., 2019).

[2] https://creativecommons.org/licenses/by/4.0/

Computer modelling of motor-unit anatomy

Algorithms to construct motor-unit fibre distributions have already been employed, for example, by Navallas et al. (2010), Röhrle et al. (2012), Carriou et al. (2016), Robertson et al. (2017) and Botelho et al. (2019), and are able to capture some anatomical features of motor-unit territories, such as territory overlap and their varying sizes. Common to almost all algorithms is a three-step process to construct motor-unit anatomy: First, motor-unit size is determined in terms of the number of fibres it contains. Second, a territory center is selected in the muscle cross-sectional area or volume and third, fibres are assigned to the territory in relation to the territory center. The differences lie in the search algorithms, for example, some assign fibres completely randomly, while maintaining a constant fibre density within the territory, while others use a Gaußian distribution about the territory centers.

However, these algorithms typically do not allow for the restriction of motor-unit types to a subregion of muscle cross-sectional area and idealise both motor-unit territories *and* muscle geometries. For example, muscle cross-section is most commonly represented as a two-dimensional circle (exceptions being Röhrle et al. (2012) and Botelho et al. (2019)). Furthermore, these algorithms make no attempt to replicate or differentiate healthy (young or aged) and pathological motor-unit anatomy. Therefore, these methods may not be suitable for three-dimensional muscle geometries and cannot describe pathological or aged motor-unit distributions.

1.3 Research Goals

The aim of this thesis is to develop a motor-unit driven, three-dimensional, musculoskeletal model at the joint- (and limb-) scale. This is achieved by integrating motor-unit anatomy and activity with macroscopic, continuum-mechanical constitutive relations of skeletal muscle, and is demonstrated via an anatomically realistic, three-dimensional model at the joint-scale. Furthermore, the limitations of existing methods to model motor-unit anatomy are addressed via a novel motor-unit anatomy algorithm, which also has the ability to generate healthy, aged, and pathological fibre distributions.

This necessitates the following research goals:

1. Develop a continuum-mechanical constitutive relation of the musculotendon complex able to account for spatio-temporal motor-unit information.
2. Develop a method to compute individual motor-unit activity.
3. Develop a method to generate anatomically realistic motor-unit anatomy, able to capture healthy, aged, and diseased states.
4. Develop a work-flow to integrate the motor-unit information into the musculotendon complex constitutive relation.
5. Develop an anatomically realistic prototype model and carry out case-studies to demonstrate and highlight the applicability of the integrated neuro-musculoskeletal model.

The methods, workflows, and models developed in this thesis aim at providing deeper insights into the functional heterogeneity of muscles. This has applications in augmenting and calibrating non-invasive experimental techniques to infer muscle activity, informing movement rehabilitation protocols and predicting musculoskeletal surgery outcomes.

1.4 Prototype Masticatory System Model and Case-Studies

The integrated neuro-musculoskeletal modelling approach is demonstrated via a prototype model of the masticatory system. Independent case-studies are carried out with the prototype model to highlight the potential of modelling the neuromuscular and musculoskeletal systems in an integrated sense at the joint-scale. These are introduced, in turn, below.

The influence of masseter motor-units on bite force

Bite force is commonly used to evaluate masticatory performance (Röhrle et al., 2018a). However, masticatory muscle forces are rarely measured directly. Biomechanical models can approximate underlying changes in muscle function related to changes in bite force. Most biomechanical models, however, treat masticatory muscles as line-segments (e.g. Ackland et al., 2017; Stansfield et al., 2018). Furthermore, models that *do* treat the masseters as volumetric muscles, treat them as single contractile units (Röhrle et al., 2007; Weickenmeier et al., 2017). This may oversimplify the function of the masseter, which has shown to be highly task-specific (e.g. Schindler et al., 2014; Guzmán-Venegas et al., 2015).

The aim of this case-study is to quantify the influence of masseter motor-unit recruitment on bite force predictions in comparison to a status-quo approach. The prototype model is used to simulate a maximum voluntary bite force. The simulation is repeated, but with the masseters treated as single contractile units. Differences in both bite force and masseter intramuscular pressure are used to quantify the contribution of individual motor-units to bite force.

Sensitivity of motor-output to motor-unit anatomy

The masseter is typically split into two or three distinct compartments, and motor-units are generally confined within them (Tonndorf et al., 1994). However, the anatomy of masseters can vary considerably between individuals (Cioffi et al., 2012) and this may affect the motor-unit anatomy within the masseter. Its motor-units display task specificity, in that they are selectively recruited for particular bite force directions (e.g. Ogawa et al., 2006). The degree to which the anatomy of motor-units influences masticatory function is not well understood.

The aim of this case-study is to quantify the influence of motor-unit anatomy on joint-function. By systematically varying the motor-unit distribution parameters, multiple prototype models are generated—each with a unique masseter motor-unit anatomy. All models are supplied with the same sub-maximal activity, and the resulting spread of bite forces used as a marker of changes in masticatory motor-output.

Regional activity and intramuscular pressure

Intramuscular pressure is a technique to infer muscle activity. It operates by measuring the hydrostatic fluid pressure within a muscle's fascicles, and shows good agreement with electromyography in predicting joint force (e.g. Aratow et al., 1993; Ateş et al., 2018). During sub-maximal muscle contractions, some regions of the muscle may remain inactive since a fraction of motor-units are recruited. The intramuscular pressure sensor, therefore, may be positioned in a passive, non-recruited region. From a mechanical standpoint, contracting

fibres generate local increases in pressure, i.e., due to law of Laplace (Basford, 2002), and these pressures would be laterally transmitted to the passive regions (e.g. Turrina et al., 2013). However, the (relative) ability of such "passive pressures" to predict joint force remains unclear.

The aim of this case-study is to quantify the predictive abilities of passive and active pressures during a sub-maximal contraction. To this end, the prototype model is used to simulate a sub-maximal bite force by partially recruiting the masseters. Pressures in the passive and active regions are then correlated to the bite force to quantify their predictive ability. Furthermore, by analysing prototype models with various motor-unit anatomies, statistical analysis of the pressure-force correlation coefficients is carried out.

Determining motor-unit twitch properties

Identification of motor-unit contractile properties is important in understanding whole muscle contraction. Despite its many limitations, such as breakdown of the linear summation assumption or sensitivity to motor-unit firing synchronicity (Negro et al., 2014; Dideriksen et al., 2018), spike-triggered-averaging remains a popular technique to measure twitch properties in vivo. Recently, alternative methods, for example, using deconvolution techniques (Negro et al., 2017), have been proposed to overcome certain limitations of spike-triggered-averaging.

Regardless of the method, in vivo measurement of twitch forces restricts (twitch) force measurement at some point biomechanically removed from the muscle. For example, bite force is used to measure masticatory muscle twitches (McMillan et al., 1990). Typically, moment arm and torque computations are used to estimate muscle twitch forces. However, such analyses may be oversimplified, for example, muscle attachment idealised to a point as well as the use of simplified anatomical and rigid geometry.

The aim of this case-study is to quantify the accuracy of using bite force as a measure of masseter twitch response. This is done by individually stimulating masseter motor-units and comparing the forces at the masseter origin and at the molar. Additionally, linear summation of twitch forces is a common assumption of many biomechanical models. The validity of linear summation is quantified by comparing the twitch response of simultaneously stimulated motor-units and the algebraically summed twitch response of individually stimulated motor-units.

Structural and functional changes during ageing and neuromuscular disorders

The breakdown of motor-neurons during ageing and neuromuscular disorders causes pathological functioning of motor-units and can also lead to a total loss of a motor-neuron. This severs the link between the nervous system and muscle fibres, which may either be revived by reinnervation or may eventually atrophy. This process occurs in repeated cycles of denervation and reinnervation and causes reorganisation of motor-unit fibre distribution.

The neuromuscular changes that occur during ageing and neuromuscular disorders are complex, interconnected (Larsson et al., 2018) and challenging to isolate experimentally. For example, the sole contribution of motor-unit remodelling, including atrophy, to loss of muscle function is unclear.

The aim of this case-study is to quantify the force loss caused by muscle remodelling that is typical of ageing and neuromuscular disease. Several prototype models are created, each with varying degrees of motor-unit remodelling, including atrophy. The models are identical

in all other aspects and are supplied with the same recruitment protocol. The simulated maximum voluntary bite force between the healthy, aged, and disordered models are compared to investigate changes in masticatory function.

1.5 Outline

The intermediate chapters, between the introduction and discussion, fall into one of four categories: background and theory (Chapters 2 & 3), modelling the musculoskeletal and neuromuscular systems (Chapters 4 & 5), integration of the neuromuscular and musculoskeletal models (Chapters 6 & 7), and development of the prototype model with associated case-studies (Chapters 8 & 9).

The thesis continues by providing basic physiological background of the neuromuscular system in Chapter 2. It covers neuromuscular anatomy and functioning, including musculotendon complex tissues, excitation-contraction coupling, motor-units and their recruitment.

In this thesis, three-dimensional musculoskeletal system movement is modelled by the theory of continuum mechanics. The mathematical formulation of the theory, including contact mechanics, is briefly given in Chapter 3. Continuum-mechanical problems are typically discretised via the finite element method, which is also briefly covered in the chapter.

The solution of the continuum-mechanical problem is not complete without a description of the materials involved. Large strain, hyperelastic constitutive relations, typical of soft biological tissues, are covered in Chapter 4. Then, specific constitutive relations of the musculotendon complex and other biological tissues are presented (research goal 1), including characterisation of the material parameters to experimental data.

Skeletal muscle activity is based on the sum of individual motor-unit activity and anatomy. The computation of physiologically realistic motor-unit activity and anatomy is covered in Chapter 5. The combination of a recruitment model with cross-bridge- and calcium-dynamics models to compute motor-unit activity is covered first (research goal 2). The larger part of the chapter focuses on the computation of motor-unit anatomy: Focusing first on the approximation of the microstructure, including case-studies of the biceps brachii, lateral pterygoid and masseter. Second, describing the method to generate motor-unit anatomy (research goal 3). The chapter ends by characterising the motor-unit anatomy method and relating distribution parameters to common motor-unit territory metrics.

In Chapter 6, the (macroscopic) mechanical musculoskeletal description and the (microstructural) neuromuscular information are integrated (research goal 4). The chapter begins by describing the process to homogenise the motor-unit territory distributions, and quantifies the error introduced by modelling assumptions. The remainder of the chapter details the implementation of the model, i.e., in a commercial finite element package. Convergence studies are carried out to guide element choice and judge incompressibility behaviour. Finally, the integrated neuro-musculoskeletal finite element model is demonstrated on an idealised geometry.

With the integrated model at hand, Chapter 7 describes the development of a prototype masticatory model (research goal 5). First, a brief physiological background of the masticatory system is given. Then the geometrical development of the model is detailed with an emphasis on the masseters, including the definition of the motor-unit anatomy. In the last section of the chapter, the role of masseter motor-units in generating bite force is investigated and compared to a status-quo model.

In Chapter 8, the prototype masticatory model is used for a series of specialised case-studies (research goal 5). These have already been outlined in Section 1.4, and are: sensitivity of masticatory motor-output to masseter motor-unit anatomy, regional activity and intramuscular pressure, determining motor-unit twitch properties and the influence of ageing and neuromuscular disorders on masticatory motor-output. The impact of ageing and disease on motor-output requires an extension of the motor-unit anatomy method and is therefore covered separately in Chapter 9 (research goal 3).

Although most chapters contain isolated discussions, Chapter 10 discusses and summarises the thesis as a whole. It starts with the major contributions before moving onto the general limitations of the proposed methods and models. The next section then deals with the overall findings and implications of the thesis in the field of biomechanical musculoskeletal simulation. The thesis ends by taking a broader view and proposing future research directions.

1.6 List of Publications

Some research presented in this thesis has previously been published in the following articles.

Peer-reviewed international publications

Saini, H., Ackland, D. C., Gong, L., Cheng, L. K. and Röhrle, O. "Occlusal Load Modelling Significantly Impacts the Predicted Tooth Stress Response during Biting: A Simulation Study". *Computer Methods in Biomechanics and Biomedical Engineering* **23**.7 (2020), pp. 261–270.

Röhrle, O., **Saini**, H., Lee, P. V. S. and Ackland, D. C. "A Novel Computational Method to Determine Subject-Specific Bite Force and Occlusal Loading during Mastication". *Computer Methods in Biomechanics and Biomedical Engineering* **21**.6 (2018), pp. 453–460.

Röhrle, O., **Saini**, H. and Ackland, D. C. "Occlusal Loading during Biting from an Experimental and Simulation Point of View". *Dental Materials* **34**.1 (2018), pp. 58–68.

Peer-reviewed Conference proceedings

Walter, J. R., **Saini**, H., Maier, B., Mostashiri, N., Aguayo, J. L., Zarshenas, H., Hinze, C., Shuva, S., Köhler, J., Sahrmann, A. S., Chang, C.-m., Csiszar, A., Galliani, S., Cheng, L. K. and Röhrle, O. "Comparative Study of a Biomechanical Model-Based and Black-Box Approach for Subject-Specific Movement Prediction". *International Conference of the IEEE Engineering in Medicine & Biology Society (EMBC)*. IEEE, 2020, pp. 4775–4778.

Saini, H., Altan, E., Ramasamy, E., Klotz, T., Gizzi, L. and Röhrle, O. "Predicting Skeletal Muscle Force from Motor-Unit Activity Using a 3D FE Model". *Proceedings in Applied Mathematics and Mechanics* **18**.1 (2018), e201800035.

2 Physiological Background of the Neuro-Musculoskeletal System

The tremendous variety of movements that the human body is capable of, is made possible by the way in which bones, connective tissues and skeletal muscles (the musculoskeletal system) are organised and also by the way in which they are controlled and regulated by the nervous system (the neuromuscular system). The musculoskeletal system is highly varied, involving a multitude of different joint-types, and various sizes, shapes, arrangements, and compositions of some six hundred and forty muscles. Despite this variety, individual muscle and tendons (musculotendon complex) share commonalities, being adapted to each joint. The anatomy and function of the musculotendon complex are discussed in Section 2.1.

Such a complex movement apparatus requires an appropriately rich and varying control mechanism to exploit its potential, and to do so efficiently. While voluntary movement is initiated and planned by the central nervous system, it is the peripheral nervous system which directly innervates the skeletal muscles and causes them to contract. The organisation and recruitment principles of the neuromuscular system are discussed in Section 2.2.

2.1 The Musculotendon Complex and Muscle Contraction

While bones and connective tissues provide, quite literally, the skeleton or framework for human movement, the driver of movement is skeletal muscle contraction. The musculotendon complex is composed of connective tissues and the skeletal muscle itself. A brief description of each of these components is given in the following.[1]

The diversity of the size, shape, and arrangements of skeletal muscles enables, in part, the wide range of human movement tasks. A selection of muscle properties is given in Table 2.1. The number of fibres in a muscle range from about ten thousand, e.g., lumbircales-1 up to almost a million, e.g., masseter. The shape of muscles also varies according to the tasks they perform, e.g., the short and thick masseter can produce large forces over a short distance while the long and slender Sartorius produces force quickly and over a larger contraction range. Additionally, the arrangement of muscle fibres is also specialised between muscles, classified as parallel, fusiform, or (uni-, bi- and multi-) pennate. Most muscles have a fusiform arrangement, e.g., biceps brachii. In pennate muscles, fibres insert into tendons at some oblique angle, typically not exceeding 20 degrees in humans (e.g. Chleboun et al., 2001; Kawakami et al., 2006). The pennated fibres enable a greater cross-section of fibres, termed *physiological* cross-sectional area, within the same muscle volume. This comes at the cost of shorter fibres, which operate over a shorter (optimal) range (e.g. Gans, 1982; Chleboun et al., 2001) compared to parallel or fusiform fibre arrangements.

[1] Further details on these and other topics, e.g., vasculature, can be found in Kandel et al. (2000), MacIntosh et al. (2005) and Korthuis (2011).

Table 2.1: *Structural information for select muscles. Muscle volumes are given for males (M), females (F) and mixed/not-specified (NS). The superscirpt $(\cdot)^*$ indicates data from Enoka (1995), and with $(\cdot)^\dagger$ from MacIntosh et al., 2005.*

			Volume/cm^3			
Muscle	α-MN	Num. fibres	M	F	NS	Source
lumbricales-1	93*	$1.0 \times 10^{4*}$	–	–	–	
sartorius	–	$1.3 \times 10^{5\dagger}$	100[(a)]	161[(a)]	–	[(a)]Amabile et al. (2017)
brachiorad.	333*	$1.3 \times 10^{5*}$	–	–	65[(b)]	[(b)]Holzbaur et al. (2007)
tibialis ant.	445*	$2.5 \times 10^{5*}$	–	–	253[(c)]	[(c)]Belavý et al. (2011)
medial gastroc.	579*	$1.1 \times 10^{6*}$	–	–	231[(c)]	
masseter	1452[(d)]	9.3×10^{5}[(d)]	33[(e)]	22[(e)]	–	[(d)]Carlsöö (1958) [(e)]Cioffi et al. (2012)

2.1.1 Connective tissues

The epimysium is the outermost, dense connective tissue surrounding the entire muscle belly. It provides structural integrity to the muscle and reduces friction against neighbouring tissues during movement. The epimysium thickens and merges with the distal tendons of the muscle and therefore provides some degree of force transmission to the tendons (Turrina et al., 2013).

Within a muscle, bundles of fibres are separated into fascicles, surrounded by perimysium, which plays an important role in force transmission towards the bones (Turrina et al., 2013). Individual muscle fibres are, in turn, also wrapped in connective tissue: the endomysium. While the majority of contractile force is transmitted along muscle fibres, the endomysium facilitates lateral force transmission to the neighbouring fibres (e.g. Purslow, 2010; Turrina et al., 2013). The collagen of the three connective tissues ultimately merge with the bones via tendons, aponeurosis (found in flat muscles with wide attachment areas, e.g., masseter), fascia or directly with bone via the periosteum and thus transfers skeletal muscle force to the skeleton.

2.1.2 Sarcomeres and excitation-contraction coupling

The fundamental unit of force production within skeletal muscles is the sarcomere, which is an arrangement of thick and thin filaments (contractile proteins) between so-called Z-disks (Figure 2.1). The interaction of the thick and thin filaments gives rise to sarcomere force production. The thick filaments are composed of myosin molecules, which are coiled and have two globular heads protruding from the entire length of the filament. Surrounding the thick filaments are six thin filaments, which are primarily composed of actin molecules wrapped in the proteins tropomyosin and troponin. These two proteins act to control the interaction, and thus force generation, between actin and the myosin heads. The thin filaments are anchored at either ends of the sarcomere to the Z-disks and the thick filament is located centrally, giving rise to alternating light and dark bands observed under microscopy.

During contraction, the filaments slide relative to each other, bringing the Z-disks towards the center of the sarcomere, described by the sliding filament hypothesis, proposed (independently)

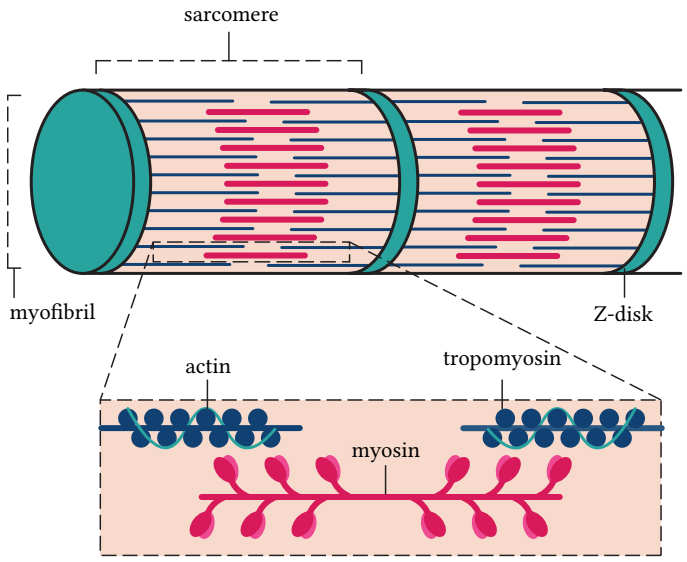

Figure 2.1: *Simplified myofibril (top) and sarcomere (bottom) structure. The myosin (with heads) forms the thick filaments (red). The actin forms the thin filament (in blue) and is surrounded by a coil of tropomyosin (green).*

by Huxley et al. (1954a) and Huxley et al. (1954b). Contraction is initiated in response to an action-potential propagating across the sarcolemma, travelling down the transverse-tubules and causing a release of calcium (Ca^{2+}) from the terminal cisternae into the sarcoplasm of the fibre. The binding of Ca^{2+} to troponin causes a conformational change removing the tropomyosin enabling the linkage of the myosin globular heads and actin, referred to as a cross-bridge. Upon linkage, myosin heads perform mechanical work and pull the actin towards the center of the sarcomere, referred to as the power-stroke state, and consume chemical energy via adenosine diphosphate.

After the power-stroke, adenosine triphosphate binds to the myosin head leading to cross-bridge detachment, where adenosine triphosphate is hydrolysed to adenosine diphosphate (and inorganic phosphate), returning the myosin head to its pre power-stroke, or primed, state. The process of cross-bridge attachment, power-stroke, detachment, and return to the primed state is referred to as cross-bridge cycling. As long as the actin binding sites remain exposed, i.e., Ca^{2+} concentration is maintained, the cross-bridge cycle repeats. The transformation of an action-potential to cross-bridge cycling and force production is called excitation-contraction coupling. Since a single action-potential does not release enough Ca^{2+} to form all cross-bridges in the muscle fibre, repeated action-potential are required in quick succession to increase Ca^{2+} concentration, thereby increasing fibre contraction strength. The number of fibres recruited and the rate of action-potential firing are governed by neural principles, discussed in Section 2.2.

2.1.3 Muscle fibres

The structure of skeletal muscle is hierarchical and is composed of several repeating units. These are, in the order of smallest to largest: sarcomeres, myofibrils, muscle fibres and fascicles (Figure 2.2). Sarcomere lengths range from 1.5–3.5 µm (Kandel et al., 2000) and are arranged in series to form the myofibrils, which have a diameter of approximately 1 µm (Colomo et al.,

1997). Myofibrils are grouped together to form muscle fibres, which have lengths ranging from 1–500 mm and diameters from 10–60 µm (Kandel et al., 2000). As previously mentioned, a single muscle may contain between 100–1,000,000 fibres.

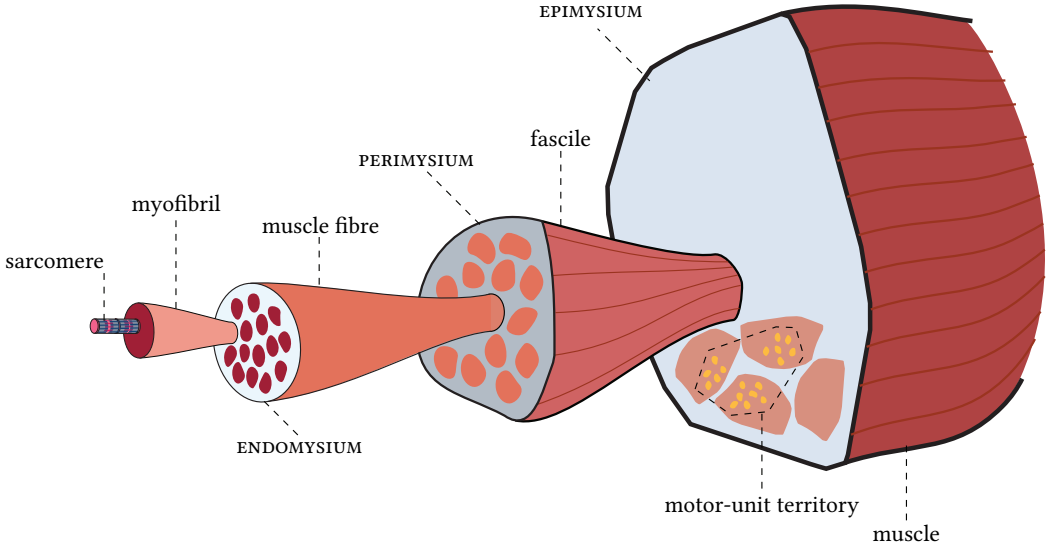

Figure 2.2: *Hierarchical structure of skeletal muscle from the largest (right) to smallest (left) components. Muscle fibres innervated by a single α-motor-neuron are shown in yellow; the region they occupy is the motor-unit territory.*

Muscle fibre contractile force

Since each cross-bridge generates force independently, the total force generated by the muscle fibre depends on the amount of overlap between the thin and thick filaments of the fibre's constituent sarcomeres. Therefore, there exists an optimal fibre (and therefore muscle) length, at which a maximum amount of overlap between the filaments in the cross-bridges is attained and thus maximum relative force is produced. As fibre length decreases, the thin filaments overlap and effectively block each other, thus reducing overlap with the thick filaments. On the other hand, as fibre length increases the thin filaments are pulled beyond the ends of the thick filaments and the filament overlap decreases. Experimental observations of the length dependence of sarcomere tension, by Gordon et al. (1966),[2] are schematically shown in Figure 2.3a.

The peak rate at which muscle fibres can contract is limited by the speed of the cross-bridge cycling. At increased contraction velocities, the speed of thin filament sliding prevents every myosin head from finding an attachment site and thus a reduction in force is observed as contraction velocity increases (Hill, 1938). Extension of fibres during a contraction results in passive stretching of the attached cross-bridges and thus a higher (resistive) force is attained (Figure 2.3b). Shortening and lengthening contractions are referred to as concentric and eccentric contractions, respectively, and those with no change in length as isometric contractions.

[2]Data points digitised via `PlotDigitizer` (Huwaldt, 2015).

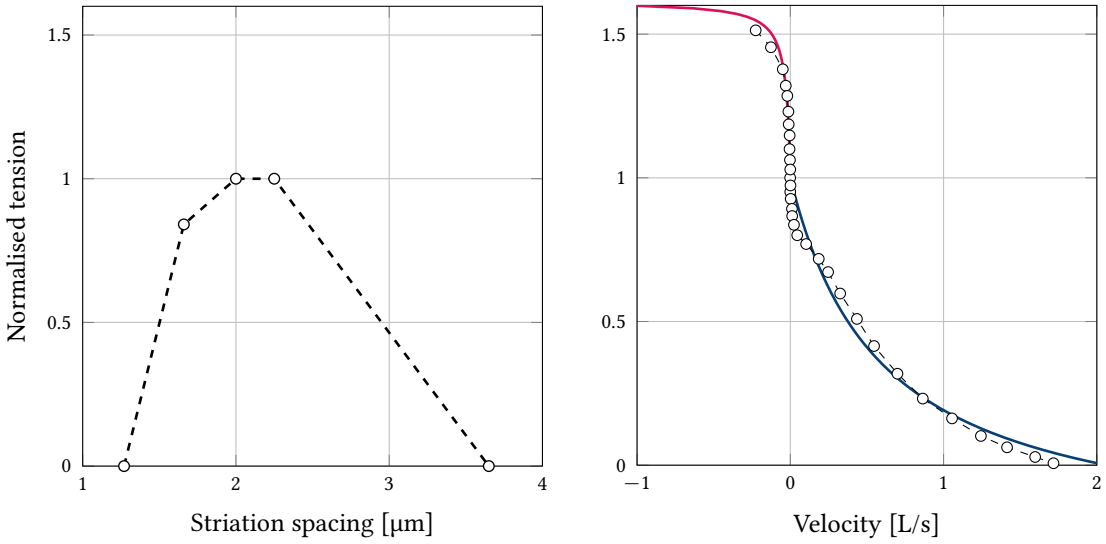

(a) *Force-length dependency.* ***(b)*** *Force-velocity dependency.*

Figure 2.3: *Force-length relationship of sarcomeres and force-velocity relationship of muscle fibres. Data points shown as circular marks connected via dotted lines. A fit to the data is shown as a solid line. (a) Experimental data from Gordon et al. (1966), (b) experimental data from Edman (1988) (fitting equation and parameters from Alcazar et al. (2019)) and eccentric and concentric contractions are shown in red and blue, respectively.*

Muscle fibre-types

Historically, the speed of contraction was used to differentiate muscle fibres—with those exhibiting low and high rates of contraction denoted as type-I (or slow) and type-II (or fast) fibres, respectively. Currently, histochemical (ATPase staining),[3] myosin isoform identification and metabolic enzyme identification are used to differentiate fibre-types. The rate of ATPase hydrolysis (energy released to reset the myosin head to the cocked position) is two to three times higher in fast fibres compared to slow fibres. An indirect measurement of this rate is the amount of ATPase within a fibre, corresponding to the intensity of staining. Traditionally, this yields an additional classification of fibre-types: type-IIA and type-IIB, with the latter containing more ATPase and having a higher rate of shortening. With recent advances in technology, up to a total of seven fibre-types in human have been classified according to histochemical staining (from slowest to fastest) as type- I, IC, IIC, IIAC, IIA, IIAB and IIB (Scott et al., 2001, and references therein).

Alternatively, energy metabolism may be used to classify muscle fibres, reflecting metabolic pathways which are either oxidative (aerobic) or glycolytic (anaerobic). This leads to three fibre-types: slow-twitch oxidative (SOG), fast-twitch oxidative (FOG) and fast-twitch glycolytic (FG). A strong enough correlation exists between type-I, -IIA and -IIB with SOG, FOG and FG fibres, therefore, these terms are often used interchangeably. Type-IIA and -IIB fibres may, however, use both glycolytic and oxidative metabolism pathways. Oxidative capacity is proportional to the amount of myoglobin and number of capillaries, giving fibres with this metabolism a

[3]Histochemical staining involves chemical reactions between some applied agent and a molecule of interest, e.g., ions, lipids, amino-acids, saccharides (such as glycogen), resulting in an observable change (or marking) of the molecule. Particular reaction procedures illicit this change for particular molecules, e.g., the Periodic Acid Schiff reaction is used for the detection of glycogen. An early review on the topic can be found in Ali Khan (1976).

reddish appearance. Conversely, fibres predominantly using glycolytic metabolism appear white.

Non-spanning muscle fibres

The classical or intuitive view of skeletal muscle fibres is that they have an approximately constant cross-section and extend "end-to-end" within a muscle, i.e., they have the same length as the muscle fascicles. Then, any and all active tension produced by the fibres is transferred (directly) to the connective tissues at either end of the muscle fibre. Experimental evidence has shown, however, that some muscle fibres in certain species, including humans, terminate within the muscle (intrafascicularly) at either or both ends of the fibre. These non-spanning muscle fibres show a progressive decrease in cross-sectional area, commonly referred to as tapering, and terminate within intramuscular connective tissue (e.g. Trotter, 1990). Such non-spanning muscles have been observed in humans, particularly in the sartorius, gracilis, biceps femoris, semitendinosus and semimembranosus muscles (Trotter, 1993, Table 4) and the brachoradialis muscle (Lateva et al., 2010, and references therein). Interestingly, neither the internal organisation of the muscle fibres, e.g., sarcomere lengths, nor the sarcomere activity, changes towards the tapered ends of the fibre.

In light of these observations, several theories have emerged to explain the occurrence of non-spanning fibres. One such theory is that the curved surface acts to reduce stress concentrations at fibre ends. Mathematical analysis of idealised fibre shapes has shown that cylindrical fibres would give rise to shear stress concentrations at the fibre end, while a conical shape acts to avoid stress concentrations (e.g. Zhang et al., 2012). This comes, however, at the trade-off of fibre volume and thus tension production, which can be mediated by a curved profile (e.g. Trotter et al., 1992). It has been proposed that the fibre adapts to the local stress environment to optimise smooth stress transmission, giving rise to a variety of fibre tapering profiles (e.g. Trotter, 1993; Monti et al., 2001, and references therein). Another reason for shorter muscle fibres is to avoid heterogeneous tension production along the fibre due to conduction delays in longer fibres (Monti et al., 2001, and references therein).

Force transmission between non-spanning fibres occurs via the intramuscular connective tissue. A distinction has to be made between in-series fibres and more general non-spanning fibres. The former may be thought of as essentially a "classical" tendon-to-tendon fibre, interrupted by connective tissue, the so-called myomuscular junction. The latter simply refers to any fibre which terminates intrafascicularly, including those which may have significant amounts of overlap with other fibres. It appears that (non tapering) in-series fibres and myomuscular junctions are a relatively rare occurrence and that *"in muscles composed of discontinuous fibres, the single muscle fibres overlap one another"* (Trotter, 1993) (see also Huijing (1999a)). Force transmission between non-spanning fibres is thought to occur largely via shear stresses over the overlapping portion of the fibres (e.g. Trotter et al., 1992).

Whether muscle fibres run the entire length of the fascicle, taper and terminate within the muscle belly or are blunted and connected via myomuscular junctions, the function of a muscle fibre remains that of tension production. As argued by Monti et al. (2001), *"[f]rom a functional viewpoint, whether these long fibres are composed of a series of shorter fibres or are a single anatomical entity may not be the important factor to consider"*. Therefore, a distinction can be made between an anatomical and a functional muscle fibre: a functional fibre is defined as comprising multiple anatomical fibres joined via connective tissue.

A particular form of non-spanning fibres are those where neighbouring fibres are divided

regularly along their length. For example, nearly all fibres in the cat's semitendinosus are divided by a connective tissue inscription approximately one third from its proximal end, dividing the muscle into two compartments, with each compartment individually innervated (e.g. Kellis et al., 2012). This in-series arrangement of (all) muscle fibres is thought to allow for control of contractile length characteristics while maintaining overall force (Monti et al., 2001, and references therein). Apart from the rectus abdominis, such muscles are generally not found in humans.

2.2 The Neuromuscular System

The organisation, planning, and execution of voluntary movement originates from the central nervous system. This process of the integration of sensory information, together with the coordination of movement is highly complex and beyond the scope of this thesis, for further details, see Kandel et al. (2000, Chapter 33).

Once the multitude of factors has been integrated by the central nervous system and the command for a voluntary movement is issued, the peripheral nervous system takes over. Motor-neurons recruit the right amount of motor-units for the required duration to best carry out the desired movement. Voluntary movement is seldom a top-down, one-way process. Whether maintaining sitting posture during a long day of writing, or quickly moving out of harms way, seemingly automatic responses integrate feedback from sensory organs. Spinal reflexes respond to sensory information from the muscles, joints, and skin, which are integrated in the spinal cord. The feedback pathways of the neuromusculoskeletal system are beyond the scope of this thesis, for further details, see Kandel et al. (2000, Chapter 35) or Gandevia et al. (2002). The central nervous system does not independently and individually control every single muscle fibre, but rather higher level recruitment principles in conjunction with the peripheral nervous system are employed to reduce mental effort involved with movement (Enoka, 1995). The organisation of the peripheral nervous system in regards to motor-control is discussed below.[4]

2.2.1 The motor-unit

The building block of force production is the motor-unit. First proposed by Liddell et al. (1925), later refined by Sherrington (1925), in which the motor-unit is defined as *"the muscle fibres innervated by the unit and the whole axon of the motoneuron"*, i.e., the α-motor-neuron and all muscle fibres that it innervates. Numbers of motor-units, and therefore α-motor-neurons, in muscles can vary between ten to several thousand (Table 2.1). The ratio of number of fibres within each muscle to the number of α-motor-neuron is referred to as the *average* innervation-ratio, and can range between approximately 110–1732 fibres, for the lumbricalis-1 and medial gastronemius, respectively (Feinstein et al., 1955) (also Table 2.1). On the other hand, the innervation-ratio indicates the number of fibres innervated by a *single* α-motor-neuron and corresponds to the increment in force when that motor-unit is recruited. Therefore, the innervation-ratio, and to a degree the average innervation-ratio, provides an indication of the

[4] The anatomical arrangement of motor-units within skeletal muscle, and the consequences it has on muscle function, is of central importance in this thesis. The state-of-the-art of these topics were therefore discussed in Chapter 1.

fineness of motor-control, where a low innervation-ratio corresponds to small force increments and thus finer control. An argument could be made that larger muscles do not require fine control, therefore the smaller the muscle (regarding raw size), the lower the innervation-ratio should be—this is partly supported by experimental data (Enoka, 1995, and references therein).

By analysing the magnitude and rate of force production in response to a single action-potential, a motor-unit can be classified as either slow- or fast-twitch. Slow-twitch motor-units produce lower force and have longer rise times compared to fast-twitch variants (Figure 2.4). The property of a motor-unit depends on the properties of its constituent muscle fibres, so slow-twitch, or type-S, and fast-twitch, or type-FR and -FF, motor-units are comprised largely of type-I, type-IIA and -IIB fibres, respectively (Section 2.1.3).

Classifying the number of motor-units within a given muscle, according to the peak twitch force produced, reveals that there are a large number of motor-units which produce a low force and a small number of motor-units that produce a large force (e.g. van Cutsem et al., 1997). Experimental results suggest that the magnitude of motor-unit force is determined largely by its innervation-ratio, and to a lesser degree by the radii of its constituent fibres and their specific-strength (Kanda et al., 1992; Enoka, 1995). Therefore, the motor-units which produce a low force are also those with low innervation-ratios. Given this correlation between force and size, the terms slow and small motor-unit are often used interchangeably; similarly for fast and large motor-units.

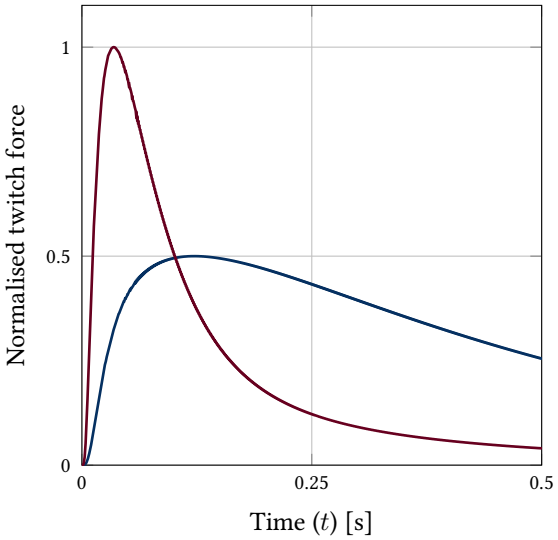

Figure 2.4: *Twitch responses of the smallest: dark-blue and largest: maroon motor-units.*

2.2.2 Recruitment of motor-units

The recruitment of motor-units within a muscle occurs according to the so-called size principle, first proposed by Henneman (1957), essentially stating that α-motor-neurons are recruited in the order or increasing size. Motor-unit size is positively correlated with α-motor-neuron size. Smaller α-motor-neurons have a larger resistance, therefore the same stimulation current results in a higher voltage potential as compared to larger α-motor-neurons, causing a discharge of an action-potential in the former but not in the latter. For this reason, smaller and larger

motor-units are often referred to as low- and high-threshold motor-units, respectively. This indicates that during a ramped voluntary contraction, the smaller motor-units which are numerous and produce low forces slowly, are recruited before those larger motor-units, which are fewer but produce large forces rapidly. This is advantageous since movements requiring low amounts of force only involve smaller motor-units, which are less fatigable and allow for finer control (due to lower innervation-ratio). The larger motor-units then effectively "stand-by" to provide short bursts of high force.

Stimulation of a motor-unit with a rapid series of action-potentials, i.e., with a time delay smaller than twitch force drop off, results in a summation of motor-unit force magnitude attaining some maximum level at a given stimulation frequency, referred to as a tetanic contraction or tetanus. The total force output of a skeletal muscle is a function of its motor-units, both regarding the number of motor-units which are recruited and the rate at which they are firing (Adrian et al., 1929). Generally, the recruitment of additional motor-units accounts for a larger portion of force increase than does the increase in their firing rate, e.g., additional recruitment accounts for $\approx$80 % of force (e.g. De Luca et al., 1982). The motor-unit firing rate(s) can be described as linearly proportional to the volitional effort placed on the muscle (Kernell, 1965). Discharge rates typically vary between 5–35 Hz, with upwards of 100 Hz observed in some muscles, e.g., the aductor policis (muscle of the hand) (Enoka, 1995, and references therein).

3 Theoretical Framework of the Mechanical Problem

The same principles that are used to predict the deformation of a spring under weight can be applied to more complex cases, for example, predicting failure stresses within a bridge or the movement of a limb. Namely, by representing the real, mechanical system as a mathematical model. Such models have proved immensely useful for the analysis of physical problems and "import" real world systems into mathematical (Euclidean) space and time. This chapter discusses the mathematical theory typically used to construct and solve problems of solid mechanics.

In mechanics, motion can be classified as kinematic or deformational. The former deals with rigid bodies undergoing large motions while the latter is described by Cowin (2013) as *"a motion in which some points on the same object move relative to one another"*. The theory used to describe and analyse deformable motion is the continuum model, typically referred to as continuum mechanics (Section 3.1).

While the calculation of the spring deformation mentioned earlier is possible on pen and paper, for example, via Hooke's law, the system of equations deriving from continuum-mechanical models makes this tedious and impractical. In fact, finding exact (or strong) solutions to most continuum-mechanical problems is not possible, instead an approximate (or weak) solution is sought after. One of the most important methods to obtain such weak solutions is the finite element method (Section 3.2). Lastly, the extension of the theory to include interactions between bodies, i.e., contact mechanics, is briefly presented (Section 3.3).[1]

3.1 Continuum Mechanics

Concerning different approaches to solve mechanical problems, Clifford Truesdell III (1919-2000), a pioneer of continuum mechanics, in "*The Non-linear Field Theories of Mechanics*" s(Truesdell et al., 2004, originally published in 1965), writes:

> *Matter is commonly found in the form of materials. Analytical mechanics turned its back upon this fact, creating the centrally useful but abstract concepts of the mass point and the rigid body, in which matter manifests itself only through its inertia, independent of its constitution; "modern" physics likewise turns its back, since it concerns solely the small particles of matter, declining to face the problem of how a specimen made up of such particles will behave in the typical circumstances in which we meet it. Materials, however, continue to furnish their masses of matter we see and use from day to day: air, water, earth, flesh, wood, stone, steel, concrete, glass, rubber, ... All are deformable. A theory aiming to describe their mechanical*

[1] Further references for the detailed treatment of continuum-mechanics, the finite element method and contact mechanics, including those used in this chapter, are: Bonet et al. (1997), Holzapfel (2000), Truesdell et al. (2004), Zienkiewicz et al. (2005), Wriggers (2006) and Cowin (2013).

behavior must take heed of their deformability and represent the definite principles it obeys.

A description of the basics of continuum mechanics follows, with the application to biomechanical problems in mind. That is, multiple bodies (muscles, bones, and other soft tissues) undergoing large deformational and/or rigid body movement and in contact with each other. First, the kinematic, strain measures and rate of deformations are treated (respectively in Sections 3.1.1, 3.1.2 and 3.1.3), followed by the concept of stress (Section 3.1.4). The focus is then shifted towards formulating the initial boundary value problem of solid mechanics, by first introducing the fundamental balance relations (Section 3.1.5) and then forming the initial boundary value problem itself (Section 3.1.7).

3.1.1 Kinematic relations

Continuum mechanics, while not excluding rigid body motion, is primarily concerned with the movement of particles relative to one another, i.e., deformational motion. Consider the muscle as a continuum body $\mathcal{B}$ comprised of material points $\mathcal{P}$, whose coordinates change over some time span $t = [0, T]$. The motions and deformations over time cause $\mathcal{B}$ to occupy a sequence of geometrical regions $\Omega_0, \ldots, \Omega$; called the configurations of $\mathcal{B}$. The configuration at the start of the motion, i.e., at $t = 0$, is referred to as the reference (or undeformed) configuration, denoted by Ω_0. The configuration at some later time $t > 0$, i.e., Ω, is referred to as the current (or deformed) configuration. For brevity, the configuration of the $\mathcal{B}$ is denoted directly via a subscript, i.e., $\mathcal{B}_0$ at $t = 0$ and $\mathcal{B}$ otherwise (Figure 3.1). The motion of a material point $\mathcal{P}$ is described by the placement function $\boldsymbol{\chi}$, which maps the initial position $\boldsymbol{X}^{\mathrm{g}}$ (in mm) in the reference (or undeformed) configuration, to a position $\boldsymbol{x}^{\mathrm{g}}$ (in mm) in the current (or deformed) configuration at time t,

$$\boldsymbol{x}^{\mathrm{g}} = \boldsymbol{\chi}(\boldsymbol{X}^{\mathrm{g}}, t). \tag{3.1}$$

The superscript $(\cdot)^{\mathrm{g}}$ indicates the coordinate-system (basis) of the vector $\boldsymbol{g}_i = \{\boldsymbol{g}_1, \boldsymbol{g}_2, \boldsymbol{g}_3\}$. Typically, the coordinate-systems which describe the reference and current coordinates are aligned (co-linear); referred to here as a "global coordinate-system". Therefore, the explicit specification of the basis system is superfluous and is usually omitted. This, however, is not the case for the development of a "local coordinate-system", which is used to simplify certain analyses, e.g., orthotropic materials under large deformations. However, to avoid cumbersome notation, the following assumes a global coordinate-system and the superscript $(\cdot)^{\mathrm{g}}$ is omitted. The local coordinate-system is introduced and discussed in Chapter 6.

To differentiate quantities by configuration, upper case and lower case variables are used for the reference and current configurations, respectively. As a side note, the configuration of a variable is independent of the basis used to describe it.

The motion of $\mathcal{B}$ is assumed to be smooth, i.e., continuously differentiable with respect to position and time, and that it can be (uniquely) inverted, i.e.,

$$\boldsymbol{X} = \boldsymbol{\chi}^{-1}(\boldsymbol{x}, t). \tag{3.2}$$

This only holds if

$$J(\boldsymbol{X}, t) = \det\left(\frac{\partial \boldsymbol{\chi}}{\partial \boldsymbol{X}}\right) \neq 0, \tag{3.3}$$

where $J(\boldsymbol{X}, t)$ is introduced as the Jacobian and where $\det(\cdot)$ denotes the determinant operator.

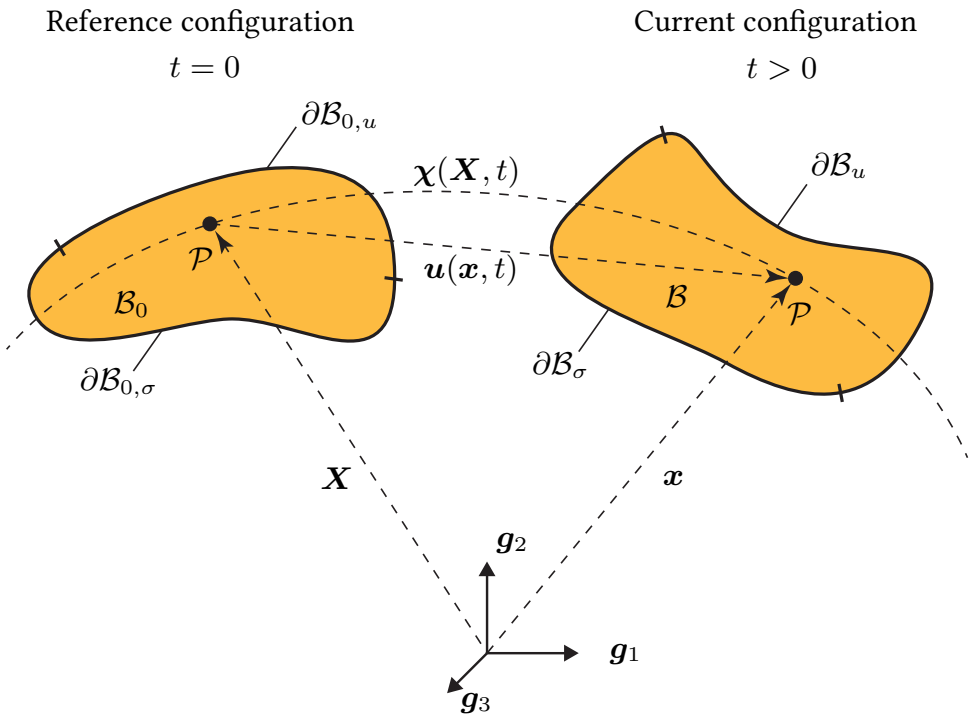

Figure 3.1: *Kinematic setting of a continuum body in the reference and current configurations.*

As will be seen later, the Jacobian plays a special role in the modelling of incompressible materials, as it describes the change in volume at $\boldsymbol{X}$.

The placement functions in Equations 3.1 and 3.2 refer to the Lagrangean (or material) and Eulerian (or spatial) description of motion, respectively. They essentially describe two different ways of looking at the same physical process. Using the analogy of a river, in the Eulerian description, the observer sits on the river bank and watches the water (particles) flow by. Whereas in the Lagrangean description, the observer is in a canoe and is "glued" to the movement of a water particle. More specifically, in the Eulerian description quantities such as displacement, velocity, pressure, and density depend on *both* position and time, i.e., the observer can look at different parts of the river at different times. While in the Lagrangean description, these quantities depend on time only, as the observer's position is fixed to any given water particle in the river.

The Eulerian description lends itself to fluid mechanics, since, as the analogy suggests, the behaviour of the river in a region is of more interest than the motion of every single water particle. On the other hand, the Lagrangean description is used in solid mechanics, since the local deformation (and the history) of individual particles and the stresses and strains they catalyse, are important. As such, the Lagrangean description is used in this thesis.

The velocities and accelerations are described in current configuration by

$$\dot{\boldsymbol{x}} = \frac{\partial \boldsymbol{x}}{\partial t}, \quad \text{and} \quad \ddot{\boldsymbol{x}} = \frac{\partial^2 \boldsymbol{x}}{\partial^2 t}. \tag{3.4}$$

Lastly, the displacement $\boldsymbol{u}$ (in mm) of a material point, in the Lagrangean description, is

given by the difference in positions between the reference and current configurations,

$$\boldsymbol{u}(\boldsymbol{X}, t) = \boldsymbol{x}(\boldsymbol{X}, t) - \boldsymbol{X}. \tag{3.5}$$

3.1.2 Deformation and strain measures

Strain is vital to analyses in solid mechanics and is derived from more fundamental deformation quantities. The seed from which almost all other deformation measures grow is the deformation gradient

$$\boldsymbol{F} = \frac{\partial \boldsymbol{\chi}(\boldsymbol{X}, t)}{\partial \boldsymbol{X}}, \tag{3.6}$$

which describes deformation and motion in the neighbourhood of a point $\boldsymbol{X}$. The deformation gradient maps material vectors to spatial vectors, e.g., line elements,

$$\mathrm{d}\boldsymbol{x} = \boldsymbol{F}(\boldsymbol{X}, t)\, \mathrm{d}\boldsymbol{X}. \tag{3.7}$$

Since the above expression is a linear transformation between the reference and current configurations, $\boldsymbol{F}$ is a two-point tensor involving both the spatial and reference coordinate-systems. If $\boldsymbol{F}$ is independent of $\boldsymbol{X}$ then the deformation is said to be homogeneous, i.e., every $\mathcal{P} \in \mathcal{B}$ experiences the same deformation. This is the case, or at least the desirable case, in material testing, e.g., dog-bone specimens aim at uniform deformation in tensile tests. For physically meaningful deformations and from Equation 3.3, it can be seen that

$$J(\boldsymbol{X}, t) = \det(\boldsymbol{F}) > 0, \tag{3.8}$$

i.e., the material neither experiences compaction to a single point ($J = 0$) nor inversion ($J < 0$). Then, it can be assumed that the inverse of the deformation gradient $\boldsymbol{F}^{-1}$ exists, and is given by the derivative of the inverse motion (Equation 3.2) with respect to the spatial coordinates

$$\boldsymbol{F}^{-1} = \frac{\partial \boldsymbol{\chi}^{-1}(\boldsymbol{X}, t)}{\partial \boldsymbol{x}}, \tag{3.9}$$

mapping spatial vectors to material vectors. If there is no motion, $\boldsymbol{F} = \boldsymbol{I}$, $\boldsymbol{x} = \boldsymbol{X}$ and $J = 1$. While the former two relations hold only if no motion is present, $J = 1$ may still hold during motion. In this case the deformation is referred to as isochoric or volume-preserving. Incompressible materials such as rubbers and biological materials typically undergo such deformations.

Whether a solid object is rotated and then stretched or stretched and then rotated, the final deformed state is assumed to be the same. The deformation gradient can be decomposed into such a pure stretch and a pure rotation via the so-called polar decomposition,

$$\boldsymbol{F} = \boldsymbol{R}\boldsymbol{U} = \boldsymbol{v}\boldsymbol{R}, \tag{3.10}$$

where $\boldsymbol{U}$ and $\boldsymbol{v}$ are called the right (or material) and left (or spatial) stretch tensors and $\boldsymbol{R}$ is the rotation tensor. The stretch tensors $\boldsymbol{U}$ and $\boldsymbol{v}$ measure the pure local stretch deformation and are positive definite and symmetric, e.g., $\boldsymbol{U} = \boldsymbol{U}^{\mathrm{T}}$ and $\boldsymbol{c}^{\mathrm{T}} \cdot \boldsymbol{U}\boldsymbol{c} > 0$, where $\boldsymbol{c}$ is an arbitrary vector. It is often convenient to express $\boldsymbol{U}$ in terms of its eigenvalues λ_i and eigenvectors $\boldsymbol{N}_i$,

i.e.,

$$\boldsymbol{U}\boldsymbol{N}_i = \lambda_i \boldsymbol{N}_i, \qquad i = \{1, 2, 3\}, \tag{3.11}$$

referred to as the principal stretches and principal directions, respectively. The principal stretches of $\boldsymbol{v}$ are identical to those of $\boldsymbol{U}$, since eigenvalues represent the physical nature of a tensor. On the other hand, the eigenvectors of the right and left stretch tensors are related to each other via the rotation tensor $\boldsymbol{R}$. As a side note, the local coordinate-system makes use of this decomposition property of the deformation tensor, where the rotation tensor rotates the local coordinate-system as well as the material (Section 6.3.2).

The rotation tensor $\boldsymbol{R}$ is proper orthogonal, i.e., $\boldsymbol{R}^{\mathrm{T}}\boldsymbol{R} = \boldsymbol{I}$ and measures the pure local rotation, i.e., the change in the local orientation. The relation between the right and left stretch tensors is given by

$$\boldsymbol{v} = \boldsymbol{F}\boldsymbol{R}^{\mathrm{T}} = \boldsymbol{R}\boldsymbol{U}\boldsymbol{R}^{\mathrm{T}}. \tag{3.12}$$

Given the polar decomposition (Equation 3.10) of $\boldsymbol{F}$, the Cauchy-Green deformation tensors can be defined according to

$$\boldsymbol{C} = \boldsymbol{F}^{\mathrm{T}}\boldsymbol{F} = \left(\boldsymbol{U}^{\mathrm{T}}\boldsymbol{R}^{\mathrm{T}}\right)\boldsymbol{R}\boldsymbol{U} = \boldsymbol{U}\boldsymbol{U} \quad \text{and} \tag{3.13}$$

$$\boldsymbol{b} = \boldsymbol{F}\boldsymbol{F}^{\mathrm{T}} = \left(\boldsymbol{v}\,\boldsymbol{R}^{\mathrm{T}}\right)\boldsymbol{R}^{\mathrm{T}}\boldsymbol{v}^{\mathrm{T}} = \boldsymbol{v}\boldsymbol{v}, \tag{3.14}$$

and are symmetric and positive definite. The right Cauchy-Green (or Green) deformation tensor $\boldsymbol{C}$ is defined entirely in the reference configuration (analogous to $\boldsymbol{U}$). Conversely, the left Cauchy-Green (or Finger) tensor $\boldsymbol{b}$ (analogous to $\boldsymbol{v}$) is defined entirely in the current configuration. Given that $\boldsymbol{F}$ is a two-point tensor, and from the polar decomposition (Equation 3.10), it follows that the $\boldsymbol{R}$ must also be a two-point tensor, mapping vectors from reference to the current configuration.

The relations between $\boldsymbol{b}$ and $\boldsymbol{C}$ can be given via Equations 3.12 and 3.14 as

$$\boldsymbol{b} = \boldsymbol{v}^2 = \boldsymbol{R}\boldsymbol{U}\boldsymbol{R}^{\mathrm{T}}\boldsymbol{R}\boldsymbol{U}\boldsymbol{R}^{\mathrm{T}} = \boldsymbol{R}\boldsymbol{U}^2\boldsymbol{R}^{\mathrm{T}} = \boldsymbol{R}\boldsymbol{C}\boldsymbol{R}^{\mathrm{T}}, \tag{3.15}$$

and similarly for $\boldsymbol{C}$

$$\boldsymbol{C} = \boldsymbol{R}^{\mathrm{T}}\boldsymbol{b}\,\boldsymbol{R}. \tag{3.16}$$

As stated above, strains (in fact, also stresses) are *concepts* used to ease certain analyses. Therefore, a wide variety of strain measures can be constructed from the basic (deformational) building blocks, tailored to a particular analysis. Typically, differences between these measures arise only when deformations are large, as is the case for biological tissues. Common strain measures to biomechanical analyses are introduced by defining a change in the squared line elements between the reference and current configurations,

$$\begin{aligned} \mathrm{d}\boldsymbol{x}\cdot\mathrm{d}\boldsymbol{x} - \mathrm{d}\boldsymbol{X}\cdot\mathrm{d}\boldsymbol{X} &= \mathrm{d}\boldsymbol{X}\cdot\boldsymbol{C}\,\mathrm{d}\boldsymbol{X} - \mathrm{d}\boldsymbol{X}\cdot\mathrm{d}\boldsymbol{X} \\ &= \mathrm{d}\boldsymbol{X}\cdot(\boldsymbol{C}-\boldsymbol{I})\,\mathrm{d}\boldsymbol{X} =: \mathrm{d}\boldsymbol{X}\cdot 2\boldsymbol{E}\,\mathrm{d}\boldsymbol{X}, \end{aligned} \tag{3.17}$$

where $\boldsymbol{E}$ is the Green-Lagrange strain tensor, i.e.,

$$\boldsymbol{E} = \frac{1}{2}(\boldsymbol{C}-\boldsymbol{I}). \tag{3.18}$$

Similarly,

$$\begin{aligned} \mathrm{d}\boldsymbol{x}\cdot\mathrm{d}\boldsymbol{x} - \mathrm{d}\boldsymbol{X}\cdot\mathrm{d}\boldsymbol{X} &= \mathrm{d}\boldsymbol{x}\cdot\mathrm{d}\boldsymbol{x} - \mathrm{d}\boldsymbol{x}\cdot\boldsymbol{b}^{-1}\,\mathrm{d}\boldsymbol{x} \\ &= \mathrm{d}\boldsymbol{x}\cdot(\boldsymbol{I}-\boldsymbol{b}^{-1})\,\mathrm{d}\boldsymbol{x} =: \mathrm{d}\boldsymbol{x}\cdot 2\boldsymbol{A}\,\mathrm{d}\boldsymbol{x}, \end{aligned} \tag{3.19}$$

where $\boldsymbol{A}$ is the Euler-Almansi strain tensor, i.e.,

$$\boldsymbol{A} = \frac{1}{2}(\boldsymbol{I}-\boldsymbol{b}^{-1}). \tag{3.20}$$

It can be seen from their definitions, that $\boldsymbol{E}$ and $\boldsymbol{A}$ are strain measures in the reference and current configurations, respectively.

3.1.3 Rate of deformation

Often, the rate of change of physical quantities is of interest. The velocity gradient $\boldsymbol{l}$ (in 1/s) in the current coordinates is given by

$$\boldsymbol{l}(\boldsymbol{x},t) = \frac{\partial \boldsymbol{v}(\boldsymbol{x},t)}{\partial \boldsymbol{x}}, \tag{3.21}$$

and can be additively decomposed into symmetric and antisymmetric (skew) parts, i.e.,

$$\begin{aligned} \boldsymbol{l}(\boldsymbol{x},t) &= \frac{1}{2}(\boldsymbol{l}+\boldsymbol{l}^{\mathrm{T}}) + \frac{1}{2}(\boldsymbol{l}-\boldsymbol{l}^{\mathrm{T}}) \\ &= \boldsymbol{d}(\boldsymbol{x},t) \quad + \boldsymbol{w}(\boldsymbol{x},t), \end{aligned} \tag{3.22}$$

where $\boldsymbol{d}$ is the so-called rate of deformation (or strain) tensor and $\boldsymbol{w}$ is the rate of rotation (or spin) tensor (both in 1/s).

The material time derivative $\mathrm{D}/\mathrm{D}t$ is introduced, which is the derivative of a material field with respect to time at a fixed position $\boldsymbol{X}$, it is also denoted in the following by $\dot{(\cdot)}$. The material time derivative of the deformation gradient $\boldsymbol{F}$ is given by

$$\dot{\boldsymbol{F}}(\boldsymbol{X},t) = \frac{\partial}{\partial \boldsymbol{X}}\left(\frac{\partial \boldsymbol{\chi}(\boldsymbol{X},t)}{\partial t}\right) = \frac{\partial \boldsymbol{V}(\boldsymbol{X},t)}{\partial \boldsymbol{X}}, \tag{3.23}$$

and the relation between $\boldsymbol{F}$ and $\boldsymbol{l}$ is given via the chain rule (applied to Equation 3.21) and Equations 3.6 and 3.9 as

$$\boldsymbol{l} = \frac{\partial \dot{\boldsymbol{\chi}}(\boldsymbol{X},t)}{\partial \boldsymbol{X}}\,\frac{\partial \boldsymbol{X}}{\partial \boldsymbol{x}} = \dot{\boldsymbol{F}}\,\boldsymbol{F}^{-1}. \tag{3.24}$$

3.1.4 Stress measures

Stress, like strain, is a crucial notion in solid mechanics and represents the internal loading within an object. Finite deformation of a body $\mathcal{B}$ causes neighbouring particles to exert forces on each other and stress is the measure of the intensity of these forces per unit area.

Consider a body cut by an imaginary plane at some point $\boldsymbol{x}$ with a (unit) normal vector $\boldsymbol{n}$ in the current configuration. Deformations give rise to a traction vector $\boldsymbol{t}$ at $\boldsymbol{x}$, acting over an infinitesimal surface area element $\mathrm{d}s$ on the plane. On the opposite side of the imaginary plane, an equal and opposite resultant force $\mathrm{d}\boldsymbol{f}$ arises. The analogous quantities to $\boldsymbol{x}$, $\boldsymbol{n}$, $\boldsymbol{t}$ and $\mathrm{d}s$ are

given in the reference configuration by $\boldsymbol{X}$, $\boldsymbol{N}$, $\boldsymbol{T}$ and $\mathrm{d}S$, respectively. Then it is assumed that

$$\mathrm{d}\boldsymbol{f} = \boldsymbol{t}(\boldsymbol{x}, t, \boldsymbol{n})\,\mathrm{d}s = \boldsymbol{T}(\boldsymbol{X}, t, \boldsymbol{N})\,\mathrm{d}S, \tag{3.25}$$

where $\boldsymbol{t}$ and $\boldsymbol{T}$ (in N/mm^2) are the Cauchy and first Piola-Kirchhoff traction vectors, respectively. The former is in the current configuration and the later in the reference configuration.

Cauchy's stress theorem, a fundamental relation in solid mechanics, can be derived by assuming that a second-order tensor (field) exists, such that,

$$\boldsymbol{t}(\boldsymbol{x}, t, \boldsymbol{n}) = \boldsymbol{\sigma}(\boldsymbol{x}, t)\,\boldsymbol{n} \quad \text{and} \tag{3.26}$$

$$\boldsymbol{T}(\boldsymbol{X}, t, \boldsymbol{N}) = \boldsymbol{P}(\boldsymbol{X}, t)\boldsymbol{N}, \tag{3.27}$$

where $\boldsymbol{\sigma}$ and $\boldsymbol{P}$ are the Cauchy and first Piola-Kirchhoff stress tensors (in N/mm^2), respectively. The stress theorem states, essentially, that $\boldsymbol{\sigma}$ or $\boldsymbol{P}$ are independent of $\boldsymbol{n}$ or $\boldsymbol{N}$, while $\boldsymbol{t}$ or $\boldsymbol{T}$ are linear in $\boldsymbol{n}$ or $\boldsymbol{N}$, respectively.

By combining Equations 3.25 and 3.26, the relation between the Cauchy and first Piola-Kirchhoff stress is given by

$$\boldsymbol{\sigma}(\boldsymbol{x}, t)\,\boldsymbol{n}\,\mathrm{d}s = \boldsymbol{P}(\boldsymbol{X}, t)\boldsymbol{N}\,\mathrm{d}S, \tag{3.28}$$

and by using Nanson's formula ($\mathrm{d}s = J\,\boldsymbol{F}^{\mathrm{T}}\mathrm{d}S$), Equation 3.28 can be written as

$$\boldsymbol{\sigma} = J^{-1}\,\boldsymbol{P}\boldsymbol{F}^{\mathrm{T}}. \tag{3.29}$$

Similarly for $\boldsymbol{P}$,

$$\boldsymbol{P} = J\,\boldsymbol{\sigma}\boldsymbol{F}^{\text{-T}}. \tag{3.30}$$

It can be seen that $\boldsymbol{\sigma}$ is in the current configuration, i.e., the current infinitesimal force ($\mathrm{d}\boldsymbol{f}$) acting over the current infinitesimal area element ($\mathrm{d}s$). On the other hand, $\boldsymbol{P}$ is a partial pull-back of $\boldsymbol{\sigma}$ in that it considers the current force over the reference area element ($\mathrm{d}S$). Two other commonly used stress measures are introduced here for completeness: namely the Kirchhoff $\boldsymbol{\tau}$ and second Piola-Kirchhoff $\boldsymbol{S}$ stresses (in N/mm^2). The Kirchhoff (or weighted) stress tensor differs from $\boldsymbol{\sigma}$ only by the volume ratio, i.e.,

$$\boldsymbol{\tau} = J\,\boldsymbol{\sigma}, \tag{3.31}$$

and also exists wholly in the current configuration. The second Piola-Kirchhoff stress tensor is a partial pull-back of $\boldsymbol{P}$, i.e.,

$$\boldsymbol{S} = \boldsymbol{F}^{-1}\boldsymbol{P}, \tag{3.32}$$

and exists wholly in the reference configuration, i.e., considering both the infinitesimal reference force and area element. The remaining stress mappings are given for reference:

$$\boldsymbol{\sigma} = J^{-1}\boldsymbol{\tau} \qquad = J^{-1}\boldsymbol{F}\boldsymbol{S}\boldsymbol{F}^{\mathrm{T}}, \tag{3.33}$$

$$\boldsymbol{\tau} = \boldsymbol{P}\boldsymbol{F}^{\mathrm{T}} \qquad = \boldsymbol{F}\boldsymbol{S}\boldsymbol{F}^{\mathrm{T}}, \tag{3.34}$$

$$\boldsymbol{P} = \boldsymbol{\tau}\boldsymbol{F}^{-T} \qquad = \boldsymbol{F}\boldsymbol{S} \quad \text{and} \tag{3.35}$$

$$\boldsymbol{S} = J\boldsymbol{F}^{-1}\boldsymbol{\sigma}\boldsymbol{F}^{-T} = \boldsymbol{F}^{-1}\boldsymbol{\tau}\boldsymbol{F}^{-T}. \tag{3.36}$$

Certain stress measures are better suited to certain analyses. For example, in a transversely isotropic material such as fibre-reinforced concrete or many biological materials, stresses along the fibre directions are of primary interest, i.e., those which are independent of the rotations applied to the body. Such a property is exhibited by the second Piola-Kirchhoff stress $\boldsymbol{S}$, which is invariant under rigid body rotation in the current configuration.

The Cauchy stress tensor can be additively decomposed into a volume changing (hydrostatic or dilatational) σ_{IMP} and volume preserving (distortional or deviatoric) $\boldsymbol{\sigma}_{\text{D}}$ parts, i.e.,

$$\boldsymbol{\sigma} = \sigma_{\text{IMP}}\, \boldsymbol{I} + \boldsymbol{\sigma}_{\text{D}}. \tag{3.37}$$

The hydrostatic stress is given by

$$\sigma_{\text{IMP}} = \frac{1}{3} \operatorname{tr} \boldsymbol{\sigma}, \tag{3.38}$$

and the distortional stress can be computed by subtracting σ_{IMP} from $\boldsymbol{\sigma}$.

3.1.5 Balance relations

Concerning conservation principles, Cowin (2013) states *"There is an aspect of the application of conservation principles of mechanics (those of mass, momentum, angular momentum, energy, etc.) that is an artisan-like skill that requires some experience on the part of the modeler"*. He goes on to write the general conversation principle *"in the form of an accounting statement"* as follows;

> [The rate of change of a quantity in a system]
> =[The amount of the quantity coming into the system per unit time]
> − [The amount of the quantity leaving the system per unit time]
> + [The amount of the quantity produced within the system per unit time]
> − [The amount of the quantity consumed within the system per unit time].

In fact, this "accounting statement" can be simplified further by assuming that the quantities are neither produced nor consumed within the system, as is done in this section. More specifically, only closed and insulated systems are considered, i.e., the mass remains fixed and no energy is transferred with the body's surroundings (Holzapfel, 2000).

In general, balance equations can be formulated in either a global (integral) or local (differential) form, expressed either with material or spatial quantities. In continuum mechanics, the local form in terms of the spatial configuration is of interest. These local balance laws are valid for each material point in the body, and are derived from their global counterparts.

Mass balance

In a closed system, mass can neither be created nor destroyed. Locally, this translates to restrictions on density ρ (in kg/cm^3), which is described by a (at least piecewise) continuous density defined in the reference and current configurations by

$$\rho_0(\boldsymbol{X}) = \lim_{\Delta V \to 0} \frac{\Delta m}{\Delta V} \quad \text{and} \qquad \rho(\boldsymbol{x}, t) = \lim_{\Delta v \to 0} \frac{\Delta m}{\Delta v}, \tag{3.39}$$

where ΔV and Δv are the volume elements in the reference and current configurations, respectively.[2]

Given that the total mass must remain constant during the motion of the body, and by taking Equation 3.39 in differential form, it can be stated that

$$\frac{\mathrm{D}m}{\mathrm{D}t} = \frac{\mathrm{D}}{\mathrm{D}t}\int_{\mathcal{B}} \rho(\boldsymbol{x}, t)\,\mathrm{d}v = 0. \tag{3.40}$$

The expression above is the global or strong form of the mass balance.

The local or weak form is derived by first considering the relationship between ρ_0 and ρ, given that the mass must remain constant during any motion;

$$\int_{\mathcal{B}} \rho_0 - \rho J\,\mathrm{d}V = 0, \tag{3.41}$$

where

$$J = \frac{\mathrm{d}v}{\mathrm{d}V} \tag{3.42}$$

is the Jacobian or volume ratio, cf. Equation 3.3. Second, since Equation 3.41 must hold for arbitrary $\mathrm{d}V$, the integrand must itself vanish at all points, giving

$$\rho_0 - \rho J = 0, \tag{3.43}$$

which must hold for all time, i.e., taking the material time derivative gives the local form of the mass balance

$$\frac{\mathrm{D}}{\mathrm{D}t}(\rho J) = \dot{\rho} + \rho\,\mathrm{div}\,\dot{\boldsymbol{x}} = 0. \tag{3.44}$$

Linear momentum balance

The conservation of momentum, $\boldsymbol{L}(t)$ (in kg mm/s), is stated in the form of Newton's second law, i.e., that the product of the mass and acceleration of the object:

$$\boldsymbol{L}(t) = \int_{\mathcal{B}} \rho\dot{\boldsymbol{x}}\,\mathrm{d}v, \tag{3.45}$$

must be balanced against the resultant force $\boldsymbol{F}(t)$ (in kg mm/s^2 $\propto$ N) acting on the body at all times t, i.e.,

$$\frac{\mathrm{D}}{\mathrm{D}t}\boldsymbol{L} = \boldsymbol{F}(t). \tag{3.46}$$

The resultant force is (additively) split into forces acting on the surface of the body $\boldsymbol{t}$ (in N/mm^2) and those acting throughout the body $\boldsymbol{b}$ (in N/mm^3). Then,

$$\frac{\mathrm{D}}{\mathrm{D}t}\int_{\mathcal{B}} \rho\dot{\boldsymbol{x}}\,\mathrm{d}v = \int_{\partial\mathcal{B}} \boldsymbol{t}\,\mathrm{d}s + \int_{\mathcal{B}} \boldsymbol{b}\,\mathrm{d}v, \tag{3.47}$$

[2]Note that in continuum mechanics ΔV does not tend to 0, but rather to the scale of a representative volume element, discussed in later Chapter 4.

which is the global form of the linear momentum balance. The local form is given by first, using Cauchy's stress theorem (Equation 3.26) to rewrite the surface integral in Equation 3.47 as

$$\int_{\partial\mathcal{B}} \boldsymbol{t}\,\mathrm{d}s = \int_{\mathcal{B}} \operatorname{div}\boldsymbol{\sigma}\,\mathrm{d}v. \tag{3.48}$$

Second, since the global form must hold for any volume, the integrand must itself vanish, giving the local form of the linear momentum balance, i.e.,

$$\operatorname{div}\boldsymbol{\sigma} + \boldsymbol{b} = \rho\ddot{\boldsymbol{x}}, \tag{3.49}$$

and is referred to as Cauchy's first equation of motion.

Moment of momentum balance

The balance of rotational momentum or moment of momentum states that the rate of change of angular momentum must equal the sum of applied moments. The global form is derived analogously to the balance of linear momentum (Section 3.1.5) and given here (about the origin) directly as

$$\frac{\mathrm{D}}{\mathrm{D}t}\int_{\mathcal{B}} \boldsymbol{x} \times \rho\dot{\boldsymbol{x}}\,\mathrm{d}v = \int_{\partial\mathcal{B}} \boldsymbol{x} \times \boldsymbol{t}\,\mathrm{d}s + \int_{\mathcal{B}} \boldsymbol{x} \times \boldsymbol{b}\,\mathrm{d}v, \tag{3.50}$$

Then, by the use of Cauchy's stress theorem (Equation 3.26) and since the resulting integrand itself must vanish;

$$\boldsymbol{x} \times (\operatorname{div}\boldsymbol{\sigma} + \boldsymbol{b} - \rho\ddot{\boldsymbol{x}}) = \boldsymbol{0}, \tag{3.51}$$

and by inserting the local forms of the mass and linear momentum balances (Equations 3.44 and 3.49, respectively), the local form of the momentum of balance can be written as

$$\boldsymbol{\mathcal{E}} : \boldsymbol{\sigma}^{\mathrm{T}} = \boldsymbol{0} \tag{3.52}$$

(see Holzapfel, 2000 for details). The above relation holds only if $\boldsymbol{\sigma}$ is symmetric and is a consequence of the local rotational momentum balance and is Cauchy's second equation of motion.

Mechanical energy balance

The balance of mechanical energy (or power theorem) states that the rate of work done by external forces $\mathcal{P}_{\text{ext}}$ on a body is equal to the sum of the rate of change of kinetic energy $\mathcal{K}(t)$ and the stress power $\mathcal{P}_{\text{def}}(t)$ supplied to the body (all in N mm/s $\propto$ J/s), i.e.,

$$\mathcal{P}_{\text{ext}}(t) = \frac{\mathrm{D}}{\mathrm{D}t}\,\mathcal{K}(t) + \mathcal{P}_{\text{def}}(t). \tag{3.53}$$

By splitting external forces into surface tractions $\boldsymbol{t}$ and body forces $\boldsymbol{b}$ (Equation 3.47), the external work is given by

$$\mathcal{P}_{\text{ext}}(t) = \int_{\mathcal{B}} \boldsymbol{b}\cdot\dot{\boldsymbol{x}}\,\mathrm{d}v + \int_{\partial\mathcal{B}} \boldsymbol{t}\cdot\dot{\boldsymbol{x}}\,\mathrm{d}s. \tag{3.54}$$

The kinetic energy (in J) obtained by generalising Newtonian mechanics to a continuum, i.e.,

$$\mathcal{K}(t) = \int_{\mathcal{B}} \frac{1}{2}\,\rho\dot{\boldsymbol{x}} \cdot \dot{\boldsymbol{x}}\,\mathrm{d}v, \tag{3.55}$$

and by using Reynold's transport theorem,

$$\frac{\mathrm{D}}{\mathrm{D}t}\mathcal{K}(t) = \int_{\mathcal{B}} \rho\dot{\boldsymbol{x}} \cdot \ddot{\boldsymbol{x}}\,\mathrm{d}v. \tag{3.56}$$

For a purely mechanical and conservative system, The rate of internal mechanical work done by stress field is

$$\mathcal{P}_{\text{def}}(t) = \int_{\mathcal{B}} \boldsymbol{\sigma} : \boldsymbol{d}\,\mathrm{d}v. \tag{3.57}$$

where $\boldsymbol{d}$ is the rate of deformation (Equation 3.22). Substituting the above expression in Equation 3.53 yields

$$\int_{\mathcal{B}} \boldsymbol{b} \cdot \dot{\boldsymbol{x}}\,\mathrm{d}v + \int_{\partial\mathcal{B}} \boldsymbol{t} \cdot \dot{\boldsymbol{x}}\,\mathrm{d}s = \int_{\mathcal{B}} \rho\dot{\boldsymbol{x}} \cdot \ddot{\boldsymbol{x}}\,\mathrm{d}v + \int_{\mathcal{B}} \boldsymbol{\sigma} : \boldsymbol{d}\,\mathrm{d}v. \tag{3.58}$$

The Cauchy stress and rate of deformation tensor is said to be work (or energy conjugate), as it represents the physical power during a deformation. Commonly used work-conjugate pairs are:

$$\{J\boldsymbol{\sigma}, \boldsymbol{d}\}\,, \{\boldsymbol{P}, \dot{\boldsymbol{F}}\} \text{ and } \{\boldsymbol{S}, \dot{\boldsymbol{E}}\}, \tag{3.59}$$

see Holzapfel (2000) for further details.

Lastly, the stress power can be expressed as the rate of change of internal energy per unit current volume $\Psi(\boldsymbol{x}, t)$ (in J/mm^3), i.e.,

$$\mathcal{P}_{\text{def}}(t) = \frac{\mathrm{D}}{\mathrm{D}t}\Psi(\boldsymbol{x}, t) = \frac{\mathrm{D}}{\mathrm{D}t}\int_{\mathcal{B}} \Psi(\boldsymbol{x}, t)\,\mathrm{d}v. \tag{3.60}$$

The (specific) internal energy is the basis for the constitutive relation of (hyperelastic) materials (Chapter 4).

3.1.6 Objectivity

The physical quantities introduced till now must be objective or frame-indifferent, meaning they must be invariant under changes in the observer's position (coordinate-system). In other words, if the coordinate-system is varied, the physical quantity itself must remain unchanged. The change of observer may be thought of as a rigid body rotation, represented by the orthogonal tensor $\boldsymbol{Q}$; then, a vector $\boldsymbol{a}$ and tensor $\boldsymbol{A}$ are objective if

$$\boldsymbol{a}^+ = \boldsymbol{Q}\,\boldsymbol{a} \quad \text{and} \tag{3.61}$$

$$\boldsymbol{A}^+ = \boldsymbol{Q}\,\boldsymbol{A}\,\boldsymbol{Q}^{\mathrm{T}}. \tag{3.62}$$

For example, the line element $\mathrm{d}\boldsymbol{x}$ subject to $\boldsymbol{Q}$ yields

$$\mathrm{d}\boldsymbol{x}^{+} = \boldsymbol{Q}\,\mathrm{d}\boldsymbol{x} = \boldsymbol{Q}\boldsymbol{F}\,\mathrm{d}\boldsymbol{X}. \tag{3.63}$$

It can be seen that vectors $\mathrm{d}\boldsymbol{x}^{+}$ and $\mathrm{d}\boldsymbol{x}$ differ in components but have the same magnitude. That is, the length of the line element does not change, only its coordinates. Furthermore, consider the Cauchy stress tensor $\boldsymbol{\sigma}$ subject to $\boldsymbol{Q}$, i.e.,

$$\boldsymbol{Q}\,\boldsymbol{t} = \boldsymbol{\sigma}^{+}\boldsymbol{Q}\,\boldsymbol{n}. \tag{3.64}$$

Comparison with Equation 3.26 gives,

$$\boldsymbol{\sigma}^{+} = \boldsymbol{Q}\,\boldsymbol{\sigma}\,\boldsymbol{Q}^{\mathrm{T}}, \tag{3.65}$$

showing that the Cauchy stress tensor is objective. It can be shown that the first and second Piola-Kirchhoff stress tensors, $\boldsymbol{P}$ and $\boldsymbol{S}$, respectively, are also objective. Furthermore, from the above expression, it can be seen that

$$\boldsymbol{F}^{+} = \boldsymbol{Q}\boldsymbol{F}. \tag{3.66}$$

Note that although $\boldsymbol{F}^{+}$ does not satisfy Equation 3.62, it is still considered to be objective. This is because $\boldsymbol{F}$ is a two-point tensor, i.e., one index describes the material coordinate which is intrinsically independent of the observer, therefore, $\boldsymbol{F}$ transforms as a vector, i.e., Equation 3.61. Lastly, substituting this relation into Equation 3.13 for $\boldsymbol{C}$ gives

$$\boldsymbol{C}^{+} = \boldsymbol{F}^{\mathrm{T}}\boldsymbol{Q}^{\mathrm{T}}\boldsymbol{Q}\boldsymbol{F} = \boldsymbol{Q}\,\boldsymbol{C}\,\boldsymbol{Q}^{\mathrm{T}}. \tag{3.67}$$

3.1.7 Initial boundary value problem

An initial boundary value problem is one where a solution is found to a system of differential equations, subjected to some boundary and initial conditions. For example, to calculate how much a steel beam will bend under a load, the way in which the beam is fixed must be known together with the load it is subjected to—the boundary conditions. The type of steel the beam is composed of must also be taking into account—the constitutive relations. And the state of the beam at the start must be known—the initial conditions. This information is combined with one (or more) of the conservation principles (Section 3.1.5) and the solution—displacement of the beam in the above example, is found such that the balance law(s), initial and boundary conditions are satisfied (subject to the constitutive relations).

Consider a body $\mathcal{B}$ at time t with surface $\partial\mathcal{B}$ (Figure 3.1), the surface may be partitioned into disjoint parts, i.e.,

$$\partial\mathcal{B} = \partial\mathcal{B}_{\mathrm{u}} \cup \partial\mathcal{B}_{\sigma} \qquad \text{with} \qquad \partial\mathcal{B}_{\mathrm{u}} \cap \partial\mathcal{B}_{\sigma} = \emptyset, \tag{3.68}$$

over which the different types of boundary conditions, are applied. The boundary conditions may be divided into two classes: Dirichlet boundary conditions, which specify displacement $\boldsymbol{u}(\boldsymbol{x}, t)$ (on $\partial\mathcal{B}_{\mathrm{u}}$) and Neumann boundary conditions, which specify surface tractions $\boldsymbol{t}(\boldsymbol{x}, t, \boldsymbol{n})$ (on $\partial\mathcal{B}_{\sigma}$). Lastly, initial conditions are given by specifying the displacements $\boldsymbol{u}$ and velocities $\dot{\boldsymbol{x}}$ in the reference configuration $t = 0$, i.e., $\boldsymbol{u}_0(\boldsymbol{X})$ and $\dot{\boldsymbol{x}}_0(\boldsymbol{X})$.

The body is subject to the momentum balance, i.e., Cauchy's first equation of motion (Equation

3.49), where the Cauchy stress tensor must be symmetric, i.e., $\boldsymbol{\sigma} = \boldsymbol{\sigma}^{\mathrm{T}}$, owing to the balance of angular momentum (Equation 3.50) and the spatial and material mass densities are related via the Jacobian, i.e., $\rho = J^{-1}\rho_0$, owing to the balance of mass (Equation 3.43).

Summarising the problem gives the strong form of the initial boundary value problem of solid mechanics as

$$\begin{aligned} \operatorname{div}\boldsymbol{\sigma} + \boldsymbol{b} &= \rho\ddot{\boldsymbol{x}}, && && \\ \boldsymbol{u} &= \hat{\boldsymbol{u}} && \text{on} && \partial\mathcal{B}_{\mathrm{u}}, \\ \boldsymbol{t} &= \hat{\boldsymbol{t}} && \text{on} && \partial\mathcal{B}_{\sigma}, \\ \boldsymbol{u}(\boldsymbol{x},0) &= \hat{\boldsymbol{u}}_0, && && \\ \dot{\boldsymbol{x}}(\boldsymbol{x},0) &= \hat{\dot{\boldsymbol{x}}}_0, && && \end{aligned} \tag{3.69}$$

where $\hat{(\cdot)}$ are the prescribed values. As mentioned previously, constitutive relations (discussed in the next chapter) are necessary to complete the problem formulation. Analytical solution of the strong form is rarely possible, instead a variational or weak formulation is employed to determine approximate solutions which satisfy all required conditions in a mean sense. This is the basis of the finite element method.

3.2 Finite Element Method

The boundary value problem in solid mechanics (discussed above) attempts to find displacement fields which satisfy the governing balance laws and boundary and initial conditions, subject to constitutive laws. An analytical solution of the displacement field would specify the displacement at any location within the body, that is, with an infinite spatial resolution. Finding such expressions is limited to rare and idealised cases. For real-world problems, where geometries, boundary conditions and constitutive laws become increasingly complex such as a collision of two vehicles or flexion of an elbow via contracting muscles, analytical solutions become unobtainable.

The finite element method is a numerical method which provides approximate solutions to such problems. Briefly, the finite element method reduces differential equations to a system of algebraic equations which are suited for solution via computer programs. One way to obtain an approximate solution is via the principle of virtual work (Section 3.2.1).

Essentially, it involves diving up the body into a system of smaller bodies (finite elements), which are interconnected at certain points (the nodes). Solutions (here: displacements) are then found at discrete points within the body. By considering the body as an assembly of smaller bodies, the problem is converted from a solution of partial differential equations to a system of algebraic equations. The solution of this, usually massive, system of equations is efficiently performed by computer programs.

3.2.1 Principle of virtual work

Consider a body $\mathcal{B}_0$ subject to tractions $\boldsymbol{t}$ (and body forces) which give rise to a displacement $\boldsymbol{u}$. Now, a further small, imaginary or *virtual*, displacement $\delta\boldsymbol{u}$ is imposed on $\mathcal{B}$. Work is the product of force and displacement; virtual work is the product of force and a virtual

displacement $\delta\boldsymbol{u}$; defined here by

$$\delta\boldsymbol{u} = \tilde{\boldsymbol{u}} - \boldsymbol{u}, \tag{3.70}$$

where $\tilde{\boldsymbol{u}}$ is a virtual, slightly modified form of the true displacement $\boldsymbol{u}$. The modified displacement satisfy the Dirichlet boundary conditions $\tilde{\boldsymbol{u}} = \hat{\boldsymbol{u}}$ on $\partial\mathcal{B}_\mathrm{u}$.

Then the weak form of the initial boundary value problem is obtained by multiplying Equation 3.69, in turn, by $\boldsymbol{u}$ and $\tilde{\boldsymbol{u}}$ and taking the difference. This yields (given here without derivation)

$$\int_\mathcal{B} \rho\, \ddot{\boldsymbol{x}} \cdot \delta\boldsymbol{u}\, \mathrm{d}v + \int_\mathcal{B} \boldsymbol{\sigma} : \operatorname{grad}(\delta\boldsymbol{u})\, \mathrm{d}v - \int_\mathcal{B} \boldsymbol{b} \cdot \delta\boldsymbol{u}\, \mathrm{d}v = \int_{\partial\mathcal{B}_\sigma} \hat{\boldsymbol{t}} \cdot \delta\boldsymbol{u}\, \mathrm{d}s. \tag{3.71}$$

Since $\boldsymbol{u}$ and $\tilde{\boldsymbol{u}}$ satisfy the boundary conditions, $\delta\boldsymbol{u} = \tilde{\boldsymbol{u}} - \boldsymbol{u} = \boldsymbol{0}$ on $\partial\mathcal{B}_\mathrm{u}$. Similarly for the initial conditions;

$$\begin{aligned} \int_\mathcal{B} \boldsymbol{u}(\boldsymbol{x}, 0) \cdot \delta\boldsymbol{u}\, \mathrm{d}v &= \int_\mathcal{B} \boldsymbol{u}_0 \cdot \delta\boldsymbol{u}\, \mathrm{d}v \quad \text{and} \\ \int_\mathcal{B} \dot{\boldsymbol{x}}(\boldsymbol{x}, 0) \cdot \delta\boldsymbol{u}\, \mathrm{d}v &= \int_\mathcal{B} \dot{\boldsymbol{x}}_0 \cdot \delta\boldsymbol{u}\, \mathrm{d}v. \end{aligned} \tag{3.72}$$

The above two equations together constitute the weak form of the initial boundary value problem (Equation 3.69). Alternatively, the weak form of the initial boundary value problem in the reference configuration reads

$$\int_{\mathcal{B}_0} \rho_0\, \ddot{\boldsymbol{X}} \cdot \delta\boldsymbol{U}\, \mathrm{d}V + \int_{\mathcal{B}_0} \boldsymbol{P} : \operatorname{Grad}(\delta\boldsymbol{U})\, \mathrm{d}V - \int_{\mathcal{B}_0} \boldsymbol{B} \cdot \delta\boldsymbol{U}\, \mathrm{d}V = \int_{\partial\mathcal{B}_{0,\sigma}} \hat{\boldsymbol{T}} \cdot \delta\boldsymbol{U}\, \mathrm{d}S. \tag{3.73}$$

3.2.2 Spatial discretisation and approximate solution

It can be seen that the weak form of the boundary value problem obtained via the principle of virtual work (Equation 3.71) lends itself to the finite element method since the displacements must satisfy the imposed conditions in a mean sense. The introduction of the trial solution $\delta\boldsymbol{u}$ in Equation 3.71 leads to non-zero residual term on the right hand side of the equation. The residual is computed within each of the elements (defined below) and summed over the entire body to give a global system of equations. Then, the solution is calculated such that the global weighted residual becomes zero.

The body $\mathcal{B}$ is divided into a set of subdomains $\mathcal{B}^e$, called elements, such that

$$\mathcal{B} \approx \sum_{e=1}^{N_\mathrm{e}} \mathcal{B}^e, \tag{3.74}$$

where N_e is the number of elements. Similarly, the boundary is divided into segments, such that

$$\partial\mathcal{B} \approx \sum_{e=1}^{N_\mathrm{e}} \partial\mathcal{B}^e = \sum_{e=1}^{N_\sigma} \partial\mathcal{B}^e_\sigma + \sum_{e=1}^{N_\mathrm{u}} \partial\mathcal{B}^e_\mathrm{u}, \tag{3.75}$$

recalling the surface definitions in Equation 3.68. The discretised form of the initial boundary

value problem (Equation 3.71) is then

$$\sum_{e=1}^{N_e} \left[\int_{\mathcal{B}^e} \rho\, \ddot{\boldsymbol{x}} \cdot \delta \boldsymbol{u}\, \mathrm{d}v + \int_{\mathcal{B}^e} \boldsymbol{\sigma} : \mathrm{grad}(\delta \boldsymbol{u})\, \mathrm{d}v - \int_{\mathcal{B}^e} \boldsymbol{b} \cdot \delta \boldsymbol{u}\ \mathrm{d}v \right] = \sum_{e=1}^{N_\sigma} \int_{\partial \mathcal{B}_\sigma} \hat{\boldsymbol{t}} \cdot \delta \boldsymbol{u}\, \mathrm{d}s. \tag{3.76}$$

Using the Galerkin method, both the dependent variables and their virtual forms are approximated by the same basis functions, here $\boldsymbol{u}$ and $\delta \boldsymbol{u}$, i.e.,

$$\begin{aligned} \boldsymbol{u}(\boldsymbol{\xi}) &\approx \sum_{a=1}^{n} n_a(\boldsymbol{\xi})\, \tilde{\boldsymbol{u}}_a = \boldsymbol{n}(\boldsymbol{\xi})\, \tilde{\boldsymbol{u}}, \\ \delta \boldsymbol{u}(\boldsymbol{\xi}) &\approx \sum_{a=1}^{n} n_a(\boldsymbol{\xi})\, \delta \tilde{\boldsymbol{u}}_a = \boldsymbol{n}(\boldsymbol{\xi})\, \delta \tilde{\boldsymbol{u}}, \end{aligned} \tag{3.77}$$

where a is the node label, n is the number of nodes per element and $\boldsymbol{\xi}$ are the parametric element coordinates.

The virtual displacements are related to the virtual strains via

$$\mathrm{grad}(\delta \boldsymbol{u}) = \underbrace{\frac{1}{2}\left(\mathrm{grad}(\delta \boldsymbol{u}) + [\mathrm{grad}(\delta \boldsymbol{u})]^{\mathrm{T}}\right)}_{\delta \boldsymbol{\epsilon}} + \underbrace{\frac{1}{2}\left(\mathrm{grad}(\delta \boldsymbol{u}) - [\mathrm{grad}(\delta \boldsymbol{u})]^{\mathrm{T}}\right)}_{\delta \boldsymbol{\Omega}}, \tag{3.78}$$

where $\boldsymbol{\epsilon}$ and $\boldsymbol{\Omega}$ are the small strain (symmetric) and the small rotation (skew-symmetric) tensors. The small strain tensor can be written in matrix form (with the discretisation introduced simultaneously) as

$$\delta \boldsymbol{\epsilon} = \mathbf{S}\, \delta \boldsymbol{u} \approx \sum_{a=1}^{n} \left(\mathbf{S}\, n_a(\boldsymbol{\xi})\right) \delta \tilde{\boldsymbol{u}}_a = \mathbf{B}\, \delta \tilde{\boldsymbol{u}}, \tag{3.79}$$

where $\mathbf{S}$ is the strain-displacement matrix whose elements can be determined by considering the small strain in index notation

$$\epsilon_{i,j} = \frac{1}{2}\left(\frac{\partial u_i}{\partial x_j} + \frac{\partial u_j}{\partial x_i}\right). \tag{3.80}$$

Making the substitution for $\mathrm{grad}(\delta \boldsymbol{u})$ in Equation 3.78,[3] together with the approximations (Equations 3.77 and 3.79) in the discretised initial boundary value problem (Equation 3.76) yields, per element,

$$\delta \tilde{\boldsymbol{u}} \left[\underbrace{\int_{\mathcal{B}} \rho\, \boldsymbol{n} \cdot \boldsymbol{n}\, \mathrm{d}v}_{\mathbf{M}^e}\ \ddot{\boldsymbol{x}} + \underbrace{\int_{\mathcal{B}} \boldsymbol{\sigma} : \mathbf{B}\, \mathrm{d}v}_{\mathbf{P}^e} - \underbrace{\int_{\mathcal{B}} \boldsymbol{b} \cdot \boldsymbol{n}\, \mathrm{d}v - \int_{\partial \mathcal{B}_\sigma} \hat{\boldsymbol{t}} \cdot \boldsymbol{n}\, \mathrm{d}s}_{\mathbf{f}^e} \right] = 0. \tag{3.81}$$

As a side note, the stress $\boldsymbol{\sigma}$ is determined by the constitutive relation. Where $\mathbf{M}^e$, $\mathbf{P}^e$ and

[3] The double contraction of a symmetric tensor ($\boldsymbol{\sigma}$) and a skew-symmetric one ($\boldsymbol{\Omega}$) is zero.

$\mathbf{f}^e$ are the (element) mass, internal force and external force matrices. The introduction of an approximate solution gives rise to a (per-element) residual $\boldsymbol{R}^e$. Recall that each element is composed of n nodes; thus the global assembled system of equations is

$$\mathbf{R} = \begin{bmatrix} \mathbf{R}_1 \\ \mathbf{R}_2 \\ \vdots \\ \mathbf{R}_n \end{bmatrix}, \quad \mathbf{M} = \begin{bmatrix} \mathbf{M}_{11} & \mathbf{M}_{12} & \dots & \mathbf{M}_{1n} \\ \mathbf{M}_{21} & \mathbf{M}_{22} & & \\ \vdots & & \ddots & \\ \mathbf{M}_{n1} & & & \mathbf{M}_{nn} \end{bmatrix}, \quad \mathbf{P} = \begin{bmatrix} \mathbf{P}_1 \\ \mathbf{P}_2 \\ \vdots \\ \mathbf{P}_n \end{bmatrix}, \quad \mathbf{f} = \begin{bmatrix} \mathbf{f}_1 \\ \mathbf{f}_2 \\ \vdots \\ \mathbf{f}_n \end{bmatrix}. \tag{3.82}$$

The global system matrix $\mathbf{M}$ is the system mass matrix and describes the spatial distribution of mass within body.

The integrations in Equation 3.81 are transformed from the region $\mathcal{B}^e$ to the parametric space $-1 < \boldsymbol{\xi} < 1$ and performed numerically using Gauß quadrature. For example, in one dimension,

$$\int_{-1}^{1} f(\boldsymbol{\xi})\, d\xi = \sum_{p=1}^{N_\xi} f(\boldsymbol{\xi}_p)\, w_p, \tag{3.83}$$

where $\boldsymbol{\xi}_p$ are the Gauß quadrature points and w_p the associated weights.

3.2.3 Numerical solvers

Since the finite element method uses the same discretisation to resolve both the geometry and to perform the computations, complex geometries can give rise a large number of nodes and elements and subsequently to large systems of equations. For example, typical element numbers include 2×10^4 for a rubber bite simulation (Röhrle et al., 2018b), 4×10^5 for an aircraft crash simulation (Thai et al., 2015), and 10^6 for an automobile crash simulation (Li et al., 2015). Therefore, such problems are typically solved via computer programs.

For transient problems the temporal domain is discretised. Here, the following notation, for some arbitrary quantity $\mathbf{c}$, is introduced as $\mathbf{c}(t_{n+1}) = \mathbf{c}_{n+1}$.

Using Equation 3.82 to form a global system of balance equations (Equation 3.81),

$$\mathbf{R}_{n+1} = \mathbf{M}\,\ddot{\mathbf{u}}_{n+1} + \mathbf{P}_{n+1} - \mathbf{f}_{n+1} = \mathbf{0}. \tag{3.84}$$

Following the method employed by the commercial finite element software package `Abaqus/Explicit` (v2017, Dassault Systèmes, France) (Dassault Systèmes, 2017), the update of the displacement is given by an explicit central difference scheme

$$\begin{aligned} \dot{\mathbf{u}}_{n+1/2} &= \dot{\mathbf{u}}_{n-1/2} + \frac{\Delta t_{n+1} + \Delta t_n}{2}\,\ddot{\mathbf{u}}_n, \\ \mathbf{u}_{n+1} &= \mathbf{u}_n + \Delta t_{n+1}\,\dot{\mathbf{u}}_{n+1/2}. \end{aligned} \tag{3.85}$$

Therefore, knowing the accelerations at increment n, the velocities and displacements can be advanced at $n+1$. To proceed with the solution $\mathbf{P}_{n+1}$ needs to be computed, from Equation 3.81

$$\mathbf{P}_{n+1} = \int_{\mathcal{B}} \boldsymbol{\sigma}_{n+1} : \mathbf{B}\, \mathrm{d}v, \tag{3.86}$$

where $\boldsymbol{\sigma}_{n+1}$ can be computed by the updated displacement $\mathbf{u}_{n+1}$: this is done via the constitutive

relation, i.e.,

$$\boldsymbol{\sigma}_{n+1} = f(\mathbf{u}_{n+1}, \ldots). \tag{3.87}$$

At this stage the accelerations can be advanced also, i.e.,

$$\ddot{\mathbf{u}}_{n+1} = \mathbf{M}^{-1} \left(\mathbf{f}_{n+1} - \mathbf{P}_{n+1}\right). \tag{3.88}$$

For numerical efficiency a lumped (or diagonal) mass-matrix $\mathbf{M}$ is used, the basic idea is store element masses along the diagonal of the matrix. Then the computation of $\mathbf{M}^{-1}$ becomes trivial. The updated accelerations lead to the advancement of the velocity, displacement, and stress, and the solution cycle continues.

As compared to implicit methods, the explicit method avoids the computationally demanding task of matrix inversion and does not require the tangent stiffness matrix of its constitutive relations. The major drawback of the explicit method is, however, its conditional stability. If accelerations change drastically during an increment, the method produces inaccurate results or may even lead to catastrophic failure of the simulation. To prevent such drastic changes in acceleration, the problem is solved at very small (sub-millisecond) time increments. The time step, known as the critical time step, is determined by material properties and element size, and should be equal to the smallest time taken for a (stress) wave to propagate across an element.

3.3 Contact Mechanics

The previous sections dealt with the solid mechanics problem with a single body, subjected to boundary and initial conditions. A large class of problems, however, involve interactions, such as muscle gliding along bone or a car crashing into a barrier. This section briefly introduces the theory to include contact in the solid mechanics initial boundary value problem.[4]

Consider some continuum bodies in space. The "rules" which govern the motion and deformation of each body are identical, i.e., each body is governed by its own boundary value problem and constitutive relation. As these bodies translate and deform, they may occupy the same region of space. Without some framework which tracks the bodies (and their surfaces), and allows for force transmission across shared surfaces, they would simply pass through one another. The framework of contact mechanics allows the bodies to interact with one another and extends the continuum-mechanical framework by modifying the boundary value problem such that contact-gaps, -surfaces, and -forces can be described. The interactions between the bodies are embedded within the boundary value problem, thus linking mechanical contact over the body surface with the behaviour of the bulk of the body.

Consider the problem in Figure 3.2, where two bodies, $\mathcal{B}_0^{(1)}$ and $\mathcal{B}_0^{(2)}$ in the reference configuration undergo large motions and deformations described by placement functions $\boldsymbol{x}^{(1)} = \boldsymbol{\chi}^{(1)}(\boldsymbol{X}^{(1)}, t)$ and $\boldsymbol{x}^{(2)} = \boldsymbol{\chi}^{(2)}(\boldsymbol{X}^{(2)}, t)$ (cf. Equation 3.1), arriving at their respective current configurations $\mathcal{B}^{(1)}$ and $\mathcal{B}^{(2)}$. In addition to the surfaces over which the Dirichlet and Neumann boundary conditions are applied, an additional surface over which (possible) contact

[4] References for the detailed treatment of contact mechanics and related topics of tribology include Wriggers (2006) and Laursen (2003).

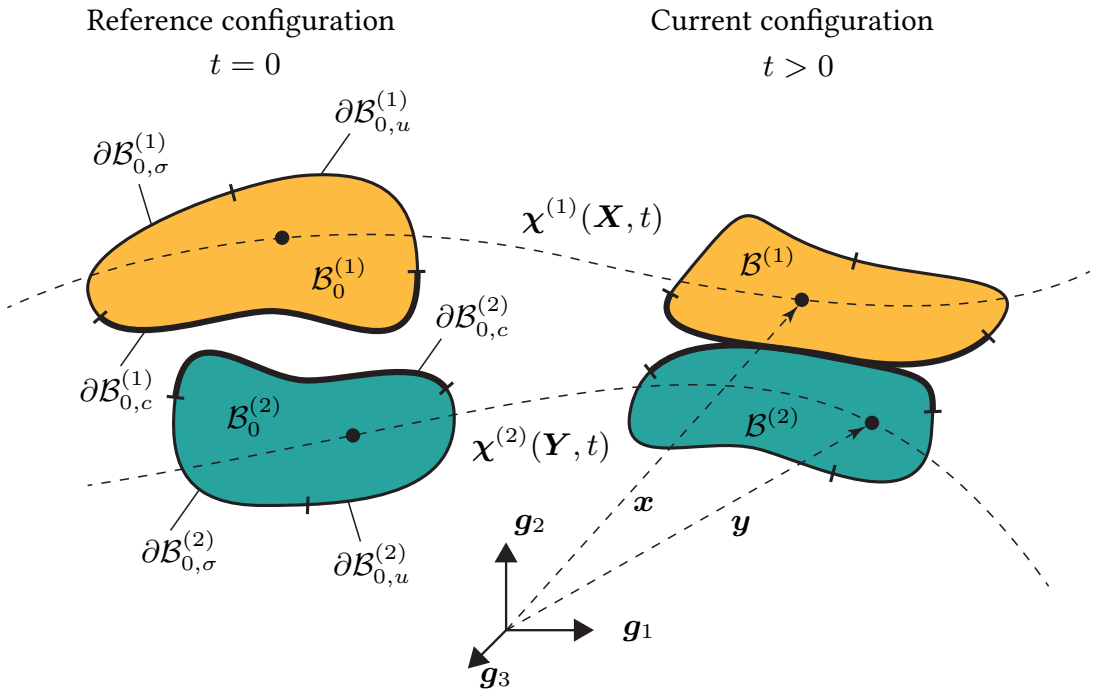

Figure 3.2: *Kinematic setting of continuum bodies in contact in the reference and current configurations. For clarity, the boundary definitions of the surfaces in the current configuration (right) are omitted.*

may occur is defined as $\partial\mathcal{B}_{\mathrm{c}}^{(i)}$, $i = \{1, 2\}$, with the properties

$$\begin{aligned} &\partial\mathcal{B}_u^{(i)} \cup \partial\mathcal{B}_\sigma^{(i)} \cup \partial\mathcal{B}_c^{(i)} = \partial\mathcal{B}^{(i)}, \quad \text{and} \\ &\partial\mathcal{B}_u^{(i)} \cup \partial\mathcal{B}_\sigma^{(i)} = \partial\mathcal{B}_u^{(i)} \cup \partial\mathcal{B}_c^{(i)} = \partial\mathcal{B}_\sigma^{(i)} \cup \partial\mathcal{B}_c^{(i)} = \emptyset. \end{aligned} \tag{3.89}$$

For the description of contact between bodies it is convenient to denote one surface over which the contact is parametrised, i.e., the surface whose points will be monitored with respect to the second surface. The reference surface is typically denoted the master surface and the other the slave, here $\partial\mathcal{B}^{(2)}$ is chosen as the slave surface. Furthermore, the slave surface is parametrised by a set of convected coordinates $\boldsymbol{\xi} = \{\xi_1, \xi_2\}$, which can be thought of as being "engraved" on the surface of $\partial\mathcal{B}^{(2)}$.

For every point on the master surface $\boldsymbol{x}^{(1)} \in \partial\mathcal{B}^{(1)}$, the closest point on the slave surface $\tilde{\boldsymbol{x}}^{(2)} \in \partial\mathcal{B}^{(2)}$ can be found by a minimum distance problem, i.e.,

$$d^{(2)}(\boldsymbol{\xi}) = \left\|\boldsymbol{x}^{(1)} - \tilde{\boldsymbol{x}}^{(2)}\right\| = \min_{\boldsymbol{x}^{(2)}} \left\|\boldsymbol{x}^{(1)} - \boldsymbol{x}^{(2)}(\boldsymbol{\xi})\right\| \quad \forall\, \boldsymbol{x}^{(1)} \in \partial\mathcal{B}^{(1)}. \tag{3.90}$$

The tangent vectors at $\boldsymbol{x}^{(2)}$ (to $\boldsymbol{\xi}$) are computed via

$$\boldsymbol{a}_\alpha = \frac{\partial \boldsymbol{x}^{(2)}(\boldsymbol{\xi})}{\partial \boldsymbol{\xi}^\alpha}, \tag{3.91}$$

where $\alpha = \{1, 2\}$. Then the normal (outward from the slave to the master surface) is given

simply by the cross-product of the tangential vectors, i.e.,

$$\boldsymbol{n}^{(2)} = \frac{\boldsymbol{a}_1 \times \boldsymbol{a}_2}{\|\boldsymbol{a}_1 \times \boldsymbol{a}_2\|}. \tag{3.92}$$

The fundamental relation, the so-called gap function, can then be defined as the closest absolute distance between both surfaces, i.e.,

$$g_{\mathrm{N}}(\boldsymbol{X}^{(1)}, t) = -\boldsymbol{n} \cdot \big(\boldsymbol{x}^{(1)}(\boldsymbol{X}^{(1)}, t) - \tilde{\boldsymbol{x}}^{(2)}(\boldsymbol{X}^{(2)}, t)\big). \tag{3.93}$$

It should be noted that the name gap function as defined here is a misnomer, as $g > 0$ does not indicate a positive distance or gap between the bodies but rather an interpenetration of the two. To prevent interpenetration of the bodies, a resultant contact pressure $t_{\mathrm{N}}(\boldsymbol{X}, t)$ must arise (in the direction $\boldsymbol{n}$) when $g_{\mathrm{N}} > 0$. These physical considerations leads to the so-called Karush-Kuhn-Tucker (KKT) optimality conditions, i.e.,

$$g_{\mathrm{N}}(\boldsymbol{X}^{(1)}, t) \leq 0, \qquad t_{\mathrm{N}}(\boldsymbol{X}^{(1)}, t) \geq 0, \quad \text{and} \quad t_{\mathrm{N}}\, g_{\mathrm{N}} = 0. \tag{3.94}$$

The conditions mean: First, that interpenetration of the two bodies is not permitted. Second, that the pressure that arises must be positive, i.e., directed towards the surface and third, that pressure can only arise when contact occurs.

3.3.1 Tangential contact

The gap function only describes interactions normal to the surfaces. Frequently, however, relative or tangential movement and contact accompanies normal contact. Applying the balance of linear momentum at the contact boundary $\partial\mathcal{B}_{\mathrm{c}}^{(1)} = \partial\mathcal{B}_{\mathrm{c}}^{(2)}$ in the reference configuration, the first Piola-Kirchhoff stress is

$$\boldsymbol{T}_{\mathrm{c}}^{(1)}(\boldsymbol{X}^{(1)}, t)\, \mathrm{d}A^{(1)} = \boldsymbol{P}^{(1)}\, \boldsymbol{N}\, \mathrm{d}A^{(1)} = -\boldsymbol{T}_{\mathrm{c}}^{(2)}(\tilde{\boldsymbol{X}}^{(2)}, t)\, \mathrm{d}A^{(2)}. \tag{3.95}$$

In other words, the traction must be equal and opposite across the contacting surfaces. The contact traction $\boldsymbol{T}_{\mathrm{c}}^{(2)}$ can be decomposed into normal and tangential components, t_{N} and $\boldsymbol{t}_{\mathrm{T}}$, respectively, i.e.,

$$\boldsymbol{T}_{\mathrm{c}}^{(2)} = \boldsymbol{t}_{\mathrm{T}} + t_{\mathrm{N}}\, \boldsymbol{n}, \tag{3.96}$$

where $\boldsymbol{t}_{\mathrm{T}} \cdot \boldsymbol{n} = 0$. Since the tangential component is in the tangent space of $\partial\mathcal{B}_{\mathrm{c}}^{(2)}$, it can be resolved via the base vectors $\boldsymbol{a}^{\alpha}$ ($\alpha = \{1, 2\}$) (Equation 3.91) via

$$\boldsymbol{t}_{\mathrm{T}} = -t_{\mathrm{T}_\alpha}\, \boldsymbol{a}^{\alpha}, \tag{3.97}$$

where $\boldsymbol{a}^{\alpha}$ are contravariant vectors associated with $\boldsymbol{a}_{\alpha}$. The surface tractions $\boldsymbol{t}_{\mathrm{T}}$ then provide the basis of a frictional constitutive law. A popular choice is the Coulomb friction law, i.e.,

$$\Phi = \|\boldsymbol{t}_{\mathrm{T}}\| - \mu\, t_{\mathrm{N}} \leq 0, \tag{3.98}$$

where μ is the coefficient of friction and Φ is the so-called slip function. The magnitude of the tangential traction is limited by that of the normal traction, and μ dictates this proportionality and is referred to as the coefficient of friction. Typical values of μ for contacting surfaces

are: 0.2–0.4 for concrete-steel, 0.04–0.06 for steel-teflon, 0.06–0.10 for cartilage-cartilage with various lubricating solutions (Merkher et al., 2006; Wriggers, 2006).

Friction resists tangential movement and therefore, if the friction is high enough no relative tangential motion should occur. This is described via the tangential velocity, which can be expressed as

$$\boldsymbol{\nu}_{\mathrm{T}} = \dot{\zeta}\,\frac{\boldsymbol{t}_{\mathrm{T}}}{\|\boldsymbol{t}_{\mathrm{T}}\|} \qquad \text{with} \qquad \dot{\zeta} \geq 0 \quad \text{and} \quad \dot{\zeta}\,\boldsymbol{\Phi} = 0, \tag{3.99}$$

where $\dot{\zeta}$ is the consistency parameter defined piecewise according to

$$\dot{\zeta} = \begin{cases} = 0, & \text{if} \quad \Phi < 0 \quad (\text{stick}) \\ > 0, & \text{else if} \quad \|\boldsymbol{t}_{\mathrm{T}}\| = \mu\, t_{\mathrm{N}} \quad (\text{slip}). \end{cases} \tag{3.100}$$

The expressions (Equations 3.99)$_{2-3}$ reflect two key physical constraints: first, no slip occurs while the tangential tractions $\boldsymbol{t}_{\mathrm{N}}$ are below the Coulomb limit ($\mu\, t_{\mathrm{N}}$) and second, any slip that does occur must be linearly proportional to the frictional stress exerted. These inequalities, together with the KKT optimality conditions (Equation 3.94) specify the additional constraints imposed on a system when incorporating finite deformation, frictional contact.

3.3.2 Weak formulation of the contact problem

The strong form of the contact problem can then be obtained by the standard initial boundary value problem of solid mechanics (Equations 3.69) subject to the normal and tangential contact conditions given in Equations 3.94 and 3.98–3.99, respectively. The weak form is derived similarly to the initial boundary value problem discussed in Section 3.1.7, i.e., multiplication by a test function which vanishes at the Dirichlet boundary surface and performing an integration over the body domain, now with an additional term describing the contact work over $\partial\mathcal{B}_{\mathrm{c}}^{(i)}$.

As previously mentioned, contact is typically parametrised over the slave surface, furthermore, only the active contact surface contributes to contact work. Then, the weak form of the large deformation solid mechanics problem with contact is given (directly) by

$$\begin{aligned} \sum_{i=1}^{2} \int_{\mathcal{B}_0^{(i)}} \boldsymbol{P}^{(i)} : \mathrm{Grad}(\delta\boldsymbol{U}^{(i)}) + \rho_0^{(i)}\,\ddot{\boldsymbol{X}}^{(i)} \cdot \delta\boldsymbol{U}^{(i)}\,\mathrm{d}V - \int_{\mathcal{B}_0^{(i)}} \boldsymbol{B}^{(i)} \cdot \delta\boldsymbol{U}^{(i)}\,\mathrm{d}V \\ - \int_{\partial\mathcal{B}_{\sigma,0}^{(i)}} \hat{\boldsymbol{T}}^{(i)} \cdot \delta\boldsymbol{U}^{(i)}\,dS + \int_{\tilde{\partial}\mathcal{B}_{\mathrm{c},0}^{(2)}} \left(\delta\boldsymbol{U}^{(1)} - \delta\boldsymbol{U}^{(2)}\right) \cdot \left(t_{\mathrm{N}}\,\boldsymbol{n} + \boldsymbol{t}_{\mathrm{T}}\right)\,\mathrm{d}A = 0, \end{aligned} \tag{3.101}$$

where $\tilde{\partial}\mathcal{B}_{\mathrm{c},0}^{(2)}$ denotes the active contact boundary (on the slave surface). The above expression is analogous to Equation 3.73 with an additional contact virtual work term.

4 Constitutive Modelling of the Musculoskeletal System

The initial boundary value problem in Chapter 3 describes the continuum-mechanical system in terms of kinematic and deformation measures, stresses, and balance principles. These equations, however, do not distinguish the type of material(s) within the system. Using, again, the analogy of a spring—the material that the spring is made of is critical to determining its deformation under a certain weight. This information is provided by the constitutive relations. Whereas the balance principles must hold for all materials, constitutive relations hold only for the particular material they describe. In *"Biomechanics—Mechanical Properties of Living Tissues"*, Yuan-Cheng Fung (Fung, 1993) writes:

> *[O]bservations of living organisms can be made at various levels of size: e.g., at the level of the naked eye, ..., or at the limit of scanning tunneling microscopes. ...And the images of a biological entity look very different at different levels of magnification. This suggests that we can define a continuum of the real world with a specific bound on the lower scale of size.*

The bound on the lower scale of size is linked to the concept of the representative volume element, which plays a fundamental role in continuum mechanics, and by extension, in continuum-mechanical constitutive relations. The representative volume element assumes that a point in the continuum body represents the averaged microstructure in the volume surrounding that point. Typically, at volumes smaller than the representative volume element, the density and behaviour of the material becomes heterogeneous.

Therefore, continuum-mechanical constitutive relations must describe material behaviour at a macroscopic scale. This poses certain challenges for skeletal muscle models. First, force production occurs at the microscopic level, where (myosin and actin) filaments in the sarcomere slide past each other and convert chemical energy to mechanical energy. The cross-bridge dynamics lead to the characteristic properties of muscle contraction such as the force-length f_l and force-velocity f_v relationships. Second, due to the fibrous structure of muscles, this active force (or stress) is transmitted predominantly along a preferred direction, i.e., along the muscle fibres, impacting the passive behaviour of muscle as well. Third, muscle fibres are neither recruited individually nor all-at-once, instead bundles of fibres are stimulated together by an α-motor-neuron (the motor-unit). Therefore, there are several "microscopic" features of muscle behaviour that need to be captured by a macroscopic constitutive description of skeletal muscles.

Several macroscopic, continuum-mechanical, constitutive relations of skeletal muscle have been proposed in the last few decades, and have addressed the first two issues described above. Given a muscle body $\mathcal{B}$, the two primary variables are the stretch $\lambda(\boldsymbol{x})$ ($\boldsymbol{x} \in \mathcal{B}$) and activity parameter. The characteristics of muscle contraction are modelled using phenomenological approaches, for example, by defining f_l directly as a function of fibre stretch $f_\mathrm{l}(\lambda)$ (similarly for $f_\mathrm{v}(\dot{\lambda})$) (e.g. Zajac, 1989). Typically, the activity parameter acts to scale the active stress between

0 and 1, corresponding to fully-passive and -active behaviour, respectively. Muscle structure is represented by a fibre orientation field, which acts as a preferred direction along which the active stress is transmitted.

The passive behaviour of skeletal muscles is typical of soft biological tissues, exhibiting the so-called "J-shaped" stress-strain behaviour (e.g. Takaza et al., 2013). These materials are initially compliant and undergo stiffening to prevent damage at high levels of stretch. Additionally, soft biological tissues (skeletal muscles included) are highly incompressible due to their large water content (e.g. Böl et al., 2014). This is responsible for the characteristic bulging of skeletal muscles—as shortening along the fibres takes place, volume is conserved by thickening in the off-fibre directions.

In summary, a vast majority of macroscopic constitutive relations describe skeletal muscle as transversely isotropic, nearly or purely incompressible, and additively split the active and passive stress responses (so-called active-stress approach) (e.g. Johansson et al., 2000; Blemker et al., 2005b; Tang et al., 2009; Chi et al., 2010; Röhrle et al., 2017). Some relations treat the passive behaviour of muscle as viscoelastic (e.g. Wheatley et al., 2017). This effect, however, is assumed to be small (Tian et al., 2011) and thus is typically not considered. For recent reviews on the topic see Dao et al. (2018) and Röhrle et al. (2019).

In line with state-of-the-art methods, a slightly modified constitutive relation of skeletal muscles is developed. The key difference is the way in which the muscle activation parameter is computed, which is modified to account for *individual* motor-unit anatomy and activity. Status-quo constitutive relations of skeletal muscle treat muscle activity in an averaged sense, that is, a temporally varying but spatially constant activity is applied throughout the muscle. This is justified by assuming that motor-units are uniformly distributed and by doing so, the ability to model the functional heterogeneity of muscles is lost. To replicate the motor-unit driven recruitment of muscles, the activity is decomposed into spatial and temporal components representing motor-unit anatomy and activity, respectively. This modification, however, does not *characterise* motor-unit anatomy and activity, which is dealt with in Chapter 5.

This chapter is organised as follows: First, building on the continuum-mechanical theory introduced in Chapter 3, the theory of hyperelastic constitutive modelling, in general, is presented (Section 4.1). Second, the constitutive relation of the musculotendon complex is described (Section 4.2). The majority of this section deals with the muscle and is then generalised to account for connective tissues in the musculotendon complex. Other soft tissues and bones are idealised as linear elastic and are described briefly (Section 4.3). Lastly, the musculotendon complex constitutive relations are characterised with experimental data to describe the transversely isotropic behaviour of a general human skeletal muscle (Section 4.4).[1]

4.1 Hyperelasticity

Soft biological tissues are often described via hyperelastic material constitutive relations. Originally developed for rubber materials, such relations derive from a (specific) strain-energy Ψ (in J/mm^3 $\propto$ N/mm^2), which is *"...the mechanical work required in a reversible process to produce a particular state of strain"* (Mooney, 1940). Recalling that the first Piola-Kirchhoff stress $\boldsymbol{P}$ is work-conjugate to time derivative of the deformation gradient $\dot{\boldsymbol{F}}$ (Equation 3.59),

[1]Further references for the detailed treatment of continuum-mechanical constitutive relations, including those used in this chapter, are: Fung (1993) and Holzapfel (2000).

then the work done between $t = [0, T]$ can be written as

$$\Psi = \int_0^T \boldsymbol{P} : \frac{\partial \boldsymbol{F}}{\partial t}\, dt, \tag{4.1}$$

and differentiating both sides by time yields

$$\frac{\partial \Psi}{\partial t} = \boldsymbol{P} : \frac{\partial \boldsymbol{F}}{\partial t}. \tag{4.2}$$

Then, using the chain rule, the rate of the strain-energy can be expressed as

$$\frac{\partial \Psi}{\partial t} = \frac{\partial \Psi}{\partial \boldsymbol{F}} \frac{\partial \boldsymbol{F}}{\partial t}. \tag{4.3}$$

Comparing Equations 4.2 and 4.3, yields

$$\boldsymbol{P} = \frac{\partial \Psi(\boldsymbol{F})}{\partial \boldsymbol{F}}. \tag{4.4}$$

The above relation can be expressed for the Cauchy and second Piola-Kirchhoff stresses by using the mappings in Equations 3.29 and 3.32

$$\boldsymbol{\sigma} = J^{-1}\, \frac{\partial \Psi(\boldsymbol{F})}{\partial \boldsymbol{F}}\, \boldsymbol{F}^{\mathrm{T}}, \qquad \boldsymbol{S} = \boldsymbol{F}^{-1}\, \frac{\partial \Psi(\boldsymbol{F})}{\partial \boldsymbol{F}}. \tag{4.5}$$

The strain-energy is assumed to be objective, i.e., the energy within the system is independent of rigid body motions,

$$\Psi(\boldsymbol{F}) = \Psi(\boldsymbol{F}^{+}) = \Psi(\boldsymbol{Q}, \boldsymbol{F}), \tag{4.6}$$

using Equations 3.66 and 3.63 (in the reference configuration). Setting $\boldsymbol{Q} = \boldsymbol{R}^{\mathrm{T}}$ and using the right polar decomposition (Equation 3.10),

$$\Psi(\boldsymbol{Q}, \boldsymbol{F}) = \Psi(\boldsymbol{R}^{\mathrm{T}}, \boldsymbol{F}) = \Psi(\boldsymbol{U}). \tag{4.7}$$

The expression above shows that the strain-energy of a hyperelastic material is dependent purely on the stretch, i.e.,

$$\Psi(\boldsymbol{F}) = \Psi(\boldsymbol{U}). \tag{4.8}$$

For biological materials with a preferred direction, such as skeletal muscles, it is convenient to formulate constitutive relations in terms of the second Piola-Kirchhoff stress $\boldsymbol{S}$, since it has the property of being invariant under rigid body rotations (in the current configuration). As such, the strain-energy is formulated in terms of the right Cauchy-Green deformation tensor $\boldsymbol{C}$ (Equation 3.13), which is work-conjugate to $\boldsymbol{S}$,

$$\Psi(\boldsymbol{F}) = \Psi(\boldsymbol{C}). \tag{4.9}$$

Considering $\Psi(\boldsymbol{C})$, via the chain rule and using Equation 3.13

$$\frac{\partial \Psi(\boldsymbol{F})}{\partial \boldsymbol{F}} = \frac{\partial \Psi(\boldsymbol{C})}{\partial \boldsymbol{C}}\, \frac{\partial \boldsymbol{C}}{\partial \boldsymbol{F}} = 2\boldsymbol{F}\, \frac{\partial \Psi(\boldsymbol{C})}{\partial \boldsymbol{C}}. \tag{4.10}$$

The expression in Equations 4.4 and 4.5_{1-2} then become;

$$\boldsymbol{P} = 2\boldsymbol{F}\,\frac{\partial \Psi}{\partial \boldsymbol{C}}, \qquad \boldsymbol{\sigma} = 2J^{-1}\,\boldsymbol{F}\,\frac{\partial \Psi}{\partial \boldsymbol{C}}\,\boldsymbol{F}^{\mathrm{T}}, \quad \text{and} \quad \boldsymbol{S} = 2\frac{\partial \Psi}{\partial \boldsymbol{C}}, \tag{4.11}$$

respectively, and describe the general constitutive relation for a hyperelastic material. That is, the characterisation of the stress response requires the definition of the strain-energy Ψ.

4.1.1 Incompressibility and quasi-incompressibility

Given the large water content in soft biological materials they can be considered as incompressible. In the continuum-mechanical framework, this implies the volume ratio between the reference and current configurations must equal unity, i.e., $J = 1$ (Equation 3.42). This constraint, on the deformation, is typically added to the strain-energy function via the Lagrangean method, i.e.,

$$\hat{\Psi} = \Psi(\boldsymbol{C}) - p\,(J - 1), \tag{4.12}$$

where Ψ is the purely incompressible material behaviour and p is the Lagrange multiplier (in N/mm^2), corresponding in this context to the hydrostatic pressure, which enforces the incompressibility condition. To determine the stress response, the above equation is differentiated with respect to $\boldsymbol{F}$, then together with Equations 4.4, 4.5_2 and 4.10 (derivation skipped), the second Piola-Kirchhoff stress can be expressed as

$$\boldsymbol{S} = 2\frac{\partial \Psi}{\partial \boldsymbol{C}} - p\,\boldsymbol{C}^{-1}. \tag{4.13}$$

The hydrostatic pressure p, being a kinematic constraint, can only be enforced by taking the balance relations and boundary conditions into account. The enforcement of this constraint requires considering the pressure as an independent variable in the balance relations.

Alternatively, the material can be treated as *nearly* incompressible by adding a penalty term $\tilde{\Psi}(J)$ to the strain-energy function to enforce the incompressibility condition (e.g. Oden, 1978; Simo et al., 1982). Where $\tilde{\Psi}(J)$ is chosen such that $\tilde{\Psi}(J \to 0) = \tilde{\Psi}(J \to \infty) = \infty$ and that the reference configuration results in a stress-free state. Then, the strain-energy for the nearly incompressible material is given by

$$\hat{\Psi} = \Psi(\boldsymbol{C}) + \tilde{\Psi}(J). \tag{4.14}$$

Thus the constrained optimisation of incompressible strain-energy is recast into an unconstrained optimisation problem of the nearly incompressible strain-energy. Note that Equation 4.14 is not a split of strain-energy into purely dilatational (volume-changing) and distortional (volume-preserving) parts, but rather the penalty term essentially replaces the incompressibility constraint enforced via p in Equation 4.12 and is commonly referred to as the coupled formulation. With the numerical implementation of the constitutive relation in mind, the nearly incompressible constitutive relations are chosen and are solely discussed in the following.

4.1.2 Isotropy

Assuming that the nearly incompressible strain-energy $\hat{\Psi}$ is unchanged under rotations, it may then be represented in terms of the principal invariants of its arguments,

$$\hat{\Psi} = \Psi(I_1, I_2) + \tilde{\Psi}(I_3), \tag{4.15}$$

where

$$I_1(\boldsymbol{C}) = \operatorname{tr} \boldsymbol{C}, \quad I_2(\boldsymbol{C}) = 1/2 \left[(\operatorname{tr} \boldsymbol{C})^2 - \operatorname{tr}(\boldsymbol{C}^2)\right], \quad I_3(\boldsymbol{C}) = \det \boldsymbol{C} = J^2. \tag{4.16}$$

The stresses, given their definitions in Equations 4.11_{1-3}, may now be expressed in terms of the invariants using the following relations,

$$\frac{\partial \hat{\Psi}(\boldsymbol{C})}{\partial \boldsymbol{C}} = \sum_{i=1}^{3} \frac{\partial \hat{\Psi}}{\partial I_i} \frac{\partial I_i}{\partial \boldsymbol{C}}, \tag{4.17}$$

and

$$\frac{\partial I_1}{\partial \boldsymbol{C}} = \boldsymbol{I}, \qquad \frac{\partial I_2}{\partial \boldsymbol{C}} = I_1 \boldsymbol{I} - \boldsymbol{C}, \qquad \frac{\partial I_3}{\partial \boldsymbol{C}} = I_3 \boldsymbol{C}^{-1}. \tag{4.18}$$

Lastly, the strain-energy and associated stress relations may also be formulated in terms of the principal stretches of $\boldsymbol{U}$ or $\boldsymbol{b}$ (Equation 3.11), i.e.,

$$\hat{\Psi}(\boldsymbol{C}) = \hat{\Psi}(\lambda_i), \tag{4.19}$$

where i=$\{1, 2, 3\}$. The partial derivative in Equation 4.17 can be written in terms of the principle stretches λ_i and directions $\boldsymbol{N}_i$ (Equation 3.11) as

$$\frac{\partial \hat{\Psi}(\boldsymbol{C})}{\partial \boldsymbol{C}} = \sum_{i=1}^{3} \frac{\partial \hat{\Psi}}{\partial \lambda_i^2} \frac{\partial \lambda_i^2}{\partial \boldsymbol{C}} = \sum_{i=1}^{3} \frac{1}{\lambda_i} \frac{\partial \hat{\Psi}}{\partial \lambda_i} \boldsymbol{N}_i \otimes \boldsymbol{N}_i. \tag{4.20}$$

The principle stretches are further subject to the condition $J = \lambda_1 \lambda_2 \lambda_3 = 1$, if the material is perfectly incompressible.

4.1.3 Transverse isotropy

In addition to the typical J-shaped stress-strain response, several biological tissues exhibit differing mechanical responses along various direction, for example, arteries (Dobrin, 1978), tendons (Kolz et al., 2015) and myocardium (Demer et al., 1983). Owing to its microscopic structure, skeletal muscle displays preferred fibre directions, along which the majority of the force is transmitted. Skeletal muscle may be therefore idealised as a ground material (connective tissues) with a single fibre family exhibiting a single preferred direction (muscle fibres), i.e., as a transversely isotropic material.

Considering a point $\boldsymbol{X} \in \mathcal{B}_0$ that now displays a preferred fibre direction $\boldsymbol{a}_0(\boldsymbol{X})$, $|\boldsymbol{a}_0| = 1$ in the reference configuration. Analogous to Equation 3.7, $\boldsymbol{a}_0$ is mapped to the current configuration via

$$\lambda \, \boldsymbol{a}(\boldsymbol{X}, t) = \boldsymbol{F}(\boldsymbol{X}, t) \, \boldsymbol{a}_0(\boldsymbol{X}), \tag{4.21}$$

where $|\boldsymbol{a}| = 1$. In other words, λ corresponds to the stretch along the current (unit) fibre direction $\boldsymbol{a}$ and is often computed in the reference configuration via

$$\lambda\,\boldsymbol{a}\cdot\lambda\,\boldsymbol{a} = \lambda^2 = \boldsymbol{F}\,\boldsymbol{a}_0\cdot\boldsymbol{F}\,\boldsymbol{a}_0 = \boldsymbol{a}_0\cdot\boldsymbol{C}\,\boldsymbol{a}_0, \tag{4.22}$$

using Equation 3.13.

The fibre orientation is used to construct a so-called structural tensor (for further details, see Holzapfel (2000) and Schröder et al. (2003));

$$\boldsymbol{M} = \boldsymbol{a}_0\otimes\boldsymbol{a}_0. \tag{4.23}$$

The strain-energy must remain objective under rigid body motions and in addition to I_1, I_2, I_3 (Equation 4.16) the following invariants are introduced

$$I_4 = \boldsymbol{a}_0\cdot\boldsymbol{C}\,\boldsymbol{a}_0 = \lambda^2, \qquad I_5 = \boldsymbol{a}_0\cdot\boldsymbol{C}^2\,\boldsymbol{a}_0. \tag{4.24}$$

The nearly incompressible strain-energy is now given by

$$\hat{\Psi} = \Psi(I_1, I_2, I_4, I_5) + \tilde{\Psi}(I_3), \tag{4.25}$$

and the stresses (Equations 4.11_{1-3}) may now be expressed in terms of the invariants using Equations 4.17 and 4.18, together with

$$\frac{\partial I_4}{\partial \boldsymbol{C}} = \boldsymbol{M}, \qquad \frac{\partial I_5}{\partial \boldsymbol{C}} = \boldsymbol{a}_0\otimes\boldsymbol{C}\,\boldsymbol{a}_0 + \boldsymbol{a}_0\,\boldsymbol{C}\otimes\boldsymbol{a}_0. \tag{4.26}$$

Lastly, the transversely isotropic strain-energy and stresses can be expressed in the principal directions. Setting $\boldsymbol{N}_1 = \boldsymbol{a}_0$, $\lambda_1 = \lambda$, and expanding the summation in Equation 4.20 gives

$$\frac{\partial\hat{\Psi}(\boldsymbol{C},\boldsymbol{M})}{\partial\boldsymbol{C}} = \frac{1}{\lambda}\frac{\partial\hat{\Psi}}{\partial\lambda}\,\boldsymbol{M} + \frac{1}{\lambda_2}\frac{\partial\hat{\Psi}}{\partial\lambda_2}\,\boldsymbol{M}_2 + \frac{1}{\lambda_3}\frac{\partial\hat{\Psi}}{\partial\lambda_3}\,\boldsymbol{M}_3, \tag{4.27}$$

where $\boldsymbol{M}_2 = \boldsymbol{M}_3 = (1/2)\,(\boldsymbol{I} - \boldsymbol{M})$ for transverse isotropy (e.g. Odegard et al., 2008).

4.2 Musculotendon Complex

The constitutive relation of skeletal muscle is developed first, and then generalised to describe the musculotendon complex. The constitutive relation is a modified form of Röhrle et al. (2017), and is a transversely isotropic, nearly incompressible, hyperelastic material model.

The active behaviour is modelled by the active-stress approach, where the passive and active stresses are additively split, i.e.,

$$\boldsymbol{S}_{\text{muscle}}(\boldsymbol{C},\boldsymbol{M},\alpha_{\text{M}}) = \boldsymbol{S}_{\text{passive}}(\boldsymbol{C},\boldsymbol{M}) + \alpha_{\text{M}}\,\boldsymbol{S}_{\text{active}}(\boldsymbol{C},\boldsymbol{M}), \tag{4.28}$$

where $\boldsymbol{S}$ is the second Piola-Kirchhoff stress tensor (without loss of generality), and α_{M} is the activity parameter that scales the active stress between 0 and 1, corresponding to passive and active behaviour, respectively.

The passive response of skeletal muscle is further split into contributions from the isotropic

"bulk" (connective tissues) and along the muscle fibres, i.e.,

$$\boldsymbol{S}_{\text{passive}}(\boldsymbol{C}, \boldsymbol{M}) = \boldsymbol{S}_{\text{isotropic}}(\boldsymbol{C}) + \boldsymbol{S}_{\text{anisotropic}}(\boldsymbol{C}, \boldsymbol{M}), \tag{4.29}$$

Both passive responses are modelled by a hyperelastic material response and are therefore derived from strain-energy functions (Section 4.2.1 and 4.2.2).

Passive stresses arise due to external deformation of the muscle, that is, they arise only if there is non-zero strain imposed on the muscle. On the other hand, the active response of muscles is only partly dependent on mechanical deformation, i.e., incremental change in active stresses can occur when there is no incremental change in the strains. This is possible due to activation of the muscle, which gives rise to stress within the muscle—independent of the strain incrementation. Thus, the active stress does not warrant a strain-energy potential for its derivation (e.g. Ambrosi et al., 2012) and the stress formulation is directly introduced (Section 4.2.3). Note that the active response is dependent on the mechanical deformation via the force-length relationship.

4.2.1 Isotropic response

The isotropic response in Equation 4.29 represents the connective tissue between the muscle fibres, e.g., epimysium and endomysium, and is characterised as hyperelastic. As explained earlier and in Section 4.1, a nearly incompressible formulation is chosen due to numerical reasons. The isotropic strain-energy Ψ_{iso} can then be given by

$$\hat{\Psi}_{\text{isotropic}}(I_1, I_2, I_3) = \Psi_{\text{isotropic}}(I_1, I_2) + \tilde{\Psi}_{\text{isotropic}}(I_3), \tag{4.30}$$

where Ψ is the incompressible strain-energy and $\tilde{\Psi}$ is an energetic penalty term which enforces the incompressibility condition $J = 1$ (see Section 4.1.1), given here by,

$$\tilde{\Psi}_{\text{isotropic}}(I_3) = c\,(J-1)^2 - d\,\ln J, \tag{4.31}$$

where c is the penalty parameter and d is a dependent material parameter (both typically in N/mm^2=MPa). The parameter d ensures a stress-free reference configuration, and depends on the particular form of $\Psi^{\text{isotropic}}$ (Holzapfel, 2000). As $c \to \infty$ the strain-energy is amplified for $J \neq 1$ (Figure 4.1). For alternate penalty formulations see Simo et al. (1982) and Ciarlet (1988, Chapter 4).

Biological tissues can be characterised by a large diversity of hyperelastic constitutive laws (e.g. Chagnon et al., 2015, and references therein). Here, the Mooney-Rivlin law is used, which has the following strain-energy function

$$\Psi_{\text{isotropic}}(I_1, I_2) = c_1\,(I_1 - 3) + c_2\,(I_2 - 3), \tag{4.32}$$

where c_1, c_2 are material parameters (in MPa). Then, using Equations 4.11_3, 4.17 and 4.18_{1-3}, the second Piola-Kirchhoff stress is given by

$$\begin{aligned} \boldsymbol{S}_{\text{isotropic}} &= 2\frac{\partial \Psi_{\text{iso}}}{\partial \boldsymbol{C}} = 2\left(\frac{\partial \Psi}{\partial \boldsymbol{C}} + \frac{\partial \tilde{\Psi}}{\partial \boldsymbol{C}}\right) \\ &= 2\,(c_1 + I_1 c_2)\,\boldsymbol{I} - 2c_2\,\boldsymbol{C} + 2cJ(J-1)\,\boldsymbol{C}^{-1} - d\,\boldsymbol{C}^{-1}. \end{aligned} \tag{4.33}$$

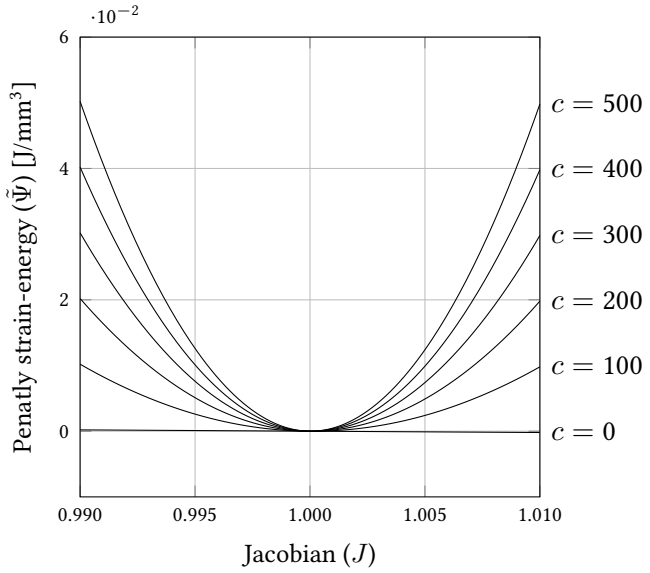

Figure 4.1: *Penalty strain-energy function against volumetric change with varying penalty parameters.*

Using the assumption of a stress-free reference configuration, the above expression can be solved for d (in MPa), giving,

$$d = 2(c_1 + 2c_2). \tag{4.34}$$

4.2.2 Anisotropic-passive response

The anisotropic response represents the passive resistance of the muscle along the fibre direction. A strain-energy function from Balzani et al. (2006) is used, which describes soft biological tissues and satisfies conditions of polyconvexity, yields a stress-free reference configuration, and provides good fitting capabilities. Assuming that muscle fibres only provide resistance under tension, the strain-energy has the form:

$$\Psi_{\text{anisotropic}}(I_4) = \begin{cases} c_3\,(I_4 - 1)^{c_4} + c_5\,(I_4 - 1)^{c_6} & \text{if } \lambda \geq 1, \\ 0 & \text{otherwise,} \end{cases} \tag{4.35}$$

where c_3, c_5, c_4 and c_6 are material parameters; the former two are in MPa, while the latter are unitless. Recall that $\lambda = \sqrt{I_4}$ is the fibre stretch (Equation 4.24).

The second Piola-Kirchhoff stress is derived similarly to the isotropic stress, together with Equation 4.26. Since, however, the $\Psi_{\text{anisotropic}}$ is dependent on I_4 alone, the second Piola-Kirchhoff stress reduces to

$$\boldsymbol{S}_{\text{anisotropic}} = \frac{\partial \Psi}{\partial I_4}\,\boldsymbol{M}. \tag{4.36}$$

Giving,

$$\boldsymbol{S}_{\text{ansiotropic}} = \begin{cases} 2\,c_3\,c_4 \boldsymbol{M}\,(I_4 - 1)^{c_4 - 1} + 2\,c_5\,c_6\,\boldsymbol{M}\,(I_4 - 1)^{c_6 - 1} & \text{if } \lambda \geq 1, \\ 0 & \text{otherwise.} \end{cases} \tag{4.37}$$

4.2.3 Anisotropic-active response

The anisotropic-active response, as motivated above, does not explicitly warrant a mechanical strain-energy potential, since the activation supplied to the stress arises due to biochemical sources. Therefore, the active stress formulation is directly introduced as

$$\boldsymbol{S}_{\text{active}} = \frac{P_{\text{max}}}{I_4}\,\alpha_{\text{M}}\,f_{\text{l}}(\lambda)\,\boldsymbol{M}, \tag{4.38}$$

where $\alpha_{\text{M}} = [0, 1]$ is the degree of activation of the muscle, $\lambda = \sqrt{I_4}$, P_{max} is the maximum specific-strength of the muscle (in MPa), and $f_{\text{l}}(\lambda)$ is the normalised amount of actin-myosin overlap, i.e., dictating the force-length relationship of the active stress. Here, this is defined as

$$f_{\text{l}} = \exp\left(-\left|\frac{\frac{\lambda}{\lambda^{\text{opt}}} - 1}{w_i}\right|^{v_i}\right), \tag{4.39}$$

where $i = \text{asc}$ for $\lambda \leq \lambda^{\text{opt}}$ and $i = \text{dsc}$ for $\lambda > \lambda^{\text{opt}}$, corresponding to the ascending and descending branches of the force-length relationship, respectively.

4.2.4 Accounting for motor-unit anatomy and activity

As it stands, the activity parameter scales the active stress uniformly for all points $\boldsymbol{x}$ in the muscle body $\mathcal{B}$. To account for both motor-units distribution and activity, the "traditional" activity parameter is decomposed correspondingly into spatial and temporal components. That is,

$$\alpha_{\text{M}} \rightarrow \alpha_{\text{M}}(t, \boldsymbol{x}) = \sum_{i=1} \alpha_i(t)\;\hat{\kappa}_i(\boldsymbol{x}(\boldsymbol{X}, t)), \tag{4.40}$$

where the muscle activation now depends on the sum of motor-unit activities $\alpha_i(t)$ and their distribution within the muscle $\hat{\kappa}_i(\boldsymbol{x})$. Decomposition of muscle activity in such a way requires certain assumptions on the spread of activity within the motor-unit. It can be seen in the above equation that a scalar activity is applied simultaneously to all spatial positions of a motor-unit. This implies that the activity of all fibres and sarcomeres within the motor-unit are synchronised, i.e., action-potential propagation is instantaneous once it arrives at the neuromuscular-junction. The errors introduced by this assumption are quantified in Section 6.2.

The territory distributions are (normalised) volume fractions at each point within the muscle, and are related in the current and reference configurations by the placement function, i.e.,

$$\hat{\kappa}_i(\boldsymbol{x}) = \boldsymbol{\chi}(\hat{\kappa}_i(\boldsymbol{X}), t). \tag{4.41}$$

In other words, the motor-unit distributions $\hat{\kappa}_i(\boldsymbol{X})$ are defined in the reference configuration and subsequently transported with the deforming material. Of course, the two quantities—$\alpha_i(t)$ and $\hat{\kappa}_i(\boldsymbol{X})$—must be defined in a physiologically realistic manner. Their definition is covered in Chapter 5.

4.2.5 Musculotendon complex

The overall stress response of the muscle is given by substituting Equations 4.33, 4.37, 4.38, and 4.40 into Equation 4.28;

$$\begin{aligned}\boldsymbol{S}_{\text{muscle}} &= 2\,(c_1 + I_1\,c_2)\,\boldsymbol{I} - 2c_2\,\boldsymbol{C} + 2cJ(J-1)\,\boldsymbol{C}^{-1} - d\,\boldsymbol{C}^{-1} \\ &+ \left(2\,c_3\,c_4\,(I_4-1)^{c_4-1} + 2\,c_5\,c_6\,(I_4-1)^{c_6-1}\right)\boldsymbol{M} \\ &+ \left(\frac{1}{I_4}\,P_{\max}\,\alpha_{\text{M}}(\boldsymbol{X},t)\,f_{\text{l}}(\lambda)\right)\boldsymbol{M},\end{aligned} \tag{4.42}$$

subject to the condition in Equations 4.37 and f_{l} is determined via Equation 4.39.

Owing to their function of (uniaxial) load transmission between muscle and bone, tendons have highly varied mechanical properties along different directions, being much stiffer along the major (collagen) fibre direction (e.g. Lynch et al., 2003). Therefore, the tendons may also be considered as fibres embedded in an extracellular matrix and the same constitutive relations used for the skeletal muscles are employed.

The skeletal muscle constitutive relation (Equation 4.42) is generalised by introducing two parameters: $\tilde{P}_{\max}$ and γ_{M}. The first parameter acts to scale the passive muscle response in proportion to the maximum specific-strength and is computed via

$$\tilde{P}_{\max} = \frac{P_{\max}}{P^0_{\max}}, \tag{4.43}$$

where $P^0_{\max}$ is a reference maximum specific-strength (in MPa) used to characterise the active force-length response and $P_{\max}$ is the corresponding value for the muscle under consideration.

The second parameter denotes the type of tissue being modelled, where $\gamma_{\text{M}} = 1$ represents pure muscle tissue, $\gamma_{\text{M}} = 0$ represents pure tendon tissue and $0 < \gamma_{\text{M}} < 1$ is a mixture of the two. Tissue parameters are used to scale and interpolate the material parameters to yield the overall musculotendon complex material parameters according to

$$c_i^{\text{MTC}} = \gamma_{\text{M}}\,\tilde{P}_{\max}\,c_i^{\text{musc}} + (1-\gamma_{\text{M}})\,c_i^{\text{tend}}, \tag{4.44}$$

where $i = 1, \ldots, 6$ are the material parameters in Equations 4.33 and 4.37. Note the parameter c is an incompressibility parameter (Equation 4.31), which remains constant for all tissues and d is a dependent material parameter (Equation 4.34). The superscripts $(\cdot)^{\text{musc}}$ and $(\cdot)^{\text{tend}}$ are introduced to differentiate material parameters for muscle and tendon, respectively. Note that $\tilde{P}_{\max}$ only scales the passive response of the muscle parameters.

By substituting c_i^{MTC} into Equations 4.33 and 4.37, $\boldsymbol{S}^{\text{MTC}}_{\text{isotropic}}$ and $\boldsymbol{S}^{\text{MTC}}_{\text{anisotropic}}$ are obtained, respectively. The overall musculotendon complex stress response is given by

$$\boldsymbol{S}^{\text{MTC}}(0 < \gamma_{\text{M}} < 1) \rightarrow \boldsymbol{S}^{\text{MTC}} = \boldsymbol{S}^{\text{MTC}}_{\text{isotropic}} + \boldsymbol{S}^{\text{MTC}}_{\text{passive}} + \gamma_{\text{M}}\,\boldsymbol{S}_{\text{active}}, \tag{4.45}$$

and for pure muscle and tendon, correspondingly, by

$$\boldsymbol{S}^{\text{MTC}}(\gamma_{\text{M}} = 1) \rightarrow \boldsymbol{S}^{\text{musc}} = \boldsymbol{S}^{\text{musc}}_{\text{isotropic}} + \boldsymbol{S}^{\text{musc}}_{\text{passive}} + \boldsymbol{S}_{\text{active}} \quad \text{and} \tag{4.46}$$

$$\boldsymbol{S}^{\text{MTC}}(\gamma_{\text{M}} = 0) \rightarrow \boldsymbol{S}^{\text{tend}} = \boldsymbol{S}^{\text{tend}}_{\text{isotropic}} + \boldsymbol{S}^{\text{tend}}_{\text{passive}}. \tag{4.47}$$

Other stress measures can be obtained by using the mappings in Equations 3.33-3.36, for

example, the musculotendon complex Cauchy stress is

$$\boldsymbol{\sigma}^{\mathrm{MTC}} = J^{-1}\,\boldsymbol{F}\,\boldsymbol{S}^{\mathrm{MTC}}\,\boldsymbol{F}^{\mathrm{T}}. \tag{4.48}$$

4.3 Other Soft Tissues and Bones

During human movement, skeletal muscles and connective tissues undergo large deformations and exhibit non-linear material behaviour. Bones, on the other hand, experience much smaller strains given their higher stiffness and can thus be treated as linear elastic. Other soft tissues considered in this thesis, such as the periodontal ligament or the articular discs are also assumed to behave linear elastically. This oversimplification of their behaviour was justified by the fact that the stress response in and around these regions was not of primary interest.

In a linear elastic material, stresses are a function of strain only, i.e.,

$$\boldsymbol{\sigma} = \boldsymbol{C} : \boldsymbol{\epsilon}, \tag{4.49}$$

where $\boldsymbol{C}$ is the fourth-order symmetric tensor of elastic material coefficients and $\boldsymbol{\epsilon}$ is the infinitesimal strain tensor defined by

$$\boldsymbol{\epsilon} = \frac{1}{2}\Big((\mathrm{grad}(\boldsymbol{u}))^{\mathrm{T}} + \mathrm{grad}(\boldsymbol{u})\Big), \tag{4.50}$$

recalling that $\boldsymbol{u}$ is the displacement (Equation 3.5). Due to the symmetries of the stress and strain tensors and in the case of isotropic elasticity, the non-zero components of $\boldsymbol{C}$ can be written (in Voigt notation) as

$$C_{1,1} = C_{2,2} = C_{3,3} = \lambda_{\mathrm{L}} + 2\mu_{\mathrm{L}}, \tag{4.51}$$
$$C_{4,4} = C_{5,5} = C_{6,6} = \mu_{\mathrm{L}}, \tag{4.52}$$
$$C_{1,2} = C_{1,3} = C_{2,3} = \lambda_{\mathrm{L}}, \tag{4.53}$$

where λ_{L} and μ_{L} are the so-called Lamé coefficients (both in MPa). Equation 4.49 can then be expressed as

$$\boldsymbol{\sigma} = \lambda_{\mathrm{L}}\,\mathrm{tr}\,\boldsymbol{\epsilon} + 2\mu_{\mathrm{L}}\,\boldsymbol{\epsilon}. \tag{4.54}$$

Lamé coefficients are related to the commonly used Young's modulus E (in MPa) and Poisson's ratio ν via

$$E = \frac{\mu_{\mathrm{L}}(3\lambda_{\mathrm{L}} + 2\mu_{\mathrm{L}})}{\lambda_{\mathrm{L}} + \mu_{\mathrm{L}}} \quad \text{and} \tag{4.55}$$
$$\nu = \frac{\lambda_{\mathrm{L}}}{2(\lambda_{\mathrm{L}} + \mu_{\mathrm{L}})}. \tag{4.56}$$

4.4 Material Characterisation

Although the constitutive relations demarcate types of material, i.e., rubber from stone, the parameters within a constitutive relation characterise the response of a particular material. For example, in the one-dimensional Hooke's law $f = k\,x$, the relation between the force f and extension x demarcates linearly elastic materials, while the material parameter k characterises

the stiffness of a particular spring. Similarly the independent material parameters c_{1-6}^{musc}, c_{1-6}^{tend}, and P_{max} characterise the response of a particular musculotendon complex.

Since the constitutive relations describe the relation between stress and strain at individual points $\mathcal{P}$ within a continuum body $\mathcal{B}$, experimental data should be obtained from muscle samples experiencing homogeneous deformations. In other words, determining material parameters at the whole muscle scale, or with specimens containing geometric non-linearities, or multiple materials is not ideal.

The musculotendon complex responses and associated material parameters are characterised by in vivo experimental data obtained from literature: $\boldsymbol{S}_{\text{isotropic}}^{\text{musc}}$ and $\boldsymbol{S}_{\text{anisotropic}}^{\text{musc}}$ to Takaza et al. (2013), $\boldsymbol{S}_{\text{active}}$ to Gordon et al. (1966) and Gollapudi et al. (2009) and $\boldsymbol{S}_{\text{anisotropic}}^{\text{tend}}$ to Kolz et al. (2015).

Under the assumption of homogeneous deformation, i.e., all points $\mathcal{P} \in \mathcal{B}$ experience the same deformations, stresses, and strains, the constitutive relations can be reformulated in terms of principle stretches and directions (Equations 4.20 and 4.27). Then by aligning the principal directions with experimental (loading and constraint) directions, the determination of the material parameters is greatly simplified.

To simplify the fitting procedure, the purely incompressible forms of the Mooney-Rivlin relation is used. The assumption is that if the penalty parameter c is large enough, the response of the nearly incompressible formulation should sufficiently match the purely incompressible form (investigated in Section 6.3.3).

4.4.1 Non-active musculotendon complex behaviour

Muscle isotropic and passive response

The anisotropic-passive and isotropic response are characterised simultaneously. This is because of the lack of experimental data on individual fibres and the isolated (isotropic) matrix. In other words, it is difficult to experimentally isolate the contributions of the isotropic and anisotropic components to the passive response along the fibre direction. More commonly, the intact muscle (fibres and matrix) is experimentally tested (e.g. van Loocke et al., 2006; Takaza et al., 2013; Böl et al., 2014; Mohammadkhah, 2017).

The anisotropic-passive and isotropic responses were fit by comparing the predicted uniaxial stress responses (given below) to the experimental tensile response of Takaza et al. (2013). Briefly, the experiments were performed on excised samples of the longissimus dorsi muscle of three-month old female pigs. The samples were approximately $50 \times 10 \times 10$ mm and were loaded at a strain rate of $0.05\,\%\,\text{s}^{-1}$ and the material response was plotted as Cauchy stress against stretch (digitised here via the open source program `PlotDigitizer` (Huwaldt, 2015)). Material parameters c_{1-6}^{musc} were adjusted such that the error between the predicted and experimental responses was minimised.

Consider a uniaxial (compression or tension) displacement on a specimen of muscle, i.e., experiencing homogeneous deformation. The specimen is displaced by λ along λ_1, and the remaining directions (λ_2,λ_3) are unconstrained. This means that stress σ_1 (along λ_1) is non-zero, while $\sigma_2 = \sigma_3 = 0$.

The incompressibility constraint enforces a constant volume throughout the deformation, i.e., $J = 1$ (Equation 3.42) and can be expressed in terms of the principle directions as

$$J = \lambda_1 \lambda_2 \lambda_3 = 1. \tag{4.57}$$

Under this assumption, the deformations for (homogeneous) uniaxial displacement by the amount λ can be expressed as

$$\lambda_1 = \lambda, \qquad \lambda_2 = \frac{1}{\sqrt{\lambda}}, \qquad \lambda_3 = \lambda_2. \tag{4.58}$$

Since experimental data is often formulated in terms of the true stress, the passive muscle stress (Equation 4.42 with $\alpha_{\mathrm{M}} = 0$) is expressed as the Cauchy stress, using Equations 4.11_2 and 4.20. Then for uniaxial loading the Cauchy stresses in the principle directions $\sigma_{\text{passive},i}$ are

$$\begin{aligned} \sigma_{\text{passive},1} &= -p + 2\lambda^2 \left(\lambda^2 - 1\right)^{c_6 - 1} c_5 c_6 + 2\lambda^2 \left(\lambda^2 - 1\right)^{c_4 - 1} c_3 c_4 + 4\lambda c_2 + 2\lambda^2 c_1 \\ \sigma_{\text{passive},2} &= \sigma_{\text{passive},3} = -p + 2\lambda c_2 + \frac{2c_2}{\lambda^2} + \frac{2c_1}{\lambda}, \end{aligned} \tag{4.59}$$

where p is the hydrostatic pressure enforcing the incompressibility constraint (cf. Equation 4.13), and is determined by the boundary condition that the off-axis stresses must be zero. Then

$$p = \frac{\left(2\lambda^3 + 2\right)\, c_2 + 2\lambda c_1}{\lambda^2}. \tag{4.60}$$

Since the problem is multi-dimensional, non-smooth and with multiple possible local minima, a gradient free search-based optimisation method was used (e.g. Hooke et al., 1961). Briefly, the direct-search method proceeds as follows: First, let $R(x_1, x_2, \ldots, x_n)$ be the objective function to be minimised, here: the difference between the experimental and predicted stresses,

$$R(\mathbf{c}) = \sum_{i=1}^{N} \left(\sigma_{\text{passive},1}(\lambda_i, \mathbf{c}) - \sigma^{\text{exp}}_{\text{passive},1}(\lambda_i)\right)^2, \tag{4.61}$$

where $\mathbf{c}$ is the vector of material parameters and λ_i is the current stretch. Second, starting with some base point $B^0 = R(\mathbf{c}^0)$, each parameter is perturbed and the objective function evaluated. Third, the perturbed parameters which result in the minimal objective function are selected to be the next base point $R(\mathbf{c}^1) = B^1$. The process is repeated until $R(\mathbf{c}^i)$ falls below some tolerance value. The optimisation was performed in `MATLAB` (R2018a, The MathWorks, Inc., USA) using the patternsearch function.

The optimised parameters c^{musc}_{1-6} are given in Table 4.1. The resulting parameters were used to predict the (homogeneous) passive and isotropic material responses in uniaxial tension, and are plotted together with the experimental data in Figure 4.2.

Tendon response

It is assumed that the tendon extracellular matrix behaviour is identical to that of the skeletal muscle and as such the parameters $c^{\text{tend}}_1, c^{\text{tend}}_2$ are taken as those identified for the skeletal muscle. This leaves the parameters of the anisotropic-passive response c^{tend}_{3-6} to capture the in-fibre stiffness of the tendon. Experimental data from Kolz et al. (2015) were used, in which uniaxial tensile experiments were performed on the biceps tendon. Similar to above, the data was imported using `PlotDigitizer` and the parameters identified via optimisation methods in `MATLAB`. The optimised parameters are given in Table 4.1.

Table 4.1: *Summary of material properties for the musculotendon complex with respective sources.*

Tissue	Contribution	Parameter	Value	Source/comments
muscle	isotropic	c^{musc}	10 MPa	penalty parameter
		c_1^{musc}	2.683×10^{-6} MPa	fit to Takaza et al. (2013)
		c_2^{musc}	1.171×10^{-2} MPa	
	passive	c_3^{musc}	2.653×10^{-2} MPa	
		c_4^{musc}	2.755	
		c_5^{musc}	4.514×10^{-2} MPa	
		c_6^{musc}	5.451	
	active	w_{asc}	2.944×10^{-1}	fit to Gordon et al. (1966)
		v_{asc}	2.146	
		w_{dsc}	4.612×10^{-1}	
		v_{dsc}	3.669	
		λ_{opt}	–	muscle specific
		P_{max}	–	
		P_{max}^0	1.330×10^{-1} MPa	Gollapudi et al. (2009)
		ρ^{musc}	1.060 g/cm^3	Ward et al. (2005)
tendon	isotropic	c_1^{tend}	c_1^{musc}	
		c_2^{tend}	c_1^{musc}	
	passive	c_3^{tend}	6.407×10^3 MPa	fit to Kolz et al. (2015)
		c_4^{tend}	6.014	
		c_5^{tend}	3.031×10^1 MPa	
		c_6^{tend}	2.380	
		ρ^{tend}	ρ^{musc}	

4.4.2 Active muscle behaviour

Analogous to the passive response, the fully activated ($\alpha_{\text{M}} = 1$) active stress (Equation 4.38) can be expressed in terms of principle stretches for homogeneous loads as,

$$\sigma_{\text{active},1} = P_{\text{max}} \exp\left(- \left| \frac{\frac{\lambda}{\lambda^{\text{opt}}} - 1}{w_i} \right|^{v_i} \right). \tag{4.62}$$

The parameters $w_i, v_i, \lambda_{\text{opt}}$ govern the force-length relationship of the sarcomere by scaling the maximum isometric stress P_{max} as function of the sarcomere stretch. The experimentally measured sarcomere force-length relationship by Gordon et al. (1966) is used to characterise the force-length relationship. The data is reported as normalised isometric tetanus tension $\bar{t}_{\text{sc}}$ against the sarcomere length l_{sc} (in µm) and was was digitised using the aforementioned `PlotDigitizer`.

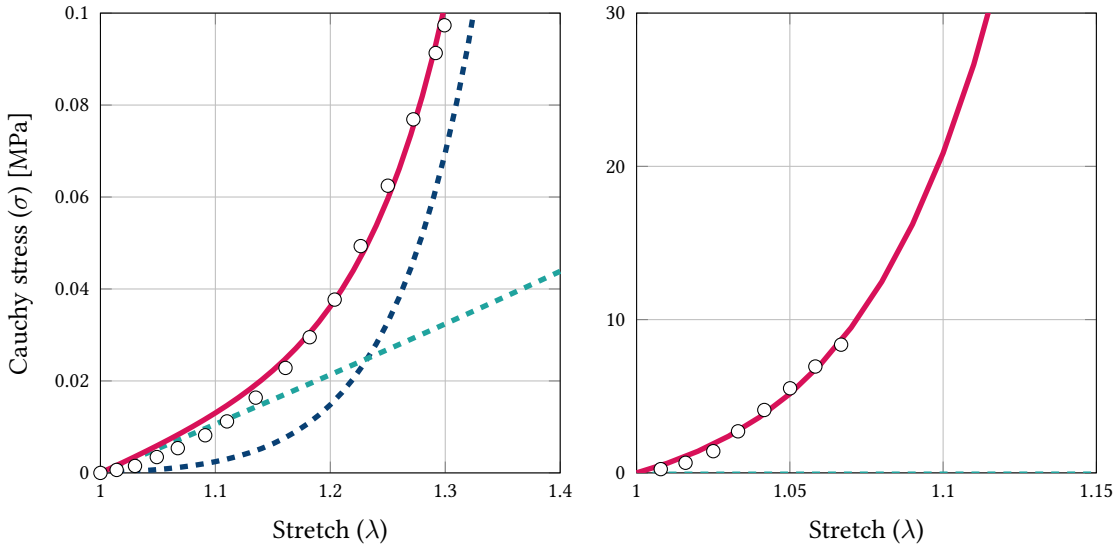

(a) *Skeletal muscle response.* ***(b)*** *Tendon response.*

Figure 4.2: *Predicted uniaxial, tensile passive-muscle and -tendon responses compared to experimental values. Individual contributions shown with dotted lines: isotropic and passive responses in green and blue, respectively and the total response with a thick, solid line. Experimental data is shown with circular markers: adapted from Takaza et al. (2013) and Kolz et al. (2015) for (a) the skeletal muscle and (b) tendon tissue, respectively.*

Sarcomere stretch λ was computed by first determining the optimal sarcomere length $l_{\text{sc}}^{\text{opt}}$ and then by assuming that the sarcomere stretch at this length unity, i.e., $\lambda = \lambda_{\text{opt}} = 1$, then

$$\lambda_i = \frac{l_{\text{sc},i}}{l_{\text{sc}}^{\text{opt}}}. \tag{4.63}$$

To obtain a reference specific-strength of the muscle, the maximum isometric tension of type-I muscle fibres was used $P_{\text{max}}^0 = 0.133$ MPa (Gollapudi et al., 2009). The normalised tension $\bar{t}_{\text{sc}}$ was then multiplied by this value to obtain the experimental active stress, i.e.,

$$\sigma_{\text{active,1}}^{\text{exp}} = P_{\text{max}}^0 \, \bar{t}_{\text{sc}}. \tag{4.64}$$

The parameters w_i and v_i were then determined by using optimisation methods in `MATLAB` to reduce the error between the $\sigma_{\text{active,1}}$ and $\sigma_{\text{active,1}}^{\text{exp}}$. The optimised parameters w_{asc}, w_{dsc}, v_{asc} and w_{dsc} are given in Table 4.1 and plotted in Figure 4.3a.

4.4.3 Overview and parameter variations

The set of parameters, and respective sources, characterising the musculotendon complex are summarised in Table 4.1. The effect of varying the amount of the connective tissue (tendon) percentage via γ_{M} on the passive response is shown in Figure 4.3b. The muscle specific parameters λ_{opt} and P_{max} were varied and the resulting uniaxial stress-strain responses are shown in Figures 4.4a and 4.4b, respectively. Lastly, the total muscle stress response is shown in Figure 4.5.

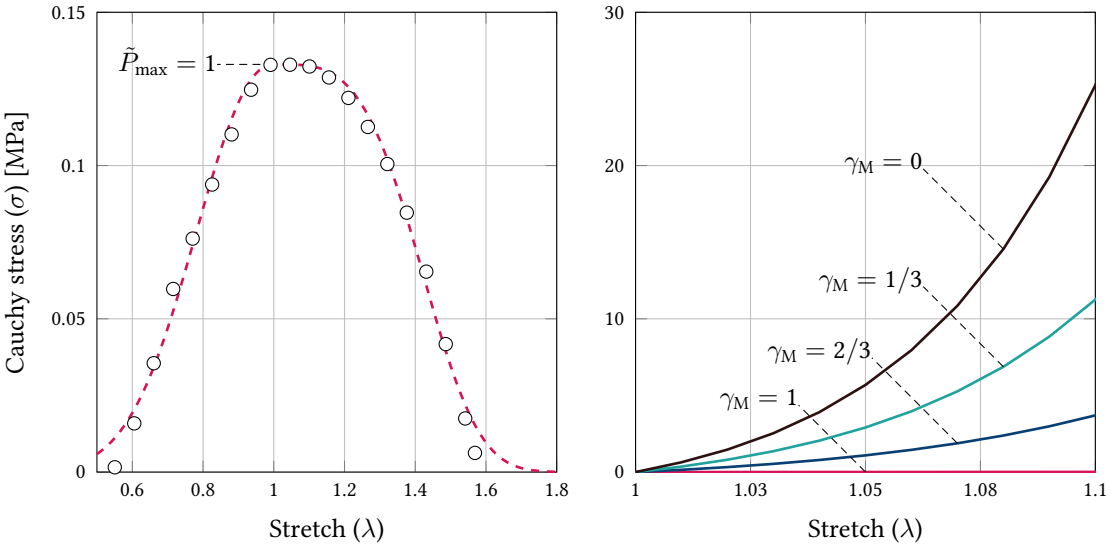

(a) ***(b)***

Figure 4.3: *(a) Unscaled active force-length with experimental data (from Gordon et al. (1966)) shown as circular marks, and (b) passive stress response for varying muscle volume fraction parameters.*

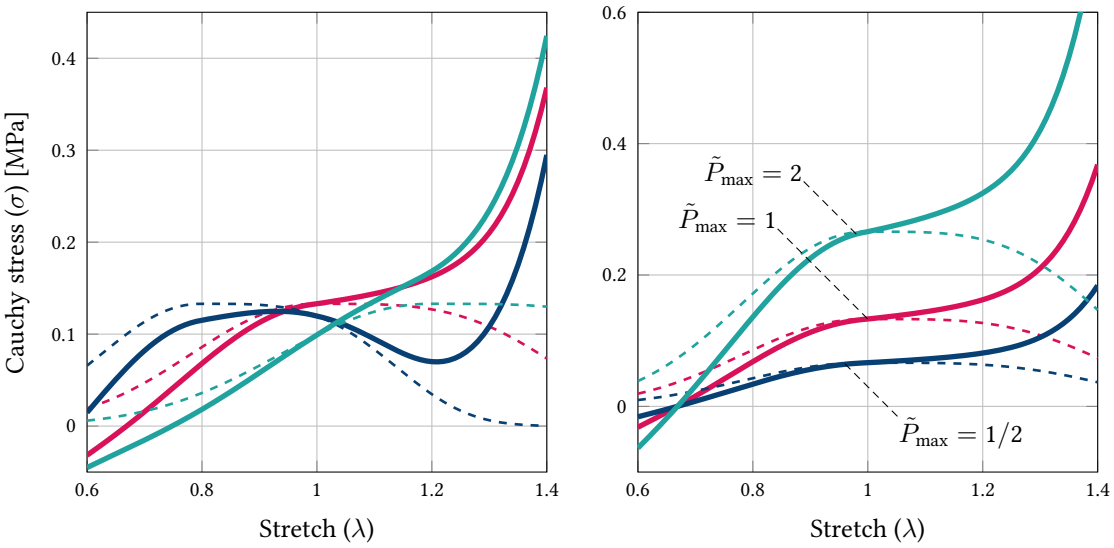

(a) *Varying λ_{opt}.* ***(b)*** *Varying P_{max}.*

Figure 4.4: *Effect of muscle specific material parameters on overall muscle stress response. The dotted lines represent the active f-l response and the solid line the total response. (a) dark-blue: $\lambda_{opt} = 0.8$, red: $\lambda_{opt} = 1.0$, green: $\lambda_{opt} = 1.2$ (b) variation in peak stress and resulting passive-scaling factor $\tilde{P}_{max}$.*

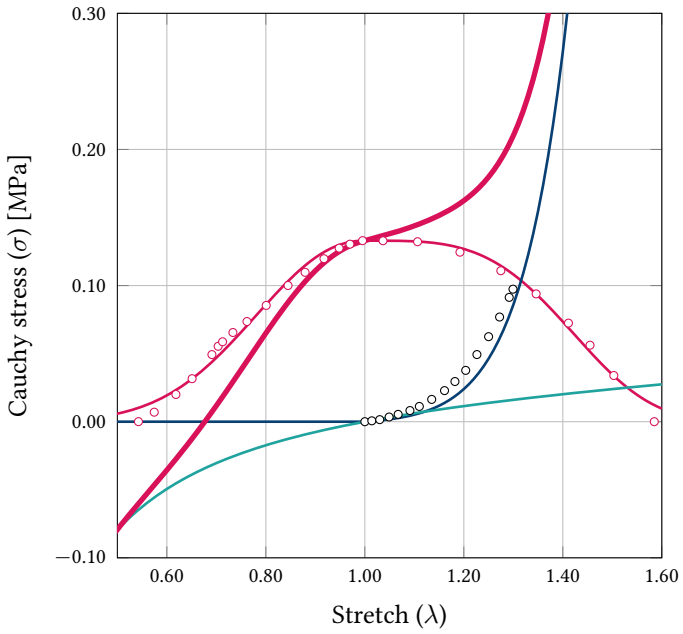

Figure 4.5: *Uniaxial stress response of the skeletal muscle, with each trace representing a different response: thick maroon: total, maroon: active, green: isotropic and dark-blue: anisotropic-passive. The experimental data derived from literature are shown as circular marks.*

5 Modelling Motor-Unit Activity and Anatomy

Muscle is unique among biological materials in its ability to contract and generate force. Skeletal muscle, as well as cardiac muscle, can do so rapidly compared to smooth muscle. Skeletal muscle comprises motor-units of varying size that often occupy subregions of the muscle's cross-sectional area. The anatomy (or architecture) of a motor-unit refers to the particular distribution of its fibres within the muscle. The selective recruitment of spatially localised motor-units is the basis of skeletal muscle functionally heterogeneity. This has a wide range of consequences for muscle function, for example, the same muscle can contribute to different tasks via selective recruitment of its motor-units. For example, the deep part of the masseter is more active during lateral jaw movement (Schindler et al., 2014), or different regions of the biceps are active during different tasks, whether due to supination or pronation (ter Haar Romeny et al., 1984) or due to contraction level alone (Borzelli et al., 2020). Regional contraction can also alter intramuscular pressure, which, in turn, regulates blood flow to mitigate fatigue (e.g. Sjøgaard et al., 1986; Sjøgaard et al., 1988). Remodelling of motor-unit anatomy can thus impact muscle function, for example, during healthy ageing (Lexell et al., 1988) and neuromuscular disorders, such as amyotrophic lateral sclerosis (ALS), Parkinson's disease or cerebral palsy (Morris, 1969; Rose et al., 1998; Kelly et al., 2018). Therefore, the modelling of motor-unit anatomy is paramount to understanding certain aspects of healthy and pathological motor-output.

Although status-quo, three-dimensional macroscopic muscle models may take motor-units into account in a *temporal* sense, i.e., by computing muscle activity from motor-unit recruitment and cross-bridge dynamics (e.g. Gielen et al., 2000; Oomens et al., 2003; Weickenmeier et al., 2017), the *spatial* distribution of motor-units in muscle is neglected. In other words, status-quo, macroscopic models use a time-varying activity that is applied uniformly throughout the muscle (e.g. Röhrle et al., 2017; Weickenmeier et al., 2017; Ramasamy et al., 2018; Péan et al., 2019) and thus cannot model regional muscle contraction and are not suited to investigate the functional heterogeneity of muscles.

This chapter presents a method to enrich continuum-mechanical muscle models with both motor-unit activity and, more importantly, their anatomy. As introduced in the previous chapter, the starting point is to decompose the (overall) muscle activity into temporal and spatial components. The focus of this chapter is the definition of physiologically realistic (temporal) motor-unit activity and their (spatial) anatomy (Figure 5.1). Motor-unit activity is computed by a somewhat standard approach (Section 5.1). Computation of the motor-unit anatomy, on the other hand, is more challenging. Motor-unit architecture is intrinsically linked to the fibre arrangement of the muscle. Macroscopic models forgo this microstructural information and instead represent this information as a fibre orientation *field*. Therefore, connectivity information of the fibres is lost. To generate anatomically plausible motor-unit architecture: First, this information is recovered by approximating the microstructure in three-dimensional models of skeletal muscles (Section 5.2). Second, a novel motor-unit architecture

algorithm is developed which innervates the reconstructed muscle fibres to generate the motor-unit distribution in three-dimensions (Section 5.3). Lastly, the performance and short-comings of the methods are discussed in Section 5.4.

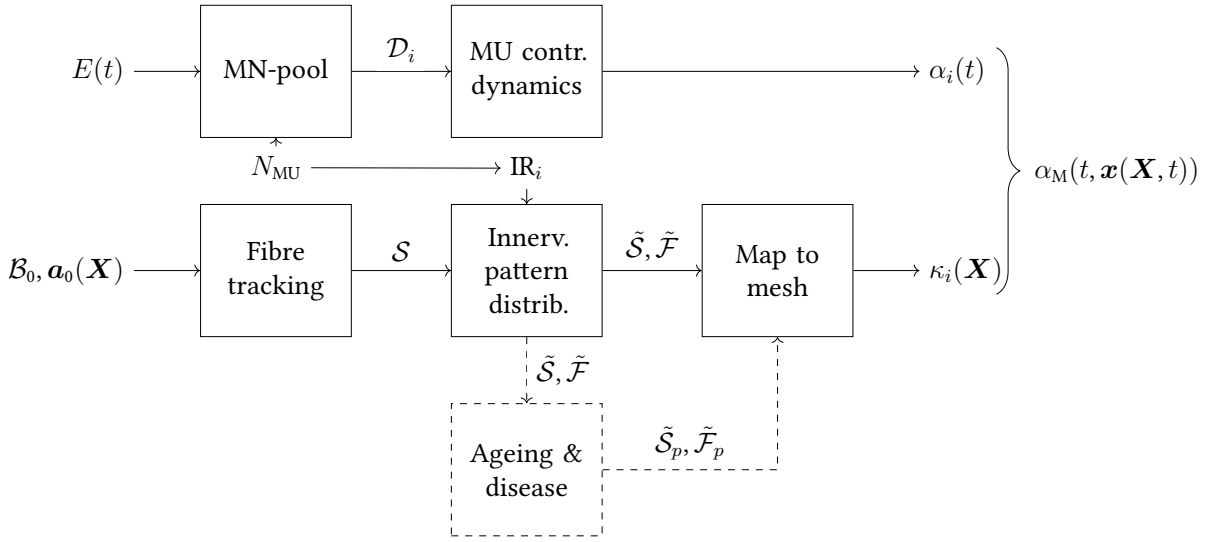

Figure 5.1: *Workflow to compute motor-unit driven muscle activity $\alpha_M(t, \boldsymbol{x})$ based on $i = 1, \ldots, N_{MU}$ motor-unit (MU) activities $\alpha_i(t)$ and MU anatomies $\kappa_i(\boldsymbol{X})$. The innervation-ratio IR_i determines the size of the MU. The voluntary excitatory drive $E(t)$ is used to compute motor-neuron firing times $\mathcal{D}_i$, which are combined with twitch properties to compute $\alpha_i(t)$. Muscle geometry $\mathcal{B}_0$ and fibre orientations $\boldsymbol{a}_0(\boldsymbol{X})$ are used to reconstruct the microstructure in the form of neuromuscular junctions (NMJs) $\mathcal{S}$ and corresponding fibres $\mathcal{F}$. The fibres are innervated at the NMJs and mapped to $\mathcal{B}_0$, forming $\kappa_i(\boldsymbol{X})$. The dotted lines show the optional step of ageing and disease, covered separately, in Chapter 9.*

5.1 Motor-Unit Activity

Voluntary movements are carried out by the recruitment of motor-units, typically across multiple muscles. This does not occur on a per-motor-unit basis, but rather according to higher-level recruitment strategies. One such robust strategy is the so-called size principle (Henneman, 1957), which states that motor-units are recruited in order of increasing force output (or size). Given that motor-unit sizes, i.e., the number of fibres they contain, vary exponentially; a large fraction of small motor-units are available for most tasks, with the larger motor-units "standing by" in case of an increased demand of force.

Once recruited, motor-units typically discharge at rates proportional to force level, limited by a maximum frequency. By recruiting additional motor-units, a muscle can increase its force output by approximately 80 %. The remaining 20 % is achieved by an increase in the discharge rate of the motor-units (e.g. De Luca et al., 1982), although this may vary between muscles (e.g. Scutter et al., 1998).

Motor-neuron pool recruitment is described by a phenomenological model of Fuglevand et al. (1993), which is briefly described in Section 5.1.1. The firing of an α-motor-neuron causes the motor-unit to contract and generate force via excitation-contraction coupling. More specifically, calcium (Ca^{2+}) currents have a cascading effect and cause cross-bridge cycling. The excitation-contraction coupling converts chemical energy into mechanical energy, which

is the basis of skeletal muscle force production.

Similar to Heidlauf et al. (2017), the Ca^{2+} and cross-bridge dynamics are described by biophysical models of Aliev et al. (1996) and Razumova et al. (1999), respectively, and are covered in Section 5.1.2. Lastly, the recruitment and cross-bridge dynamics models are characterised to describe a generic human motor-unit pool (Section 5.1.3).

5.1.1 Motor-neuron pool recruitment

The recruitment model is based on Fuglevand et al. (1993) and is only briefly covered in the following. Consider an α-motor-neuron pool with N_{MU} motor-units. Each α-motor-neuron i ($i = 1, \ldots, N_{\text{MU}}$) has a recruitment threshold R_i (in arbitrary units), above which it begins to discharge. The recruitment thresholds are normalised and follow an exponential distribution, with a large number of α-motor-neurons having a low threshold and vice versa, i.e.,

$$R_i = \exp\left(i \, \frac{\ln r_{\text{R}}}{N_{\text{MU}}} \, b\right), \tag{5.1}$$

where r_{R} is the range of recruitment thresholds and b is a shape parameter.

Volitional command for muscle contraction is described by an excitatory drive $E(t)$ (in arbitrary units). It represents the sum of all synaptic inputs to the muscle. A single, scalar, and time-varying excitatory drive is supplied to the α-motor-neuron pool. It is compared to the recruitment threshold R_i of α-motor-neuron i, which begins to discharge when the excitatory drive exceeds its recruitment threshold, i.e., $E(t) > R_i$. The mean discharge frequency (or firing rate) $\tilde{F}^{\text{R}}$ of an α-motor-neuron is not constant but rather increases as $E(t) >> R_i$, according to

$$\tilde{F}_i^{\text{R}}(t) = E(t) - R_i + F^{\text{M}} \quad \text{with} \quad E(t) > R_i \quad \text{and} \quad \tilde{F}_i^{\text{R}}(t) \leq F_i^{\text{P}}, \tag{5.2}$$

where F_i^{P} and F^{M} are the peak and minimum firing rates, respectively (all firing rates are in Hz). In the equation above, the second condition bounds the mean firing rate. The peak firing rate is described by

$$F_i^{\text{P}} = F_1^{\text{P}} - F^{\text{D}} \, \frac{R_i}{R_{N_{\text{MU}}}}, \tag{5.3}$$

where F^{D} is the range of peak firing rates and $R_{N_{\text{MU}}}$ is the recruitment threshold for the largest α-motor-neuron. The actual firing rate of the α-motor-neurons is computed by applying random perturbations about the mean firing rate $\tilde{F}_i^{\text{R}}$ according to

$$F_i^{\text{R}}(t) = \frac{\tilde{F}_i^{\text{R}}(t)}{1 + c\,Z}\,, \tag{5.4}$$

where $c = [0, 1]$ is the degree of variation and $Z_i(t)$ is selected from a normally distributed set of z-scores ranging between −3.9 and 3.9. Individual discharge times are then computed by the relation

$$F_i^{\text{R}}(t_j) = \frac{1}{t_{i,j+1}^{\text{F}} - t_{i,j}^{\text{F}}}, \tag{5.5}$$

rearranged as

$$t^{\mathrm{F}}_{i,j+1} = \frac{1}{F^{\mathrm{R}}_i(t_j)} + t^{\mathrm{F}}_{i,j}, \tag{5.6}$$

where $t^{\mathrm{F}}_{i,j}$ is the j^{th} firing time (in s) of motor-unit i and is stored in $\mathcal{D}_i = \{t^{\mathrm{F}}_1, t^{\mathrm{F}}_2, \ldots, t^{\mathrm{F}}_{\mathrm{end}}\}$.

The recruitment model (input/output) can be summarised, for an α-motor-neuron i, by

$$E(t),\ t = [0, t_{\mathrm{end}}] \rightarrow \mathcal{D}_i \ \mid\ E(t) > R_i,\ i = 1 \ldots, N_{\mathrm{MU}}, \tag{5.7}$$

where $t = [0, t_{\mathrm{end}}]$ is the duration of the excitatory drive and $\mathcal{D}_i$ are firing times for α-motor-neuron i.

5.1.2 Motor-unit contractile response

Skeletal muscle fibre cells are excitable, meaning that if a sufficiently strong current is applied, a depolarisation of the membrane potential occurs—the action-potential—before the cell returns to rest. The perturbation of the membrane potential causes ionic currents to cross the muscle fibre cell's membrane and has a cascading effect, leading ultimately to cross-bridge cycling and tension production.

Almost all models of action-potential propagation derive from the landmark model of Alan Hodgkin and Andrew Huxley (Hodgkin et al., 1952). Briefly, the essence of the model was to describe the membrane potential V_{m} as an electrical circuit: a capacitor C_{m} in parallel with ionic currents I_{ion}, and is stated here for reference:

$$C_{\mathrm{m}}\frac{dV_{\mathrm{m}}}{dt} = -I_{\mathrm{ion}}(V_{\mathrm{m}}, t) + I_{\mathrm{stim}}, \tag{5.8}$$

where I_{stim} is some applied current.

The ionic currents comprise sodium Na^+, potassium K^+, and other (leakage) currents. The behaviour of each current is scaled by its (per unit area) conductance, which themselves may depend on the membrane potential via so-called gating variables. For further details of the model, see the cited literature or Keener et al. (2009).

FitzHugh and Nagumo provided a simplified version of the Hodgkin-Huxley model, by separating fast- and slow-processes (FitzHugh, 1961; Nagumo et al., 1962; FitzHugh, 1969). For example, the gating variables of Na^+ activation operate over a much shorter time period than do the gating variables of its deactivation and those of K^+ activation. This model thus has fast v and slow w variables, the former representing excitation and the latter recovery.

In skeletal muscles, the depolarisation of the membrane causes the release of large amount of calcium Ca^{2+} from the sarcoplasmic reticulum. The Ca^{2+} is the trigger for excitation-contraction coupling. The rate at which Ca^{2+} is released and sequestered by the sarcoplasmic reticulum is slow compared to Na^+ activation, for example.

A particular extension of the FitzHugh-Nagumo model is that of Aliev et al. (1996), developed for cardiac excitation. The two-state dimensionless model's fast-process represents the membrane potential V_{m}, i.e.,

$$\frac{\mathrm{d}\tilde{V}_{\mathrm{m}}}{\mathrm{d}\tilde{t}} = -k\,\tilde{V}_{\mathrm{m}}\,(\tilde{V}_{\mathrm{m}} - a)(\tilde{V}_{\mathrm{m}} - 1) - \tilde{V}_{\mathrm{m}}\,\tilde{r} + \tilde{I}_{\mathrm{stim}}, \tag{5.9}$$

where $\tilde{(\cdot)}$ is a dimensionless quantity, I_{stim} is the stimulation current (at the neuromuscular-junction), k and a are characterisation parameters and $\tilde{r}$ is the slow-process variable, which represents the inward (repolarising) current. Note that the tilde symbol is omitted in the following for clarity.

The slow-process is assumed (similar to Heidlauf et al. (2017)) to represent the Ca^{2+} -concentration in the myoplasm (released from the sarcoplasmic reticulum) qualitatively, i.e.,

$$\frac{\mathrm{d}r}{\mathrm{d}t} = \frac{e_0 + m_1\, r}{m_2 + V_{\text{m}}}\,[-r - k\, V_{\text{m}}\,(V_{\text{m}} - a - 1)], \tag{5.10}$$

where e_0, m_1 and m_2 are characterisation parameters. A rise in Ca^{2+} -concentration leads to a conformational change in tropomyosin, enabling the linkage of the myosin-head and actin: forming a cross-bridge. Subsequently, mechanical work is performed when the myosin-head pulls the actin towards the centre of the sarcomere.

The cross-bridge dynamics are modelled by a Huxley-type biophysical model describing the cross-bridge dynamics (Razumova et al., 1999). Briefly, the model represents cross-bridges in four distinct states: detached non-activated R_{off}, detached activated D, pre-power-stroke A_1, and post-power-stroke A_2. The transitions between these states are modelled by first-order kinetics. By adjusting the rate of cross-bridge cycling, different fibre-types (slow, fast) can be realised (e.g. Schmid et al., 2019). Furthermore, by varying the maximum number of cross-bridges in the post-power-stroke state A_2^{max}, during an isometric tetanic contraction, the peak force of the sarcomere can be altered.

The Ca^{2+} dependent activation is governed by reaction rates k_{on} and k_{off}, which depend on the intracellular Ca^{2+} -concentration $r(t)$ (Equation 5.10), i.e.,

$$\begin{aligned} k_{\text{on}} &= k_{\text{on}}^0 + \left(k_{\text{on}}^{\text{Ca}} - k_{\text{on}}^0\right) \frac{r(t)\, r_0}{r(t)\, r_0 + r_{50}} \quad \text{and} \\ k_{\text{off}} &= k_{\text{off}}^0 + \left(k_{\text{off}}^{\text{Ca}} - k_{\text{off}}^0\right) \frac{r(t)\, r_0}{r(t)\, r_0 + r_{50}}. \end{aligned} \tag{5.11}$$

In the above equation, r_0 is the initial Ca^{2+} -concentration, r_{50} is the normalised concentration when half of the cross-bridges are active, and $k_{\text{on/off}}^0$ and $k_{\text{on/off}}^{\text{Ca}}$ are characterisation parameters (in 1/s). These reaction rates, together with rate coefficients f, f', g, g', h, h' (in 1/s), switch the tropomyosin-troponin thin filament between the four states of the cross-bridge according to:

$$\begin{aligned} \frac{\mathrm{d}D}{\mathrm{d}t} &= k_{\text{on}}(t)\, R_{\text{off}} + f'\, A_1 + g\, A_2 - (k_{\text{off}}(t) + f + g')\; D, \\ \frac{\mathrm{d}A_1}{\mathrm{d}t} &= f\, D + h'\, A_2 - (f' + h)\; A_1, \\ \frac{\mathrm{d}A_2}{\mathrm{d}t} &= h\, A_1 - (h' + g)\; A_2 + g'\, D \quad \text{and} \\ R_{\text{off}} &= R_{\text{T}} - A_1 - A_2 - D. \end{aligned} \tag{5.12}$$

The parameter R_{T} in the equation above, represents the total number of cross-bridges at a given filament overlap, and is typically characterised by a piecewise linear function to represent the force-length relationship of sarcomeres (Figure 2.3a). However, given that the force-length relationship is already modelled by the (three-dimensional) continuum-mechanical constitutive

relation (Equation 4.39), R_{T} is presently set to equal unity.

Recall, the states A_1 and A_2 refer to the pre- and post-power-stroke states, respectively. Therefore, the conversion of chemical to mechanical energy is represented by the transition $A_1 \rightarrow A_2$. The fraction of cross-bridges in the post-stroke state within a sarcomere is taken as the marker of its activity. The normalised activity of the sarcomere is computed via

$$\alpha(t) = \frac{A_2}{A_2^{\max}}, \tag{5.13}$$

where $A_2^{\max}$ is the maximum number of cross-bridges in the post-stroke state.

The Ca^{2+} and cross-bridge dynamics described by the equations above are assumed to be representative for all fibres of a motor-unit. This is justified by assuming that the action-potential, which is initiated by the arrival of the stimulus current at the neuromuscular-junction, travels instantly along the fibres of the motor-unit. In reality, the action-potential propagates along the fibre with a finite velocity. The consequences of this assumption on muscle contraction is investigated via a multiscale model in Section 6.1.

By applying the stimulus current I_{stim} (for some t_{stim}) at the firing times $\mathcal{D}$ computed via the recruitment model (Equation 5.5), the Ca^{2+} current flow is dictated via the behaviour of the α-motor-neuron pool (Section 5.1.1), thus coupling the recruitment and Ca^{2+} dynamics models. The stimulus current of each motor-unit is denoted by the subscript i ($i = 1, \ldots, N_{\text{MU}}$), i.e., $I_{\text{stim}} \rightarrow I_{\text{stim},i}$. This leads to per-motor-unit membrane voltage, Ca^{2+} and cross-bridge dynamics, and ultimately, per-motor-unit activity, i.e.,

$$\alpha_i(t) = \frac{A_{2,i}}{A_{2,i}^{\max}}. \tag{5.14}$$

5.1.3 Motor-unit activity: model characterisation

Muscle activity is described by the sum of the activities of its individual motor-units. Summarising the chain of events: when the excitatory drive $E(t)$, $t = [0, t_{\text{end}}]$, exceeds the recruitment threshold of α-motor-neuron i, the α-motor-neuron begins to fire at a given rate $F_i^{\text{R}}(t)$, governed by the α-motor-neuron pool properties. Firing times $\mathcal{D}_i$ are then computed retroactively from $F_i^{\text{R}}(t)$ and demarcate the times at which a stimulus current $I_{\text{stim},i}$ is supplied to motor-unit i.

The stimulus current leads to changes in Ca^{2+} -concentration $r_i(t)$, which starts the cross-bridge cycling process. When the cross-bridges transitions from the pre- to post-power-stroke states ($A_{1,i} \rightarrow A_{2,i}$, respectively), chemical energy is converted to mechanical energy. The (normalised) fraction of cross-bridges in the $A_{2,i}$ state is taken as the motor-unit activity $\alpha_i(t)$. This can be summarised together with Equation 5.7, for $t = [0, t_{\text{end}}]$ and $i = 1, \ldots, N_{\text{MU}}$, as

$$\underbrace{E(t) \rightarrow \mathcal{D}_i \;\mid\; E(t) > R_i}_{\text{recruitment model}} \rightarrow \underbrace{r(\mathcal{D}_i, \ldots) \rightarrow A_{2,i}(r(\mathcal{D}_i), \ldots) \rightarrow \alpha_i(\mathcal{D}_i)}_{\text{excitation-contraction coupling model}}. \tag{5.15}$$

The above relation shows that motor-unit activity is computed for the entire duration of the excitatory drive.

There are large number of parameters involved in this chain of events, which, when tuned appropriately, can represent a specific human skeletal muscle, e.g., masseter or triceps. Furthermore, states such as pathology, training, and fatigue can also be approximated by modifying

the biophysical recruitment and contractile processes.

Motor-unit pool size

Although individual motor-unit activity can be computed without any information about its size, the two are implicitly linked. For example, small units are assumed to fire first and have slower and weaker twitches. Therefore, motor-unit size is introduced here for convenience. The size of a motor-unit commonly refers to the number of muscle fibres it innervates, the so-called innervation-ratio. In skeletal muscles, there are many small motor-units and a few large units. The innervation-ratio is therefore characterised by an exponential distribution and modelled here by the phenomenological model of Enoka et al. (2001), i.e.,

$$\mathrm{IR}_i = \mathrm{IR}_1 \, \exp\left(i \, \frac{\ln r_{\mathrm{IR}}}{N_{\mathrm{MU}}}\right), \tag{5.16}$$

where $r_{\mathrm{IR}} = \mathrm{IR}_{N_{\mathrm{MU}}}/\mathrm{IR}_1$ (cf. Equation 5.1). The fractional innervation-ratio is computed via

$$\bar{\mathrm{IR}}_i = \frac{\mathrm{IR}_i}{\mathrm{IR}_{\mathrm{tot}}}, \tag{5.17}$$

where $\mathrm{IR}_{\mathrm{tot}}$ is the sum of all innervation-ratios, i.e., the total number of fibres in the muscle. An exemplary innervation-ratio is computed for 100 motor-units, with $\mathrm{IR}_1 = 120$ and $\mathrm{IR}_{100} = 12{,}874$, resulting in a total of 278,739 fibres (Figure 5.3a).

Motor-neuron pool recruitment

A generic, human skeletal muscle α-motor-neuron pool is constructed from $N_{\mathrm{MU}} = 100$ α-motor-neurons, numbered from the smallest to largest motor-unit, according to its innervation-ratio. The recruitment model is characterised by the parameters in Fuglevand et al. (1993), summarised in Table 5.1.

To demonstrate the behaviour of the α-motor-neuron pool, a piecewise-linear excitatory drive is prescribed: increasing from zero to its peak value $E(t) = E_{\max}$ within 0.25 s, then held constant for 1 s, followed by a decrease within 0.25 s, and lastly with a rest period of 0.5 s. The magnitude of $E_{\max}$ (in arbitrary units) is computed such that the largest α-motor-neuron is brought to its peak firing rate, i.e.,

$$E_{\max} = R_{100} + F^{\mathrm{P}}_{100} - F^{\mathrm{M}}. \tag{5.18}$$

A coefficient of variation of $c_{\mathrm{V}} = 0.2$ is used to introduce random variability in the firing rates, and the resulting firing rates are shown in Figure 5.2a.

Individual discharge times $\mathcal{D}_i$ are computed according to Equation 5.5 and are shown in Figure 5.2b. Given the linear increase in $E(t)$ and the exponential shape of R_i (Equation 5.1),

Table 5.1: *Parameters characterising a generic human muscle α-motor-neuron pool.*

F^{P}_1/Hz	F^{D}/Hz	F^{M}/Hz	r_{R}	b	c_{V}
60	10	8	30	1	0.2

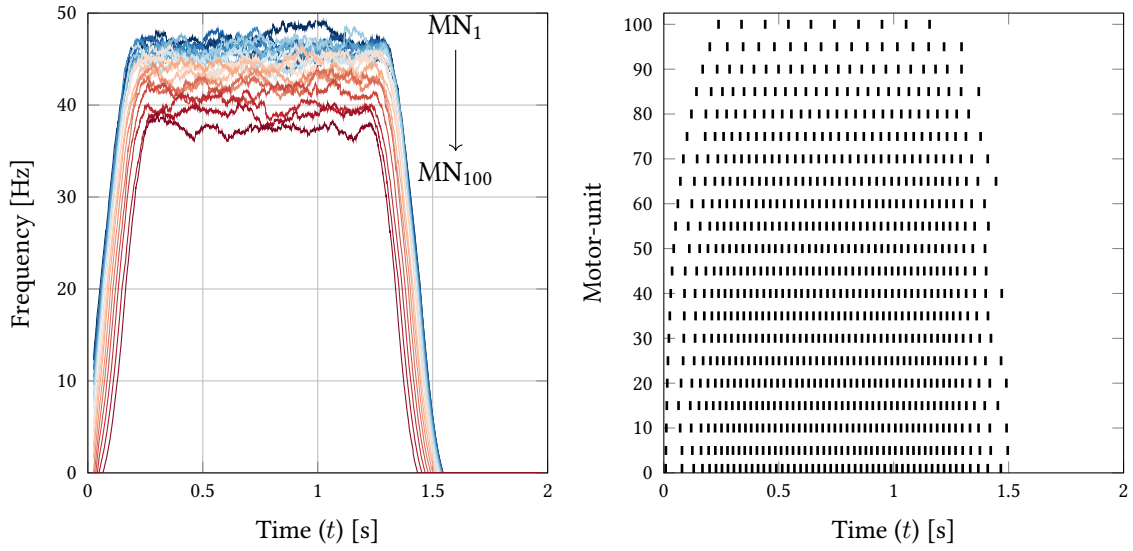

(a) *Firing rates.* **(b)** *Discharge times.*

Figure 5.2: *Motor-neuron pool recruitment behaviour. (a) Average firing rates for every 5^{th} α-motor-neuron. The ramp-up, -down and constant phases of the excitatory drive are clearly visible. (b) Discharge times for the α-motor-neuron pool with every 5^{th} α-motor-neuron plotted.*

the initial discharges follow a smooth (non-linear) pattern. The α-motor-neurons continue to discharge, subject to random variations (Equation 5.4), until $E(t) < R_i$, at which point de-recruitment of α-motor-neuron i occurs. However, due to the stochastic nature of the inter-spike-intervals, α-motor-neuron discharges become increasingly out-of-sync between each other as the contraction proceeds. This is reflected in the non-smooth derecruitment behaviour.

Motor-unit contractile response

A single stimulus leads to a so-called twitch contraction (or response) within the motor-unit, characterised by a short rise time and slower fall time. The contractile behaviour of a motor-unit is characterised by its peak twitch force F^{twitch} and the time taken to reach it, referred to as the time-to-peak (TTP). Smaller motor-units take longer to attain a lower force and the opposite is true for larger motor-units, which attain a higher force, faster. By altering the rates of Ca^{2+} flow and cross-bridge dynamics, the twitch response can be adjusted. In the following, this is achieved by changes in cross-bridge dynamics only, i.e., by altering the rate coefficients f, f', g, g', h, h' (Equations 5.12_{1-4}).

Up to seven fibre-types have been observed in human skeletal muscles (Scott et al., 2001). Human muscles, however, are rarely split into such discrete groups and instead motor-unit properties have been observed to vary continuously throughout a muscle (Heckman et al., 2012, and references therein). To reflect this, rate parameters were (non-linearly) scaled to attain smoothly varying motor-unit twitches between the "slowest" (smallest) and "fastest" (largest) motor-units.

For example, to parametrise motor-unit contractile behaviour in a pool of N_{MU} motor-units: *(i)* rate coefficients for the average twitch response (motor-unit number $N_{\text{MU}}/2$) are identified (Table 5.2), *(ii)* these coefficients are scaled to obtain the "slowest" ($i = 1$) and "fastest" ($i = N_{\text{MU}}$)

motor-units, and *(iii)* the parameters are interpolated to obtain rate coefficients, between these two extremes, for the remaining $N_{\text{MU}} - 2$ motor-units.

Similar to the previous section, a pool with 100 motor-units was constructed. The reference rate coefficients, similar to those in Heidlauf (2016), are given in Table 5.2. The remaining parameters of the excitation-contraction coupling models were based on Campbell et al. (1993), Aliev et al. (1996) and Campbell et al. (2001).

The average twitch response had a F^{twitch} of 0.1225 (arbitrary units) and a time-to-peak of 94 ms. These values were then scaled to obtain the two extremes of the motor-unit pool; multiplying by $\beta_{\text{min}} = 1/3$ and $\beta_{\text{max}} = 3$ to characterise motor-unit 1 and motor-unit 100, respectively. The corresponding twitch responses are plotted in Figure 5.3b with values $F_1^{\text{twitch}} = 0.0906$ and $\text{TTP}_1 = 123$ ms and $F_{100}^{\text{twitch}} = 0.377$ and $\text{TTP}_{100} = 35$ ms, for the slowest and fastest motor-unit, respectively.

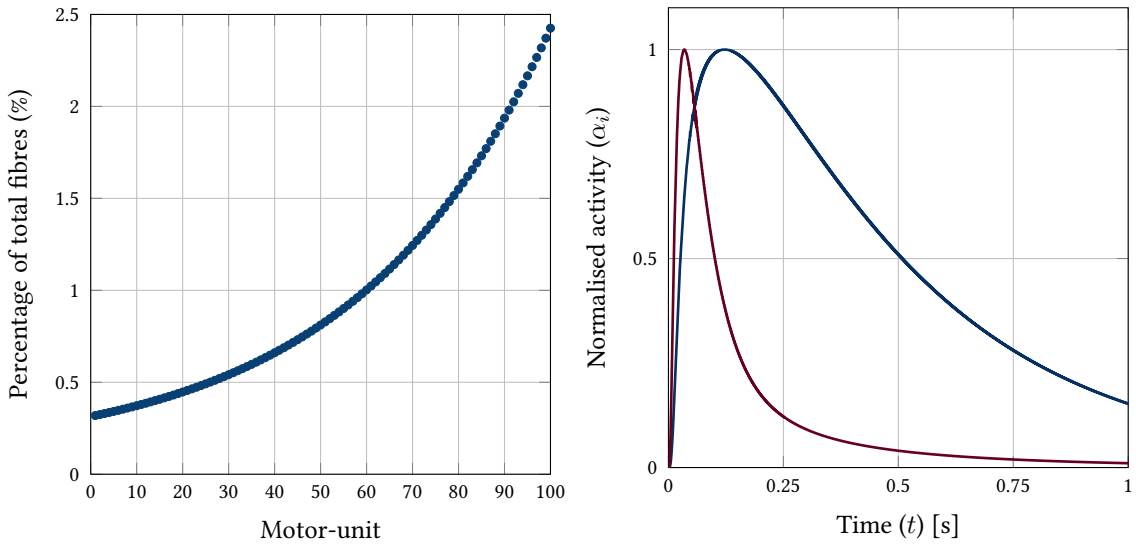

Figure 5.3: *Motor-neuron pool properties. (a) Innervation-ratio of each motor-neuron, expressed as a percentage of total fibres* (1.24×10^5) *(b) Twitch response extremes in the motor-unit pool, as normalised* $\alpha_i(t)$ *(Equation 5.14), for a three fold increase* $\beta_{100} = 3$*: red trace, and decrease* $\beta_1 = 1/3$*: blue trace of the average twitch rate coefficients.*

Then, the rate coefficients $\eta = \{f, f', g, g', h, h'\}$ for the remaining $i = 2 \ldots 99$ motor-units were interpolated by scaling the respective rate coefficients non-linearly between $\beta_{\text{min}} = 1/3$ and $\beta_{\text{max}} = 3$, i.e.,

$$\eta_i = \beta_i \, \eta \quad \text{where} \quad \beta_i = \beta_{\text{min}} \, e^{(i-1)\,\eta} \quad \text{and} \quad \eta = \frac{\log(\beta_{\text{min}}/\beta_{\text{max}})}{1 - N_{\text{MU}}}. \tag{5.19}$$

Table 5.2: *Reference values for the rate coefficients determining the cross-bridge kinetics.*

f/ms	f'/ms	h/ms	h'/ms	g/ms	g'/ms
50	500	8	6	4	0

Resulting in each motor-unit having its own set of rate-coefficients. The peak twitch and time-to-peak values for the motor-unit pool are plotted in Figure 5.4.

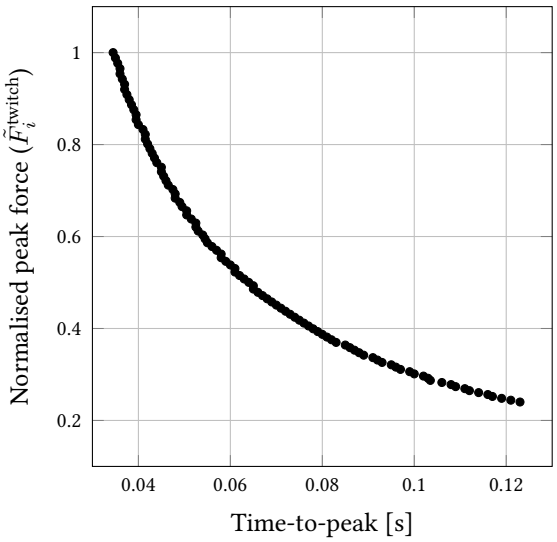

Figure 5.4: *The spread of normalised peak twitch forces (to the peak twitch force of the largest motor-unit) and times-to-peak in the motor-unit pool.*

If another stimulus is applied before a twitch force reaches zero, a summation of the force occurs. When stimulated at a high enough frequency, the individual twitches fuse into the so-called tetanus response. The rise- and fall-times of a motor-unit twitch determine this optimal frequency, typically specified by the maximum stimulation frequency in the recruitment model (Equation 5.2). The activities of the smallest and largest motor-units in response to constant stimulations at various frequencies are shown in Figures 5.5a and 5.5b, respectively. A fixed stimulus current $I_{\text{stim}} = 5$ is supplied for a fixed duration $\Delta t = 2.5$ ms at the various stimulation frequencies.

Whole muscle activity

Motor-units do not contribute equally to muscle activity since each motor-unit is of a different size. A popular approach to account for this is to weight the activity of a motor-unit by its (fractional) size $\bar{\text{IR}}$, or innervation-ratio (Equation 5.17). The total muscle activity can then be approximated via

$$\alpha(t) = \sum_{i=1}^{N_{\text{MU}}} \bar{\text{IR}}_i \, \alpha_i(t). \tag{5.20}$$

Since the activity of each motor-unit is bounded between $[0, 1]$ and since the normalised innervation-ratios must sum to unity, the activity of the entire muscle is also bounded between $[0, 1]$. The muscle activity resulting from the excitatory drive, α-motor-neuron pool and motor-unit twitch responses described in the previous sections is plotted in Figure 5.6a.

The effect of changing the number of motor-units which make up the pool, on the calculated, total muscle activity is shown in Figure 5.6b. As a higher number of motor-units are considered, the muscle activity becomes more steady. This is because increasing the number of motor-units increases the "resolution" of force production, i.e., smaller increments in force can be made.

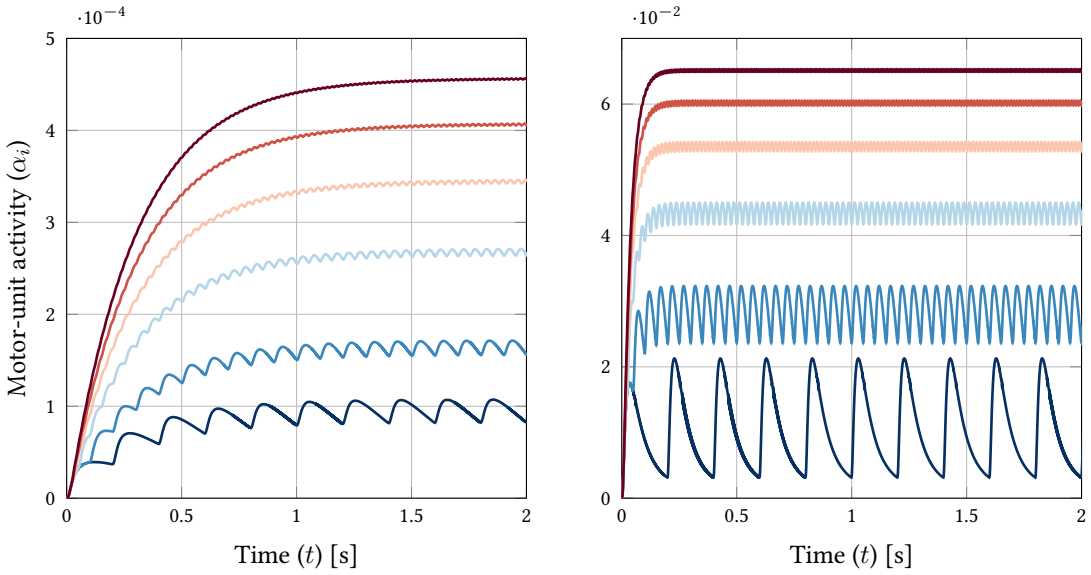

(a) *Motor-unit* 1. ***(b)*** *Motor-unit* 100.

Figure 5.5: *Motor-unit activity in response to sustained stimulation at fixed frequencies. The traces are colour coded from the lowest frequency: dark-blue, to the highest frequency: maroon. The frequencies for motor-unit* $1 = \{5, 10, 20, 30, 40, 50\,\text{Hz}\}$ *and motor-unit* $100 = \{5, 20, 40, 60, 80, 100\,\text{Hz}\}$.

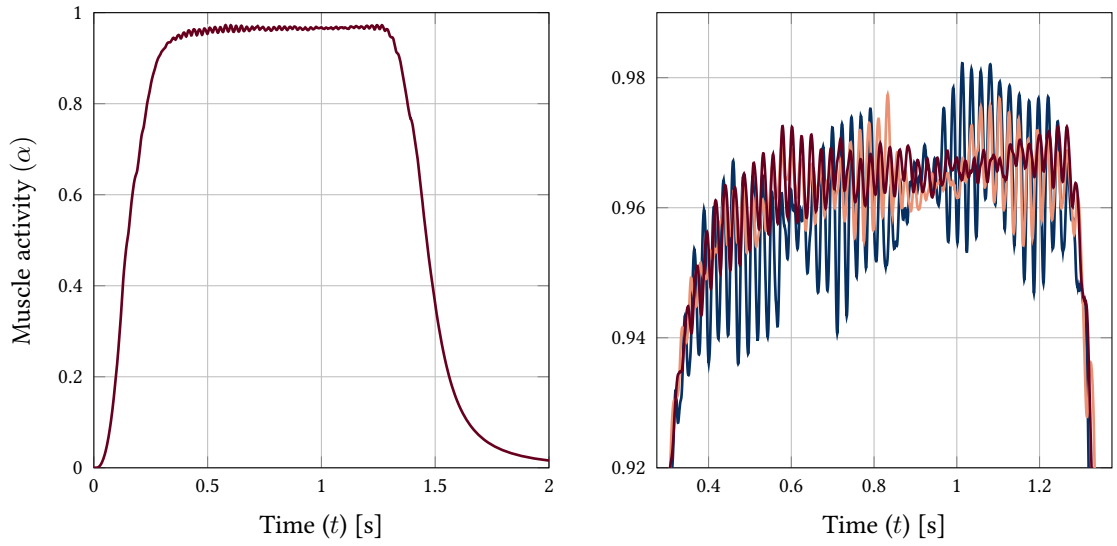

(a) *Muscle activity.* ***(b)*** *Zoom of activity.*

Figure 5.6: *Muscle activity computed as the weighted sum of individual motor-unit activity. (b) Effect of the number of motor-units in the pool with dark blue: 20 units, cream: 50 units and maroon: 100 units.*

5.2 Reconstructing Skeletal Muscle Microstructure

Macroscopic skeletal muscle models forgo the modelling of the fibre microstructure, thus significantly reducing model complexity and computational cost when compared to multiscale models. Obviously, these models have their own drawbacks, such as the smearing of local deformation across several fibres. More detrimentally, when fibres are removed from the muscle, any connectivity information is also lost, i.e., the path traced by the fibres within the muscle is no longer known. This makes the definition of anatomically realistic motor-units very challenging, since a motor-unit occupies the region spanned by its constituent muscle fibres.

In this thesis, this hurdle is overcome by reconstructing "microstructural fibre-scaffolds" from the fibre orientation field. This is done via a streamline tracing method similar to Kupczik et al. (2015), but with additional constraints placed on the seed-point definition such that they form a two-dimensional manifold within the muscle. This is to ease the subsequent definition of motor-unit anatomy.

5.2.1 Fibre orientation interpolation

The fibre orientation at a point $\boldsymbol{Y}$ in the muscle $\mathcal{B}_0$ can be computed by averaging the fibres in a subregion $\Omega \subset \mathcal{B}_0$ about $\boldsymbol{Y}$. Repeating this process throughout the muscle yields a set of local fibre directions; the fibre orientation field $\boldsymbol{a}_0(\boldsymbol{Y}_k)$, where $\boldsymbol{Y}_k$ ($k = 1, \ldots, N_{\text{FO}}$), are the discrete set of points at which the averaging has been performed. The streamline tracing method used to (later) construct the fibre-scaffolds, however, requires fibre orientation at *arbitrary* locations within the muscle geometry. Therefore, the fibre orientation field is spatially interpolated via radial basis interpolation. First, the method is introduced using a generic example and is subsequently adapted to fibre orientation interpolation.

Radial basis interpolation (RBI) is a mesh-less method that interpolates higher-dimensional scattered data. The principle of RBI can be demonstrated with a one-dimensional example. Consider a problem with a set of measurements m_i ($i = 1, \ldots, N$) at data sites X_i, RBI yields a function $s(X)$ which provides the measurement values at locations *other* than the data sites. Furthermore, the RBI function is subject to the interpolation condition, meaning that it must exactly equal the measured values at the data sites, i.e., $s(X_i) = m_i$. Typically, a linear combination of basis functions ϕ and weights τ may be used to determine $s(X)$, i.e., $s(X) = \sum_i^N \tau_i \, \phi_i$. For example, the basis function may be a polynomial with $\phi_i^N = 1, X, X^2, \ldots, X^{N-1}$. However, such an approach becomes impractical for higher-dimensional data. Alternatively, a basis function can be chosen that *translates* to the data sites—the so-called basic function:

$$\phi_i(\boldsymbol{X}) = \|\boldsymbol{X} - \boldsymbol{X}_i\|, \tag{5.21}$$

which is the Euclidean distance from each data site and where $\boldsymbol{X}$ is the vector of the (one-dimensional) data sites. This yields a set of basic functions, each centred about a data site. The interpolation function then becomes

$$s(\boldsymbol{X}) = \sum_{i=1}^{N} \tau_i \; \phi_i(\|\boldsymbol{X} - \boldsymbol{X}_i\|). \tag{5.22}$$

Subject to the interpolation condition, the weights must be determined such that the interpola-

tion function equals the measured values at the data sites. Then, the above equation can be written as a linear system, i.e.,

$$\mathbf{B}\,\mathbf{t} = \mathbf{m}, \tag{5.23}$$

where $\mathbf{B}$ is the matrix of basis functions evaluated by $\mathrm{B}_{i,j} = \phi_i(\|\boldsymbol{X}_i - \boldsymbol{X}_j\|)$, and has dimensions $N \times N$, $\mathbf{t}$ is the matrix of (unknown) weights and $\mathbf{m}$ the matrix of (known) measurements, each with dimensions $N \times 1$. The above system of equations are solved for $\mathbf{t}$, and then $s(\boldsymbol{X})$ can be determined via Equation 5.22.

Typically, the Euclidean distance is not used as the basic function since it is discontinuous at the data site. There are several choices for the basic function (e.g. Chen et al., 2005), among which is the multi-quadratic function;

$$\phi_i(\|\boldsymbol{X} - \boldsymbol{X}_i\|) = \sqrt{1 + (\epsilon\,\|\boldsymbol{X} - \boldsymbol{X}_i\|)^2}, \tag{5.24}$$

where ϵ is a shape parameter.

Returning to the interpolation of the fibre orientations: the data sites and measured values are now respectively $\boldsymbol{Y}_k$ and $\boldsymbol{a}_0(\boldsymbol{Y}_k)$, and the interpolation function is $\hat{\boldsymbol{a}}_0(\|\boldsymbol{X} - \boldsymbol{Y}_k\|)$. The matrix of basis functions $\mathbf{B}$ has components $\mathrm{B}_{i,j} = \phi_i(\|\boldsymbol{Y}_i - \boldsymbol{Y}_j\|)$ and dimensions $N_{\mathrm{FO}} \times N_{\mathrm{FO}}$. The weights and measurements both have dimensions of $N_{\mathrm{FO}} \times 3$, since the fibre orientations are specified in three-dimensions. Substituting these matrices into Equation 5.23 and solving for $\boldsymbol{t}$ yields the weights.

Then, consider a set of points where the fibre orientation is desired $\boldsymbol{X}_r^{\mathrm{micro}} \in \mathcal{B}_0$ ($r = 1, \ldots, N_{\mathrm{micro}}$). The fibre orientation at these points can be interpolated by using RBI, i.e.,

$$\hat{\boldsymbol{a}}_0(\|\boldsymbol{X}_r^{\mathrm{micro}} - \boldsymbol{Y}_i\|) = \sum_{i=1}^{N} \tau_i\ \phi_i(\|\boldsymbol{X}_r^{\mathrm{micro}} - \boldsymbol{Y}_i\|). \tag{5.25}$$

5.2.2 Seed-point surface generation and fibre-scaffold tracking

With the aim of defining anatomically congruent motor-unit territories, microstructural fibre-scaffolds $\mathcal{F}_k$ ($k = 1, \ldots, N_{\mathrm{FS}}$) are constructed within the muscle. The fibre-scaffolds are composed of a set of coordinates within the muscle, forming a path which conforms, locally, to the fibre orientations (computed at each coordinate by radial basis interpolation). Once the muscle is fully populated with (equidistant) fibre-scaffolds, they are used to generate motor-unit anatomies within the muscle (Section 5.3).

The fibre-scaffolds are traced using streamline tracing, which has its application in fluid dynamics. The streamline is the path traced by a particle within the velocity field of a fluid. By replacing the velocity field with the fibre orientation filed, the streamline represents the fibre-scaffold. Such an approach provides adequate agreement with experimentally measured muscle fibre anatomy (Choi et al., 2013; Kupczik et al., 2015; Handsfield et al., 2017).

The requirements of fibre-scaffolds are two-fold: first, they should run from tendon-to-tendon (or aponeuroses) and second, they should be uniformly spaced (perpendicular to their main direction). The highly varied and complex nature of muscle architecture makes this challenging, e.g., the masseter has attachment areas both to tendons and aponeuroses, or the lateral pterygoid, which splits into multiple heads. This is addresses by placing restrictions on the way the streamline computations are initiated.

The scaffold/streamline procedure requires a starting point or seed-point $\boldsymbol{s}_k$ ($k = 1, \ldots, N_{\mathrm{FS}}$)

per fibre-scaffold, i.e., the point at which the particle is "dropped into" the fluid. To meet the demands mentioned above, the streamline tracing and seed-point generation are set to occur iteratively. After each scaffold is traced, the mid-point is computed retroactively. At this mid-point, a set of equidistant seed-points are generated. These neighbouring seed-points lie on a plane perpendicular to the fibre direction of the previously traced scaffold's mid-point. If the newly generated seed-points either lie outside the muscle geometry or collide with existing seed-points, they are deemed unfeasible and removed from subsequent streamline computations. The streamline tracing is then repeated at the feasible seed-points, and the process continues. In other words, the generation of fibre-scaffolds proceeds outwards from a genesis fibre-scaffold until no feasible seed-points remain. The fibre tracing itself is discussed later. This process yields a set of seed-points $\mathcal{S} = \{\boldsymbol{s}_1, \boldsymbol{s}_2, \ldots, \boldsymbol{s}_{N_{\text{FS}}}\}$, located mid-way between the fibre-scaffolds. The process is summarised in Algorithm 1.

The neighbouring seed-points $\mathbf{q}$ are determined via a fixed stencil (Algorithm 1, line 4). Consider a generic point $\boldsymbol{X}_r^{\text{micro}}$ in the muscle about which the neighbouring seed-points are computed via

$$\mathbf{q} = \Lambda_{\text{s}}\, \mathbf{W}\, \mathbf{e} + \boldsymbol{X}_r^{\text{micro}}, \tag{5.26}$$

where Λ_{s} is the perpendicular spacing (in mm), $\mathbf{W}$ is a weight-matrix and $\mathbf{e}$ contains the set of basis vectors perpendicular to $\hat{\boldsymbol{a}}_0(\boldsymbol{X}_r^{\text{micro}})$. The weight matrix $\mathbf{W}$ is chosen to give a stencil of 8 points, with a Chebyshev distance of Λ_{s} from $\boldsymbol{X}_r^{\text{micro}}$, then

$$\mathbf{q} = \begin{bmatrix} \boldsymbol{s}_1 \\ \boldsymbol{s}_2 \\ \vdots \\ \\ \\ \\ \boldsymbol{s}_8 \end{bmatrix}, \quad \mathbf{W} = \begin{bmatrix} 1 & 0 \\ -1 & 0 \\ 0 & 1 \\ 0 & -1 \\ 1 & 1 \\ 1 & -1 \\ -1 & 1 \\ -1 & -1 \end{bmatrix}, \quad \mathbf{e} = \begin{bmatrix} \boldsymbol{e}_2 \\ \boldsymbol{e}_3 \end{bmatrix}. \tag{5.27}$$

Tracking a single fibre-scaffold

Each fibre-scaffold is tracked using a deterministic streamline method and results in a set of microstructural points per fibre-scaffold $\mathcal{F}_k = \{\boldsymbol{X}_{r,k}^{\text{micro}}\}$ $(r = 1, \ldots, N_k^{\text{micro}})$. Since tracing begins from the mid-point of the scaffolds, it proceeds in both forward and reverse directions, dictated by the tracing direction $\beta = 1$ or -1, i.e.,

$$\boldsymbol{X}_{r+1,k}^{\text{micro}} = \boldsymbol{X}_{r,k}^{\text{micro}} + \beta\, \hat{\boldsymbol{a}}_0(\boldsymbol{X}_{r,k}^{\text{micro}})\, \Lambda_{\text{f}}, \tag{5.28}$$

where Λ_{f} is the spacing along the fibre (in mm) and the fibre orientation interpolation is performed via Equation 5.25. The tracking proceeds until a fibre point lies outside the geometry or collides with another fibre point. When this occurs, the process is returned to the seed-point and proceeds in the reverse direction, i.e., $\beta = -1$. The tracking process is summarised in Algorithm 2.

Algorithm 1 Pseudocode to generate the seed-point surface.

choose a starting point $\boldsymbol{X}_1^{\text{micro}}$
$\mathcal{S} \leftarrow \boldsymbol{s}_1 = \boldsymbol{X}_1^{\text{micro}}$ ▷ $\mathcal{S}$ is the set of seed-points
$\hat{\boldsymbol{a}}_0(\boldsymbol{X}_1^{\text{micro}}) = f(\boldsymbol{X}_1^{\text{micro}}, \mathbf{t}, \mathbf{B})$ ▷ interpolate fibre orientation (Equation 5.25)
$\bar{\mathbf{q}}_1 = f(\boldsymbol{X}_1^{\text{micro}}, \hat{\boldsymbol{a}}_0(\boldsymbol{X}_1^{\text{micro}}), \Lambda_{\text{s}})$ ▷ compute seed-point stencil (Equation 5.26)
$\bar{\mathbf{q}}_1 = \mathbf{q}_1$ ▷ assume all initial seed-points are viable
$i = 1$

while $\bar{\mathbf{q}}_i \neq \emptyset$ **do**
    $\mathcal{S} \leftarrow \bar{\mathbf{q}}_i$
    track scaffolds at the viable seed-points $\rightarrow \mathcal{F}_i$ ▷ Algorithm 2
    $\bar{\mathbf{q}}_i \leftarrow \texttt{midpoint}(\mathcal{F}_i)$ ▷ compute fibre mid-points and update stencil loc.
    $\hat{\boldsymbol{a}}_0(\boldsymbol{X}_i^{\text{micro}}) = f(\bar{\mathbf{q}}_i, \mathbf{t}, \mathbf{B})$ ▷ interpolate fibre orientation at stencil locations
    $\mathbf{q}_{i+1} = f(\bar{\mathbf{q}}_i, \hat{\boldsymbol{a}}_0(\boldsymbol{X}_i^{\text{micro}}), \Lambda_{\text{s}})$ ▷ compute next seed-point stencil(s)
    check feasibility$\rightarrow \bar{\mathbf{q}}_{i+1}$ ▷ feasible if within muscle geometry and non-overlapping
    $i = i + 1$
end while

Algorithm 2 Pseudocode to track a fibre-scaffold from a seed-point.

given some seed-point $\boldsymbol{s}_k \in \mathcal{S}$ ▷ $\mathcal{S}$ is the set of seed-points
start tracking fibre-scaffold $\mathcal{F}_k \leftarrow \boldsymbol{X}_{1,k}^{\text{micro}} = \boldsymbol{s}_k$
edge_found $= 0$
$r = 1$

while edge_found < 2 **do**
    $\beta = 1 - 2\,\text{edge\_found}$ ▷ tracking direction
    $\hat{\boldsymbol{a}}_0(\boldsymbol{X}_{r,k}^{\text{micro}}) = f(\boldsymbol{X}_{r,k}^{\text{micro}}, \mathbf{t}, \mathbf{B})$ ▷ interpolate fibre orientation (Equation 5.25)
    $\boldsymbol{X}_{r+1}^{\text{micro}} = \boldsymbol{X}_{r,k}^{\text{micro}} + \beta\, \hat{\boldsymbol{a}}_0(\boldsymbol{X}_{r,k}^{\text{micro}})\, \Lambda_{\text{f}}$ ▷ proceed along streamline

    if $\boldsymbol{X}_{r+1}^{\text{micro}}$ is inside geometry **and** does not collide with another fibre point **then**
        $\mathcal{F}_k \leftarrow \boldsymbol{X}_{r+1,k}^{\text{micro}} \leftarrow \boldsymbol{X}_{r+1}^{\text{micro}}$
    else
        $\boldsymbol{X}_{r+1}^{\text{micro}} = \boldsymbol{s}_k$ ▷ return to origin
        edge_found $=$ edge_found $+ 1$
    end if
    $r = r + 1$
end while

5.2.3 Case-studies

The fibre tracking and seed-point surface generation methods were tested by application to a variety of realistic muscle geometries. Given the multitude of demands placed on the human musculoskeletal system, muscles are diverse in their shape and internal structure. The architecture of muscles may be broadly classified as: parallel, fusiform, convergent, circular, unipennate, bipennate, and multipennate. In addition to a "simple" fusiform muscle, dual-head and multipennate muscles were used in the case-studies (Table 5.3).

Table 5.3: *Overview of muscles for the seed-point generation algorithm case-study.*

Muscle	Architecture	
lateral pterygoid	parallel/dual head	Figure 5.7
biceps brachii	fusiform	Figure 5.8
masseter	multipennate	Figure 5.9

Muscle geometries were derived from anatomical imaging and a (finite-element) mesh fitting proceedure (Bradley et al., 1997), carried out in `CMISS` (Blackett et al., 2005). Briefly, magnetic resonance images from the visible human project (Spitzer et al., 1996) were used to generate a cloud of 3D data points, which served as a basis for the fitting procedure. By reducing the error between the mesh surface and the data points, the anatomical shape is approximated. Further details concerning the lateral pterygoid and masseter models are given in van Essen et al. (2005) and for the biceps model, in Sprenger (2016) and Röhrle et al. (2017).

The fibre orientations within the models were defined semi-automatically within the commercial finite element package `Abaqus/CAE` (v2017, Dassault Systèmes, France). First, a major-axis describing the dominant fibre direction within each muscle was defined, and second the major-axis was interpolated within the muscle volume such as to conform to selected muscle boundaries.

The masseter was divided into two compartments by manually defining an oblique plane. The plane was defined based on qualitative anatomical data and resulted in a smaller deep head and a larger superior head. Separate major-axes were then defined within each masseter head. The axis was pointed slightly posterio-cranially and anterio-cranially in the deep and superior heads, respectively (e.g. Belser et al., 1986; Ebrahimi, 2015). For the lateral pterygoid and biceps a single major-axis was defined, aligned along the main or long axes of the muscles.

For all muscles, the scaffold tracing process was started by using the muscle center-of-mass as the initial seed-point (Algorithm 1, line 1). For the lateral pterygoid and biceps, the stencil spacing was set as $\Lambda_\mathrm{s} = 2\,\mathrm{mm}$ (Equation 5.26) with the spacing along scaffold as $\Lambda_\mathrm{f} = 2\,\Lambda_\mathrm{s}$ (Algorithm 2, line 8), and $\Lambda_\mathrm{s} = \Lambda_\mathrm{f} = 1\,\mathrm{mm}$ for the masseter.

The scaffold tracing algorithm was implemented in the programming language `MATLAB` (R2018a, The MathWorks, Inc., USA). Details of the implementation, e.g., interface with the finite element mesh are given in Section 6.3.1. The influence of the reconstructed microstructure resolution on computation time was determined by generating the microstructure for the biceps at various spacings: $\Lambda_\mathrm{s}^i = \{2, 3, 4\,\mathrm{mm}\}$ and $\Lambda_\mathrm{f}^i = 2\,\Lambda_\mathrm{s}^i$ and comparing the elapsed computational times.

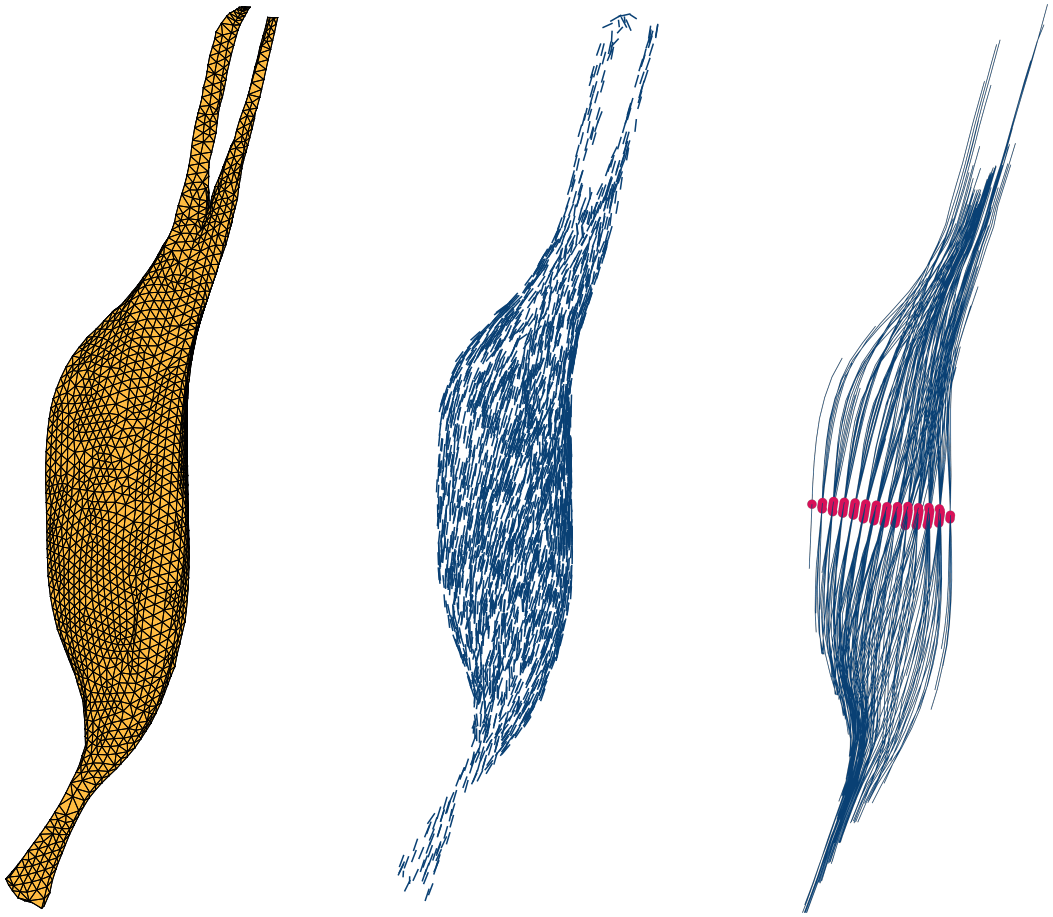

(a) *Boundary triangulation* ***(b)*** *Fibre orientations* ***(c)*** *Scaffolds and seed-points*

Figure 5.7: *Biceps brachii (fusiform muscle) microstructure reconstruction case-study. In (c)* 50% *of fibre-scaffolds are randomly plotted and seed-points are shown in red.*

Results

The scaffold tracing was performed on a desktop computer with a quad-core processor (`Intel Core i7-4790K @ 4GHz`) with 24 GB of memory. The triangulated surface mesh, semi automatically generated fibre orientation field and results of the scaffold tracing algorithm are shown in Figures 5.8, 5.7 and 5.9 for the biceps, lateral pterygoid, and masseter, respectively. The number of tracked fibre-scaffolds for these muscles were 577, 1171, and 1154 respectively. The number of scaffolds traced in the biceps for $\Lambda_{\mathrm{s}}^{i} = \{2, 3, 4\,\mathrm{mm}\}$ were 577, 271 and 146, respectively. The corresponding computational times were t_{comp} 564 s, 166 s and 68 s.

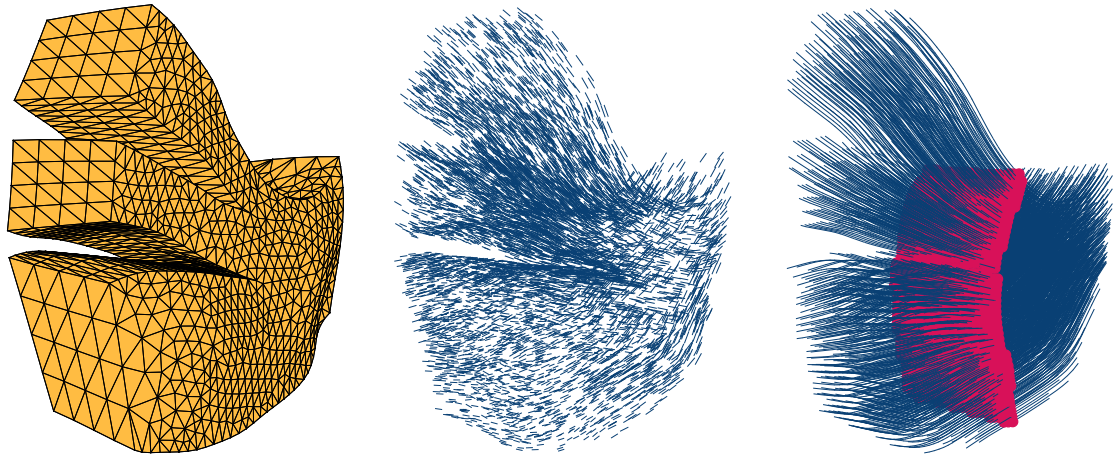

(a) *Boundary triangulation* ***(b)*** *Fibre orientations* ***(c)*** *Scaffolds and seed-points*

Figure 5.8: *Lateral pterygoid (parallel/dual head muscle) microstructure reconstruction case-study. In (c) 75% of fibre-scaffolds are randomly plotted and seed-points are shown in red.*

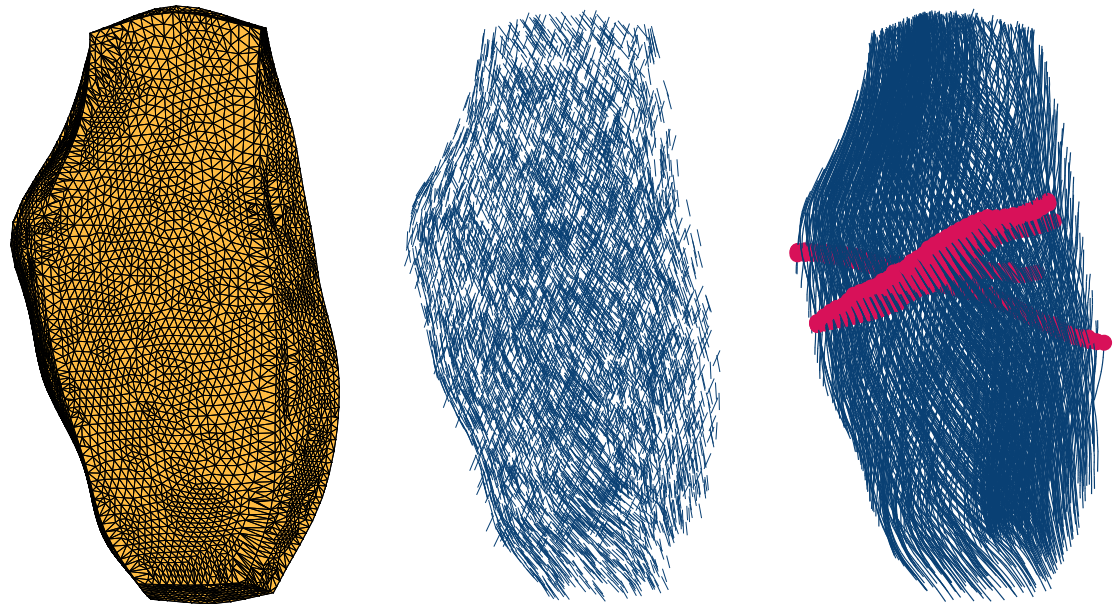

(a) *Boundary triangulation* ***(b)*** *Fibre orientations* ***(c)*** *Scaffolds and seed-points*

Figure 5.9: *Masseter microstructure (multipennate muscle) reconstruction case-study. In (c) 50% of fibre-scaffolds are randomly plotted and seed-points are shown in red.*

5.3 Motor-Unit Anatomy in Three-Dimensional Skeletal Muscle Models

The specific arrangement of a motor-unit's fibres refers to its anatomy. Since the fibres of a motor-unit are innervated by terminal axons of a single α-motor-neuron, the *innervation pattern* of an α-motor-neuron is the basis of motor-unit anatomy. Skeletal muscles may contain between 10^2 to 10^3 α-motor-neurons innervating between 10^3 to 10^6 fibres. While the microstructure may be simplified in multiscale computational models, the numbers are still at the lower end of this range. This makes the manual definition of the innervation pattern, i.e., manually connecting individual α-motor-neuron terminal axons to individual muscle fibres, quite tedious.

Motor-unit anatomy varies between muscles of an individual and between the same muscle of different individuals. This is due to various factors, such as age, pathological conditions and physical activity (e.g. Morris, 1969; Lexell et al., 1991; Cioffi et al., 2012; Messi et al., 2016). However, some general anatomical features of mammalian motor-unit territories can be observed: they are locally confined to a subregion of the muscle, they overlap with multiple other territories, they have irregular shapes, and they have varying degrees of fibre-type clustering within a territory (e.g. Edström et al., 1968; Bodine-Fowler et al., 1990; Roy et al., 1995; van Dijk et al., 2016; Lapatki et al., 2019; Birkbeck et al., 2020). Furthermore, certain motor-unit types may be located preferentially within certain regions of the muscle, for example, larger motor-units are found deeper within the tibialis anterior (Mesin et al., 2010). Therefore, given the lack of high resolution experimental data of motor-unit fibre distributions, a semi-stochastic method is used that characterises motor-unit territories. This enables the definition of motor-unit territories by a few of parameters, while capturing their hallmark anatomical features.

Innervation patterns exhibiting these properties are formed on the reconstructed micro-structural fibre-scaffolds (Section 5.2), namely, by connecting each virtual α-motor-neuron terminal axon in a semi-stochastic manner with the virtual neuromuscular-junctions of the fibre-scaffolds. The method proceeds similarly to existing methods to generate innervation patterns, i.e., first, motor-unit size is computed, second, a motor-unit territory centre is determined, and third, fibres about the motor-unit territory centre are assigned to the motor-unit (e.g. Schnetzer et al., 2001; Navallas et al., 2010; Röhrle et al., 2012). Key differences include the ability to preferentially position smaller/larger motor-units over the muscle cross-section, and to control the degree of territory clustering and overlap in a straightforward manner. The virtual innervation parameters are characterised by using an idealised geometry to generate 100 motor-unit territories over approximately 120,000 fibres (Section 5.3.5).

5.3.1 Motor-unit size

Recall that the microstructure reconstruction yields fibre-scaffolds $\mathcal{F}_k$ ($k = 1, \ldots, N_{\text{FS}}$) and associated seed-points $\boldsymbol{s}_k$. The first step in the innervation procedure is to determine how many fibre-scaffolds are to be innervated for α-motor-neuron i ($i = 1, \ldots, N_{\text{MU}}$). The number of (anatomical) fibres per α-motor-neuron is described by its innervation-ratio, modelled here by an exponential distribution (Equation 5.16). The number of fibre-scaffolds is, however, typically lower and therefore motor-unit size is recast according to

$$\text{IR}_i^{\text{SP}} = \lceil \bar{\text{IR}}_i \, N_{\text{FS}} \rceil, \tag{5.29}$$

where $\lceil \cdot \rceil$ is the ceiling function, rounding up to the nearest integer. Assuming that the smallest motor-unit must contain at least one fibre-scaffold, i.e., $\text{IR}_1^{\text{SP}} = 1$; the following must be satisfied

$$N_{\text{FS}} \geq \frac{1}{\lceil \bar{\text{IR}}_1 \rceil}. \tag{5.30}$$

The seed-point of each fibre-scaffold is located at its mid-point and may be thought of as the virtual fibre's neuromuscular-junction. In the following, the term seed-point and neuromuscular-junction are used interchangeably.

5.3.2 Motor-unit territory location and overlap

The innervation process of an α-motor-neuron is described here in terms of its "central" axon and "peripheral" axons. Note that this is for sake of explanation and no such distinction exists in reality. Innervation of motor-units is performed from smallest (number 1) to largest (number N_{MU}). The innervation procedure for a given α-motor-neuron i ($i = 1, \ldots, N_{\text{MU}}$) proceeds as follows: First, the central axon innervates a random neuromuscular-junction $\boldsymbol{s}_k$, and is denoted by $\boldsymbol{c}^i$. The superscript $(\cdot)^i$ is introduced to signify that a quantity now belongs to motor-unit i. Second, the remaining $(\text{IR}_i^{\text{SP}} - 1)$ peripheral α-motor-neuron axons continue to (randomly) innervate "free" neuromuscular-junctions about the central axon $\boldsymbol{c}^i$, within a distance R (in mm) (Figure 5.10b), i.e.,

$$f_{\text{d}}(\mathcal{S}^{\text{u}}, \boldsymbol{c}^i) < R, \tag{5.31}$$

where f_{d} is a distance metric (discussed later) and $\mathcal{S}^{\text{u}}$ is introduced as the set of currently uninnervated neuromuscular-junctions.

Once the desired number of seed-points IR_i^{SP} have been innervated, the central axon for α-motor-neuron $i+1$ innervates another (uninnervated) neuromuscular-junction $\boldsymbol{c}^{i+1}$. Then, the peripheral axons of α-motor-neuron $i+1$ subsequently seek out free neuromuscular-junctions about $\boldsymbol{c}^{i+1}$. The process continues for the remaining α-motor-neurons. Since motor-unit sizes are determined by the total number of seed-points, the following holds:

$$\sum_{i=1}^{N_{\text{MU}}} \text{IR}_i^{\text{SP}} = N_{\text{FS}}. \tag{5.32}$$

Meaning that when all α-motor-neurons are linked to the seed-points, there are no uninnervated seed-points or neuromuscular-junctions remaining, i.e., $\mathcal{S}^{\text{u}} = \emptyset$.

Each seed-point does not have the same probability of being innervated by an α-motor-neuron's central axon $\boldsymbol{c}^i$, since, the search space (for $\boldsymbol{c}^i$ selection) is restricted to a subregion of the muscle's cross-section. This is achieved by (manually) selecting a reference point $\boldsymbol{c}_{\text{MUT}}$, and limiting the neighbourhood for α-motor-neuron *central* axon innervation within a distance D (in mm) (Figure 5.10a) about this point, i.e.,

$$f_{\text{d}}(\mathcal{S}^{\text{u}}, \boldsymbol{c}_{\text{MUT}}) < D. \tag{5.33}$$

This is analogous to Equation 5.31, however, while R restricts the innervation of the *peripheral* axons (of a given α-motor-neuron), D restricts the innervation of the *central* axons. The reference point $\boldsymbol{c}_{\text{MUT}}$ remains fixed for the entire innervation process.

As α-motor-neurons continue to innervate, a fewer number of uninnervated neuromuscular-

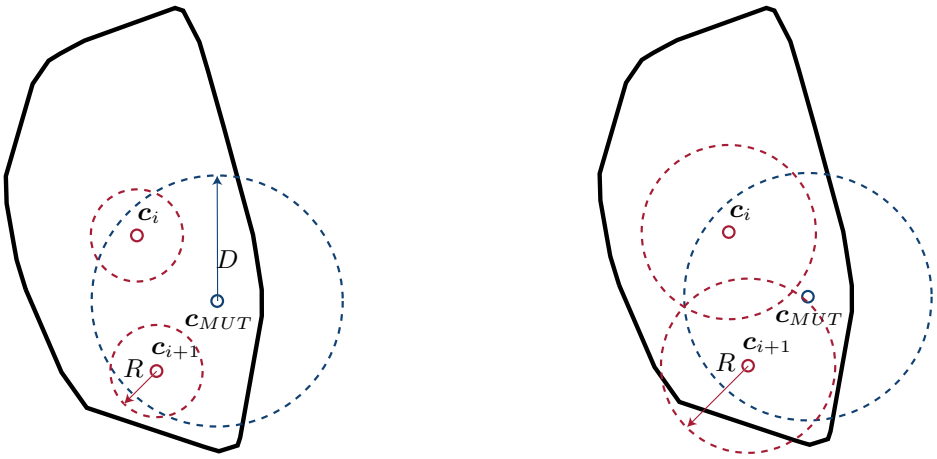

(a) *Clustered* ***(b)*** *Overlapped*

Figure 5.10: *Schematic of select motor-unit territory distribution parameters combinations to highlight (a) clustered territories with small territory search space (R) about the territory centers (b) overlapping territories. In both examples, the distance D, controls the regional confinement of the territories. Recall that smaller territories are assigned first. A Euclidean distance is shown for illustrative purposes.*

junctions remain. This can lead to problems of over-crowding. First, the central axon may not fit within $f_\mathrm{d} < D$ about $\boldsymbol{c}_\mathrm{MUT}$. Similarly for the peripheral axons, there may be no free neuromuscular-junction within $f_\mathrm{d} < R$ about $\boldsymbol{c}^i$. When this occurs, the selection distances R and D are incremented by ΔR and ΔD (in mm), and the searches repeated. The pseudocode to generate the innervation pattern is given in Algorithm 3.

5.3.3 Motor-unit territory shape

The distance metric f_d, which defines the search space for the peripheral axons, influences the shape of the innervation pattern and ultimately the motor-unit territory. For example, a Euclidean distance would result in circular innervation patterns. Strictly speaking, since the distance metric only influences the search space, the parameters R and D together with the stochastic nature of the algorithm, also influence the final innervation pattern. The distance measure is generalised to allow for increased control over motor-unit territory shape and is taken as the generalised ellipsoidal distance, i.e.,

$$f_\mathrm{d}(\mathbf{a},\mathbf{b})^2 = (\mathbf{a}-\mathbf{b})\,\mathbf{V}\,(\mathbf{a}-\mathbf{b})^\mathrm{T}, \tag{5.34}$$

where $\mathbf{V}$ is a weighting matrix which acts to scale the distance measure along its eigenvectors $\mathbf{v}_1, \mathbf{v}_2, \mathbf{v}_3$ by the amount given by its eigenvalues, i.e., by $\lambda_1, \lambda_2, \lambda_3$. For example, $\mathbf{V} = \boldsymbol{I}$ (identity matrix) gives the Euclidean distance (resulting in spherical search spaces). Setting $\mathbf{V} = \mathrm{diag}(\lambda_1, \lambda_2, \lambda_3)$ results in a weighted Euclidean distance, which skews the search space along the global axes. Yet the muscle may not necessarily be aligned with the global axes. To account for this, a symmetric positive definite $\mathbf{V}$ is chosen, resulting in skewed distances along arbitrary major axes, which are specified by the eigenvectors $\mathbf{v}_i$. The weighting matrix $\mathbf{V}$ is computed by specifying the desired skew values λ_i, the major-axis $\mathbf{v}_1$ and at least one perpendicular axis $\mathbf{v}_2$, then

$$\mathbf{V} = \mathbf{T}\,\mathbf{B}\,\mathbf{T}^\mathrm{T}, \tag{5.35}$$

where $\mathbf{T} = [\mathbf{v}_1, \mathbf{v}_2, \mathbf{v}_3]$ and $\mathbf{B} = \mathrm{diag}(\lambda_1, \lambda_2, \lambda_3)$.

In summary, by the choice of $\boldsymbol{c}_{\mathrm{MUT}}$, D, ΔD, R, ΔR, $\mathbf{v}_i$ and λ_i, $i = 1, 2, 3$, the distribution and shape of the innervation pattern can be controlled, subject to stochastic nature of the selection in the algorithm. Additionally, a "global distribution parameter" $\mathit{\Pi}$ (in mm) is defined as the sum of the clustering and overlap parameters, i.e.,

$$\mathit{\Pi} = (R + \Delta R) + (D + \Delta D). \tag{5.36}$$

Algorithm 3 Pseudocode to label seed-points to motor-units.

1: select $\boldsymbol{c}_{\mathrm{MUT}} \in \mathcal{S}$
2: set $\mathcal{S}^{\mathrm{u}} = \mathcal{S}$

3: **while** $\mathcal{S}^{\mathrm{u}} \neq \emptyset$ **do**
4: compute neighbourhood for central axon: $\mathcal{T}_{\mathrm{c}} = \boldsymbol{s} \subset \mathcal{S}^{\mathrm{u}} \mid f_{\mathrm{d}}(\mathcal{S}^{\mathrm{u}}, \boldsymbol{c}_{\mathrm{MUT}}) < D$
5: **if** $\mathcal{T}_{\mathrm{c}} = \emptyset$ **then**
6: $D = D + \Delta D$
7: go to line 4
8: **end if**
9: $\boldsymbol{c}^i \leftarrow \boldsymbol{s} = \mathrm{rand}\ \mathcal{T}_{\mathrm{c}}$ ▷ the central axon of α-motor-neuron i innervates a random neuromuscular-junction
10: remove $\boldsymbol{c}^i$ from $\mathcal{S}^{\mathrm{u}}$

11: $\mathrm{IR}_i^{\mathrm{a}} = 0$
12: **while** $\mathrm{IR}_i^{\mathrm{a}} \leq \mathrm{IR}_i^{\mathrm{SP}}$ **do**
13: compute neighbourhood for peripheral axons: $\mathcal{T}_{\mathrm{p}} = \boldsymbol{s} \subset \mathcal{S}^{\mathrm{u}} \mid f_{\mathrm{d}}(\mathcal{S}^{\mathrm{u}}, \boldsymbol{c}^i) < R$
14: **if** $\mathcal{T}_{\mathrm{p}} = \emptyset$ **then**
15: $R = R + \Delta R$
16: go to line 13
17: **end if**
18: $\boldsymbol{s}^i \leftarrow \boldsymbol{s} = \mathrm{rand}\ \mathcal{T}_{\mathrm{p}}$ ▷ the peripheral axon of α-motor-neuron i innervates a random neuromuscular-junction
19: $\mathrm{IR}_i^{\mathrm{a}} = \mathrm{IR}_i^{\mathrm{a}} + 1$
20: remove $\boldsymbol{s}^i$ from $\mathcal{S}^{\mathrm{u}}$
21: **end while**

22: $i = i + 1$
23: **end while**

Summary

The innervation process results in a set of labelled seed-points $\mathcal{S} \rightarrow \tilde{\mathcal{S}}$ or $\boldsymbol{s}_k \rightarrow \boldsymbol{s}_k^i$. The labelling of the seed-points is mapped directly to the corresponding fibre-scaffolds $\mathcal{F}_k \rightarrow \mathcal{F}_k^i$. And since each fibre-scaffold is composed of a set of microstructural points, the motor-unit assignment is simultaneously mapped to these points as well, i.e., $\boldsymbol{X}_{k,r}^{\text{micro}} \rightarrow \boldsymbol{X}_{k,r}^{\text{micro},i}$. At this stage, the motor-unit anatomy is described in a discrete sense in the muscle geometry. The discrete motor-unit distribution parameter κ_i is defined by

$$\kappa_i(\boldsymbol{X}_{r,k}^{\text{micro},j}) = \begin{cases} 1 & \text{if } i = j,\ \forall\,\{r,k\} \\ 0 & \text{otherwise,} \end{cases} \tag{5.37}$$

where $\{i,j\} = 1,\ldots,N_{\text{MU}}$ iterate over the motor-units, $k = 1,\ldots,N_{\text{FS}}$ iterates over the fibre-scaffolds and $r = 1\ldots,N_k^{\text{micro}}$ iterates over the microstructural points within a fibre-scaffold.

5.3.4 Fibre distribution metric

To quantify the innervation patterns, a measure of fibre-type distribution is implemented. The measure, the so-called co-dispersion index developed by Lester et al. (1983), describes the distribution of (type-I and -II) fibre-types within a muscle biopsy. Note that smaller (type-S) motor-units are composed of type-I muscle fibres, and larger (muscle-F) motor-units of type-II. This classification is only to facilitate co-dispersion index calculation and does not dictate the underlying fibre-types, which, as mentioned, have continuously varying twitch properties.

The co-dispersion index ranges from -1 to $+1$ and indicates the randomness of fibre-type distribution. A value of 0 indicates a perfectly random mixture, larger negative values indicate a tendency towards *"regular intermixing"* or a *"checkboard"* pattern and larger positive values indicate segregation of fibre-types. The index is derived from a nearest neighbour search and statistical (chi-squared) analysis. Further details can be found in the aforementioned literature.

5.3.5 Motor-unit anatomy: model characterisation

The algorithm to innervate the fibre-scaffolds and generate the innervation patterns was implemented in `MATLAB`. The procedure to generate innervation patterns is governed by several parameters, classified as: (i) placement parameter $\boldsymbol{c}_{\text{MUT}}$, (ii) distribution parameters D, ΔD, R, and ΔR, and (iii) shape parameters $\boldsymbol{v}_i$ and λ_i, $i = 1,2,3$. The influence of these parameters is investigated by applying them to an idealised geometry. However, since the effects of the placement and shape parameters are relatively straightforward to predict, only the distribution parameters are varied, while the rest are kept constant.

Methods

To remove any geometrical effects, an idealised geometry with uni-directional fibre orientation was used. The cuboid had dimensions $L_{\text{x}} = 200\,\text{mm}$ and $L_{\text{y}} = L_{\text{z}} = L_{\text{w}} = 40\,\text{mm}$ with the fibre orientation aligned with the global x-axis. A perpendicular spacing $\Lambda_{\text{s}} = 0.375\,\text{mm}$ and (along) fibre spacing $\Lambda_{\text{f}} = 2\,\Lambda_{\text{s}}$ were used to trace approximately 12,000 fibres.

A total of 100 motor-units were modelled and the innervation-ratios computed via Equation 5.16. In terms of the fibre-scaffolds, this yielded innervation-ratios of $\text{IR}_1^{\text{SP}} = 6$ and $\text{IR}_{100}^{\text{SP}} = 554$

Table 5.4: *Parameter variations for innervation pattern generation. Values given as fractions of* $L_y = L_z = 40\,\mathrm{mm}$*, apart from* Π *which is given as an absolute value.*

ID	$R/L_\mathrm{w}\,\mathrm{mm}$	$D/L_\mathrm{w}\,\mathrm{mm}$	$\Delta R/L_\mathrm{w}\,\mathrm{mm}$	$\Delta D/L_\mathrm{w}\,\mathrm{mm}$	Π/mm
1	0.025	0.025	0.025	0.025	4
2		0.125			8
3		0.250			13
4		0.375			18
5	0.125	0.025			8
6		0.125			12
7		0.250			17
8		0.375			22
9	0.250	0.025			13
10		0.125			17
11		0.250			22
12		0.375			27
13	0.375	0.025			18
14		0.125			22
15		0.250			27
16		0.375			32
17	0.750	0.025			33
18		0.125			37
19		0.250			42
20		0.375			47
21	0.025	0.025	0.025	0.125	8
22				0.250	13
23				0.375	18
24			0.125	0.025	8
25				0.125	12
25				0.250	17
27				0.375	22

for the smallest and largest motor-units, respectively (Equation 5.29).

The placement parameter $\boldsymbol{c}_{\text{MUT}} = [100, 20, 20]$ mm was fixed at the center of mass of the geometry. The shape parameters $\lambda_1 = 1$, $\lambda_2 = \lambda_3 = 2$ were chosen to skew the territory shapes slightly. An overview of the distribution parameter variations is given in Table 5.4. The search space parameters (R and D) were varied in distribution IDs 1–20. The search-increment parameters (ΔR and ΔD) were varied in distribution IDs 21–27. The visual distribution of muscle fibres as well as quantitative metrics, such as motor-unit territory area and co-dispersion index were computed. The muscle fibres were plotted over the muscle's cross-section and were colour-coded from the smallest to largest motor-units to reveal the qualitative influence of each distribution parameter.

Since the computation of the co-dispersion index requires classifying the fibres as either type-I or -II, motor-units 1–75 were classified as type-S, i.e., comprising type-I fibres, and the remaining as type-F. Another common experimentally obtained motor-unit territory metric is its area or coverage, expressed as a percentage of total muscle cross-sectional area. This was computed as by first taking the area created by a convex hull about the fibres of a given motor-unit territory and dividing it by the muscle cross-sectional area (1600 mm^2).

Results

Innervation Patterns. A total of 27 distribution parameters variations were considered (Table 5.4) with the program taking between 60–160 s to perform the assignments on a desktop computer with a quad-core processor (`Intel Core i7-4790K @ 4GHz`) with 24 GB of memory.

The motor-unit territories are shown in Figures 5.11 and 5.13 for distributions IDs 1–20 and 21–27, respectively. Additionally, boundaries of selected motor-unit territories are shown in Figures 5.12 and 5.14.

A large variety of territory patterns were generated with a few parameters; increasing R and D lead to an increasing overlap of the territories (Figure 5.11). Increasing D alone, which can be seen along the rows of Figure 5.11, lead to the dispersion of smaller territories throughout the muscle cross-section. Conversely, increasing R alone, lead to an increased overlap of territory fibres, seen along the columns of Figure 5.11. The individual effects of R and D are more clearly seen in the territory boundaries (Figure 5.13). While increasing the iteration parameters ΔR and ΔD had a similar effect, this appeared largely on edges of the territories. A concentration of fibres at the centre of the territory was observed (Figure 5.12). Again, this is more clearly seen in the territory boundary (Figure 5.14).

Motor-unit territory areas. As the distribution parameters allow for a wider spread of the territory fibres, the area of the territory increases. To compare the two, the global distribution parameter $\mathit{\Pi}$ (Equation 5.36) is compared to the *mean* territory area per distribution (Figure 5.15a). Between the two, a highly statistically significant ($p < 1 \times 10^{-3}$) relation was observed, with a Spearman rank correlation coefficient of $r = 0.81$.

Further correlation metrics were analysed (not plotted): the correlation between mean territory area and D was statistically insignificant ($p > 0.05$). On the other hand, R was statistically significantly correlated to mean territory area ($p < 1 \times 10^{-3}$) with a Spearman rank correlation coefficient of $r = 0.96$.

Fibre-type mixing. Co-dispersion index values ranged between $+0.14$ and $+0.94$. The influence of the global distribution parameter $\mathit{\Pi}$ on the co-dispersion index is shown in Figure 5.15b. They were significantly correlated ($p < 1 \times 10^{-3}$) with a Spearman rank correlation coefficient $r = -0.91$. The co-dispersion index continued to fall as the distribution parameters

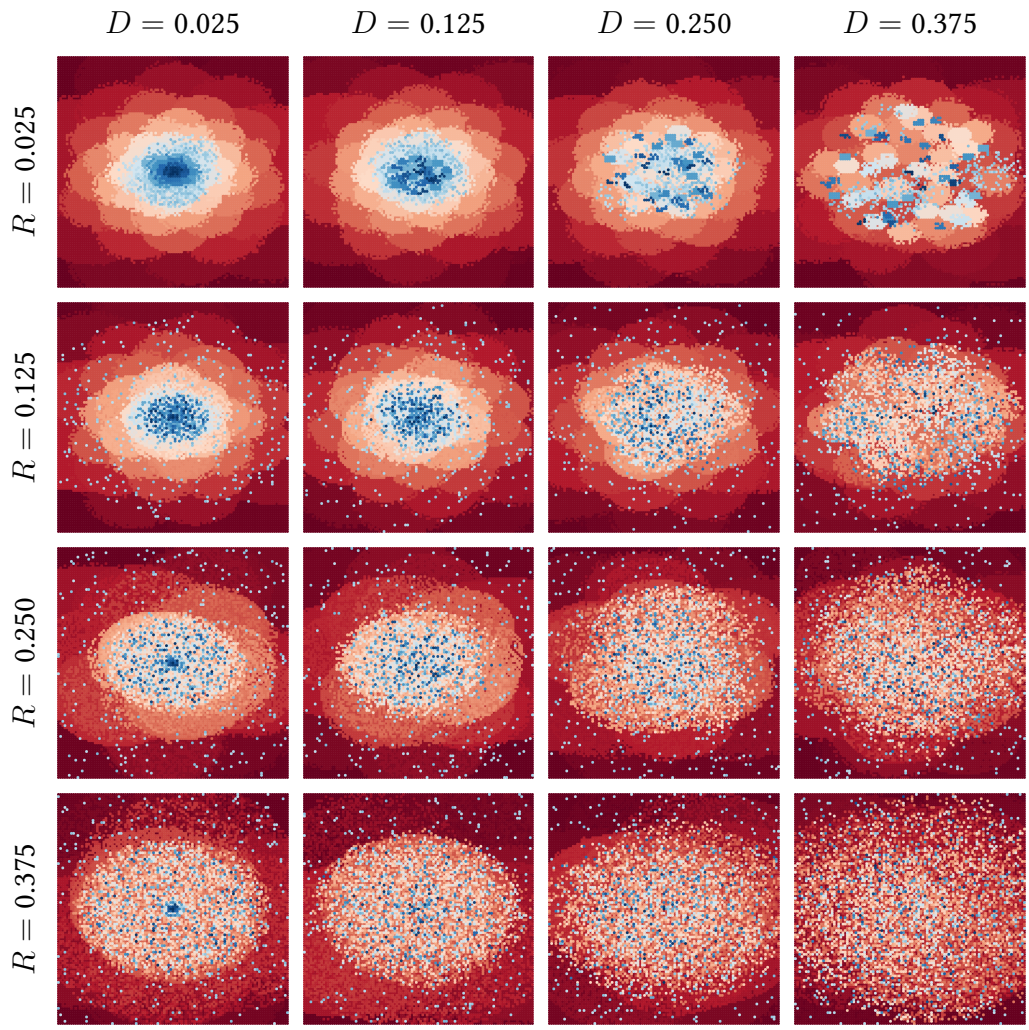

Figure 5.11: *Fibre distributions generated by varying R and D over the idealised muscle cross-section. Corresponding parameter values are indicated along the top and left edges. Fibres belonging to the smallest to largest units are colour-coded from dark-blue (to cream) to maroon, respectively.*

rose until co-dispersion index ≈ 0, where increasing Π beyond ≈ 33 had little to no effect on co-dispersion index.

Lastly, the outcome measures—the co-dispersion index and territory area—were compared to each other (Figure 5.16). They showed a statistically significant ($p < 1 \times 10^{-3}$) correlation, with a Spearman rank correlation coefficient $r = -0.92$.

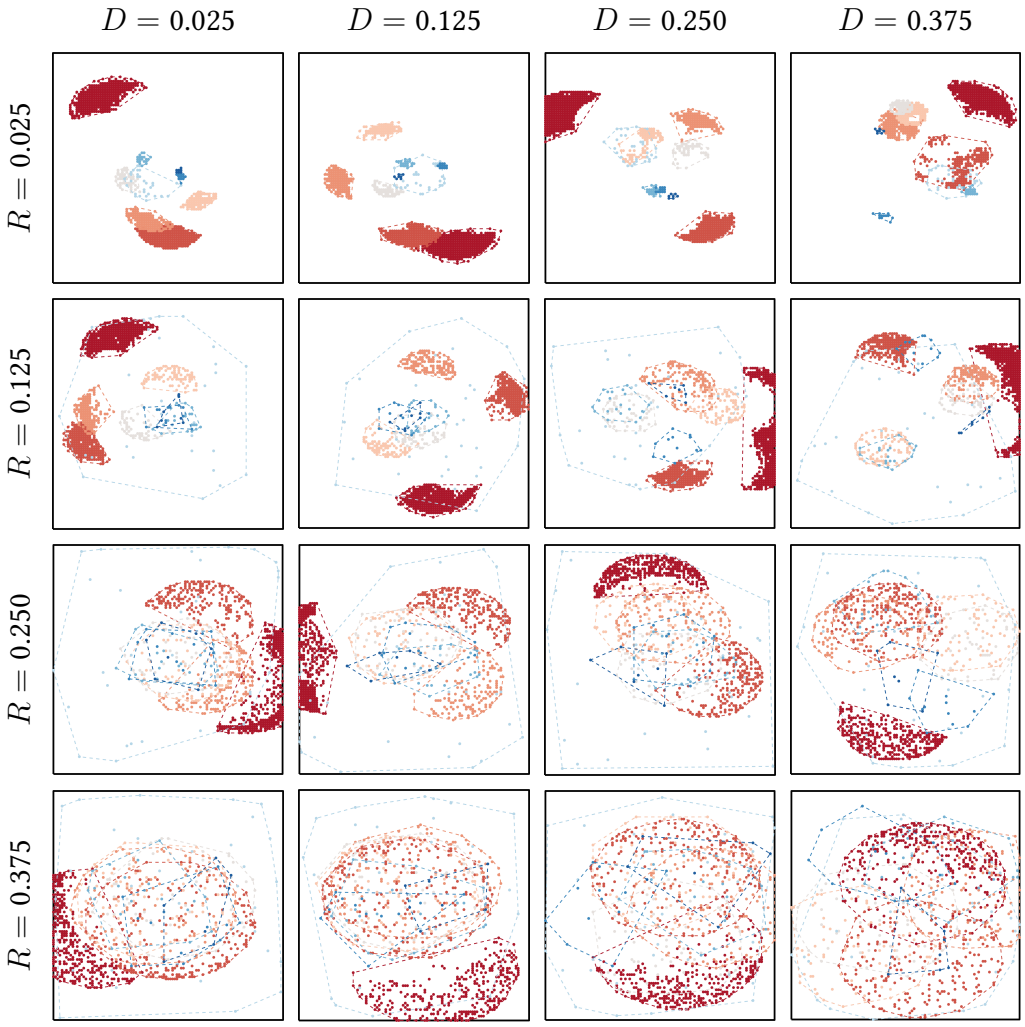

Figure 5.12: *Territory boundaries generated by varying R and D over the idealised muscle cross-section. Corresponding parameter values are indicated along the top and left edges. Fibres belonging to the smallest to largest units as well territory boundaries are colour-coded from dark-blue (to cream) to maroon, respectively.*

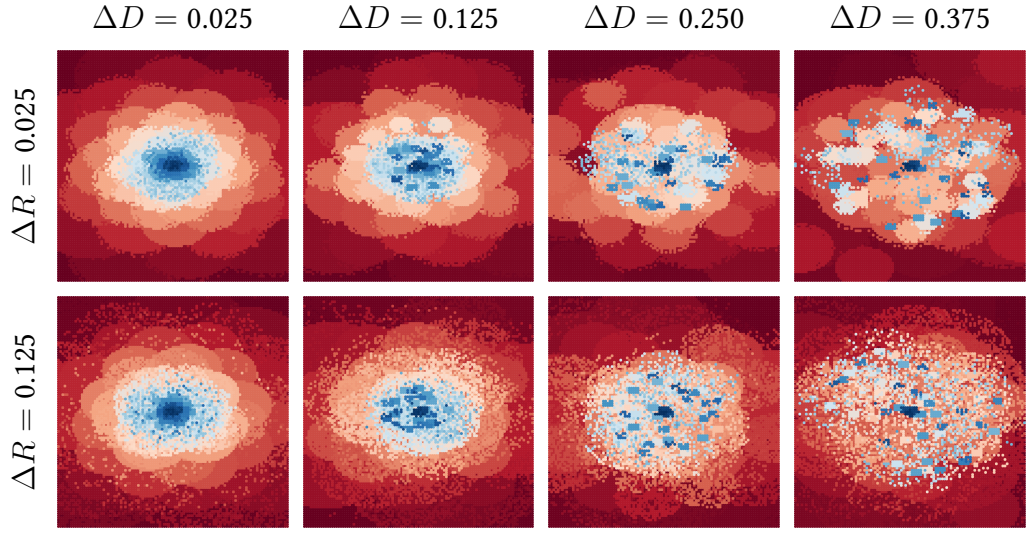

Figure 5.13: *Fibre distributions generated by varying ΔR and ΔD over the idealised muscle cross-section. Corresponding parameter values are indicated along the top and left edges. Fibres belonging to the smallest to largest units are colour-coded from dark-blue (to cream) to maroon, respectively.*

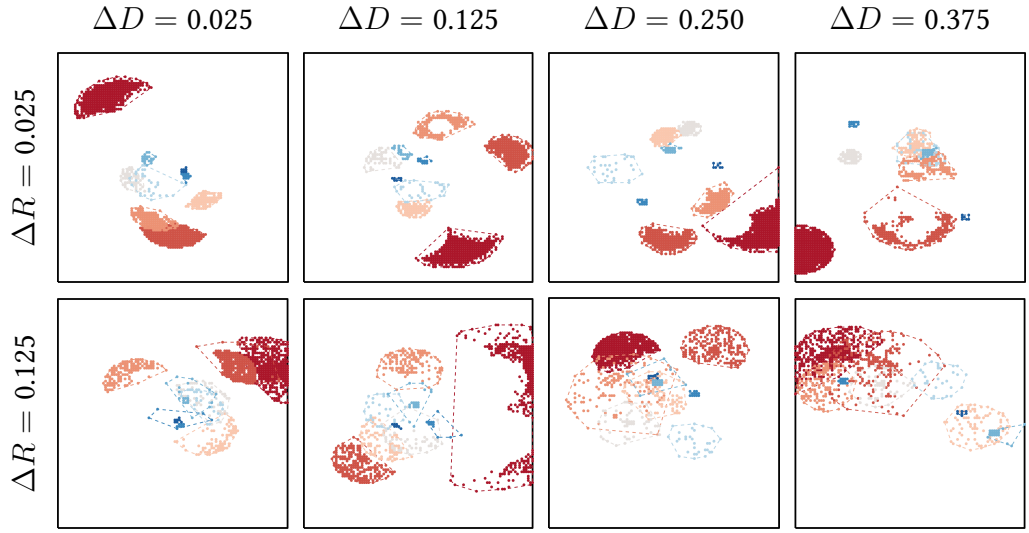

Figure 5.14: *Territory boundaries generated by varying ΔR and ΔD over the idealised muscle cross-section. Corresponding parameter values are indicated on the boundaries. Fibres belonging to the smallest to largest units as well territory boundaries are colour-coded from dark-blue (to cream) to maroon, respectively.*

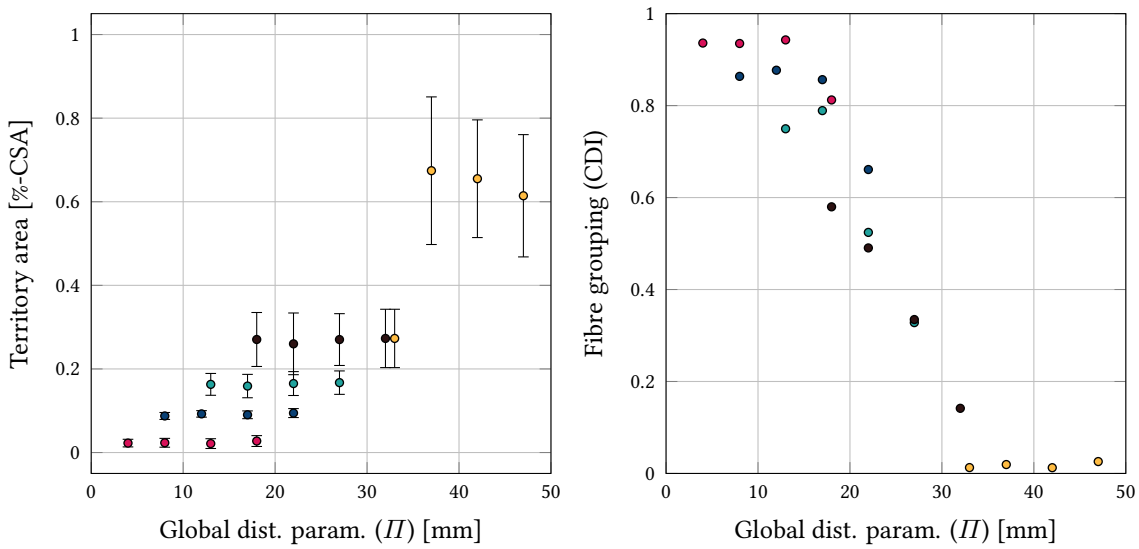

Figure 5.15: *Relationship between motor-unit anatomy and fibre dispersion and territory size. The marks are colour-coded according to the value of R: maroon: $R = 1\,\mathrm{mm}$, dark blue: $R = 5\,\mathrm{mm}$, green: $R = 10\,\mathrm{mm}$, black: $R = 15\,\mathrm{mm}$ and yellow: $R = 30\,\mathrm{mm}$. (a) Bars show interquartile range.*

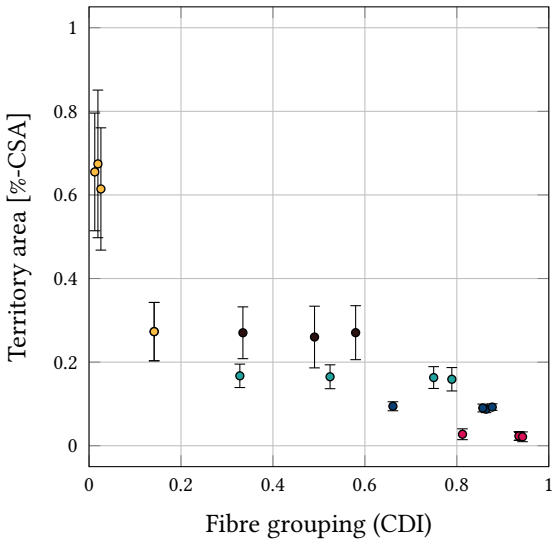

Figure 5.16: *Relationship between fibre dispersion and territory area. Colour-coding as in Figure 5.15, and bars show interquartile range.*

5.4 Discussion

First, the implications and drawbacks of the motor-unit activity model are discussed (Section 5.4.1). The majority of the discussion then focuses on the motor-unit territory definition. Starting with the reconstruction of the microstructure and the idealisations that accompany it (Section 5.4.3). Then the approach to construct motor-unit territories is contrasted against other models proposed in literature (Section 5.4.3). Lastly, the plausibility of the generated motor-unit territories is discussed in relation to experimental observations (Section 5.4.4).

5.4.1 Motor-unit activity

Models of biophysical processes within the muscle microstructure, together with an α-motor-neuron recruitment model, are used to compute motor-unit activity. The advantage of this approach is that changes in biophysical processes can be altered to account for various muscle states, for example, Ca^{2+} dynamics have been found to be responsible for twitch slow-down in aged muscle (Larsson et al., 2018, and references therein).

The biggest obstacle to tuning these parameters is the lack of experimental data. The amalgam of parameters in the source models: i.e., Fuglevand et al. (1993), Aliev et al. (1996) and Razumova et al. (1999), are obtained from experiments performed by various research groups, over several decades, on various muscles from various species of mammals. However, certain trends can be observed for most healthy muscles. For example, Fuglevand et al. (1993) state *"[t]he peak firing rates that have been observed in human muscle during ballistic isometric contractions have generally ranged from 20 to* 45 imp/s*"* (see references therein). Such observations can lead to a set of parameters and models which describe human motor-output *in general*, and can reveal relative effects of neural input alterations on motor-output, e.g., influence of firing synchronising on force output (Taylor et al., 2002).

The computation of certain models (such as the ones used currently) require miniscule times steps leading to high computational times. Since, however, activity is pre-computed and unidirectionally coupled with the mechanics model, the computational efficiency of the activity computations has no bearing on the finite element simulation. But if a two-way coupling is desired, then simpler models may become more attractive. For example, Ramírez et al. (2010) forgo ionic and cross-bridge dynamics calculations and simply convolute fixed twitch-shapes with firing times, which would reduce computational overhead drastically compared to the biophysical models used presently. Further α-motor-neuron pool models (among others) can be found in Röhrle et al. (2019).

Given the modular nature of the current approach, both the α-motor-neuron pool model and the twitch force model can be matched to specific research questions or technical constraints. The current models provide a good trade-off between model complexity and granular control of motor-unit properties.

5.4.2 Reconstruction of microstructure

A deterministic streamline method was used to recover fibre connectivity by forming 1D fibre scaffolds within the muscle. Both the spacing between and along the fibres governs the spatial resolution of the microstructure, and the method requires interpolation of the fibre orientation field at each of the microstructural points. This is computationally demanding as the cost

increases exponentially with decreasing spacing ,e.g., reducing the inter-fibre spacing by a factor of two resulted in an 8-fold increase in computational time.

Alternative methods to compute virtual fibres include laplacian methods (Bayer et al., 2012; Choi et al., 2013; Sathar et al., 2015; Handsfield et al., 2017), and mapping methods (Blemker et al., 2005a). These methods do not require a pre-existing fibre orientation field, but rather use information about muscle geometry together with templates and/or inflow/outflow boundary conditions to generate the virtual fibres. While these methods may be more computationally efficient, the advantage of the present method is that a continuous seed-point plane is generated automatically at the mid-point of the virtual fibres, which simplifies the subsequent motor-unit anatomy algorithm. Nevertheless, the current work-flow to generate motor-unit anatomy is not restricted to a specific fibre-reconstruction method.

Most fibre reconstruction methods assume that all fibres run end-to-end in the muscle. This is not always the case in human skeletal muscles and non-spanning have been observed in several muscles such as the sartorius, gracilis, biceps femoris, semitendinosus, brachoradialis and semimembranosus muscles (Trotter, 1993; Lateva et al., 2010). Furthermore, in cats, non-spanning motor-unit territories have been observed, which spanned about half of the tibialis anterior length (Roy et al., 1995).

From the perspective of the method, inclusion of non-spanning fibres is relatively straight forward. Once the fibre-scaffolds have been reconstructed, a *maximum fibre length* may be (randomly) imposed, which would cleave existing fibre-scaffolds into multiple sections. This would result in fibre segments that still conform to the muscle structure. The innervation process may become slightly more complex since the seed-points, or neuromuscular-junctions, no longer lie on a continuous surface, but this does not pose a major challenge. However, it's worth considering the difference between an anatomical and functional fibre; a fibre may be anatomically split into segments, but if one of these segments contract, the force would still be transmitted to the tendons via the connective tissues. In other words, the behaviour would resemble an anatomically intact fibre. Therefore, non-spanning fibres were not considered in the current method.

5.4.3 Motor-unit territory anatomy models

Over the past few decades, most research in constructing motor-unit anatomy has focused on the relative size difference and overlapping of motor-unit territories. While the current method to assign innervation patterns (and generate motor-unit territories) shares some similarities with those found in literature, there are several key differences. The main similarity is that the motor-unit territory definition is split into three steps; first, determining motor-unit size based on innervation-ratio; second, definition of a motor-unit territory centre; and third, innervation of fibres within the motor-unit territory boundary (e.g. Shenhav et al., 1986; Cohen et al., 1987; Stashuk, 1993; Schnetzer et al., 2001; Navallas et al., 2010; Röhrle et al., 2012; Robertson et al., 2017; Botelho et al., 2019), including the previous version of the current method (**Saini** et al., 2018). Besides Röhrle et al. (2012) and Botelho et al. (2019), all algorithms were applied to idealised geometries with idealised (circular) motor-unit territories shapes. Although this may not be the limitation of these methods.

The key differences include the ability to confine certain motor-unit-types within a subregion of the muscle cross-sectional area. For example, smaller (type-S) motor-units are preferentially located in the superficial regions of the tibialis anterior (Henriksson-Larsén et al., 1985; Mesin

et al., 2010). However, some muscles, such as the masseter, show evidence both for preferential localisation (Eriksson et al., 1983; Tonndorf et al., 1994) and against it (van Dijk et al., 2016; Lapatki et al., 2019).

Additionally, the current approach allows for heterogeneous fibre distribution within a territory, which is not possible in several of the aforementioned methods, where motor-unit fibre distribution is ordered about the motor-unit territory centre, e.g., Gaußian distribution (Shenhav et al., 1986; **Saini** et al., 2018). Alternatively, some innervation strategies control for certain anatomical statistics, such as enforcing a constant motor-unit fibre density throughout the territory. But animal studies have shown that the distribution of fibres within a motor-unit territory is heterogeneous and may be clustered (e.g Bodine et al., 1988; Bodine-Fowler et al., 1990; Tonndorf et al., 1994; Roy et al., 1995). The clustering of territory fibres may be influenced by neuromuscular development after birth, where muscle fibres undergo a pruning process, being initially innervated by multiple α-motor-neurons, followed by elimination of all but one of the synapses (e.g. Bennett, 1983; Pfeiffer et al., 1985; Dahm et al., 1988). This process is thought to leave behind "holes" in territories, which are apparent in some distributions in Figures 5.12 and Figures 5.14. Since the algorithm proceeds iteratively—from the smallest to the largest motor-units—previously innervated fibres block the innervation of a subsequent motor-unit and give rise to gaps or holes within the territory.

The novel combination of the virtual fibre reconstruction method and the motor-unit anatomy method means that three-dimensional motor-unit territories can be defined, taking only muscle geometry with a fibre orientation field as a starting point.

5.4.4 Plausibility of motor-unit territories

A large variety of patterns were generated with a few parameters. The range of co-dispersion index ranged between $+0.14$ and $+0.94$ for the distributions considered. Healthy muscle of young adults shows co-dispersion index values close to 0 (Brenner et al., 1987), or even slightly negative, whereas older and neuromuscular-disordered muscles show more positive values, e.g., $+0.74$ for Charcot-Marie-Tooth disease (Lester et al., 1983). This suggests that, even without cycles of denervation and reinnervation (Chapter 9), the algorithm is able to produce a range of healthy and pathological motor-unit territories; at least in terms of the co-dispersion index alone.

No negative co-dispersion index values were observed within the range of distribution parameters tested. As the search-space for both the central α-motor-neuron axon and the peripheral axons was increased, the chance of fibre-type mixing increases also. Resulting in a reduction of the co-dispersion index. However, at some stage the search-space exceeded the cross-sectional area of the muscle. Beyond this point, the fibre-type mixing only varied minimally due to the stochastic nature of the algorithm and co-dispersion index hovered around 0.

A checker-board pattern gives rise to negative co-dispersion index values. This may be incorporated in the current motor-unit anatomy algorithm by facilitating fibre-types to group together. For example, Cohen et al. (1987) used a "repulsion factor" to repel certain fibre-types from each other. It may seem counter-intuitive that fibre repulsion leads to clustering, for example, if type-II fibres are repelled, then type-I clusters form between them, leading to the aforementioned checker-board type pattern. There is some evidence for this in healthy human muscles, albeit in a small number of subjects (Willison et al., 1980; Lester et al., 1983, e.g.). The

co-dispersion index is but one of several ways in which fibre-type distribution is quantified, (c.f. Jennekens et al., 1971; Venema, 1988; Sjöström et al., 1992) and the motor-unit anatomy method is not restricted to its use.

Although, the co-dispersion index is computed via a pairwise analysis of neighbouring fibres, it seems to be related to the motor-unit territory area, which requires the location of all of its fibres simultaneously (Figure 5.16). The co-dispersion index values showed an inverse relationship with the average territory area, with a linear-fit yielding an R-squared value of 0.78. Consider small territory areas—the chances of finding mixed fibre-type neighbours decreases, and co-dispersion index would increase. Conversely, larger territory sizes increase the changes of fibre-type intermixing and reduce the co-dispersion index.

The relationship between co-dispersion index and territory area may only be observable if the *entire* population of fibres is used for the fibre-mixing computation, as was the case in this comparison. This is atypical for experimental measurements, where biopsy numbers are kept as low as possible. However, a randomly selected biopsy may not be representative of the (average) fibre mixing seen in the muscle. Such a model can provide insights into the optimal number and size of biopsies which are still representative of the muscle fibre distribution. For example, by taking variations on the size and number of virtual biopsies, and comparing the biopsy co-dispersion index values to that obtained from the entire muscle.

The average of the 100 motor-unit territory areas between the 27 distributions considered ranged between 2–67 % of the muscle cross-sectional area. Mammalian muscle territories occupy, on average, 24 % (range: 13–35 %) of the cross-sectional area in rats (Kugelberg et al., 1970; Larsson et al., 1991; Kanda et al., 1992) and 32 % (range: 19–44 %) of the cross-sectional area in cats (Bodine et al., 1988; Rafuse et al., 1996). The distributions which produced territory in these ranges were distributions 13–16 with mean territory area 27 % (range: 8–46 %) of the cross-sectional area. In fact, only the parameter R seemed to affect the motor-unit territory area size strongly (Figure 5.15a), as this parameter governs the search area of the peripheral α-motor-neuron axons (Equation 5.31). The search distance for distributions 13–16 was $R = 15\,\text{mm}$ and considering the (ellipsoidal) shape, yields a search area of 353 mm^2—which is 22 % of the muscle cross-sectional area. This corresponds well with the observed mean territory area. The significantly strong relationship between territory area and the parameter R suggests that R can be interpreted as mean territory size.

6 Integrating & Implementing the Neural and Skeletal Muscle Models

Till now, the mechanical description of skeletal muscles (constitutive relation), motor-unit anatomy (motor-unit discrete distribution factor), and motor-unit activity were treated in isolation. This chapter integrates these components and also describes the implementation of the integrated model, together with the required assumptions, modifications, and numerical considerations required to do so.

In the current modelling framework, skeletal muscles are described at the macroscopic scale by a continuum-mechanical constitutive relation. The constitutive relation averages microstructural properties of skeletal muscle, for example, muscle fibres are described via a fibre orientation field, fibre deformation via (local) stretch, and the force-length relationship via a phenomenological model. Muscle activity is decomposed into spatial and temporal components to account for individual motor-unit anatomy and activity, respectively. These components, however, are described microstructurally, i.e., computed via cross-bridge dynamics and individually reconstructed muscle fibres (Chapter 5). Therefore, the muscle activity must be homogenised in order to be integrated with the skeletal muscle constitutive relation (Section 6.1).

By decomposing muscle activity into per-motor-unit activity and anatomy, certain assumptions are required on the spread of activity within the motor-unit. That is, the volumetric motor-unit is scaled by a single time-varying activity, which requires the assumption that the action-potential propagates instantly throughout the motor-unit once it arrives at the neuromuscular-junction. In reality, the action-potential propagates along the fibres of a motor-unit in a finite amount of time. The impact of assuming instant action-potential propagation on the mechanical response is investigated by using a multiscale, multi-physics skeletal muscle model to simulate a contraction both with finite and infinite action-potential propagation (Section 6.2).

Prior to implementing the integrated model for use with a commercial finite element solver, certain adaptations and numerical investigations are required. This includes: the re-expression of the musculotendon complex constitutive relation in a local coordinate-system, investigation of the incompressibility behaviour and element type performance (Section 6.3). Then, the integrated model is demonstrated with an idealised geometry and compared to the status-quo modelling approach (Section 6.4). Lastly, the limitations and plausibility of the integrated model are discussed (Section 6.5).

6.1 Homogenising Motor-Unit Territories

The process of innervation pattern generation is briefly summarised—starting from the muscle geometry $\mathcal{B}_0$ and the fibre orientation $\boldsymbol{a}_0(\boldsymbol{X})$, $\boldsymbol{X} \in \mathcal{B}_0$. First, the microstructure is reconstructed using a streamline tracing method (Section 5.2.2) resulting in a set of neuromuscular-junctions

or seed-points $\mathcal{S} = \{\boldsymbol{s}_k\}$ ($k = 1, \dots, N_{\text{FS}}$) and corresponding fibre-scaffolds $\mathcal{F}_k$. The fibre-scaffolds comprise a set of microstructural points, i.e., $\mathcal{F}_k = \{\boldsymbol{X}^{\text{micro}}_{r,k}\}$ ($r = 1, \dots, N^{\text{micro}}_k$). Second, an iterative, semi-stochastic approach is used to innervate the N_{FS} seed-points by N_{MU} α-motor-neurons (Section 5.3). This process yields a set of innervated seed-points, i.e., $\boldsymbol{s}_k \rightarrow \boldsymbol{s}^i_k$. Where the superscript indicates that the quantity belongs to motor-unit i.

Since each seed-point corresponds to a fibre-scaffold, the innervation of a seed-point by α-motor-neuron i translates to the entire fibre-scaffold i.e., $\mathcal{F}_k \rightarrow \mathcal{F}^i_k$ and to all microstructural points that it contains, i.e., $\boldsymbol{X}^{\text{micro}}_{r,k} \rightarrow \boldsymbol{X}^{\text{micro},i}_{r,k}$. For clarity, the subscripts $(\cdot)_{r,k}$ are omitted, i.e., $\boldsymbol{X}^{\text{micro},i}$. In summary, the innervation process yields each point $\boldsymbol{X}^{\text{micro}} \in \mathcal{B}_0$ grouped into a motor-unit; thereby defining κ_i. The next step is the homogenisation of this microstructural information to the macroscopic continuum-mechanical scale.

Recall, the concept of the representative volume element, which assumes that $\boldsymbol{X} \in \mathcal{B}_0$ represents the averaged microstructure in the volume surrounding $\boldsymbol{X}$. Basically, the size of the representative volume element is one at which the microstructure can be no longer seen with the naked eye. Below this scale the density and behaviour of the material starts to become heterogeneous.

The challenge arises when microstructural properties below the scale of the representative volume element need to be considered. Presently, this is the motor-unit territory distribution described by the innervated $\boldsymbol{X}^{\text{micro},i}$. A common approach to account for such heterogeneous microstructural variations is the statistical volume element (e.g. Beran, 1968; Kröner, 1972; Schröder et al., 2011).

Essentially, the probability of finding a microstructural point of motor-unit i in a region about the macroscopic material point $\boldsymbol{X}$ is computed. Since the continuum body is spatially discretised by the finite element method, the Gauß points are used as the material point about which the statistical homogenisation is carried out.

Let the finite element mesh be composed of $p = 1, \dots, N_{\text{GP}}$ Gauß points with coordinates $\boldsymbol{\xi}_{0,p}$. Then, at each microstructural point $\boldsymbol{X}^{\text{micro},i}$, a nearest neighbour search is carried out to identify the closest Gauß point. Since the spatial resolution of the microstructural points is much finer than the Gauß points, this results in multiple microstructural points having a single Gauß point as their nearest neighbour.

For a Gauß point p ($\boldsymbol{\xi}_{0,p}$), let the number of associated microstructural points be N^p_{GP}. Then, the probability of finding a point of a given motor-unit about $\boldsymbol{\xi}_{0,p}$ is computed by

$$\hat{\kappa}_i(\boldsymbol{\xi}_{0,p}) = \frac{1}{N^p_{\text{GP}}} \sum_{j=1}^{N^p_{\text{GP}}} \kappa_i \left(\boldsymbol{X}^{\text{micro},i}_j\right). \tag{6.1}$$

Recall that κ_i is the discrete motor-unit distribution with the property $\kappa_i(\boldsymbol{X}^{\text{micro}}_i) = 1$ (Equation 5.37). That is, about a given Gauß point, the total number of neighbouring microstructural points that belong to a given motor-unit are divided by the total number of neighbours. This assumes that all fibre-scaffolds are of the same diameter, whereas in reality muscle fibres show varying sizes.

Since each $\boldsymbol{X}^{\text{micro},i}$ is assigned to at least one motor-unit, together with the equation above, the following holds

$$\sum_{i=1}^{N_{\text{MU}}} \hat{\kappa}_i(\boldsymbol{\xi}_{0,p}) \stackrel{!}{=} 1. \tag{6.2}$$

The distribution factor complements the motor-unit activity $\alpha_i(t)$ and forms the second pillar for the computation of muscle activity (now at the Gauß points) $\alpha_{\mathrm{M}}(t, \boldsymbol{\xi}_p)$ (Equation 4.40), restated here for convenience:

$$\alpha_{\mathrm{M}}(t, \boldsymbol{\xi}_p) = \sum_{i=1}^{N_{\mathrm{MU}}} \alpha_i(t)\ \hat{\kappa}_i(\boldsymbol{\xi}_p). \tag{6.3}$$

Analogous to Equation 4.41, the positions of the Gauß points in the current and reference configuration are related by the placement function, i.e.,

$$\boldsymbol{\xi}_p = \boldsymbol{\chi}\left(\boldsymbol{\xi}_{0,p}, t\right), \tag{6.4}$$

where $\boldsymbol{\xi}_{0,p}$ is the Gauß point in the reference configuration.

6.2 Muscle Activity Decomposition: Assumption on Action-Potential Propagation

The models of excitation-contraction coupling describe the temporal change in membrane potential and Ca^{2+} concentrations in a muscle cell, in response to current stimuli at the neuromuscular-junction, and the subsequent cross-bridge dynamics (Section 5.1). Once depolarisation is initiated at the neuromuscular-junction, the action-potential propagates along the fibre, leading to Ca^{2+} and cross-bridge dynamics in its wake. The time taken between stimulation at the neuromuscular-junction and fibre-tension production is the so-called electromechanical delay and typically ranges between 8–100 ms (Schmid et al., 2019, and references therein).

The current model is developed to primarily investigate movements, where the time span is typically in seconds. Since this is well above the electromechanical delay, the relative duration of action-potential propagation is quite small. Therefore, the action-potential is assumed to propagate instantly, synchronising the Ca^{2+} and cross-bridge dynamics along the fibre. Furthermore, by assuming that the stimulus current arrives at all neuromuscular-junctions of a motor-unit at the same time instance, the Ca^{2+} behaviour of the entire motor-unit is essentially characterised by a single representative sarcomere. This greatly simplifies the modelling framework since electrophysiology no longer needs to be modelled.

To assess the errors in force production introduced by this assumption, a multiscale and multi-physics chemo-electro-mechanical skeletal muscle model is used (Heidlauf et al., 2014; Heidlauf, 2016). The model is used to simulate a contraction, both with finite and infinite action-potential propagation. Full details of the model can be found in the cited literature and only a short description of the model follows.

The model links the physiological and anatomical structure of the neuromuscular system and consists of one-dimensional muscle fibres embedded in a three-dimensional continuum-mechanical model of skeletal muscle tissue. Within the fibres the entire excitation-contraction coupling pathway is considered, including (i) the propagation of action-potentials along the muscle fibres caused by the stimulus of α-motor-neurons, (ii) the induced calcium dynamics serving as an intracellular second messenger to (iii) enable cross-bridge cycling and local tension production in the fibre.

The microscopic muscle fibre models are then coupled to a macroscopic continuum-

mechanical model to predict the deformations and reaction forces on the tissue scale. This is done in a similar manner to that described in the previous section. Gauß point stresses are computed by averaging the local tension contributions of the fibres in their neighbourhood. The deformation of the macroscopic muscle geometry is, in turn, used to update the geometrical configuration of the muscle fibres as the contraction proceeds.

6.2.1 Methods

To avoid geometrical influences, an idealised cuboid representation of a musculotendon complex was used (Figure 6.1a), with length L, width W and height H of $40 \times 10 \times 10$ cm. Both muscle and tendon tissue had the same cross-section, with the muscle and tendon lengths of $5/7\,L$ and $2/7\,L$, respectively. The musculotendon complex was discretised by seven Taylor-Hood elements, employing tri-linear and tri-quadratic Lagrangean shape functions.

The muscle was populated with 16 fibres, which were discretised by linear Lagrangean finite elements. They were split into 5 motor-units with innervation-ratios of 2, 2, 2, 4 and 5, respectively (Figure 6.1a). The territories were generated with parameters $D = R = \Delta R = \Delta D = 1/4\,W$, $\mathbf{W} = \boldsymbol{I}$ and $\boldsymbol{c}_{\mathrm{MUT}} = [L/2, W/2, H/2]$.

The motor-units were stimulated with a fixed firing rate, taken as 27.8, 17.3, 14.0, 10.4 and 6.7 Hz for motor-units 1 to 5, respectively, and recruited with an offset 10 ms with respect to the previous motor-unit (Figure 6.1b). The stimulation consisted of a current pulse injected into the central node (virtual neuromuscular-junction) of the corresponding fibres. Instantaneous propagation of action-potential was modelled by delivering the stimulus to all fibre nodes simultaneously. It is important to note that for this case, the homogenisation of the microscopic active stresses yields the same results as the activity mapping described in Section 6.1.

Besides the geometry, all model parameters were adapted from the baseline experiment in Schmid et al. (2019). The computations were performed using the open source software library `OpenCMISS` (Bradley et al., 2011) with a simulation time of 870 ms.

6.2.2 Results

The simulations with and without action-potential propagation were performed with `OpenCMISS` on a desktop computer with a quad-core processor (`Intel Core i7-4790K @ 4GHz`) with 24 GB of memory, resulting in a computational times of 12 h and 6 h, respectively. Snapshots of both models during various time steps are shown in Figure 6.2. The reaction forces for both, summed over the nodes at the fixed tendon end, are shown in Figure 6.3.

The average difference in the time taken for the force to attain a given value, i.e., time-to-force, between both models was 16.6 ms, with both models reaching the same maximum force magnitude of 39 N. Further, electromechanical delay was calculated for both conditions by the time difference between the (first) stimulus and the time at which the musculotendon complex force increases by 1 % of the maximum (twitch) force (Mörl et al., 2012). The electromechanical delays for the cases with and without action-potential were 18.8 ms and 8.2 ms, respectively.

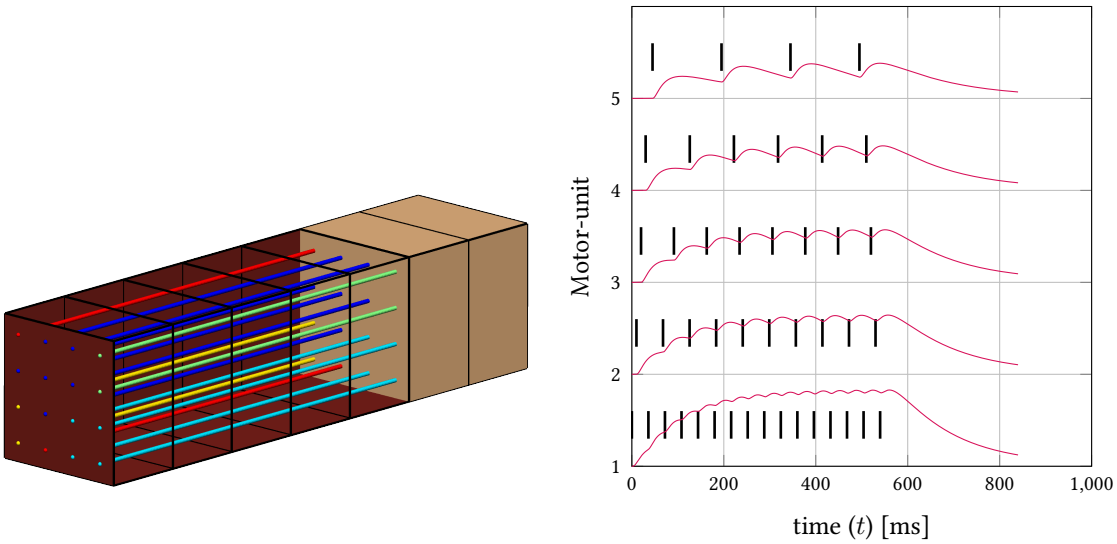

(a) *Geometry and innervation pattern.* ***(b)*** *Motor-unit activity.*

Figure 6.1: *Multiscale neuromuscular simulation architecture and activation for action-potential comparisons. (a) Maroon and light brown denote muscle and tendon, respectively. The top and side muscle surface is removed to show the fibre distribution, which are colour-coded according to the motor-unit distribution, motor-unit 1: red, 2: yellow, 3: light green, 4: light blue and 5: dark blue. (b) α-Motor-neuron firing times in black, with the twitch response shown in red.*

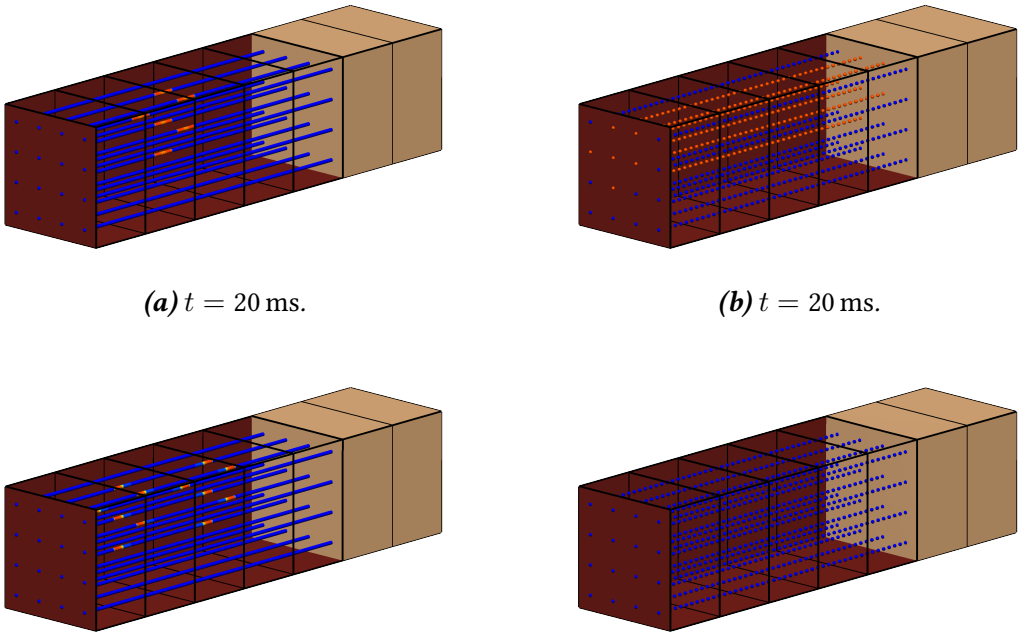

(a) $t = 20$ ms. ***(b)*** $t = 20$ ms.

(c) $t = 120$ ms. ***(d)*** $t = 120$ ms.

Figure 6.2: *Snapshots of multiscale simulation (left) with and (right) without action-potential propagation. Normalised transmembrane voltage between blue (0) and red (1) after stimulation of motor-unit 5.*

6.3 Implementing the Neuro-Musculoskeletal Model

Neural information (motor-unit anatomy and activity) is computed via a workflow implemented in `MATLAB` (R2018a, The MathWorks, Inc., USA) (Section 6.3.1) and takes as inputs: muscle geometry (with a fibre orientation field) and excitatory drive. The former is used to perform; microstructure reconstruction, α-motor-neuron innervation, and statistical homogenisation, forming three-dimensional motor-unit territories in the muscle geometry $\hat{\kappa}_i(\boldsymbol{X})$; and the latter is used to compute individual motor-unit activities $\alpha_i(t)$. Outputs from the neural information workflow are integrated in the constitutive relation of the musculotendon complex $\alpha_{\mathrm{M}}(\alpha_i(t), \hat{\kappa}_i(\boldsymbol{\xi}))$, which is modelled by a `FORTRAN` user-material, developed for the finite element solver `Abaqus/Explicit` (v2017, Dassault Systèmes, France) (Section 6.3.2).

Before demonstrating the integrated finite element model, certain numerical aspects have to be verified. First, recall that the incompressibility is controlled by a penalty-parameter (Section 4.2.1). The impact of the penalty-parameter on model-accuracy and computational-time was quantified by comparing simulated results to a perfectly-incompressible analytical solution (Section 6.3.3).

Second, the drawbacks inherent to some element formulations, such as volumetric locking or "hourglassing", should be minimised. The physical reliability of the elements was tested with a convergence analysis (Section 6.3.4). Finally, an idealised integrated model was generated and compared to a status-quo continuum model to demonstrate differences in activity and motor-output (Section 6.4).

6.3.1 Pre-computing neural information in MATLAB

The workflow to compute individual motor-units activity $\alpha_i(t)$ ($i = 1, \ldots, N_{\mathrm{MU}}$) and their distribution maps $\hat{\kappa}_i(t)$, is implemented in `MATLAB`. This neural information is computed according to the procedures described in Chapter 5. The workflow is organised in six main steps:

1. Read in and extract finite element mesh and fibre orientation information (described below),
2. Compute the activation of all motor-units (Section 5.1),
3. Track fibre-scaffolds within the muscle volume (Section 5.2),
4. Generate innervation patterns on the seed-point plane (Section 5.3),
5. Generate motor-unit territories via homogenisation at Gauß points of the finite element mesh (Section 6.1),
6. Generate output for the musculotendon user-material (described below).

A global settings file is used to govern key processes in the workflow and is divided into three major sections: (i) script options, (ii) characterisation parameters, and (iii) plotting options. Script options specify environment variables such as number of cores to be used, the operating system on which the workflow is being executed and which steps to be performed, e.g., on subsequent runs the extraction and tracking of fibres may no longer be necessary. The largest section is the parameter section, which is further split into each of the steps as outlined above. For example, information about the α-motor-neuron pool such as the number of motor-units N_{MU} and the innervation-ratios (Equation 5.16) or motor-unit territory distribution parameters D and R (Algorithm 3) are specified here.

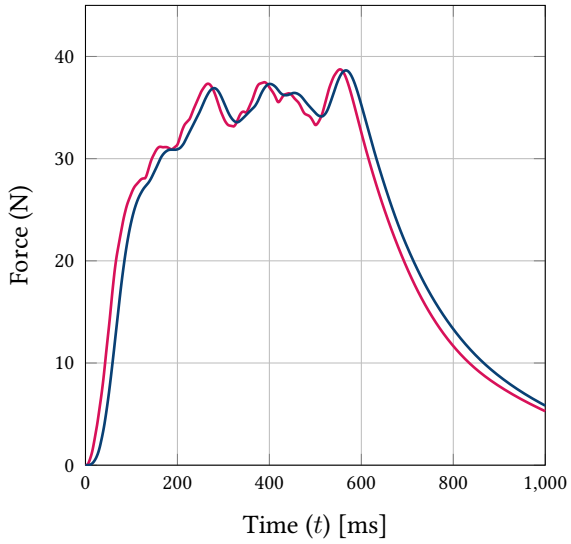

Figure 6.3: *Reaction force measured at the tendon for both models with action-potential propagation: dark-blue trace, and without action-potential propagation: maroon trace.*

Mesh extraction

The workflow to pre-compute the neural information is closely tied to the finite element solver used, therefore several calls are made to `Abaqus/Explicit` to extract mesh information automatically and for verification purposes. The geometry is imported from an `Abaqus` input-deck, which contains the nodal coordinates $\mathbf{N}$, element connectivities and per-element fibre orientations.

The input-deck does not however, contain information about the Gauß points, and it must be extracted by other means. A dummy user-material is used to access the ID numbers and coordinates of the Gauß points. The element type can then be determined based on the number of nodes and Gauß points per element (cf. Table 6.1). Note that muscle geometries with mixed-element types are currently not supported.

An important aspect in the fibre-tracing algorithm is restricting the process within the geometry of the muscle (Algorithm 2). The `MATLAB` function `boundary` returns a triangulated surface $\mathbf{K}$ based on the node points $\mathbf{N}$ of the geometry, i.e.,

$$\mathbf{K} = \texttt{boundary}(\mathbf{N}, s_\mathrm{f}), \tag{6.5}$$

where s_f is a shrink factor, which yields a convex-hull when it is set to unity.

Based on this triangulation, voxelisation, and ray-tracing techniques are used to test if any arbitrary point $\boldsymbol{c}$ lies within the surface via the function `intriangulation` (Aitkenhead, 2013; Korsawe, 2016), i.e.,

$$\texttt{intriangulation}(\boldsymbol{c}, \mathbf{K}) = \begin{cases} 1, & \text{if } \boldsymbol{c} \text{ is within the muscle boundary,} \\ 0, & \text{otherwise.} \end{cases} \tag{6.6}$$

6.3.2 Integrated neuromuscular model in Abaqus/Explicit

The finite element neuro-musculoskeletal model is constructed from two main parts; a file describing the geometry, boundary conditions, material properties and solver settings—the input-deck; and a file describing the constitutive relation of the muscle—the user-material.

The generation of an input-deck or input-file is routine in finite element analyses; whether it describes the simulation of a single element or the simulation of a car crash, the structure of such a file is essentially the same. Typically, the input-deck contains the descriptions required for the solution of the initial boundary value problem (Section 3.1.7). In `Abaqus`, the input-deck contains: geometrical information (e.g., nodal coordinates, element connectivity and fibre orientations), material information (e.g., constitutive parameters), solver settings (e.g., solver type and numerical damping), contact and boundary conditions, and output settings. For further information, see Dassault Systèmes (2017).

What is more interesting, is the generation of the user-material—since the user-material is where the integrated neuromuscular model manifests itself. In other words, it is the user-material which integrates motor-unit activities $\alpha_i(t)$, territory distribution factors $\hat{\kappa}_i(\boldsymbol{\xi})$ and combines them with the continuum-mechanical constitutive relation to compute passive and active stresses at each Gauß point within the musculotendon finite element model.

Hyperelastic user-materials: special considerations

Non-standard constitutive relations are implemented in `Abaqus/Explicit` via a so-called user-material. The user-material is executed at each Gauß point of the finite element model, at each time increment t_n. It must, at the very least, update the stress tensor at the current increment $\boldsymbol{\sigma}(t_{n+1}) = \boldsymbol{\sigma}_{n+1}$, depending on the deformation from the current increment ($\boldsymbol{U}_{n+1}$), which is supplied to it via `Abaqus/Explicit` (cf. Equation 3.87). Alternatively, $\boldsymbol{\sigma}_{n+1}$ can be computed from the increment in displacement $\Delta\boldsymbol{U}$ and the stress from the previous increment $\boldsymbol{\sigma}_n$.

The user-material itself is written in `FORTRAN`. Rather than being called for each Gauß point individually, blocks of Gauß points are passed to the user-material in a vector format (hence the user-material is commonly referred to as a `VUMAT`, i.e., `V`ectorised `U`ser-`MAT`erial). The block size fluctuates between 64 and 128 points and is organised by Gauß point, for example, a block of 64 may be called for the Gauß point with label 1 for 64 distinct elements.

The `VUMAT` expects the constitutive relation in a *local* coordinate-system, which co-rotates with the material. In Chapter 3, all quantities ($\boldsymbol{X}, \boldsymbol{F}, \boldsymbol{R}, \ldots$) were embedded in a three-dimensional Euclidean space with a fixed, global coordinate-system (or basis). Whether a quantity was in the reference or current configuration, the same global basis (described by the basis-vectors $\boldsymbol{g}_i$) was used. Note, the terms "reference basis" $\boldsymbol{E}_i$ and "local basis" $\boldsymbol{e}_i$ are introduced to refer to coordinate-systems in the reference and current configurations, respectively. For the global coordinate-system considered till now, $\boldsymbol{g}_i = \boldsymbol{E}_i = \boldsymbol{e}_i$.

In the local coordinate-system, the local basis rotates with the body, leaving the reference basis behind, i.e., $\boldsymbol{g}_i = \boldsymbol{E}_i \neq \boldsymbol{e}_i$[1]. In the local coordinate-system, $\boldsymbol{E}_i$ is a uniquely oriented local basis system at any point within the body in the reference configuration, which maps to $\boldsymbol{e}_i$ in the current configuration. The mapping to $\boldsymbol{e}_i$ is defined by a pure rotational transformation of $\boldsymbol{E}_i$, i.e.,

$$\boldsymbol{e}_i = \hat{\boldsymbol{R}}\,\boldsymbol{E}_i. \tag{6.7}$$

[1]The global and reference coordinate-systems are not required to be co-linear, i.e., $\boldsymbol{g}_i \neq \boldsymbol{E}_i$ is also possible.

Consider the deformation gradient $\boldsymbol{F}$ (Equation 3.7), rewritten in index notation and with basis systems (in the global coordinate-system) as

$$\boldsymbol{F}^{\mathrm{EE}} = \sum_{i,j=1}^{3} F_{i,j}^{\mathrm{EE}} \, (\mathbf{E}_i \otimes \mathbf{E}_j) \qquad \text{where} \qquad F_{i,j}^{\mathrm{EE}} = \frac{\partial x_i^{\mathrm{E}}}{\partial X_j^{\mathrm{E}}}. \tag{6.8}$$

Notice that since $\boldsymbol{g}_i = \boldsymbol{E}_i = \boldsymbol{e}_i$ are coincident, $\boldsymbol{F}^{\mathrm{EE}} = \boldsymbol{F}$. The superscripts $(\cdot)^{\mathrm{E}}$ and $(\cdot)^{\mathrm{e}}$ specify the basis system of the quantity. For example, x_i^{E} are the deformed coordinates of $\boldsymbol{x}$ in the reference basis. The two-point tensor $\boldsymbol{F}^{\mathrm{EE}}$ has a double superscript to denote that both configurations are described by the same (reference) coordinate-system. In the local coordinate-system, typically $\boldsymbol{g}_i = \boldsymbol{E}_i \neq \boldsymbol{e}_i$ and the deformation gradient is thus

$$\boldsymbol{F} = \sum_{i,j=1}^{3} F_{i,j}^{\mathrm{eE}} \, (\boldsymbol{e}_i \otimes \boldsymbol{E}_j) =: \boldsymbol{F}^{\mathrm{eE}}, \qquad \text{where} \qquad F_{i,j}^{\mathrm{eE}} = \frac{\partial x_i^{\mathrm{e}}}{\partial X_j^{\mathrm{E}}}. \tag{6.9}$$

By combining 6.7, 6.8 and 6.9, it can be shown that

$$F_{i,j}^{\mathrm{EE}} = \hat{R}_{i,k} \, F_{k,j}^{\mathrm{eE}}, \qquad \text{or} \qquad \boldsymbol{F}^{\mathrm{EE}} = \hat{\boldsymbol{R}} \, \boldsymbol{F}^{\mathrm{eE}} \tag{6.10}$$

in tensor notation (derivations and proofs are given in Nolan et al., 2019). Since $\boldsymbol{F}$ is a two-point tensor (cf. Equation 3.66), only one operation is required for the transformation between $\boldsymbol{F}^{\mathrm{EE}}$ and $\boldsymbol{F}^{\mathrm{eE}}$. Generally, for second-order tensors the standard transformation holds, i.e.,

$$\boldsymbol{A}^{\mathrm{EE}} = \hat{\boldsymbol{R}} \, \boldsymbol{A}^{\mathrm{ee}} \hat{\boldsymbol{R}}^{\mathrm{T}}, \tag{6.11}$$

where $\boldsymbol{A}^{\mathrm{ee}}$ is a generic second-order tensor in the local basis system.

In the local coordinate-system, $\hat{\boldsymbol{R}}$ is given by the rotation tensor obtained via the polar decomposition of the deformation gradient (Equation 3.10). Then Equation 6.10 can be written as

$$\boldsymbol{F}^{\mathrm{eE}} = \boldsymbol{R}^{\mathrm{T}} \boldsymbol{F}^{\mathrm{EE}} = \boldsymbol{R}^{\mathrm{T}} \boldsymbol{R} \, \boldsymbol{U} = \boldsymbol{U}, \tag{6.12}$$

recalling that $\boldsymbol{F}^{\mathrm{EE}} = \boldsymbol{F}$. This shows that the deformation gradient equals the right Cauchy-Green stretch tensor in the local coordinate-system. This is intuitive since the rotation of the basis already accounts for the rotation, thus the deformation is based on the stretch alone. Substituting this into the left and right Cauchy-Green deformation tensors (Equations 3.14 and 3.13, respectively), gives

$$\begin{aligned} \boldsymbol{b}^{ee} &= \boldsymbol{F}^{\mathrm{eE}} \, (\boldsymbol{F}^{\mathrm{eE}})^{\mathrm{T}} = \boldsymbol{R}^{\mathrm{T}} \boldsymbol{F}^{\mathrm{EE}} \, (\boldsymbol{F}^{\mathrm{EE}})^{\mathrm{T}} \boldsymbol{R} && (6.13) \\ &= \boldsymbol{R}^{\mathrm{T}} \boldsymbol{R} \, \boldsymbol{U} \, \boldsymbol{U}^{\mathrm{T}} \boldsymbol{R}^{\mathrm{T}} \boldsymbol{R} = \boldsymbol{U} \, \boldsymbol{U}, && (6.14) \end{aligned}$$

and

$$\begin{aligned} \boldsymbol{C}^{\mathrm{EE}} &= (\boldsymbol{F}^{\mathrm{eE}})^{\mathrm{T}} \boldsymbol{F}^{\mathrm{eE}} = (\boldsymbol{F}^{\mathrm{EE}})^{\mathrm{T}} \boldsymbol{R} \, \boldsymbol{R}^{\mathrm{T}} \boldsymbol{F}^{\mathrm{EE}} && (6.15) \\ &= \boldsymbol{U}^{\mathrm{T}} \boldsymbol{R}^{\mathrm{T}} \boldsymbol{R} \, \boldsymbol{U} = \boldsymbol{U} \, \boldsymbol{U}. && (6.16) \end{aligned}$$

Thus in the local coordinate-system,

$$\boldsymbol{b} = \boldsymbol{C}. \tag{6.17}$$

Consider the skeletal muscle fibre orientation $\boldsymbol{a}_0$ in the reference configuration, restating Equation 4.21, in the local coordinate-system, and using Equation 6.12:

$$\lambda\, \boldsymbol{a}^{\mathrm{e}} = \boldsymbol{F}^{\mathrm{eE}}\, \boldsymbol{a}_0^{\mathrm{E}} = \boldsymbol{U}\, \boldsymbol{a}_0^{\mathrm{E}}, \tag{6.18}$$

where $|\boldsymbol{a}| = 1$. Since the local coordinate-system rotates with the material as does the fibre orientation (affine deformation assumption)—the fibre directions in the reference and current configuration remain unchanged in this coordinate-system.

Recall, the velocity gradient $\boldsymbol{l}$ (Equation 3.22), substituting $\boldsymbol{F} = \boldsymbol{R}\boldsymbol{U}$ and using Equation 3.24, $\boldsymbol{l}$ can be written as

$$\boldsymbol{l} = \dot{\boldsymbol{R}}\, \boldsymbol{R}^{\mathrm{T}} + \boldsymbol{R}\dot{\boldsymbol{U}}\, \boldsymbol{U}^{-1}\boldsymbol{R}^{\mathrm{T}}. \tag{6.19}$$

Then the rate of deformation $\boldsymbol{d}$ (Equation 3.22), given by the symmetric part of $\boldsymbol{l}$, becomes

$$\boldsymbol{d}^{\mathrm{EE}} = \frac{1}{2}\, \boldsymbol{R}\, \left(\dot{\boldsymbol{U}}\, \boldsymbol{U}^{-1} + \boldsymbol{U}^{-1}\dot{\boldsymbol{U}}\right) \boldsymbol{R}^{\mathrm{T}} = \boldsymbol{R}\, \boldsymbol{D}^{\mathrm{EE}} \boldsymbol{R}^{\mathrm{T}}, \tag{6.20}$$

where $\boldsymbol{D}^{EE}$ is called the rotated rate of deformation tensor. Note the superscripts are selectively included to emphasise the basis. In the local coordinate-system, the mapping of the rate of deformation $\boldsymbol{d}$ (Equation 6.11) gives

$$\boldsymbol{d}^{\mathrm{ee}} = \boldsymbol{R}^{\mathrm{T}} \boldsymbol{d}^{\mathrm{EE}} \boldsymbol{R}. \tag{6.21}$$

Comparison of Equations 6.20 and 6.21 shows that

$$\boldsymbol{D}^{\mathrm{EE}} = \boldsymbol{d}^{\mathrm{ee}}. \tag{6.22}$$

That is, the rate of deformation tensor with respect to a local basis (rotating with the body) equals the rotated rate of deformation with respect to a global basis (fixed in the reference configuration), which is an intuitive result.

The Cauchy stress $\boldsymbol{\sigma}$ in the local coordinate-system $\boldsymbol{\sigma}^{\mathrm{ee}}$ is given by the mapping

$$\boldsymbol{\sigma}^{\mathrm{ee}} = \boldsymbol{R}^{\mathrm{T}} \boldsymbol{\sigma}^{\mathrm{EE}} \boldsymbol{R} = J^{-1} \boldsymbol{U}\, \boldsymbol{S}^{\mathrm{EE}}\, \boldsymbol{U}, \tag{6.23}$$

where the right most expression is obtained using Equations 3.10 and 3.33_2. Lastly, the stress power (Equation 3.55) in the local coordinate-system is given by making the appropriate substitutions (Equations 6.20 and 6.21) in Equation 3.55:

$$\mathcal{P}_{\mathrm{def}}(t) = \int_{\mathcal{B}_0} J\boldsymbol{\sigma}^{\mathrm{EE}} : \boldsymbol{d}^{\mathrm{EE}}\, \mathrm{d}V = \int_{\mathcal{B}_0} J\boldsymbol{R}\, \boldsymbol{\sigma}^{\mathrm{ee}} \boldsymbol{R}^{\mathrm{T}} : \boldsymbol{R}\, \boldsymbol{d}^{\mathrm{ee}} \boldsymbol{R}^{\mathrm{T}} \mathrm{d}V \tag{6.24}$$

$$= \int_{\mathcal{B}_0} J\boldsymbol{\sigma}^{\mathrm{ee}} : \boldsymbol{d}^{\mathrm{ee}}\, \mathrm{d}V, \tag{6.25}$$

since $\boldsymbol{R}^{\mathrm{T}}\boldsymbol{R} = \boldsymbol{I}$. Via Equation 3.60, the integrand in the above equation is the internal energy per unit volume, i.e., strain-energy. The strain-energy is used in simulation analyses to ensure physical plausibility of the system, in that the artificial or stabilisation energies are not large compared to the physical (strain-energy) of the system.

Stress update with heterogeneous activity

The overall stress response of the musculotendon complex, at a given Gauß point $\boldsymbol{\xi}_p$, can then be updated at increment $n+1$ by combining Equations 3.87 and 6.23, i.e., (dropping the superscripts that signify the coordinate-system)

$$\boldsymbol{\sigma}^{\text{MTC}}_{n+1}(\boldsymbol{\xi}_p) = J^{-1}\boldsymbol{U}_{n+1}(\boldsymbol{\xi}_p)\, \boldsymbol{S}^{\text{MTC}}_{n+1}(\boldsymbol{\xi}_p)\, \boldsymbol{U}_{n+1}(\boldsymbol{\xi}_p), \tag{6.26}$$

recalling that $\boldsymbol{U}_{n+1}$ is computed by an explicit central difference scheme (Equation 3.85). The second Piola-Kirchhoff stress update is given by making the appropriate substitutions in Equation 4.45, i.e.,

$$\begin{aligned}\boldsymbol{S}^{\text{MTC}}_{n+1} &= 2\left(c^{\text{MTC}}_1 + I_{1,n+1}\, c^{\text{MTC}}_2\right)\boldsymbol{I} - 2c^{\text{MTC}}_2\, \boldsymbol{U}^2_{n+1} + 2c\, J_{n+1}(J_{n+1}-1)\, \boldsymbol{U}^{-2}_{n+1} - d\, \boldsymbol{U}^{-2}_{n+1} \\ &+ \left(2\, c^{\text{MTC}}_3\, c^{\text{MTC}}_4\, (I_{4,n+1}-1)^{c^{\text{MTC}}_4-1} + 2\, c^{\text{MTC}}_5\, c^{\text{MTC}}_6\, (I_{4,n+1}-1)^{c^{\text{MTC}}_6-1}\right)\boldsymbol{M} \\ &+ \left(\frac{1}{I_{4,n+1}}\, P_{\max}\, \alpha_{\text{M},n+1}\, f_{\text{l}}(\lambda_{n+1})\right)\boldsymbol{M},\end{aligned} \tag{6.27}$$

where the dependence on the Gauß point $\boldsymbol{\xi}_p$ has been dropped for clarity. The invariants are updated by:

$$\begin{aligned} I_{1,n+1} &= \text{tr}\, \boldsymbol{U}^2_{n+1}, & I_{2,n+1} &= 1/2\, \left[(\text{tr}\, \boldsymbol{U}^2_{n+1})^2 - \text{tr}\, (\boldsymbol{U}^4_{n+1})\right], \\ I_{3,n+1} &= \det \boldsymbol{U}^2_{n+1} = J^2_{n+1}, & I_{4,n+1} &= \boldsymbol{a}_0 \cdot \boldsymbol{U}^2_{n+1}\, \boldsymbol{a}_0 = \lambda^2_{n+1}. \end{aligned} \tag{6.28}$$

The activity in Equation 6.27, $\alpha_{\text{M},n+1}(\boldsymbol{\xi_p})$, is computed per increment, at the Gauß point locations. The activities of the motor-unit pool are stored within the user-material via a matrix, where each column represents the activity of motor-unit i ($i = 1, \ldots, N_{\text{MU}}$) i.e.,

$$\mathbf{a}(q,i) = \begin{bmatrix} \tilde{t}_1 & \alpha_1(\tilde{t}_1) & \ldots & \alpha_{N_{\text{MU}}}(\tilde{t}_1) \\ \tilde{t}_2 & \alpha_1(\tilde{t}_2) & \ldots & \alpha_{N_{\text{MU}}}(\tilde{t}_2) \\ \vdots & \vdots & & \vdots \\ \tilde{t}_{\text{end}} & \alpha_1(\tilde{t}_{\text{end}}) & \ldots & \alpha_{N_{\text{MU}}}(\tilde{t}_{\text{end}}) \end{bmatrix}, \tag{6.29}$$

where $\tilde{t}$ typically do not correspond with the finite element solver time steps t_n and linear interpolation is used to account for any mismatches.

Similarly, the territory distribution factors at the Gauß points $\boldsymbol{\xi}_{0,p}$ ($p = 1, \ldots, N_{\text{GP}}$) are stored in a matrix $\mathbf{k_m}$, i.e.,

$$\mathbf{k_m}(\texttt{ID}^{\text{GP}}_p, i) = \begin{bmatrix} \texttt{ID}^{\text{GP}}_1 & \hat{\kappa}_1(\boldsymbol{\xi}_1) & \ldots & \hat{\kappa}_{N_{\text{MU}}}(\boldsymbol{\xi}_1) \\ \texttt{ID}^{\text{GP}}_2 & \hat{\kappa}_1(\boldsymbol{\xi}_2) & \ldots & \hat{\kappa}_{N_{\text{MU}}}(\boldsymbol{\xi}_2) \\ \vdots & \vdots & & \vdots \\ \texttt{ID}^{\text{GP}}_{N_{\text{GP}}} & \hat{\kappa}_1(\boldsymbol{\xi}_{N_{\text{GP}}}) & \ldots & \hat{\kappa}_{N_{\text{MU}}}(\boldsymbol{\xi}_{N_{\text{GP}}}) \end{bmatrix}, \tag{6.30}$$

where $\texttt{ID}^{\text{GP}}_p$ is the ID of Gauß point p. Each column of $\mathbf{k_m}$ is the distribution factor of motor-unit territory i within the muscle geometry. The rows of $\mathbf{k_m}$ represent the total motor-unit distribution at a Gauß point and (must) sum to unity (cf. Equation 6.2). Note that the above matrix is largely sparse, e.g., for smaller units non-zero distribution factors appear only at a few

Gauß points. Therefore, compression techniques were used to reduce the size of the matrix.

At a Gauß point p and time increment t_{n+1}, the muscle activity is computed in the VUMAT via

$$\alpha_{\mathrm{M},n+1}(\mathtt{ID}_p^{\mathrm{GP}}) = \alpha_{\mathrm{M}}(t_{n+1}, \mathtt{ID}_p^{\mathrm{GP}}) = \sum_{i=1}^{N_{\mathrm{MU}}} \mathbf{a}(n+1, i)\ \mathbf{k_m}(\mathtt{ID}_p^{\mathrm{GP}}, i), \tag{6.31}$$

assuming that the rows of **a** correspond to the solver time increments. At this stage, all quantities required for the stress update are known, including the heterogeneous activity computed via individual motor-unit activities and distributions. The stress update is then used to compute the local accelerations in the muscle geometry at the next time step and the solution process carries on (Section 3.2.3).

6.3.3 Incompressibility and element types

A nearly-incompressible formulation is used to model the isotropic behaviour of the musculotendon complex (Section 4.2.1), where the penalty-parameter c controls the degree of incompressibility. As $c \to \infty$, the behaviour approaches pure incompressibility. As the material becomes more incompressible, the stress propagates across the element with ever increasing speed and thus reduces the critical time step of the explicit finite element solver (Section 3.2.3). Smaller time steps lead to longer computational times. Thus, the c must be chosen appropriately to balance material behaviour accuracy and computational speed. In addition to this, certain element types are simply not well-suited for (nearly) incompressible behaviour, these should be identified and excluded.

Methods

The incompressible analyses were performed under uniaxial loading, allowing the comparison to a purely incompressible analytic-solution. A cubic geometry with $L_{\mathrm{x}} = L_{\mathrm{y}} = L_{\mathrm{z}} = L = 1\,\mathrm{mm}$ was used and meshed with a single element for the hexahedral element types and 12 elements for the tetrahedral element types. Fibre orientation was aligned with the global (vertical) y-axis ($2-$direction) and the muscle was constrained on the faces: $u_{\mathrm{x}}(x = 0, y, z) = 0$, $u_{\mathrm{y}}(x, y = 0, z) = 0$ and $u_{\mathrm{z}}(x, y, z = 0) = 0$. The muscle was initially displaced vertically downwards by $u_{\mathrm{y}} = 0.4\,\mathrm{mm}$ and then upwards by $u_{\mathrm{y}} = 0.8\,\mathrm{mm}$. The material model as described in Chapter 4 is used with material parameters given in Table 4.1.

The penalty-parameter c was increased and the forces obtained from the simulations were compared to the analytical solution. The analytical response for the purely incompressible behaviour was computed by Equations 4.59 and 4.60 (direction 2 is now the in-fibre direction) and denoted as σ_2, and compared to the stress responses from the simulations $\tilde{\sigma}_2$ via

$$\sigma_{\mathrm{err}} = \sqrt{\sum_{n=1}^{T} \frac{\left(\tilde{\sigma}_{2,n} - \sigma_{2,n}\right)^2}{T}}, \tag{6.32}$$

where σ_{err} is the root mean squared error (RMSE), and $n = 1, \ldots, T$ are the increments. The RMSE σ_{err} was computed for each element type (Table 6.1) and for a range of penalty-parameters $c = [0, 10, 25, 50, 75, 100, 250, 500]$. The computation time for each simulation was also recorded.

Results

Across all element types, on average, increasing the penalty-parameter c from 0 to 500 reduced the RMSE from 1.2×10^{-2} MPa to 2.2×10^{-6} MPa and increased the computational time by a factor of 18 (Figure 6.4b). The degree of compressibility can be quantified by the change in the Jacobian J (Equation 3.42), where any deviation from $J = 1$ reflects (undesired) volumetric changes. The values of the Jacobian at peak compression $\lambda = 0.6$ were $J = [0.5071, 0.9974, 0.9995, 0.9999]$ for $c = [0, 10, 50, 100]$, respectively. Apart from C3D8I, all elements showed convergent behaviour with increasing c.

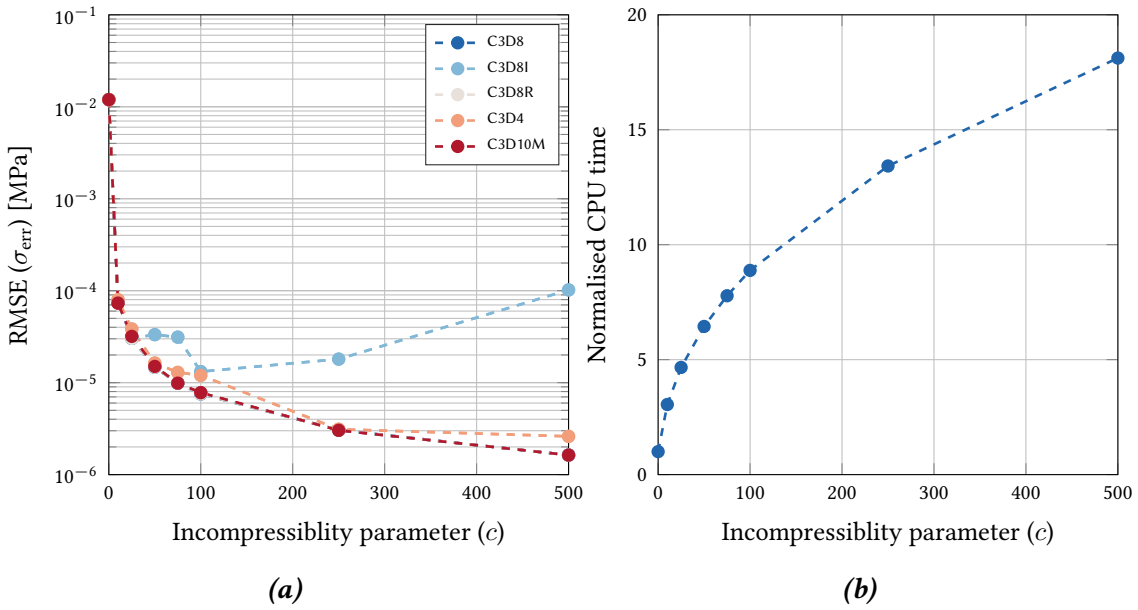

Figure 6.4: *Accuracy of incompressible behaviour and effect on computational time. (b) Normalised to computational time at $c = 0$.*

6.3.4 Convergence of element types

There are a plethora of element types in the finite element method, each suited to its own niche application. At present, an element is required that can undergo large deformation with nearly incompressible behaviour. The following is restricted to the (three-dimensional) element library provided by `Abaqus/Explicit`; classified into hexahedral (C3D8, C3D8I, C3D8R) and tetrahedral (C3D4, C3D10M) (Table 6.1). The C3D8 and C3D8I elements are fully integrated with 8 Gauß points, with the latter augmented with incompatible modes. Elements with

Table 6.1: *Element types available in `Abaqus/Explicit` with IP: Gauß points.*

	C3D8	C3D8I	C3D8R	C3D4	C3D10M
Shape	hexahedral	hexahedral	hexahedral	tetrahedral	tetrahedral
Nodes	8	8	8	4	10
IPs	8	8	1	1	4

incompatible modes have additional internal degrees of freedom with *"[t]he primary effect ... to eliminate the so-called parasitic shear stresses that are observed in regular displacement elements if they are loaded in bending"* (Dassault Systèmes, 2017).

Both the C3D8R and C3D4 element types have 1 Gauß point, the former subjected to (selective) reduced integration and augmented with hourglass control. Lastly, the C3D10M element is a 10-node tetrahedral element with 4 Gauß points, employing a modified formulation[2] including hourglass control.

Methods

To judge the convergence behaviour of the elements, an idealised geometry of the musculotendon complex was generated for each element type. The models were subjected to passive and active deformations and repeated for various mesh refinements. The predicted deformations of the models were compared to each other, i.e., an analytical solution was not computed given the complex loading conditions.

A cuboid geometry with $L_\mathrm{x} = L_\mathrm{z} = 2\,\mathrm{mm}$, $L_\mathrm{y} = 10\,\mathrm{mm}$ was used (Figure 6.5). The tendon was defined by setting $\gamma_\mathrm{M} = 0$ (Equation 4.47) within regions 3 mm from either ends of the muscle. The fibre orientation was aligned with the global y-axis and the element was constrained on the faces: $u_\mathrm{y}(x, y = 0, z) = 0$ and $u_\mathrm{z}(x, y, z = 0) = 0$. The material model as described in Chapter 4 is used with material parameters given in Table 4.1.

For the passive scenario, a combined tensile and shear force was applied to the rectangular musculotendon complex. A pressure load was applied to the top face $(x, y = L_\mathrm{y}, z)$ in the y-direction $p_\mathrm{y} = 2 \times 10^{-2}\,\mathrm{MPa}$ and simultaneously in the x-direction $p_\mathrm{x} = 1 \times 10^{-4}\,\mathrm{MPa}$.

For the active scenario, the top face was unconstrained, thus allowing the muscle to contract freely. The activity was linearly ramped between 0 and 1, and was applied homogeneously throughout the muscle, i.e., the muscle consisted of a single motor-unit.

For both scenarios, the tip-displacement $u_\mathrm{x}^\mathrm{tip}$ and $u_\mathrm{y}^\mathrm{tip}$ was measured at the (unconstrained) top, corner node $(x = L_\mathrm{x}, y = L_\mathrm{y}, z = L_\mathrm{z})$. The mesh was refined to produce Gauß points between approximately 10×10^1 to 10×10^5 across all element types.

Results

For the passive scenario, the tip-displacements $u_\mathrm{x}^\mathrm{tip}$ and $u_\mathrm{y}^\mathrm{tip}$ are plotted against the number of Gauß points for each element type in Figures 6.6a and 6.6b, respectively. Apart from C3D4, all elements showed convergent tip-displacement with mesh refinement. The best rate of

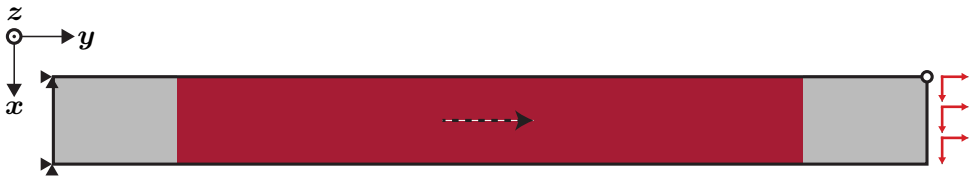

Figure 6.5: *Idealised geometry for element type convergence analysis. The muscle and tendon regions are shown in maroon and grey, respectively. The Dirichlet and Neumann boundary conditions are shown on the left and right, respectively. The node used for tip-displacement is marked on the top right.*

[2]The modified formulation is a trade-secret and thus information is not given on its exact formulation.

convergence were exhibited by the C3D10M element, followed by C3D8I, C3D8R, and C3D8 elements.

The active scenario tip-displacements are shown in Figures 6.7a and 6.7b. The tip-displacements were more chaotic than the passive case, given the dynamic nature of the deformation, i.e., unconstrained contraction. Nonetheless, they did show some convergence. Again, C3D4 performed the worst, with the convergence behaviour for the remaining elements following a similar trend as in the passive case: (best) C3D10M, C3D8I, C3D8R to C3D8 (worse).

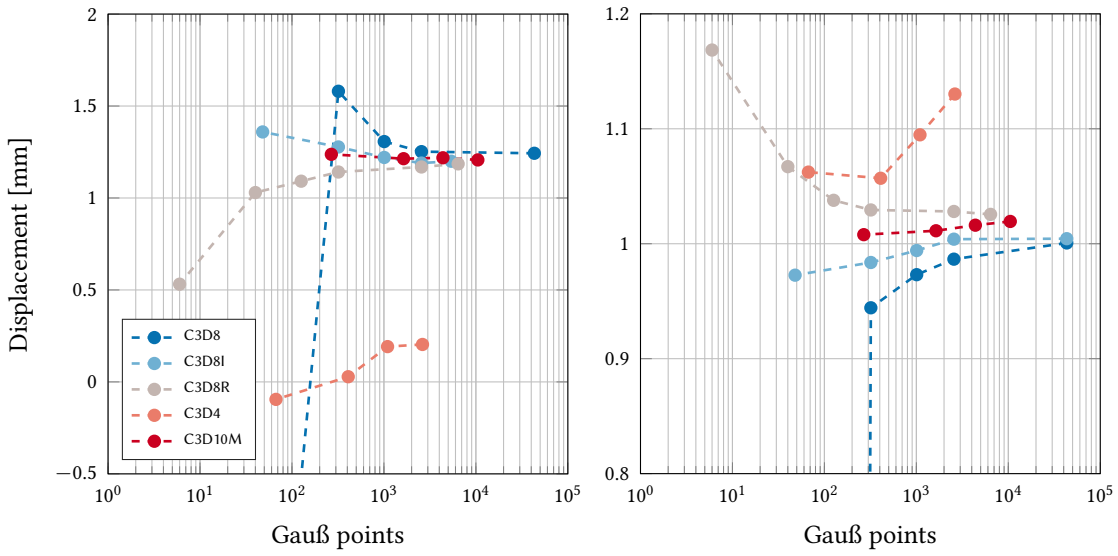

(a) u_x^{tip}. ***(b)*** u_y^{tip}.

Figure 6.6: *Convergence of different element types under mesh refinement—passive behaviour.*

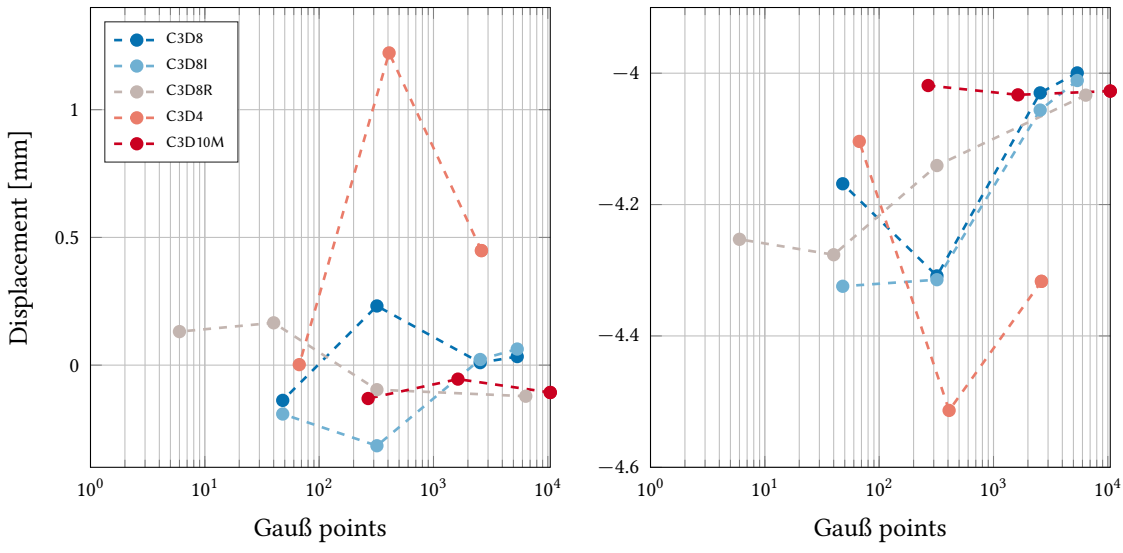

(a) u_x^{tip}. ***(b)*** u_y^{tip}.

Figure 6.7: *Convergence of different element types under mesh refinement—active behaviour.*

6.4 Demonstration of the Integrated Model

The entire workflow to arrive at a continuum-mechanical skeletal muscle constitutive relation that takes motor-unit territories (MUTs) and activities into account is summarised in the following for a motor-unit pool with index $i = 1, \ldots, N_{\text{MU}}$, One pillar of the computation involves the computation of the individual motor-unit activities, i.e.,

$$\underbrace{E(t),\ t = [0, t_{\text{end}}]}_{\text{excitatory drive}} \rightarrow \underbrace{\mathcal{D}_i \ \mid \ E(t) > R_i}_{\substack{\text{recruitment} \\ \text{model}}} \rightarrow \underbrace{r(\mathcal{D}_i, \ldots) \rightarrow A_{2,i}(r(\mathcal{D}_i), \ldots) \rightarrow \alpha_i(t)}_{\text{excitation-contraction coupling model}} \rightarrow \mathbf{a}. \quad (6.33)$$

The second pillar involves the computation of the motor-unit spatial distributions, i.e.,

$$\underbrace{\mathcal{B}_0,\ \boldsymbol{a}_0(\boldsymbol{Y})}_{\substack{\text{muscle} \\ \text{architecture}}} \rightarrow \quad \underbrace{\{\mathcal{S}, \mathcal{F}\}}_{\substack{\text{reconstructed} \\ \text{microstructure}}} \quad \rightarrow \underbrace{\{\tilde{\mathcal{S}}, \tilde{\mathcal{F}}\} \rightarrow \kappa_i(\boldsymbol{X}^{\text{micro}})}_{\text{discrete MUTs}} \rightarrow \quad \underbrace{\hat{\kappa}_i(\boldsymbol{\xi})}_{\substack{\text{homogenised} \\ \text{MUTs}}} \quad \rightarrow \mathbf{k_m}. \quad (6.34)$$

Lastly, these are integrated into a spatio-temporal weighted activity, which is used to scale the active stress in the overall musculotendon complex stress response. This is done in the user-material:

$$\alpha_{\text{M}}(t, \boldsymbol{\xi}) = f(\mathbf{a}, \mathbf{k_m}) \rightarrow \boldsymbol{S}_{\text{active}}(t, \boldsymbol{\xi}) \rightarrow \boldsymbol{S}^{\text{MTC}}(t, \boldsymbol{\xi}). \quad (6.35)$$

The integrated neuromuscular model is demonstrated with an idealised geometry. A ramped excitatory drive is supplied to the musculotendon complex to recruit all motor-units sequentially and produce a maximal contraction. The maximal contraction is compared to a status-quo approach; where the same motor-unit activities are used to compute an equivalent, spatially constant activity parameter that is applied uniformly throughout the muscle. Differences between the two models are quantified by comparing the intramuscular pressure and tendon-force.

6.4.1 Methods

The geometry used for the distribution parameter investigation (Section 5.3.5) was used here also, i.e., a cuboid geometry with $L_{\text{x}} = 200$ mm and $L_{\text{y}} = L_{\text{z}} = 40$ mm populated with approximately 12,000 fibre-scaffolds. Additionally, tendons were defined by setting $\gamma_{\text{M}} = 0$ (Equation 4.47) within regions 40 mm from either ends of the muscle, and muscle fibre orientation was aligned with the global x-axis. The tendinous ends were constrained, i.e., $u_{\text{y}}(x = 0, y, z) = 0$ and $u_{\text{z}}(x = L_{\text{x}}, y, z) = 0$.

Fibre-scaffolds were innervated by 100 motor-units, with innervation-ratios following an exponential distribution, detailed previously in Section 5.3.5 and shown in Figure 5.3a. The motor-units were recruited by a linearly increasing excitatory drive $E(t)$, which elicited a maximum ramped contraction over 1 s. The remaining model components were specified as:

1. Motor-neuron-pool parameters in Table 5.1.
2. Twitch parameters in Table 5.2, and from Campbell et al. (1993), Aliev et al. (1996) and Campbell et al. (2001).
3. Distribution parameters specified by ID 23 in Table 5.4 with shape parameters $\lambda_1 = \lambda_2 = \lambda_3 = 1$.

4. Musculotendon material parameters in Table 4.1.
5. Numerical parameters $c = 10$ and element type C3DI, with y-z plane element dimensions 2.5×2.5 mm with a x-direction dimension of 5 mm.

The excitatory drive, together with items 1 and 2 from the list above yields the individual motor-unit activities $\alpha_i(t)$ ($i = 1, \ldots, N_{\text{MU}}$). Discrete motor-unit territory distributions $\kappa_i(\boldsymbol{X}^{\text{micro}})$ are given by the distribution specified by item 3 in the list above. Applying statistical averaging at the Gauß points $\boldsymbol{\xi}_{0,p}$ ($p = 1, \ldots, N_{\text{GP}}$) yields the homogenised motor-unit distribution parameters $\hat{\kappa}_i(\boldsymbol{\xi}_{0,p})$. The total muscle fraction of each unit within the muscle is computed by summing the motor-unit distribution parameter over the entire muscle, i.e., at all Gauß points,

$$K_i = \sum_{p=1}^{N_{\text{GP}}} \hat{\kappa}_i(\boldsymbol{\xi}_{0,p}). \tag{6.36}$$

Then, the equivalent constant activation $\alpha_{\text{const}}(t)$ can be computed by weighting motor-unit activities by the total muscle fraction, i.e.,

$$\alpha_{\text{const}}(t) = \sum_{i=1}^{N_{\text{MU}}} \bar{K}_i \, \alpha_i(t), \tag{6.37}$$

where $\bar{K}_i$ is computed by dividing K_i by the sum of all total muscle fractions. As a side note, the above expression is similar to Equation 5.20, but now the volumetric distribution, instead of the innervation-ratio, acts as the weighting factor.

6.4.2 Results

The homogenisation process is qualitatively analysed. The fibre distributions of motor-units 61–80 (of 100, labelled from smallest to largest) were combined and plotted in the cross-section of the musculotendon complex model (Figure 6.8). The discrete motor-unit distribution factor κ_{61-80} is shown in Figure 6.8b. The homogenised distribution factor $\hat{\kappa}_{61-80}$ is shown in Figures 6.8c and 6.8d for a medium and coarse mesh, respectively. Note that the visualisation of field-outputs in `Abaqus/CAE` occurs at the nodes, which averages contributions from neighbouring Gauß points.

The reaction force magnitude was taken as the sum of nodal forces at a fixed tendon end over the ramped maximal isometric contraction. They are denoted $F^{\text{MU}}(t)$ and $F^{\text{const}}(t)$ (in N) for the motor-unit driven and constant-activity models, respectively. The relative force magnitude was then computed by

$$\bar{F}(t) = \frac{F^{\text{MU}}(t)}{F^{\text{const}}(t)}, \tag{6.38}$$

and is plotted against the spatially constant activity $\alpha_{\text{const}}(t)$ in Figure 6.9. The relative force difference was minuscule, with an average difference of 2 % seen at $\alpha_{\text{const}}(t) < 10$ %, and which approached 0 % beyond approximately $\alpha_{\text{const}}(t) > 30$ % (Figure 6.9a).

A snapshot of the stresses along the fibre directions σ_{11} (in Voigt notation) at $t = 0.42$ s ($\alpha_{\text{const}} \approx 50$ %) within the muscle cross-section for the two models is shown in Figure 6.10. The differences in stress output were drastic. For the motor-unit model, those motor-units which are active experience high stresses, whereas the inactive motor-units remain passive. In the

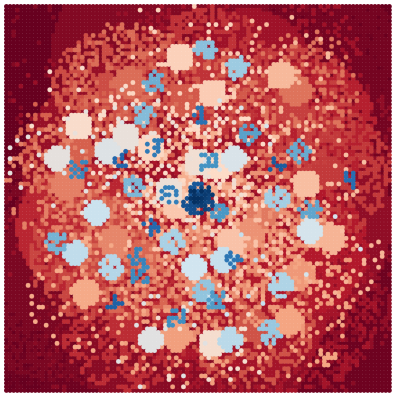

(a) *Fibre distribution of all units.*

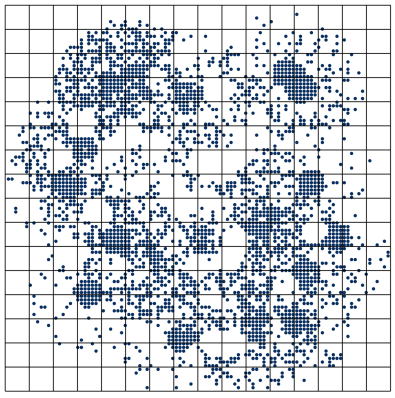

(b) *Fibre distribution of units 61-80.*

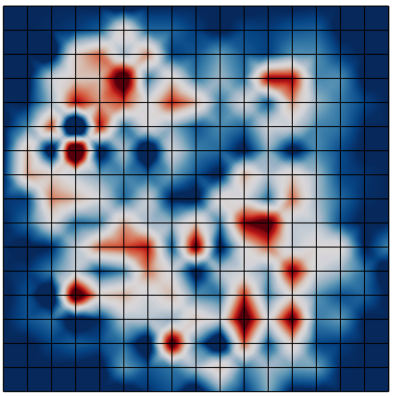

(c) *Homogenised distr. FE mesh I.*

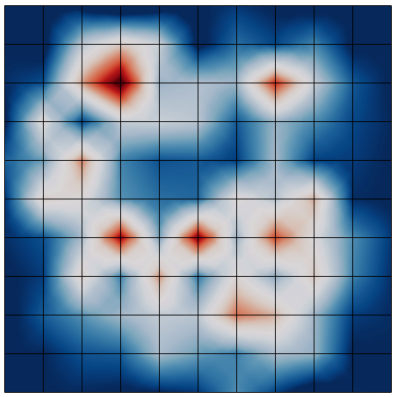

(d) *Homogenised distr. FE mesh II.*

Figure 6.8: *Homogenisation of motor-unit territories at different mesh sizes. (a) Shows all* 100 *motor-unit territories, colour coded from smallest: dark blue, to largest: maroon. (b)-(d) Motor-unit territories 61-80 are shown: (b) discrete territory distribution* κ_{61-80}*, (c) & (d) homogenised distributions* $\hat{\kappa}_{61-80}$*.*

traditional model, a spatially constant activity yields a (near) constant stress throughout the muscle cross-section.

Quantitatively, this can be seen in the plot of intramuscular pressure in Figure 6.9b. The intramuscular pressure, taken as the hydrostatic stress σ_{IMP} (in MPa, Equation 3.37), is recorded at each Gauß point within the muscle at $t = 0.42\,\text{s}$, i.e., $\sigma_{\text{IMP}}(0.42\,\text{s}, \boldsymbol{\xi}_p)$ $(p = 1, \ldots, N_{\text{GP}})$. Simultaneously, the activity is also recorded: $\alpha_{\text{M}}(0.42\,\text{s}, \boldsymbol{\xi}_p)$ for the motor-unit model and $\alpha_{\text{const}}(0.42\,\text{s}, \boldsymbol{\xi}_p) = \alpha_{\text{const}}(0.42\,\text{s})$ for the constant-activity model. The pressures and activities are then plotted against each other.

For the motor-unit model: the spread of $\sigma_{\text{IMP}}(0.42\,\text{s}, \boldsymbol{\xi}_p)$ and $\alpha_{\text{M}}(0.42\,\text{s}, \boldsymbol{\xi}_p)$ arises due to the various motor-units at differing states of contraction, and shows a statistically significant $(p < 1 \times 10^{-6})$ linear correlation, with a Spearman rank coefficient of $r = -1.0$. For the spatially constant-activity model: since $\alpha_{\text{const}}(0.42\,\text{s})$ is constant, the pressures reflect this and all values are concentrated on a single point.

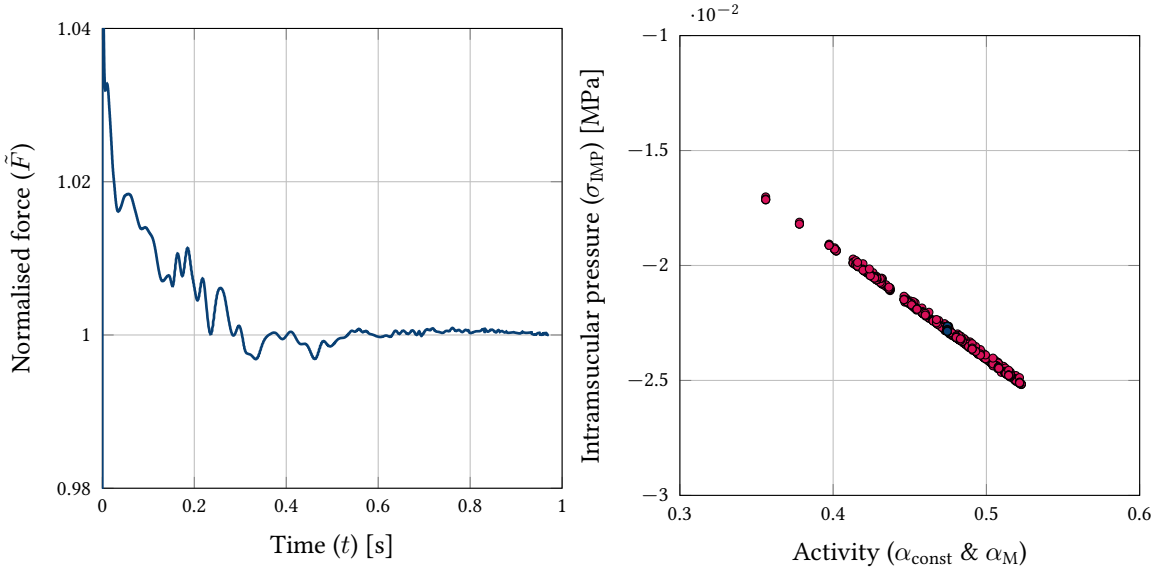

(a) *Tendon force.*

(b) *Pressure at $t = 0.42$ s.*

Figure 6.9: *Comparison of motor-output from motor-unit driven and constant-activity models. (a) Comparison of force over the duration of the simulation. (b) Snapshot of pressure against activity throughout the muscle.*

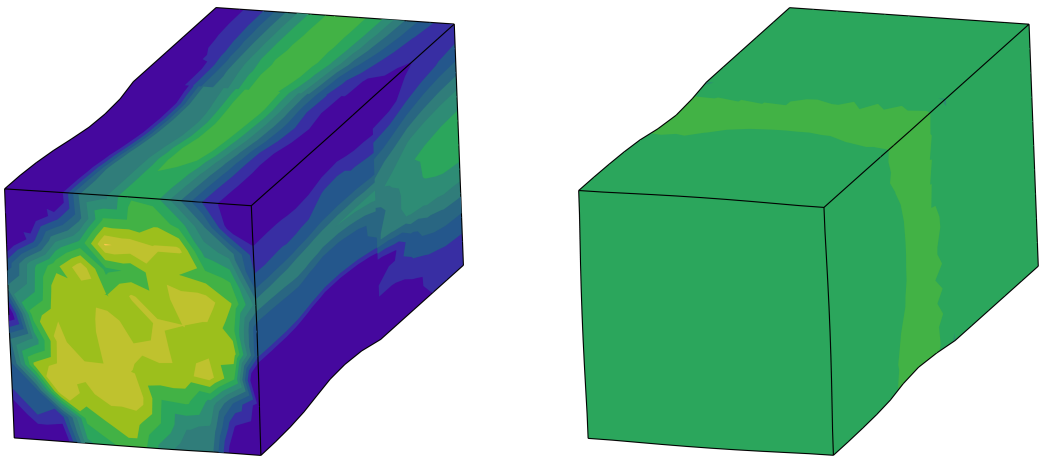

(a) *Heterogeneous activity.*

(b) *Constant activity.*

Figure 6.10: *Comparison of stress (σ_{11}) distribution between motor-unit driven and constant-activity models at $t = 0.42$ s scaled between 0 MPa: blue and 0.2 MPa: green.*

6.5 Discussion

First, the modelling limitations are discussed, including instantaneous action-potential propagation and uniform fibre radii (Section 6.5.1). Second, the drawbacks imposed by the unidirectional coupling of activity to the finite element musculoskeletal simulation are covered (Section 6.5.1). The later part deals with the numerical behaviour of the element types, including incompressibility behaviour (Section 6.5.3) and element choice (Section 6.5.2). Lastly, the demonstrator simulation and comparison to the traditional modelling approach is discussed (Section 6.5.4).

6.5.1 Modelling limitations

Errors introduced by homogenisation assumptions

By assuming that action-potential propagation (with velocity v^{AP}) occurs instantaneously along the fibre, certain errors were introduced in the mechanical response of the muscle model. These errors were quantified by using a physiologically detailed multiscale and multi-physics skeletal muscle model to simulate a contraction with $v^{\text{AP}} = 4.2\,\text{m/s}$ and $v^{\text{AP}}_{\infty} \to \infty$, and comparing the forces arising at the tendon: $F_{\text{AP}}(t)$ and $F_{\infty}(t)$, respectively.

Following a stimulus at the neuromuscular-junction of the muscle fibre, the action-potential propagates outwards with a certain speed v^{AP} and causes tension production via excitation-contraction coupling. The local fibre tension is then transmitted and summed at the tendons. The rate at which force accumulates at the tendons (time-to-force) is influenced by v^{AP}. Obviously as $v^{\text{AP}} \to \infty$, force accumulation at the tendon occurs more rapidly following a stimulus and indeed lower time-to-force values were observed for $F_{\infty}(t)$.

On average, the difference in time-to-force between the models (16.8 ms) was smaller than the time taken for the action-potential to propagate towards the fibre ends (34 ms). This implies that the musculotendon complex generates force rapidly following the activation of sarcomeres at the neuromuscular-junction and therefore the impact on electromechanical delay of instantaneous action-potential propagation cannot be computed simply via muscle geometry and conduction velocity. Furthermore, $F_{\infty}(t)$ was less steady, in that the influence of individual motor-unit twitch forces were more clearly visible in the global force response. Again, this is intuitive since the twitch forces are not "temporally smoothed" via the propagating action-potential, instead being instantly transmitted to the muscle-tendon interface.

The time-to-force for 1 % maximal force, i.e., electromechanical delay, was computed as 18.8 ms and 8.2 ms for $F_{\text{AP}}(t)$ and $F_{\infty}(t)$, respectively. Time-to-force and electromechanical delay are influenced by several factors such as the relative and overall musculotendon complex length, conduction velocity, mechanical properties of the musculotendon complex and the twitch properties (e.g. Cavanagh et al., 1979; Hopkins et al., 2007; Nordez et al., 2009; Schmid et al., 2019). These factors would also increase the discrepancy in time-to-force when instantaneous action-potential propagation is assumed. For example, Schmid et al. (2019) showed that a low muscle-to-tendon ratio, long fibres, stiff muscles and soft tendons act to (individually) increase electromechanical delay (by approximately 20 ms). These results in combination with those currently presented, show that if the temporal resolution of interest is above approximately 500 ms, neglecting action-potential propagation has a negligible effect on the predicted mechanical response of muscle contraction.

Homogeneous fibre properties

The homogenisation of the discrete motor-unit (fibre) microstructure assumes that each fibre has an equal diameter. In reality, type-I and -II fibres may differ in size, for example, Polgar et al. (1973) reported human type-II fibres were (statistically significantly) larger than type-I fibres in 30% of measurement sites; the opposite was true only for 2% of the sites. Furthermore, mammalian fibre sizes may vary *within* fibre-types and have been shown to be normally distributed about a mean diameter (e.g. Hegarty et al., 1971).

In addition to idealising muscle fibre cross-sectional area, the contractile properties of the fibres may also be oversimplified. Factors which govern the peak force of a motor-unit in the current model are: activation, specific tension and innervation-ratio. The activity of each motor-unit is normalised (Equation 5.14) between $[0, 1]$ and the specific tension is not specified per fibre, but rather by the specific-strength of the whole muscle, i.e., P_{max}, and is constant over the entire muscle (Equation 4.38). Innervation-ratio varies between motor-units, determining the volume that a motor-unit occupies in the muscle. Therefore, neglecting geometrical effects and assuming full activation of all motor-units, differences in peak force between motor-units depend solely on innervation-ratio.

Experimental measurement of individual motor-unit anatomy and function by Kanda et al. (1992) on the rat's gastrocnemius showed that innervation-ratio was indeed the dominant factor in predicting peak motor-unit force. However, *within* a motor-unit type, the fibre diameter and specific tension also played a role in predicting tension output. They showed that mean muscle fibre cross-sectional area increased proportionally with innervation-ratio (Figure 6.11a), meaning that determining motor-unit size by innervation-ratio alone may lead to underestimations of its total volume. Second, as innervation-ratio increased, so did the *normalised* specific tension, that is, the motor-unit force over the territory area (Figure 6.11b). Therefore, not only do larger motor-units occupy more space, but they produce a greater force *per unit of area.*

In the current model, both of these factors are neglected (Figure 6.11). In both figures, the dotted line indicates the behaviour of the current model: fibre area and specific tension remain flat across all motor-units. This means that the current model underpredicts not only the volume occupied by larger motor-units but also their specific-strength. The differences in specific-strength would lead to more heterogeneous motor-output, for example, the intramuscular pressures would show a wider spread since some regions would contract with more force than others (for the same level of activity). This may weaken the strongly linear relationship observed between activity and intramuscular pressure. In short, taking such properties into account would only enhance the functional heterogeneity of the muscle models. Methods to compensate for this are discussed as part of the limitations and proposed solutions of the thesis (Section 10.1).

Pre-computed neural activity

Pre-computing neural activity may be computationally efficient, but it prevents any feedback from the muscle contraction from occurring. For example, regional variations in intramuscular pressure within the muscle may influence blood flow (Sejersted et al., 1995, and references there in) & (Sjøgaard et al., 1988) which has been associated with fatigue (e.g. Murthy et al., 2001). And neural adaptations to the fatiguing muscle include a decrease in α-motor-neuron firing rate, i.e., the so-called "muscle wisdom hypothesis" (Marsden et al., 1983) (cited in Garland et al.

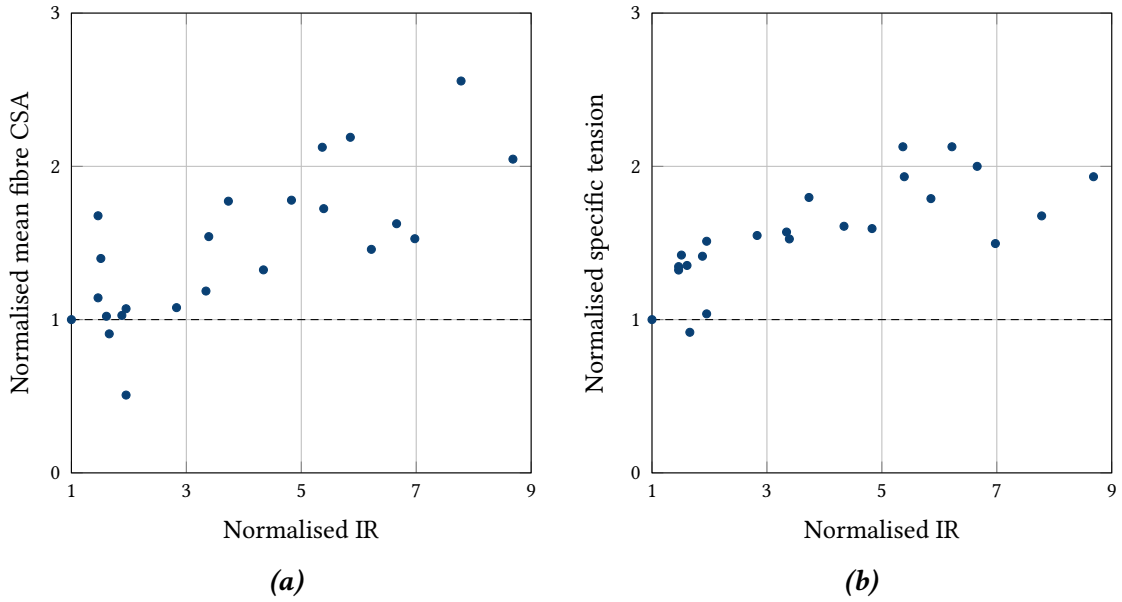

Figure 6.11: *Dependence of motor-unit anatomy on innervation-ratio. Data obtained from Kanda et al. (1992, Table 1) & normalised to smallest motor-unit. Dotted lines represent relationships in the current model. (a) CSA: cross-sectional area.*

(2002)). While the current approach can predict variations in intramuscular pressure in any given motor-unit, this information cannot flow back to models of neural activity and affect their firing rates.

Another example of feedback occurs via muscle spindles, which are sensitive to local stretch and may influence the firing rates of their own muscle or even other muscles (e.g. Naito et al., 1996). Afferent feedback is vital to explain and understand some diseases (e.g. de Vlugt et al., 2012; Mugge et al., 2012). Again, while local stretch in the motor-unit is predicted, it is to no avail since it cannot enter the neural activity computations.

In the current implementation framework, establishing a link between mechanical quantities (such as intramuscular pressure and stretch) and neural activity is not straight forward. The main challenge is the inability to pass information between different regions of the muscle, i.e., between Gauß points. Stretch experienced by a single Gauß point in a motor-unit has, therefore, no way of communicating with the rest of the motor-unit's Gauß points. Adjusting firing rates for the entire motor-unit must occur "outside" the user-material. Again, this is because the user-material itself exists in isolation at each Gauß point.

One possibility to enable communication between the Gauß points is via the `Abaqus` user-subroutine `VUEXTERNALDB`, which is executed at each increment of the analysis. Within this subroutine communication to the "outside world" can be made (Dassault Systèmes, 2017). Computational time is a concern with such an approach, which could be mitigated by simplifying certain neural activity models, for example, the model in Ramírez et al. (2010) avoids ionic and cross-bridge dynamics calculations and convolutes fixed twitch-shapes with firing times, reducing computational overhead.

6.5.2 Accuracy of incompressibility

Skeletal muscle tissue is incompressible, for example, Böl et al. (2014) reported for a volume change of $\Delta J = 1\%$ ($J = 0.99$) for a fibre stretch of $\lambda = 0.7$ (compression). The advantages of an explicit finite element solution method is numerical stability, flexibility of user-material modelling (i.e., tangent stiffness matrix is not required) and the ability to model high-dynamic events with short time-steps, e.g., a single muscle twitch. The drawback is, however, that a purely incompressible material cannot be modelled, due to the nature of the algorithm.[3]

Instead, a nearly incompressible formulation is used, where the degree of incompressibility is controlled via the penalty-parameter c. And as c tends to infinity, the material approaches purely incompressible behaviour, which comes at a computational cost (Figure 6.4). A good balance between incompressibility and computational time is achieved for penalty-parameters between 10–50. Perhaps, trial simulations may be run with lower values for sake of shorter computational times and selected simulations subsequently rerun with high values. The incompressibility would especially influence highly confined regions of the muscle and also impact intramuscular and contact pressure values. But the choice of an appropriate penalty-parameter can drastically reduce the errors introduced by the nearly incompressible formulation presently used.

6.5.3 Element choice

Out of all element types tested, the linear tetrahedral C3D4 was the clear loser. The remaining element types behaved similarly, especially at higher Gauß point numbers, converging to a similar tip-displacement value. The choice between these element types comes down to the application. Since musculoskeletal models typically have very complex geometries, it is typically very difficult to obtain a purely hexahedral mesh. By process of elimination this results in the C3D10M as the element of choice. This element showed good convergence behaviour and in fact also gave good estimates even at lower resolutions.

6.5.4 Demonstration of the integrated model

The total reaction force produced by both models, referred to in the following as the motor-unit driven activity model and (spatially) constant-activity model, was quite similar. The force magnitudes converged above 30 % activation. In a sense, this provides assurance that the motor-unit activity model is behaving properly. At full activation, all regions of the muscle are active and both models are expected to converge. Conversely, differences should only arise at lower activity levels, where differences in spatial activity exist. Yet this was seen only to a small degree. This is (as will be seen in the next chapter) due to the idealised geometry and uniform fibre directions—both of which do not hold in real muscles.

The structural heterogeneity of muscle architecture would only amplify the differences seen in overall force output. Instead, what these results show is that, keeping everything equal, activating a small region of the muscle more intensely produces a (slightly) higher force, than smearing that same activity over the entire muscle. This may be due to changes is local stiffness, changes in the force-length relationship, and how the force is transmitted to the tendon.

[3] The enforcement of the incompressibility constraint requires knowledge of the boundary conditions at the current time increment, which only the implicit method is capable of.

The stresses and intramuscular pressures on the other hand were drastically different between the two approaches. At 50 % activation, the intramuscular pressure was strongly linearly related to the activity in the motor-unit driven model. These results show that pressure, at least in this very idealised case, is an excellent indicator of muscle activity, increasing locally where the motor-units are contracting. While the constant-activity approach can be used to predict pressure changes *over time*, only the motor-unit driven model is able to predict *regional* changes in pressure at a snapshot of the contraction.

7 A Prototype Integrated Neuro-Musculoskeletal Model: The Masticatory System

Concerning skeletal muscles and their coordination in human movement, Roger M. Enoka and Keir G. Pearson write (introduction to Chapter 34 in Kandel et al. (2000)):

> *Any action—ascending a flight of stairs, typing on a keyboard, even holding a pose—requires coordinating the movement of body parts. This is accomplished by the interaction of the nervous system with muscle. The role of the nervous system is to activate just those muscles that will exert the force needed to move in a particular way. This is not a simple task: Not only must the nervous system decide which muscles to activate and how much to activate them in order to move one part of the body, but it must also control muscle forces on other body parts and maintain posture.*

In fact, as alluded to in previous chapters, the nervous system does not just coordinate movement at the level of entire muscles but can recruit certain regions of muscles, i.e., via the motor-units, to achieve a desired movement. The variation of muscle architecture together with the selective recruitment and positioning of motor-units is the basis for functional heterogeneity in skeletal muscles. This phenomenon has many other names, including "selective activation", "inhomogeneous activation", "task-dependence/specificity" and "functional[] complex[ity]" (e.g. Pratt et al., 1991; Holtermann et al., 2005; Holtermann et al., 2009; Miyamoto et al., 2012).

The major muscles of the masticatory system—temporalis, pterygoid group and the masseters—are prime examples of functionally heterogeneous muscles. Perhaps the most studied muscle in terms of its functional heterogeneity is the masseter, which has been shown to be preferentially active during different jaw movements or bite forces (e.g. Belser et al., 1986; Hannam et al., 1994; Blanksma et al., 1997; Schindler et al., 2005; Ogawa et al., 2006; Schindler et al., 2014). The nervous system is able to extract such functional diversity from the masseters due to a combination of: the intricate internal architecture of the muscle, particular motor-unit anatomy, and specialised recruitment strategies.

Bite force is a commonly used metric to asses and diagnose masticatory function, including the evaluation of dental implant performance (e.g. Fontijn-Tekamp et al., 2000; Kogawa et al., 2006; Kshirsagar et al., 2011; Hasan et al., 2016). Biomechanical models can reveal the underlying mechanisms behind changes in bite force. These virtual models, however, typically simplify the anatomy and neglect motor-unit anatomy of the masticatory muscles (e.g. Koolstra et al., 1992; Korioth et al., 1992; Röhrle et al., 2007; Weickenmeier et al., 2017) and thus cannot capture the functional heterogeneity of the masticatory muscles.

To both show-case the integrated neuro-musculoskeletal method developed in this thesis, and to investigate the impact such a model would have on bite force prediction, a prototype model of the masticatory system is developed and used to simulate a maximum voluntary

bite force. The prototype model consists of the mandible, molar (with associated structures), temporomandibular joints and masseters. First, physiological background of the masticatory system, with a focus on the masseters, is provided (Section 7.1). Then the development of the prototype model is described (Section 7.2). Lastly, the maximum voluntary bite force simulations are covered (Section 7.3).

7.1 The Masticatory System: Introduction and Anatomy

The complex and varying functions of the masticatory system are facilitated by the arrangement of muscles that attach to the mandible and drive it about the temporomandibular joints. Muscles on either side of the mandible: masseters, temporalis, and pterygoid group, make up the muscles of mastication (Figure 7.1). The anatomy of the masticatory system is briefly discussed in the following with the focus on the internal organisation of the masseter, further details about the remaining masticatory muscles can be found in Lund (1991), Hannam et al. (1994) and van Eijden et al. (2001).

7.1.1 Other soft tissues and bones

Teeth are multi-layered structures, with a hard outer cap (enamel) surrounding a (relatively) softer, intermediate region (dentin), and a central void filled with nerves and blood supply (pulp). They insert into the mandible and maxilla via one or more roots and are attached to the bone surface via the periodontal ligament. The periodontal ligament is largely composed of collagen fibrils, which anchor into the surrounding bones to provide stabilisation and help resist compressive forces. As with most bones in the human body, the mandible and maxilla are composed of a hard outer shell (cortical bone) and a spongy inner core (cancellous bone).

The intricate movements required of the mandible during, for example, talking, chewing, and biting, are made possible by the muscles of mastication and the temporomandibular joints. The mandible is attached to the temporal bone of the skull on either side via the temporomandibular joints. At first glance, it might appear that the temporomandibular joints act as a simple a hinge joint, rotating the mandible about the axis constructed between the left and right mandibular condyles. Although this rotary opening and closing dominates mandibular movement, rotations about the remaining (posterior-anterior, cranial-caudal) axes also occur. In fact, the mandible is also able to translate along either of the axes.

7.1.2 Masseters

The masseter is typically considered as comprising three heads: superior, intermediate, and deep heads. The thicker, superior head arises from the anterior two-thirds of the zygomatic arch and inserts from the angle of the mandible, anteriorly to the ramus. The thinner, inferior head arises from the deep surface of the zygomatic arch and inserts on the upper part of the ramus. The intermediate part lies between the superior and deep heads. Each head is separated by aponeuroses arising from both the zygomatic arch and the mandible and are roughly aligned with the sagittal plane. However, the arrangement and orientation of the aponeuroses can show a large amount of variety between individuals (e.g. Cioffi et al., 2012).

Viewed in the sagittal plane, the fibres of the superior head are roughly aligned cranio-anteriorly, i.e., between the zygomatic arch and the ramus of the mandible. Conversely, fibres

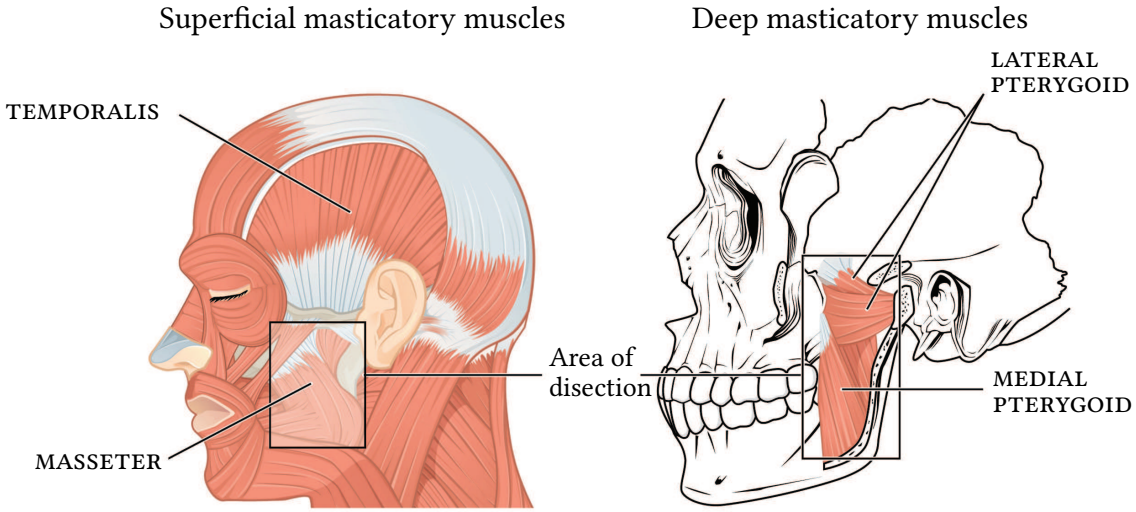

Figure 7.1: *Skeletal muscles of the masticatory system with major muscles of mastication labeled. Image adapted from OpenStax (2020).*

of the deep head are aligned cranio-posteriorly. Recalling that the fibres further show a pennation with the aponeuroses.

Motor-unit recruitment and twitch properties

As with most muscles, the majority of motor-units in the masseter are recruited at low force levels, with approximately 50 % of motor-unit being recruited for a 20 % bite force level (Scutter et al., 1998). The summation of twitches starts at approximately 7 Hz (Nordstrom et al., 1989), with the fusion frequency ranging from approximately 37–64 Hz in the masseters of rabbits (Kwa et al., 1995a; Kwa et al., 2002).

Spike-triggered averaging was used to determine the range of twitch behaviours in human masseters. The twitch rise-times ranged between 25–67 ms and peak-forces between 5×10^{-3}–1.3×10^{-2} N (van Eijden et al., 2001, Table 4). The limitations of the spike-triggered averaging approach, specifically in the masticatory system are investigated in a subsequent case-study (Section 8.3).

Fibre distribution and motor-unit territories

The fibres in the masseter are largely of type-I, comprising approximately 60–70 % of all muscle fibres (Eriksson et al., 1983). These slow twitch fibres are not uniformly distributed across the masseter but rather have the highest density in the anterior deep part, with the posterior and superior portions having approximately equal amounts of type-I and -II (mostly IIb) fibres. Given that there is a correlation between histochemical fibre-type and contraction properties, the fibre-type distribution alone provides an indication of the distribution of type-S and type-FR/-FF motor-units within the masseter. Recall that type-S motor-units are composed of type-I fibres and type-FF/FR of type-II/IIb, respectively.

By combining (paired) needle electrodes, scanning electromyography (EMG) and magnetic resonance imaging, McMillan et al. (1991) determined lengths of 32 motor-unit territories as

ranging between 0.3–19 mm (mean 6.1 mm) and 0.1–10 mm (mean 3.2 mm) along the anterio-posterior and medio-lateral axes, respectively. Also using scanning EMG, Tonndorf et al. (1994) measured average motor-unit territory dimensions between 0.75–10.3 mm (4–57 % of medio-lateral length) and found that 89 % of the motor-unit territories were confined within tendinous sheets of the masseter.

More recent studies are able to decipher a larger number of motor-units, van Dijk et al. (2016) measured the spans of 161 motor-units via needle EMG and found motor-unit spans ranging between 0.7–8.6 mm. Lapatki et al. (2019) used high-density EMG combined with advanced signal-processing techniques to obtain 190 motor-units spans, ranging between 1.2–7.9 mm. Both these studies found no preference of smaller or larger motor-units being located either deeper or superficially in the masseter.

Traditionally, drawing a concave boundary around the outermost fibres of the motor-unit was used to identify the motor-unit territory. As such, masseter motor-unit territory shapes are often generalised as being elliptical with the main axis oriented anterio-posteriorly (pigs—Herring et al. (1991); humans—McMillan et al. (1991) and Tonndorf et al. (1994)). With the advent of high-resolution medical imagining techniques, the deformation of a motor-unit can be observed, and is typically taken as its territory. For example, intricate territory shapes have also been observed (in the lower leg muscles), e.g., "crescent", "circular" or "spider" as classified by Birkbeck et al. (2020). Motor-unit territories in the masseter are typically smaller than those of the limb muscles, i.e., they occupy a smaller percentage of the masseter cross-sectional area (e.g. Stålberg et al., 1986).

Summary

Motor-unit territories in the masseter are relatively small compared to the limbs and are generally confined within tendinous sheets. Regions of the cross-section may contain varying fractions of certain types of motor-unit territories. Additionally, masseter motor-unit territories are often elliptical in shape, with the main axis aligned posterio-anteriorly, but may also contain more intricate shapes. This, combined with anatomical structure of the masseter—a broad attachment area, internal compartmentalisation via several aponeuroses and varying fibre orientations—permits the masseter muscle to produce a variety of force vectors depending on the particular task and thus shows a high degree of task specificity. Regarding the internal organisation of the human masticatory muscles, Hannam et al. (1994) state *"[t]hese difference in regional morphology clearly imply functional differentiation. It is logical to presume that there are practical advantages to be gained by an internal architecture as complex as this"*.

7.2 Modelling the Masticatory System

In broad terms, computer models of the human masticatory system typically consist of a muscle-driven mandible model, which articulates about the temporomandibular joints. However, the complexity of the anatomical models of the bones, muscles, and other soft tissues varies considerably, which can also be said of the material models and boundary conditions. Masticatory muscles are either represented implicitly, i.e., via force or pressure boundary conditions applied at their attachment areas, as one-dimensional (Hill-type) segments or, more recently, as three-dimensional (continuum-mechanical) volumes.

Early biomechanical investigations of the masticatory system were carried out by Barbe-

nel (1972), who used rigid models of the mandible to investigate the relationship between occlusal force and temporomandibular joint kinematics in 2D. Osborn et al. (1985) used a simplified three-dimensional model of the mandible with 26 individual muscle forces to generate temporomandibular joint torques.

One of the first three-dimensional models with 6 degrees of freedom and a rigid mandible driven by 16 individual muscle forces was proposed by Koolstra et al. (1988) and validated in Koolstra et al. (1992). Anatomically realistic geometric information about skull size, muscle attachments and cross-sectional areas were obtained from cadaveric studies. Alternatively to treating the mandible as purely rigid, Korioth et al. (1992) introduced a simplified three-dimensional deformable jaw model, where muscle actions were taken as pressures applied directly onto the mandibular surface. Röhrle et al. (2018b) used a similar approach, together with contact mechanics, to simulate a static bite of a rubber.

In recent decades, advances in medical imaging and segmentation procedures, computational power and muscle modelling, among others, have found their way into dental biomechanics, enabling medical-image derived three-dimensional models of masticatory bones, muscles, and associated structures. Such models have shown deviation in muscle force lines of action as muscle geometry and fibre orientation evolve during jaw movement (Röhrle et al., 2007). Furthermore, volumetric muscle models allow prediction of structural changes such as muscle thickening (Weickenmeier et al., 2017) during a static bite.

Typically, these models idealise the masseter, fusing the superior and deep heads. Furthermore, the muscle is activated using a spatially constant activity, i.e., regional contractions are not modelled. This may oversimplify the masseter anatomy and function, which has a highly individualistic and complex internal structure (Cioffi et al., 2012).

This section describes the development of an integrated neuro-musculoskeletal masticatory system model, which models the mandible, temporomandibular joints, first (right) molar, and associated dental structures. The masseter is divided into the deep and superior heads, each with its own unique fibre orientation distribution. The masseters are additionally populated by individual motor-units.

7.2.1 Geometry and meshing

The prototype model was developed in the finite element software `Abaqus/CAE` (v2017, Dassault Systèmes, France). The development of the mandbile, articular discs, fossae, periodontal ligament, pulp, dentin and enamel models is detailed in Röhrle et al. (2018b) and **Saini** et al. (2020), and is only briefly covered in the followed. The focus here is instead on the masseters.

Data sources for the masticatory model were the visible human project (Spitzer et al., 1996) ("VM-data"), and computed-tomography scans of one healthy male subject (age: 34 years, weight: 105 kg) with no history of temporomandibular disorders ("subject-data"). All geometrical models besides the masseters were based on subject-data. This model was used for preliminary investigations, e.g., to investigate the influence of occlusal loading on the stress distribution within the molar and mandible (Appendix A). Given the advantages of magnetic resonance imaging in regards to soft-tissues, the VM-data based masseter models were used, i.e., muscles were not segmented from the computed-tomography subject-data. The alignment of the masseters and mandible is discussed below.

Other soft tissues and bones

The model was based on anatomical images obtained from one healthy male subject with no history of temporomandibular disorders (age: 34 years, weight: 105 kg). Computed-tomography was used to obtain a series of images with a voxel size of 15.625 μm^3.

The mandible, mandibular second molar and the left and right fossae were manually segmented. Only the outer cortical bone type was modelled. The mandibular second molar was split into enamel, pulp and dentin. Since dentin and cementum have similar mechanical properties, the two were fused. The geometries of the left and right articular discs were taken as the volume between the mandibular condyles and the glenoid fossae. Similarly, the periodontal ligament geometry was based on the mandibular molar root geometry and defined as a uniform layer with an approximate thickness of 0.20 mm. The resulting meshes were imported into `Abaqus/CAE`. An overview of mesh statistics, including element types, is given in Table 7.1.

Masseters

Masseter geometries were based on the visible human project, and have been previously presented in van Essen et al. (2005) and Röhrle et al. (2007). The visible human (VM) masseters ("VM-masseters") were imported into `Abaqus/CAE` and meshed with tetrahedral elements (Table 7.1). Additionally, the VM mandible ("VM-mandible") was also imported.

The VM-masseters were combined with the subject-data mandibular model (and other dental structures). This necessitated alignment of the VM and subject-data models. To align the masseters with the subject-data mandible; first, mandibles from both data-sources were aligned, and then the same transformation applied to the VM-masseters. More specifically: First, landmark points on the VM-mandible were identified to construct a local coordinate-system $\mathcal{C}^{\mathrm{VM}}_{\mathrm{mand}}$. Second, the same landmark points were identified on the subject's mandible to form a second local coordinate-system $\mathcal{C}^{\mathrm{SB}}_{\mathrm{mand}}$. Third, a transformation matrix $\boldsymbol{Q}$ was found to rotate

Table 7.1: *Mesh details of the prototype masticatory model. The masseters element type was the 10-node tetrahedral `C3D10M`, the remaining element types were the 4-node tetrahedral `C3D4`. Art.: articular and lig.: ligament.*

	Elements	Nodes
Dentin	15,031	3647
Enamel	10,289	2673
Periodontal lig.	8544	2902
Art. disc-left	5343	1308
Art. disc-right	5112	1251
Fossa-left	2471	879
Fossa-right	2614	765
Masseter-left	4345	7083
Masseter-right	4047	6604
Mandible	15,334	7628
Total	73130	34740

and translate $\mathcal{C}^{\text{VM}}_{\text{mand}}$ to $\mathcal{C}^{\text{SB}}_{\text{mand}}$. Neither models were scaled.

Then, the same $\boldsymbol{Q}$ was applied to align the VM-masseters with the subject's mandibular model. Small, manual adjustments were further required due to model interpenetration caused by the mismatch in mandibular and masseter geometry. Note that the jaw model was positioned such that the left-right, posterior-anterior and caudal-cranial anatomical axes (order corresponds to positive direction) were aligned with the global x-, y- and z-axes, respectively (Figure 7.2).

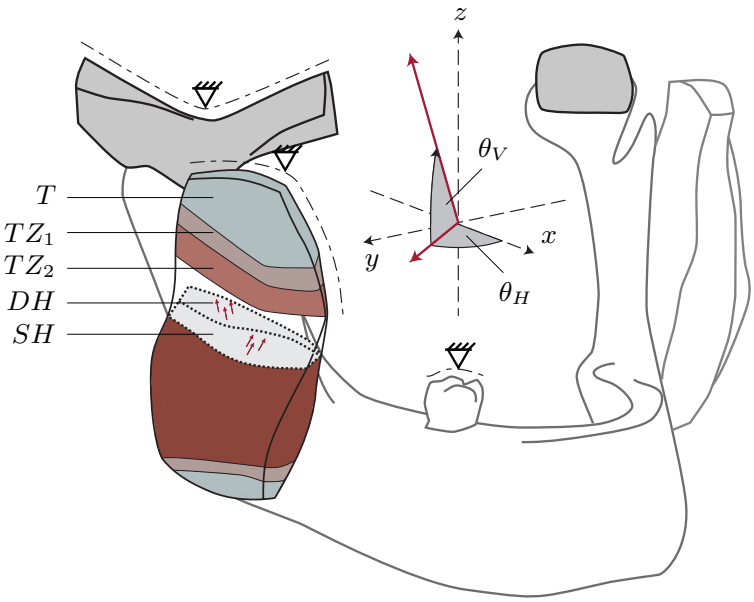

Figure 7.2: *Schematic of the prototype masticatory model. The left fossa is not shown to reveal the articular disc. Triangular symbols denote fixed displacement boundary conditions (indicated on the right side of the model only) with the area over which they are applied indicated by dash-dotted lines. The muscle architecture and muscle, tendon and transition regions are shown for the right masseter, where T: tendon, TZ_{1-2}: transition zone 1 and 2, DH: deep head and SH: superior head, with arrows symbolising fibre directions in each head. The width of the mandible (taken posteriorly, between the widest points) is* ≈ 115 mm. *Lastly, the coordinate system and the angular description of force vectors are also shown in the middle of the figure, with the horizontal plane angle θ_H and elevation angle θ_V. The x, y, and z axes are aligned with the posterior-anterior, left-right and caudal-cranial axes, respectively.*

7.2.2 Masseter architecture and motor-unit pool

The architecture of the masseter was covered in Section 5.2.3, and additional details are given here. Left and right masseter models were separated into a smaller, deep and a larger, superior part. Splitting of the masseter heads and the subsequent assignment of fibre orientations were based on qualitative literature and anatomical data, i.e., not based on direct anatomical imaging.

The fibre orientations within the finite element models were defined semi-automatically within `Abaqus/CAE` via a two-step process. First, a vector describing the major-axis or predominant fibre direction within each part was manually defined. Second, this major-axis was automatically interpolated within the muscle volume such as to conform to selected (control) muscle surfaces. The major-axes for the deep and superior right masseter were $\boldsymbol{a}^{\text{R}}_{\text{dp}} = [0.5, -0.2, -1]$ and $\boldsymbol{a}^{\text{R}}_{\text{sp}} = [0, 0.6, -1]$, respectively.

The control surfaces for each head were selected as follows. For the superior head: the superficial, posterior, anterior, and surface dividing the heads were selected as the control surfaces. For the deep head: the same surfaces were selected except the superficial surface, which was replaced with the deep surface, i.e., the surface closest to the mandible. The resulting fibre orientation field for the left masseter is shown in Figure 5.9b.

The microstructure was reconstructed in the masseters as described in Section 5.2.3. Briefly, both the spacing perpendicular to and along the fibre-scaffolds was $\Lambda_s = \Lambda_f = 1\,\text{mm}$. This resulted in 1154 and 1105 fibre-scaffolds (and seed-points) in the left and right masseters, respectively (Figure 5.9c).

The masseter was further divided (this time along the caudal-cranial axis) into different regions representing the muscle belly, tendon, and two transition zones in between. This was achieved by varying the parameter γ_M (Section 4.2.5) with $\gamma_M = 1$ for pure muscle, $\gamma_M = 2/3$ and $\gamma_M = 1/3$ for the transition zones TZ_1 and TZ_2, respectively and $\gamma_M = 0$ for pure tendon tissue. The tendons were defined at either ends of the masseter; extending over the entire cross-section. The selection of the tendinous and transition regions was done manually based on qualitative anatomical data (Figure 7.2).

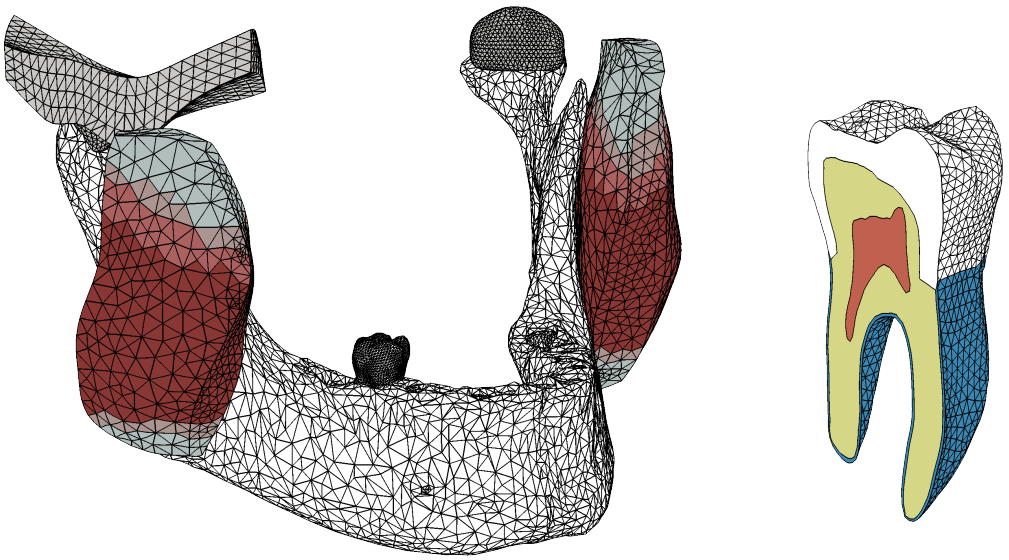

(a) ***(b)***

Figure 7.3: *Finite-element mesh of the prototype masticatory model, with node and element numbers for each part given in Table 7.1. (a) The entire model, with the muscle, transition-zones and tendons colour-coded as in Figure 7.2. The left fossa is not shown to reveal the articular disc. The width of the mandible (taken posteriorly, between the widest points) is* $\approx 115\,\text{mm}$. *(b) A zoom of the saggital cross-section of the molar, with the: periodontal ligament in blue, dentin in cream, pulp in light-red, and enamel in white. The distance from cusp to root of the molar is* $\approx 22\,\text{mm}$.

Motor-unit pool

The masseter was populated with 50 so-called "meta" motor-units or meta-units $\breve{\text{MU}}_k$ ($k = 1, \ldots, \breve{N}_{\text{MU}}$). The breve symbol $\breve{(\cdot)}$ differentiates meta-unit quantities from corresponding motor-unit quantities. Meta-units were formed by grouping several motor-units in terms of

their innervation-ratio. By doing so, the fibre distribution of a meta-unit, i.e., its territory, can be thought of as an agglomeration of the fibre distributions of the motor-unit territories that it contains.

Each masseter comprises $N_{\mathrm{MU}} = 1452$ motor-units (Carlsöö, 1958). This means that each meta-unit, sequentially, corresponds to $\rho_{\mathrm{MU}} = N_{\mathrm{MU}}/\breve{N}_{\mathrm{MU}} = 1452/50 \approx 29$ motor-units. For example, $\breve{\mathrm{MU}}_1 = \mathrm{MU}_1 \cup \mathrm{MU}_2 \cup \ldots \cup \mathrm{MU}_{29}$ or more generally

$$\breve{\mathrm{MU}}_k = \bigcup_{i=(k-1)\,\rho_{\mathrm{MU}}+1}^{k\,\rho_{\mathrm{MU}}} \mathrm{MU}_i. \tag{7.1}$$

First, innervation-ratios were computed for motor-units and subsequently grouped into meta-units. Innervation-ratios of the motor-units are described by an exponential distribution (Equation 5.17), and is characterised by: total number of motor-units N_{MU} and the innervation-ratios of the first (smallest) and last (largest) motor-units in the pool, here IR_1 and IR_{1452}. The innervation-ratios for the remaining motor-units, $\mathrm{IR}_{2,\ldots,1451}$, are exponentially distributed between these two extremes. Innervation-ratios $\mathrm{IR}_1 = 200$ and $\mathrm{IR}_{1452} = 1479$ were chosen and yielded 929,182 fibres (computed by summing all innervation-ratios), which is similar to the number reported in literature, i.e., 929,000 (Carlsöö, 1958).

The innervation-ratios for the meta-units were computed by simply summing the innervation-ratios of the corresponding motor-units, i.e., (analogous to Equation 7.1)

$$\breve{\mathrm{IR}}_k = \sum_{i=(k-1)\,\rho_{\mathrm{MU}}+1}^{k\,\rho_{\mathrm{MU}}} \mathrm{IR}_i. \tag{7.2}$$

The number of fibre-scaffolds tracked in the left and right masseter were $N_{\mathrm{FS}}^{\mathrm{L}} = 1154$ and $N_{\mathrm{FS}}^{\mathrm{R}} = 1105$, respectively (Section 7.2.2). The meta-unit innervation-ratios were recast accordingly. For the left masseter, this yielded innervation-ratios of $\mathrm{IR}_1^{\mathrm{SP}} = 8$ and $\mathrm{IR}_{100}^{\mathrm{SP}} = 53$ for the smallest and largest motor-units, respectively (Equation 5.29).

In summary, the mappings from the realistic number of fibres and motor-units to those used in the model were (for the left masseter):

$$\underbrace{\begin{matrix}\mathrm{IR}_{\mathrm{total}} = 929{,}000 \\ N_{\mathrm{MU}} = 1479\end{matrix}}_{\text{real anatomy}} \xrightarrow[\mathrm{IR}_1,\mathrm{IR}_{1479}]{\rho_{\mathrm{MU}}} \underbrace{\begin{matrix}\breve{\mathrm{IR}}_{\mathrm{total}} = 929{,}182 \\ \breve{N}_{\mathrm{MU}} = 50\end{matrix}}_{\text{meta-units}} \xrightarrow{N_{\mathrm{FS}}^{\mathrm{L}}} \underbrace{\begin{matrix}\breve{\mathrm{IR}}_{\mathrm{total}}^{\mathrm{SP}} = 1154 \\ \breve{N}_{\mathrm{MU}} = 50\end{matrix}}_{\substack{\text{discretised} \\ \text{meta-units}}}.$$

Recruitment and twitch properties

From a recruitment perspective, grouping of motor-units into a meta-unit essentially synchronises their discharge behaviour. The discharge times of the meta-units cannot be computed by "summing" or collapsing the firing times of the underlying motor-units, as this would increase the firing-frequency beyond physiological limits. Instead, an effective discharge frequency is computed per meta-unit, which represents the average discharge behaviour of the motor-units it contains.

The (meta) α-motor-neuron pool contains $\breve{N}_{\mathrm{MU}} = 50$ neurons. Minimum and maximum α-motor-neuron firing rates ($\breve{F}^{\mathrm{M}}$ and $\breve{F}^{\mathrm{P}}$) were taken as 7 Hz and 34 Hz, respectively. The range

of firing rates ($\breve{F}^{\mathrm{D}}$) was 64 Hz. Motor-neuron recruitment thresholds were distributed such that approximately 50 % of the α-motor-neuron pool was recruited at 20 % excitatory drive. Twitch responses were characterised by the values in Table 5.2 and from Campbell et al. (1993), Aliev et al. (1996) and Campbell et al. (2001). The time-to-peak and peak twitch force for the smallest meta-unit were $\breve{F}_1^{\mathrm{twitch}} = 0.0906$ and $\breve{\mathrm{TTP}}_1 = 123\,\mathrm{ms}$, respectively. The largest meta-unit had a time-to-peak a factor 3.0 shorter and a peak twitch force a factor of 35 larger.

Meta-unit territories

With the desired number of seed-points per meta-unit at hand, the way in which they are distributed, i.e., their territory within the masseter, was defined. Meta-unit territory distributions were assigned by specifying the distribution and shape parameters (Section 5.2).

Smaller territories were assigned first, i.e., the algorithm proceeds sequentially by assigning smaller meta-unit territories about the reference point $\boldsymbol{c}_{\mathrm{MUT}}$ before larger ones. The reference points were chosen such that the initial assignment of small territories occurs anteriorly and deep within the masseter. The reference points for the left and right masseters were specified with respect to the center of the seed-point plane ($\boldsymbol{c}_{\mathrm{CoP}}^k$) as $\boldsymbol{c}_{\mathrm{MUT}}^{\mathrm{L}} = \boldsymbol{c}_{\mathrm{CoP}}^{\mathrm{L}} + [11.9, 6.3, -0.2]\mathrm{mm}$ and $\boldsymbol{c}_{\mathrm{MUT}}^{\mathrm{R}} = \boldsymbol{c}_{\mathrm{CoP}}^{\mathrm{R}} + [-12.2, 6.2, -2.3]\mathrm{mm}$ for the left and right masseter, respectively. For the masseters, the x-, y- and z- axes are approximately aligned with the left-right, posterior-anterior and caudal-cranial directions (Figure 7.2).

Two distribution parameters are chosen as exemplary meta-unit fibre distributions—distribution A and B. The distribution parameters were set as fractions of the masseter cross-sectional area, with $\mathrm{CSA}^{\mathrm{L}} = 620\,\mathrm{mm}^2$ and $\mathrm{CSA}^{\mathrm{R}} = 626\,\mathrm{mm}^2$. For distribution A: $D^k = \mathrm{CSA}^k \times 1.60 \times 10^{-2}/\mathrm{mm}$, $\Delta D^k = \mathrm{CSA}^k \times 3.125 \times 10^{-3}/\mathrm{mm}$, $R^k = \mathrm{CSA}^k \times 1.60 \times 10^{-3}/\mathrm{mm}$, $\Delta R^k = \mathrm{CSA}^k \times 6.25 \times 10^{-3}/\mathrm{mm}$, with $k = \{\mathrm{L}, \mathrm{R}\}$. For distribution B: all parameters were identical as in distribution A, except D^k, which was increased by a factor of 10.

The distribution parameters were chosen to allow for slight overlapping of the territories, thus keeping them locally confined within the muscle (Figure 7.4). For both distributions, the shape parameters were constant, $\lambda_1 = 1, \lambda_2 = \lambda_3 = 5$, and were chosen such that ellipsoidal- shaped territories were formed, with their main-axis aligned along the masseters posterior-anterior axis.

7.2.3 Constitutive modelling and characterisation

The masseters were modelled as transversely isotropic hyperelastic materials (Section 4.2) and the remaining structures were treated as linear elastic (Section 4.3). The muscle model was characterised by the parameters outlined in Table 4.1, with the muscle specific parameters chosen as $\tilde{P}_{\mathrm{max}} = 7.5$ and $\lambda_{\mathrm{opt}} = 0.95$. The former resulted in a specific-strength of $P_{\mathrm{max}} = 1\,\mathrm{MPa}$. The linear elastic parameters and densities are given in Table 7.2.

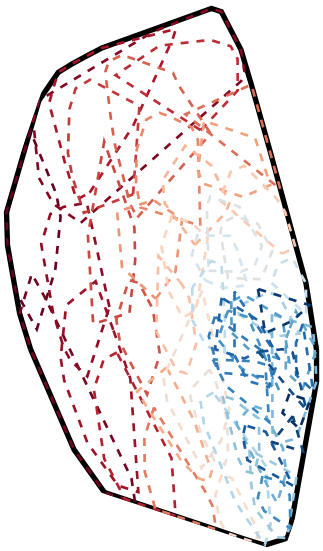

(a) *Meta-unit territories: A.*

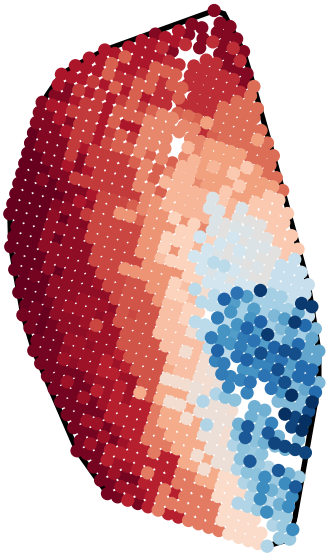

(b) *Meta-unit fibre dist.: A.*

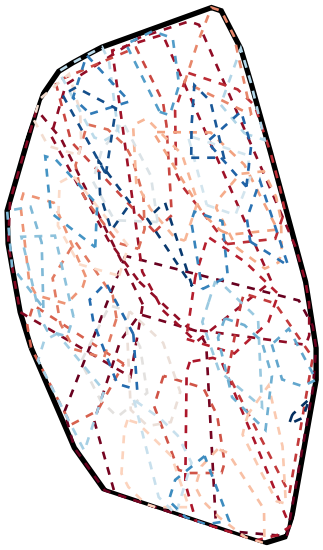

(c) *Meta-unit territories: B.*

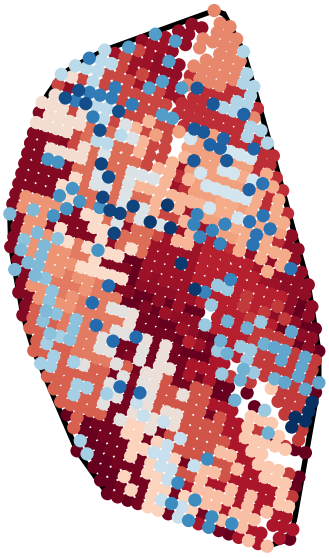

(d) *Meta-unit fibre dist.: B.*

Figure 7.4: *Meta-unit territory distribution in the left masseter simulation model of selected meta-units shown in the seed-point plane of the left masseter. The cross-sections are oriented such that the following page-to-anatomical direction relations hold: left-superior, top-posterior, right-medial (or deep), and bottom-anterior. The dotted lines show the convex boundaries around the territory and the thick, solid black boundary the outline of the muscle cross-section. Fibres belonging to the smallest to largest units are colour-coded from dark-blue (to cream) to maroon, respectively. The cross-sectional area is approximately* $630\,\mathrm{mm}^2$.

7.3 The Influence of Masseter Motor-Units on Bite Force: Comparison to the Status-Quo Models

The forces which arise between the mandibular and maxillary teeth are typically referred to as bite forces or occlusal forces. Bite force is commonly used to evaluate masticatory

Table 7.2: *Material properties in finite element model of the masticatory system, where PDL: periodontal ligament.*

Material	E/MPa	ν	source	ρ/g cm^{-3}	source
Cancellous bone	1.37×10^3	0.30	Moga et al. (2013)	0.55	O'Mahony et al. (2000)
Cortical bone	1.45×10^4	0.32		1.79	Dechow et al. (1993)
Dentin	1.86×10^4	0.31		2.14	Manly et al. (1939)
Enamel	8.00×10^4	0.33		2.89	
Pulp	2.10	0.45		0.70	-
PDL	68.9	0.45		0.70	Wang et al. (2015)
Disc	30.9	0.40	Hirose et al. (2006)	1.10	Bortel et al. (2017)

function, for example, according to gender (Miyaura et al., 1999), age (Peyron et al., 2004), weight (Shiau et al., 1993) and ethnicity (Shinogaya et al., 2001), and is strongly connected with dental status and masticatory performance (Fontijn-Tekamp et al., 2000). For example, the maximum voluntary bite force may be used to diagnose pre-existing masticatory pathologies such as temporomandibular joints disorders (Bonjardim et al., 2005; Kogawa et al., 2006; Testa et al., 2018), malocclusion (Bakke, 2006) and mandibular fractures (Kshirsagar et al., 2011). Furthermore, maximum voluntary bite force can be used to asses the performance of dental implants through comparison of post-intervention and expected values (Fontijn-Tekamp et al., 2000; Rismanchian et al., 2009; Biswas et al., 2013; Al-Omiri et al., 2014; Hasan et al., 2016).

Since the muscle forces which produce bite force cannot be measured directly, computer models are vital in analysing bite force development. Often, such models represent masticatory muscles as line-segments (e.g. Korioth et al., 1992; Ackland et al., 2017; Stansfield et al., 2018). A couple of biomechanical studies have modelled the masseter as a volumetric muscle to simulate jaw movement and bite force (Röhrle et al., 2007; Weickenmeier et al., 2017). While these models account for structural changes in the muscle, such as changes in pennation angle and contact with neighbouring tissues, they treat the masseter as a single contractile unit. Given that the basis of masseter functional heterogeneity is the selective recruitment of its motor-units, these models may not capture the subtleties of bite force development.

The prototype neuro-musculoskeletal model of the masticatory system was used to simulate a maximal bite based on the regional contraction of the masseters. The masseters were populated with meta-units, which were sequentially recruited to simulate a maximum voluntary bite force. Then, the model is cloned to form a status-quo masticatory model, i.e., treating the masseters as single contractile units and the bite force simulation is repeated. The comparison of bite force and intramuscular pressure in the masseters quantifies the differences between the proposed and status-quo modelling approaches.

7.3.1 Methods

Boundary and interaction conditions

The molar occlusal surface, left and right fossae, and masseter origin were fixed in space (Figure 7.2). The temporomandibular joints was modelled by affixing the articular discs to the mandibular condyles, allowing them to glide (frictionless) along the surface of the fossae. The masseters were attached (by a tie-constraint in `Abaqus`) to the mandible over manually defined attachment areas, extending caudally from approximately the middle of the ramus to the angle of the mandible.

In light of the occlusal boundary load investigations (Appendix A), the molar was not fixed at a single or limited number of points, but rather over the entire occlusal area (shown schematically in Figure 7.2) to prevent any stress concentrations. The bite force was taken as the sum of forces over these occlusal surface nodes. In summary, no boundary conditions were directly applied to the mandible. Instead, the mandible was held in place by attachments to the articular dics, periodontal ligament and masseters.

Masseter architecture and meta-unit territories

The masseter architecture and meta-unit number was unchanged from the descriptions in Section 7.2.2. The arrangement of the meta-unit territories was chosen as distribution A (Figures 7.4a and 7.4b).

Meta-unit activity

The models used to compute individual meta-unit activation are described in Section 5.1. An activation protocol that elicits a maximal contraction was used. This was achieved by increasing the excitatory drive $E(t)$ linearly from 0 to 1.1 over $\Delta t = 0.7$ s, the excitatory drive was then held constant for 0.3 s. This resulted in individual activities $\breve{\alpha}_i(t)$ for each meta-unit (Figure 7.5a), which were combined with their distribution factors $\breve{\breve{\kappa}}_i(\boldsymbol{\xi})$[1] (where $\boldsymbol{\xi}$ are the Gauß points) to compute the left and right masseter activity $\alpha^{\mathrm{L}}_{\mathrm{MU}}(t, \boldsymbol{\xi})$ and $\alpha^{\mathrm{R}}_{\mathrm{MU}}(t, \boldsymbol{\xi})$, respectively and is referred to as the motor-unit model.

This spatially constant activity, representing status-quo models (Figure 7.5b), was computed by a weighted sum of $\alpha_i(t)$ and $\hat{K}_i(\boldsymbol{\xi})$ (Equation 6.37), yielding equivalent activity $\alpha_{\mathrm{const}}(t)$ for each of the left and right masseters. The equivalent (spatially constant) activities were applied (uniformly) to the masseters, i.e., $\forall\, \boldsymbol{\xi} \in \mathcal{B}$ and is referred to as the (spatially) constant-activity model.

Maximal static bite simulation

Two prototype models were generated: one with individual meta-unit distributions and activities and one with where a single, equivalent activity was applied uniformly throughout the masseters. The activities described above were supplied to both masseters to simulate a maximal static bite. The bite force, measured at the molar occlusal surface, and the intramuscular pressure in the right masseter were used as markers of motor-output and compared between the models to quantify the difference between the motor-unit and constant-activity approaches.

[1] The breve symbol differentiating the meta-unit and motor-unit quantities is neglected in the following, for sake of clarity.

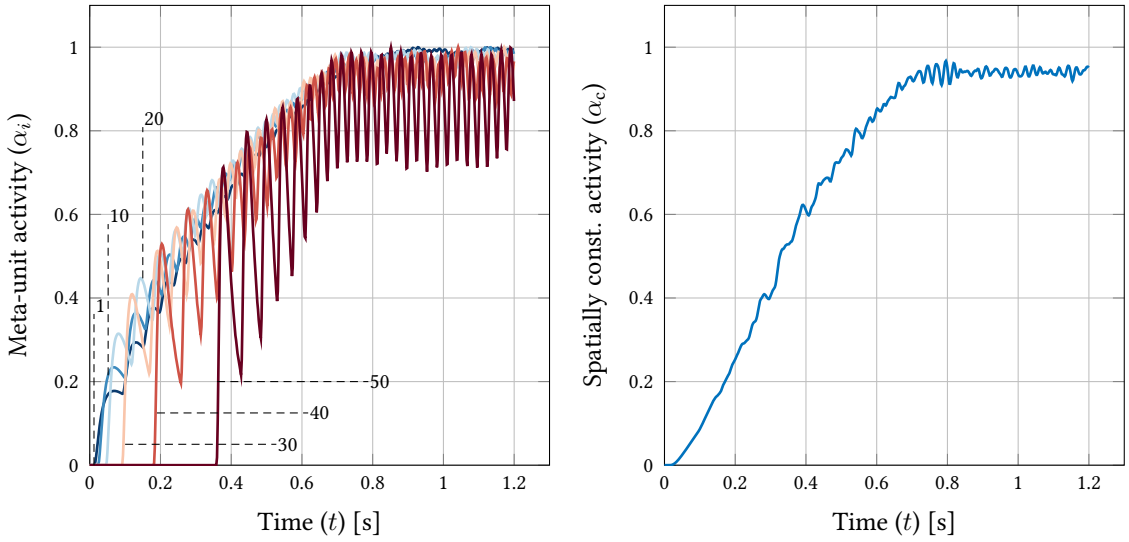

(a) *Individual meta-unit activity.* ***(b)*** *Equivalent constant activity.*

Figure 7.5: *Activation protocols for the maximal case for the (a) motor-unit model (meta-unit numbers indicated), and the (b) constant-activity model. Fibres belonging to the smallest to largest units are colour-coded from dark-blue (to cream) to maroon, respectively.*

7.3.2 Results

All simulations were performed with `Abaqus/Explicit` (v6.14-3, Dassault Systèmes, France), using an `AMD Opteron 6373` (2.3 GHz, 32 cores) with 24 GB memory,[2] resulting in computation times of approximately 10–15 h. The bite force components along the left-right, posterior-anterior and caudal-cranial axes are denoted, respectively, F^k_{LR}, F^k_{PA} and F^k_{CC} (in N). The superscript $k = \{\mathrm{const}, \mathrm{MU}\}$ denotes the constant- and motor-unit models. Snapshots of the finite element masticatory model at different stages of the contraction are shown from an oblique angle and in the horizontal plane in Figures 7.9 and 7.10, respectively.

Bite force magnitude

The peak forces along the caudal-cranial axis obtained from both models were within 1 % of each other, with $F^{\mathrm{const}}_{\mathrm{CC}}(t = 0.84\,\mathrm{s}) = 701\,\mathrm{N}$. At this time instance, the forces along the left-right axis were also within 1 % of each other, with $F^{\mathrm{const}}_{\mathrm{LR}} = -82\,\mathrm{N}$. For F_{PA} a greater difference was observed between the two models, with $F^{\mathrm{MU}}_{\mathrm{PA}}$ being 89 % of the constant-activity model $F^{\mathrm{const}}_{\mathrm{PA}} = 9.6\,\mathrm{N}$.

The bite force components showed a greater difference between the two models below maximal contraction. To highlight these force dissimilarities, the *relative* forces are plotted over the masseter activity. The relative force components $\bar{F}_j$, $j = \{\mathrm{LR}, \mathrm{PA}, \mathrm{CC}\}$ are computed by dividing the absolute values of each force-component of the motor-unit model by those from the constant-activity model, i.e.,

$$\bar{F}_j(t) = \frac{|F^{\mathrm{MU}}_j(t)|}{|F^{\mathrm{const}}_j(t)|}, \tag{7.3}$$

[2]Part of the `LEAD` cluster at the University of Stuttgart.

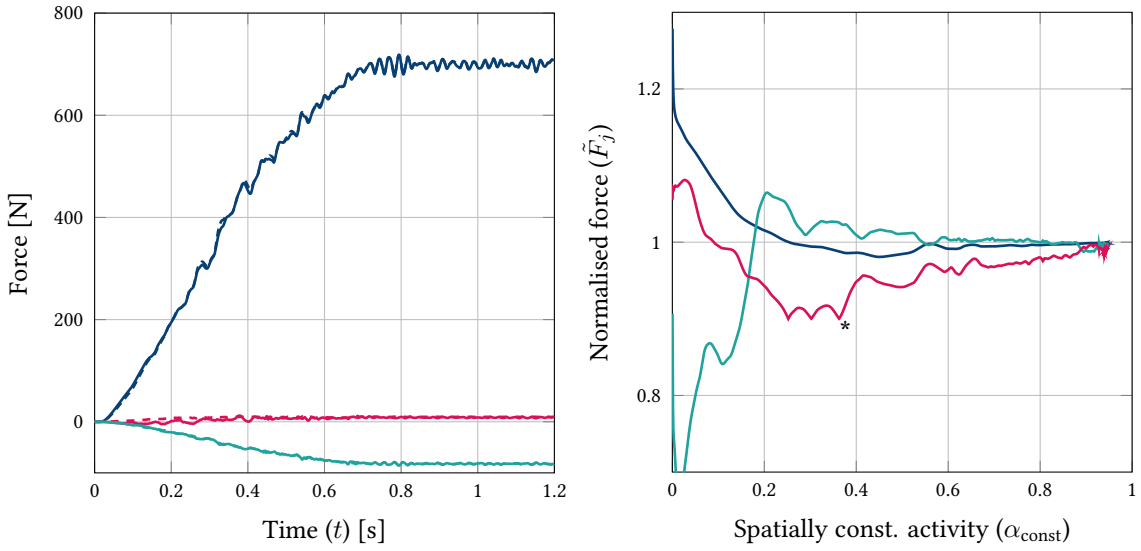

(a) *Bite force components.* ***(b)*** *Bite force difference.*

Figure 7.6: *Bite force output for the maximal activation protocol between motor-unit driven and constant-activity models. The blue trace is of the caudal-cranial component, the red trace is of the posterior-anterior component and the green trace of the left-right component. (a) Traces of the individual bite force components taken at the right first mandibular molar for the model with spatially constant (dotted) and motor-unit driven (solid) activations. (b) Relative force between the two models, *indicates that the error curve has been scaled and offset by* $0.9 + 0.1\,\bar{F}_{PA}$ *for visualisation purposes.*

and are plotted in Figure 7.6b.

In general, all force components showed a convergent behaviour at higher levels of activity. The component, $\bar{F}_{\text{CC}}$, showed the fastest convergence, falling below $\pm 2\,\%$ difference at 20 % activation. The $\bar{F}_{\text{LR}}$ component dropped below a $\pm 2\,\%$ difference after 40 % activation. The $\bar{F}_{\text{PA}}$ component showed the highest deviation and only dropped below 4 % difference once the masseters were fully activated.

The mean differences for the $\bar{F}_{\text{CC}}$, $\bar{F}_{\text{LR}}$ and $\bar{F}_{\text{PA}}$ below 50 % activity were 5 %, 7 % and 26 %, respectively. The mean differences above 50 % activity were 1 %, 1 % and 18 %.

Bite force orientation

The angles of the bite force in the horizontal plane θ^k_{H} and in elevation θ^k_{V} (in degree, $k = \{\text{const}, \text{MU}\}$) are shown for the maximal activation protocol in Figures 7.7a and 7.7b, respectively. The angles are computed according to

$$\theta^k_{\text{H}} = \texttt{atan2}\left(F^k_{\text{PA}}, F^k_{\text{LR}}\right) \quad \text{and} \tag{7.4}$$

$$\theta^k_{\text{V}} = \texttt{atan2}\left(F^k_{\text{CC}}, \sqrt{(F^k_{\text{LR}})^2 + (F^k_{\text{PA}})^2}\right), \tag{7.5}$$

where `atan2` is the four-quadrant inverse tangent. Snapshots of θ^k_{H} at various time-steps are also plotted in the horizontal (x-y plane) in Figure 7.10.

The elevation angle converged between the two models after 20 % activity, showing only a $\approx 1^\circ$ difference below the activation level. The horizontal plane angle, on the other hand,

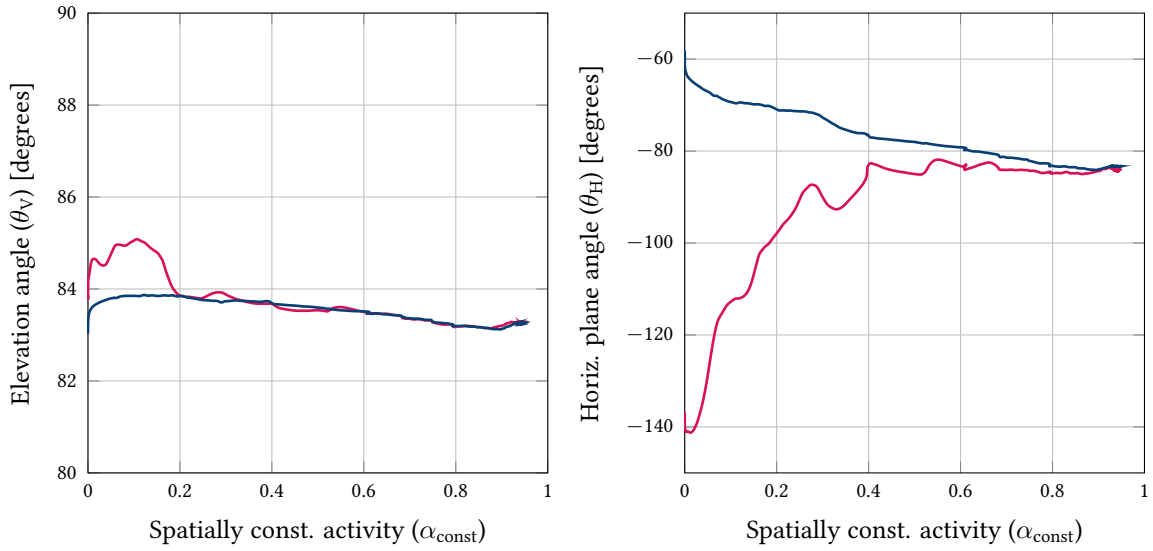

(a) *Vertical angle.* ***(b)*** *Horizontal angle.*

Figure 7.7: *Angle of bite force components. The blue traces correspond to the constant-activity model and the red trace to the motor-unit-activity model.*

showed drastic differences. Initially pointed cranio-posteriorly in the motor-unit model, and being reoriented to face cranio-posteriorly after approximately 30 % activity, and eventually converging with the constant-activity model at full activation. The constant-activity model did not show a reversal of the bite force, instead it was directed cranio-posteriorly for the entire contraction.

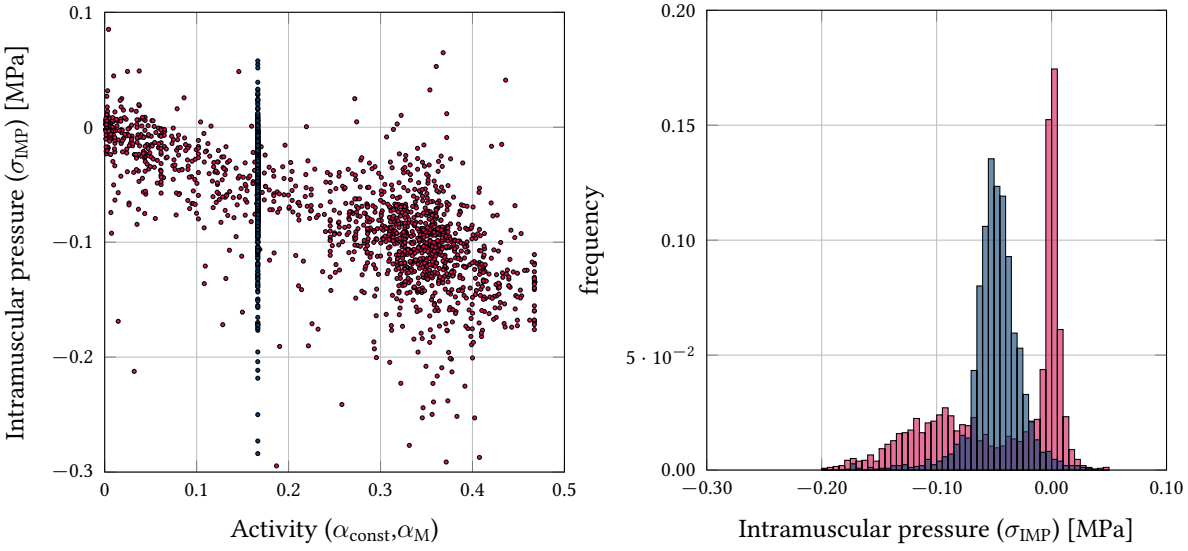

(a) ***(b)***

Figure 7.8: *Snapshot of intramuscular pressure distribution in the right masseter during sub-maximal contraction for both motor-unit- and constant-activity models. The snapshot is taken at ≈ 17 % activity. The red marks and histogram represent the motor-unit model. The blue marks and histogram represent the constant-activity model.*

Intramuscular pressure

While bite force reveals the overall masticatory system output, the motor-output within the masseter was investigated via the distribution of intramuscular pressure. A snapshot of intramuscular pressures σ_{IMP} (in MPa) and activity, at all points, in the right masseter muscle was taken at approximately 17 % activity. The pressures and activities are correlated at each point and plotted in Figure 7.8a, for both constant-activity and motor-unit models.

The motor-unit model showed a statistically significant ($p < 1 \times 10^{-6}$) linear correlation between activity and intramuscular pressure, with a Spearman rank coefficient of $r = -0.84$. In the constant-activity model, since the activity is constant at a given time-step, the spread of intramuscular pressures is localised at this activity level.

The same intramuscular pressure values are plotted as a histogram (Figure 7.8b). This reveals the frequency of occurrence of the pressure in the right masseter at a given time snapshot. Pressures in the constant-activity model were approximately uniformly distributed about a mean pressure of −0.055 MPa (negative is compressive). The motor-unit model exhibited a non-symmetric, bimodal pressure distribution, indicating two distinct clusters of high and zero pressure, with a larger portion of the muscle experiencing the latter. The high pressure region was centred around −0.095 MPa.

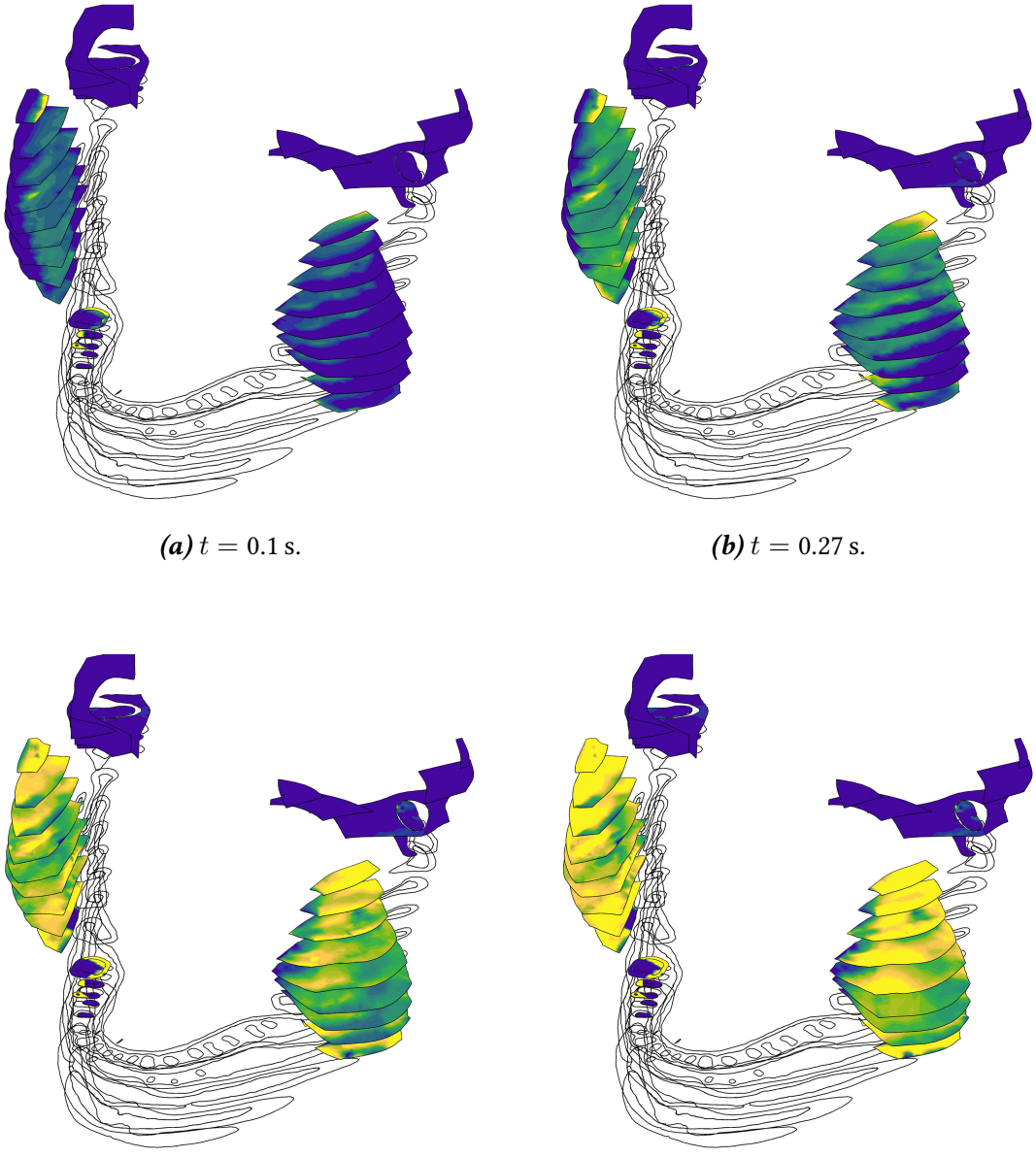

(a) $t = 0.1$ s. ***(b)*** $t = 0.27$ s.

(c) $t = 0.51$ s. ***(d)*** $t = 0.75$ s.

Figure 7.9: *Evolution of stress in the masseters during the maximal contraction simulation for the motor-unit driven model. The finite element model is sliced every* 10 mm *along the caudal-cranial axis. Stresses are colour-coded between* 0 MPa*: blue and* 1 MPa*: yellow. The width of the mandible (taken posteriorly, between the widest points) is* $\approx$ 115 mm.

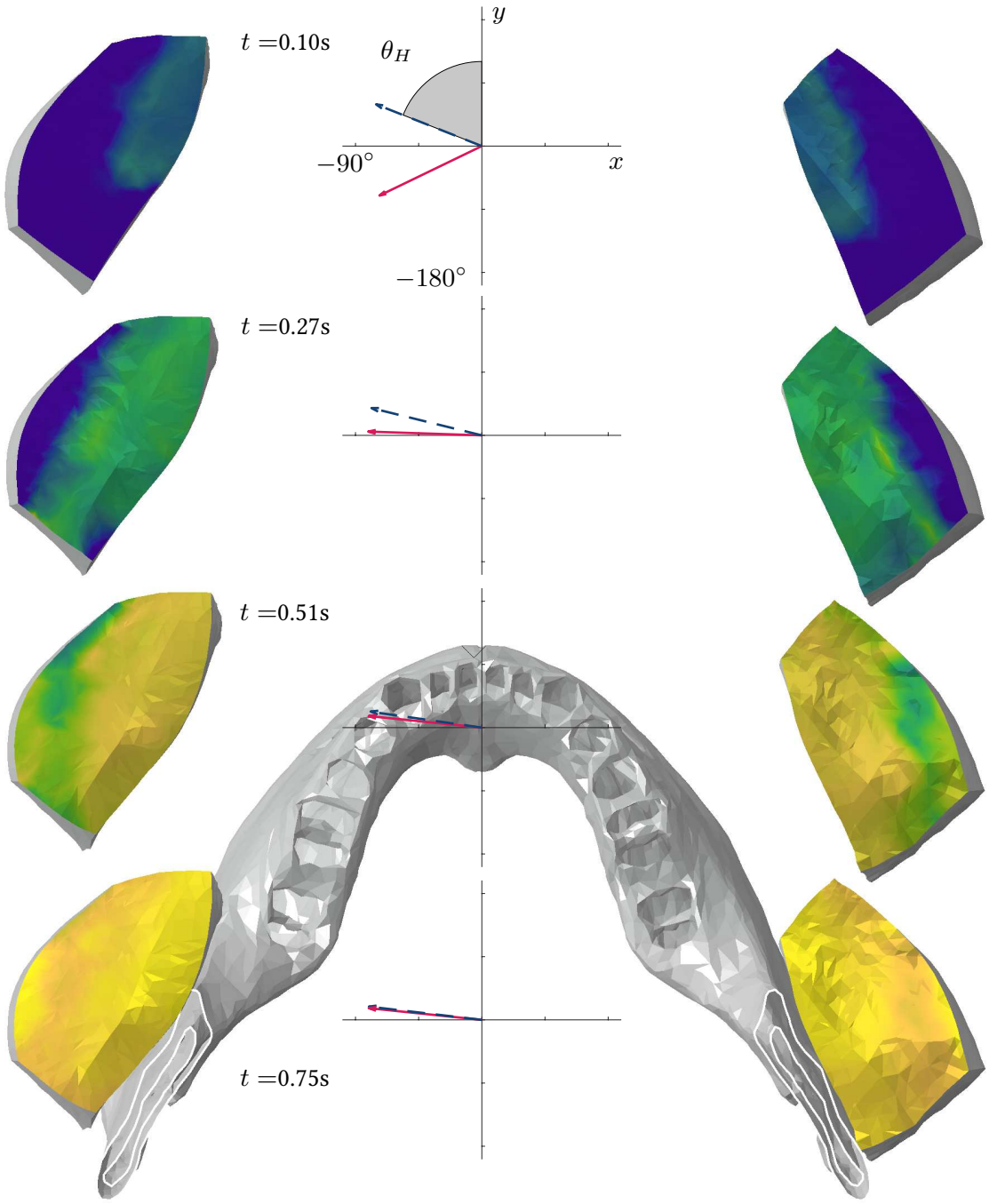

Figure 7.10: *Spread of contraction in the masseter cross-section during the maximal contraction simulation for the motor-unit driven model. Activity is colour-coded between $\alpha_M(t, \boldsymbol{\xi}) = 0$: blue and $\alpha_M(t, , \boldsymbol{\xi}) = 1$: yellow. The width of the mandible (taken posteriorly, between the widest points) is $\approx 115\,\mathrm{mm}$. Plots of the horizontal angle of the resultant bite force are plotted in the middle at the corresponding time steps, with the dotted blue line representing the constant-activation case and the solid red line representing the heterogeneous activation case.*

7.4 Discussion

First, the plausibility of the motor-unit anatomy in the masseters is discussed (Section 7.4.1). Before moving onto model limitations, including the lack of other masticatory muscles and artificial scaling of muscle strength (Section 7.4.2). Lastly, the implications of modelling motor-units on bite force prediction, as compared to the constant-activity model, are discussed both in terms of bite force and intramuscular pressure (Section 7.4.3).

7.4.1 Motor-unit anatomy

For distribution ID A, the placement parameters for masseters, $\boldsymbol{c}^k_{\text{MUT}}$, $k = \{\text{L}, \text{R}\}$, were chosen such that the smaller (or type-S) territories were located anteriorly and within the deep part of the masseter. The distribution parameters, R^k, ΔR^k, D^k, and ΔD^k, $k = \{\text{L}, \text{R}\}$, were chosen to limit the overlap between territories. This resulted in segregated territories with a strong preference of smaller and larger units located in deep and superior heads respectively (Figure 5.10). Lastly, the shape parameters, λ_i, $i = \{1, 2, 3\}$, $\boldsymbol{v}^k_1$ and $\boldsymbol{v}^k_2$, $k = \{\text{L}, \text{R}\}$ were chosen such that the territories were elongated along the posterior-anterior axis of the masseters, which has been observed in humans (McMillan et al., 1991; Tonndorf et al., 1994) and for pig masseters (Herring et al., 1991).

A larger portion of type-I fibres, i.e., those typically comprising type-S motor-units, were found to be preferentially located in the deep portion of the human masseter (Eriksson et al., 1983). Tonndorf et al. (1994) used scanning electromyography and found larger territories in superior regions of human masseters. This has further been observed in several mammalian masseters (van Eijden et al., 2001, and references therein).

More recent studies, using advanced scanning electromyography techniques, however, provide evidence against this preferential location of motor-unit type in the masseter. For example, van Dijk et al. (2016) found no significant difference between the sizes of superficial and deeper motor-unit territories. Lapatki et al. (2019) found a weak correlation between masseter depth and territory (medio-lateral) length, however both smaller and larger territories were found throughout the muscle thickness.

Currently, recruitment of motor-units is governed by the size principle. That is, smaller motor-units are recruited prior to larger ones. Therefore, functional heterogeneity is influenced by preferential location of the territories. For example, if smaller motor-unit territories are uniformly distributed over the muscle's cross-section, then their recruitment would result in a (close to) uniform contraction of the muscle.

However, it appears that the masseter can recruit sub-volumes of the muscle by recruiting adjacent motor-units (e.g. Schindler et al., 2014). This may occur by modification of the recruitment thresholds, for example, due to bite force direction (Ogawa et al., 2006) and/or contraction velocity (Romaiguère et al., 1989). Such changes in recruitment thresholds may alter the order of motor-unit recruitment and result in regional contraction of the muscle. That is, neighbouring motor-units of different sizes may be recruited together. This implies that a part of the functional heterogeneity of muscles arises at the level of motor-unit recruitment. This is not possible in the current modelling frame-work, where motor-unit recruitment is solely governed by their size.

Mammalian skeletal muscles typically show anywhere between 10-50 motor-unit fibres at a given region of the muscle (Edström et al., 1968; Burke et al., 1973). For the meta-units, corresponds to at least 2-3 overlapping territories, which was not the case in distribution A.

The meta-territories, instead, showed only a slight overlap at their boundaries with 1-2 other territories. This indicates that the territories in the current model may be more concentrated than what may be found in reality. The influence of changes in motor-unit confinement is investigated in the next chapter.

7.4.2 Modelling limitations

The consequences of grouping of motor-units into meta-units is not limited to the modelling of the masticatory system and is therefore discussed in Section 10.1.2. The remaining limitations are discussed below.

Other masticatory muscles

The bite force analyses were carried out only with the masseters. Obviously, in reality additional muscles contribute to biting, namely the temporalis, and the pterygoid group, which are typically co-activated in most masticatory tasks, even below maximum bite force (e.g. van Eijden et al., 1990). Neglecting these muscles oversimplifies the bite, both in terms of force-direction and -magnitude. But since the focus was on the comparison of two activity methods, a *relative* difference in bite force, even produced by an idealised model, was sufficient. In fact, the remaining masticatory muscles also show compartmental function (e.g. Blanksma et al., 1997; Phanachet et al., 2003; Schindler et al., 2005), and their inclusion may lead to further deviations between the two approaches.

Scaling of masseter specific-strength

The cross-sectional strength of the masseters in the prototype model was $1\,\mathrm{N/mm^2}$, obtained by scaling the reference value by 7.5 (Section 4.2.5). Typically, cross-sectional strength in human muscles ranges from $0.17–0.21\,\mathrm{N/mm^2}$ in muscle of the lower leg (Kent-Braun et al., 1999; Maganaris et al., 2001), or $0.13\,\mathrm{N/mm^2}$ for a single type-I fibre (Gollapudi et al., 2009), or $0.07–0.11\,\mathrm{N/mm^2}$ in knee extensors (Maughan et al., 1983). The value used in the present study were a factor 5-10 above these values.

While the current model captures some anatomical features of the masseter, the complex internal organisation of multiple aponeuroses and varying pennation angles (e.g. Cioffi et al., 2012) was neglected. Such an architecture would act to increase the physiological cross-sectional area and increase masseter force output. The simplification of the internal masseter structure was compensated by scaling the specific-strength (somewhat haphazardly). A rough approximation shows that reducing the specific-strength by a factor of 5, i.e., $\approx 0.2\,\mathrm{N/mm^2}$, would reduce the bite force (proportionally) to $\approx 140\,\mathrm{N}$. This is well below the range for healthy adults ($456\pm178\,\mathrm{N}$) (Röhrle et al., 2018a, Table 1). Regardless of the specific-strength, given that the model was used to compare the *relative* behaviour between a status-quo and motor-unit driven model, this may not be detrimental to the conclusions drawn from the modelling comparisons.

7.4.3 Comparison to constant-activity model

Bite force

Qualitatively, the spread of both muscle activity and stress in the masseters reflects the underlying activity and structure of the motor-units (Figures 7.9 & 7.10). The anterior deep region contracts first, and as the larger motor-units are recruited, the contraction spreads posteriorly and superficially. The non-uniform stresses in the muscle also impact the stresses in the tendons (top and bottom slices of Figure 7.9) and across the attachment area. Changes in force transmission to the mandible influence the torque generated at the molar. Such an evolution of muscle activity is obviously not seen in the constant-activity model, where muscle activity is applied uniformly throughout the masseter.

At lower activation levels, the influence of individual motor-units is more pronounced since only these muscle subregions are producing active stress, predominately in the direction prescribed by their local-fibre orientation. The smaller motor-units were located anteriorly and deep within the masseter, where the local fibre orientation is directed posteriorly. Therefore, at low activation levels, the overall muscle force is dominated by these posteriorly oriented motor-units and acts to retract and elevate the mandible (Figure 7.10). This retraction behaviour was not observed for the constant-activity model.

The function of the deep region of the masseter to retract is supported by experimental observations. For example, Belser et al. (1986) found that during jaw retraction, the respective activity of superior and deep fibres was 5.5 % and 47.5 %. Additionally, Hannam et al. (1994) and Blanksma et al. (1997) found that deep fibres in the masseter contributed predominantly to jaw elevation and jaw retraction. Recording the activity of individual motor-units, Ogawa et al. (2006) found that those motor-units located deep within the masseter started firing earlier when the bite was oriented "posterio-laterally", i.e., retraction of the jaw laterally. As the bite force became more anterior, the motor-units in the superficial region became more active.

As the masseter approaches medium levels of activation, the muscle force beings to receive contributions from a larger population of motor-units. In fact, at about 50 % activation, all motor-units are recruited. Since the larger superior head of the masseter has fibres more anteriorly directed, the recruitment of these motor-units causes the resultant force to be directed anteriorly. This can be seen in the large variations in F_{PA} as compared to F_{LR} and F_{CC} over the range of activation.

At maximal activation all motor-units of the masseter are maximally recruited. Therefore, it would be expected that the bite force coincides between the two models. If, however, the *history* of deformation or muscle contraction was of interest than the two models would no longer be equivalent. For example, a certain history of compartmental activity and the associated changes in intramuscular pressure may lead to certain patterns of blood perfusion in the muscle.

When the masseters were modelled with a uniform motor-unit distribution (constant-activity model), the bite force was more steady (in its direction and magnitude) as the masseters went from inactive to fully-active. A non-smooth mandibular force was more pronounced below medium activity levels, suggesting that motor-units should be considered for investigations involving sub-maximal tasks such as speech and mastication. Additionally, since bruxism involves sub-maximal contraction (e.g. Nishigawa et al., 2001), the direction of this sustained force would be better predicted by considering compartmental activity of the masticatory muscles.

Intramuscular pressure

In the prototype motor-unit driven model, regional variations in intramuscular pressure were observed at 17 % maximum voluntary bite force (Figure 7.8a). This resulted in regions of very high pressure in the anterior deep region of the masseter, where the smaller motor-units were active. The larger, more superficially located motor-units were inactive and thus did not raise intramuscular pressure.

In the constant-activity model, pressure was distributed more uniformly within the massseter, i.e., regions of very high and low pressure were not seen. The mean pressure occurred approximately in the middle of the masseter. The spread of the pressure values despite a constant activity is due to the architectural variations in the masseter, which causes changes in the force-length relationship, and distributes the active stress non-uniformly within the muscle.

From a modelling perspective, these results show that neglecting motor-unit activity and distribution leads to errors in both pressure magnitude and more importantly in the way it is distributed throughout the muscle. This may impact predictions based on intramuscular pressure, for example, blood perfusion within the muscle, which leads to metabolic changes and influences fatigue (e.g. Sjøgaard et al., 1988; Murthy et al., 2001).

Intramuscular pressure was measured in the tibialis anterior and was found to hover around $1 \times 10^{-3}\,\mathrm{N/mm^2}$ (10 mmHg) and may rise to $2 \times 10^{-2}\,\mathrm{N/mm^2}$ (200 mmHg) during contraction (Nakhostine et al., 1993). The pressure magnitudes in the simulation are an order of magnitude higher than these observations, $\approx 1 \times 10^{-1}\,\mathrm{N/mm^2}$ (750 mmHg) at 0.35 activity. This is due to the artificially scaled passive stiffness parameters, which were scaled together with the specific-strength (see discussion above).

Conversely, passive stiffness was not scaled in the idealised case and here a lower pressure was observed, i.e., $\approx 1.75 \times 10^{-2}\,\mathrm{N/mm^2}$ (131 mmHg) at 0.35 activity (Figure 6.9b). This is one of the disadvantages when material parameters are (crudely) scaled to account for modelling errors, and motivates the need for more precise muscle-architectural models. That is, by modelling the aponeuroses of the masseter the mechanical advantages of pennated muscle would yield a higher force-output, while keeping intramuscular pressure within physiological limits.

Another drawback is that the intramuscular pressure in the simulation at rest is $0\,\mathrm{N/mm^2}$. This is due to the theoretical framework, which operates from a stress-free, reference configuration. Possible solutions include applying a baseline activity or pre-stretching the muscle to generate this pressure passively.

8 Case-Studies Using the Integrated Neuro-Musculoskeletal Masticatory System Model

The prototype neuro-musculoskeletal model of the masticatory system, developed in the previous chapter, opens up multiple avenues to investigate the relationship between motor-unit anatomy, activity, and masticatory motor-output. Certainly, any conclusions drawn from such analyses need to be interpreted with care, as only a single joint with a single anatomical layout is considered. Despite this limitation, these exploratory case-studies can be used to discover patterns, anomalies, and test hypotheses to help direct future analyses.

With this in mind, the masticatory model is used to address the following questions, each being introduced in its respective section:

1. What is the influence of masseter motor-unit distributions on bite force? (Section 8.1)
2. How robust is masseter intramuscular pressure in the passive regions as a predictor of bite force? (Section 8.2)
3. Is bite force an accurate representative of masseter motor-unit twitch force? (Section 8.3)

Additionally,

4. How does the motor-unit remodelling that occurs during ageing and neuromuscular disorders manifest itself in bite force? Since this investigation extends the motor-unit anatomy algorithm, it is treated in a separate chapter (Section 9).

8.1 Compartmental Activity of Masseters and Bite Force

The masseter has a complex internal architecture, with multiple and individually varying aponeuroses compartmentalising the muscle (Cioffi et al., 2012). Masseter motor-units are smaller compared to limb muscles (van Eijden et al., 2001) and may be largely confined within the aponeuroses (Tonndorf et al., 1994). Furthermore, individual motor-units show a high degree of functional selectivity, i.e., firing preferentially in certain bite directions (Ogawa et al., 2006; Schindler et al., 2014). Given that motor-units are highly specialised in the masseters, alterations in their architecture would impact motor-output. Furthermore, motor-unit anatomy is individualistic due to factors such as gender (Jaworowski et al., 2002),[1] age (Lexell et al., 1991) and physical training (Howald, 1982; Messi et al., 2016). When injury or neuromuscular

[1] while not explicitly measuring motor-unit territory, the differences in fibre-type distributions may be taken as a marker for territory arrangement

disorders are considered, the variety in motor-unit anatomy increases even further (Johnson et al., 1973b; Lester et al., 1983). The sensitivity of masticatory motor-output to changes in masseter motor-unit anatomy has not been quantified.

To this end, a sensitivity analysis using the prototype masticatory system model (Section 7.3) is carried out. By fixing the recruitment and firing rate of the α-motor-neurons, and changing only the distribution of fibres they innervate in the masseters, the sensitivity of the resulting bite force to changes in motor-unit anatomy can be quantified. A change in motor-unit territory does not involve a structural change per se, rather it corresponds to a change in the fibres recruited by an α-motor-neuron.

In a first set of variations, the amount of dispersion (via D and ΔD) and overlap with neighbouring motor-unit territories (via R and ΔR) were varied. Then, in a second set of variations, these dispersion and overlap parameters were fixed, and the relative position of smaller and larger motor-unit territories were varied (via $\boldsymbol{c}_{\text{MUT}}$), e.g., smaller territories located posteriorly/superiorly in one case and in the middle of the muscle in another.

8.1.1 Methods

Only meta-unit territory arrangements and meta-unit activities were altered in the following; the rest of the prototype masticatory model, as described in the previous chapter, remained unmodified. The co-dispersion index (Section 5.3.5) is used to quantify the meta-unit distributions in the masseters. The calculation of the co-dispersion index requires a split between type-I and -II fibres. Therefore, meta-units 1–37 were assumed to be type-S, i.e., composed of type-I fibres, and the remaining, larger meta-units (38–50) were type-F.

Motor unit activity

Individual meta-unit activity was computed by supplying a sub-maximal excitatory drive $E(t)$ (Equation 5.2) to the same α-motor-neuron pool and biophysical models as described in Section

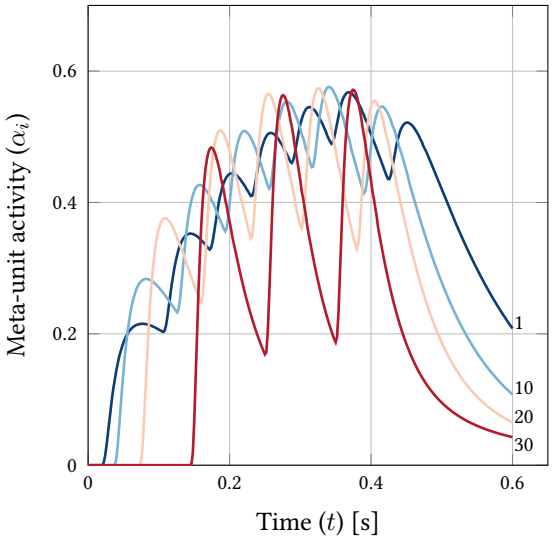

Figure 8.1: *Activation protocols for the sub-maximal case for the motor-unit driven model (meta-unit numbers indicated).*

Table 8.1: *Motor-unit anatomy parameters for the meta-unit territory distribution variations in the masseter. Only changed parameters are shown, i.e., blanks refer to the parameters in distribution 0. All parameters are multiplied with the cross-sectional area of the masseter in question; CSA_k, $k = \{L, R\}$, for the left and right masseter being $620\,\mathrm{mm}^2$ and $626\,\mathrm{mm}^2$, respectively. The location of the central anchor point $\boldsymbol{c}_{MUT}$ is indicated by anatomical positions, A: anterior, D: deep, S: superficial, P: posterior and M: middle.*

ID k	$\boldsymbol{c}^{\mathrm{L}}_{\mathrm{MUT}}$	$\boldsymbol{c}^{\mathrm{R}}_{\mathrm{MUT}}$	R/CSA_k	D/CSA_k	$\Delta R/\mathrm{CSA}_k$	$\Delta D/\mathrm{CSA}_k$
0	A/D	A/D	1.60×10^{-3}	1.60×10^{-2}	6.25×10^{-3}	3.125×10^{-3}
1	A/D	A/D	2.40×10^{-2}			
2	A/D	A/D		1.60×10^{-1}		
3	A/D	A/D			3.125×10^{-2}	
4	A/D	A/D				9.375×10^{-2}
5	A/D	A/D	2.40×10^{-2}	4.80×10^{-1}		
6	A/D	A/D	1.60×10^{-2}	1.60×10^{-1}		
7	A/S	A/S				
8	P/D	P/D				
9	P/S	P/S				
10	M	M				

7.3.1. The excitatory drive $E(t)$ was linearly increased from 0 to 0.375 over $\Delta t = 0.25$ s held constant for $\Delta t = 0.1$ s and then decreased linearly to 0 over $\Delta t = 0.25$ s.

Masseter architecture and meta-unit territories

The distribution used in the previous chapter—distribution A—is referred to here as the reference meta-unit territory, with ID 0. Distribution B from the previous chapter is assigned ID 2. Note that for all territory variations the parameters $\lambda_1 = 1, \lambda_2 = \lambda_3 = 5$ (Equation 5.35), which influence meta-unit territory shape, were kept constant.

Variations in meta-unit territory distributions (of both masseters simultaneously) were produced by scaling distribution 0's parameters (Table 8.1).[2] The parameters were scaled individually (distribution IDs 1-4), and simultaneously (distribution IDs 5 and 6). The motor-unit territories (besides those in Figure 7.4) over the masseter's cross-section are plotted in the Appendix B. The co-dispersion index was computed for each distribution. Then, fixing the distribution parameters to those in the reference distribution (ID 0), the reference point $\boldsymbol{c}_{\mathrm{MUT}}$ was repositioned over the muscle's cross-section (technically, the seed-point surface). Since smaller territories are assigned prior to larger ones, the location of $\boldsymbol{c}_{\mathrm{MUT}}$ dictates the location of the smaller meta-unit territories. This holds only when the distribution parameters allow for local confinement of the territories, i.e., if D, $R \to \infty$, then the location of $\boldsymbol{c}_{\mathrm{MUT}}$ becomes irrelevant.

[2]The influence of distribution parameter scaling on the motor-unit territory distribution can be seen in the study performed on an idealised geometry (Section 5.3.5).

Sub-maximal static bite simulation

Each of the 10 distribution parameter variations were used to generate a pair of masseters, which, in turn, formed 10 separate prototype masticatory models. The same meta-unit activity was supplied to each of the prototype models to simulate a sub-maximal static bite. The spread of the bite forces was used to quantify the influence of the varying motor-unit territory distributions.

8.1.2 Results

The bite forces, for $k = \{1, \ldots, 10\}$ distributions, were measured along the left-right, posterior-anterior and caudal-cranial axes and are denoted as $F^k_{\mathrm{LR}}(t)$, $F^k_{\mathrm{PA}}(t)$ and $F^k_{\mathrm{CC}}(t)$, respectively. The magnitude of the bite force is denoted as F^k_{M}. All forces are in N. The spread of bite forces for distributions $k = \{1, \ldots, 6\}$ and IDs $k = \{7, \ldots, 10\}$ are shown in Figures 8.2a and 8.2b, respectively.

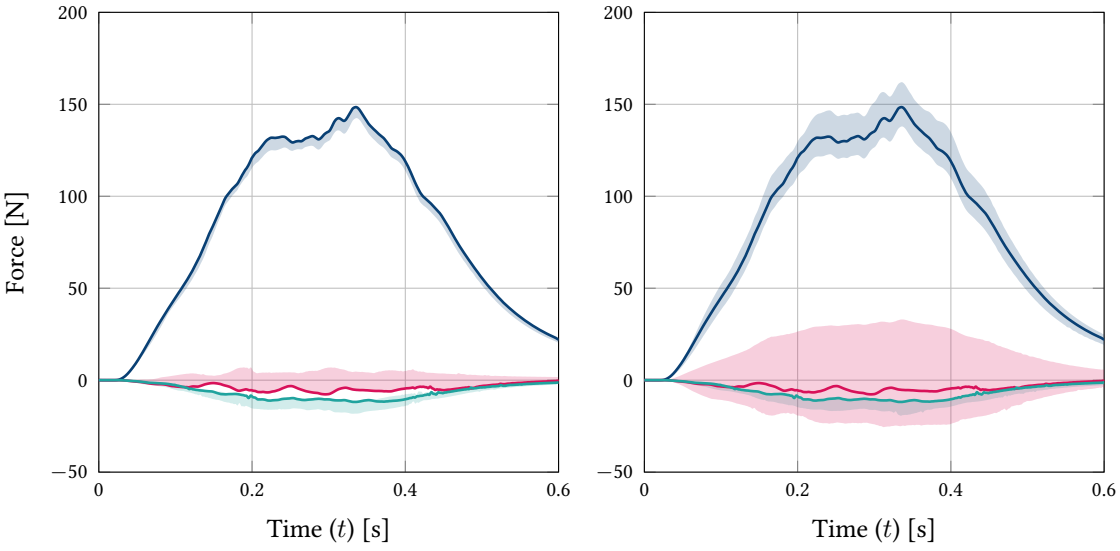

(a) *Dist. IDs 1–6.* ***(b)*** *Dist. IDs 7–10.*

Figure 8.2: *Variation in bite forces with changing meta-unit anatomy. The solid line is from the distribution ID 0; the blue, red and green shaded regions represent the force envelopes for the caudal-cranial, posterior-anterior and left-right force components, respectively.*

The orientation of the peak bite force is described by the elevation angle θ^k_{V} and the angle in the horizontal plane θ^k_{H} (in degree), and the spread of these angles is shown in Figures 8.3a and 8.3b, respectively.

Territory spans were measured by inserting a virtual probe superficially into the masseter and moving it medially, i.e., through the thickness of the muscle. The distance covered within a certain meta-unit by the probe was taken as the span of the unit. These medio-laterial virtual scans were repeated three times for each masseter; one located posteriorly, in the middle of the muscle and anteriorly and all recordings were concatenated. Territory spans of selected distributions (in mm), together with literature values, are given Table 8.2.

The peak bite force occurred at $t = 0.34\,\mathrm{s}$. The peak bite force components, magnitude, angles, and statistics for all distributions are given in Table 8.3. The fibre-type co-dispersion

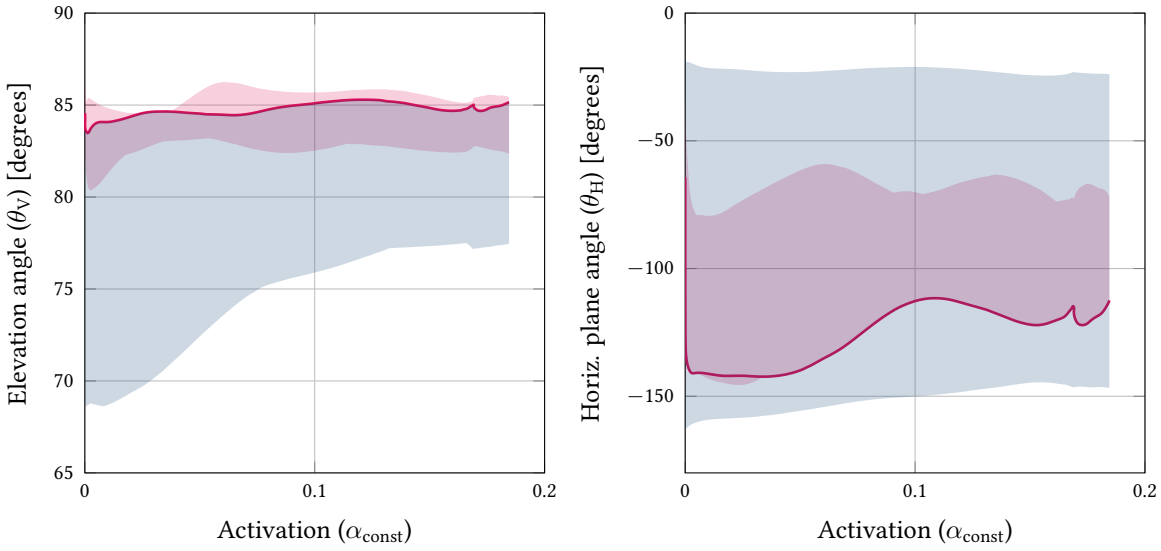

(a) *Vertical angle.* ***(b)*** *Horizontal angle.*

Figure 8.3: *Variation in bite forces angles with changing meta-unit anatomy. The red shaded region corresponds to distribution IDs 1–6 and the blue shaded region to distribution IDs 7–10. The solid red line is for distribution ID 0.*

index of the distributions is also given in Table 8.3. The values of co-dispersion index for the right masseter ranged between 0.05-0.90. To investigate the relationship between fibre-type dispersion and bite force, the peak bite force magnitude F_M^k is plotted against co-dispersion index in Figure 8.4.

Table 8.2: *Experimental and simulated motor-unit territory sizes in the human masseter. The method to determine MUT size are iEMG and HDEMG for needle and high density electromyography, respectively.* †*minimum and maximum values given as* 10^{th} *and* 90^{th} *percentiles, respectively*

	MUT length/mm		
Method	Min.	Max.	Source/comment
iEMG	0.3	19	McMillan et al. (1991)
iEMG	0.4	13.1	Tonndorf et al. (1994)
iEMG	0.7	8.6	van Dijk et al. (2016)
HDEMG	1.2	7.9	Lapatki et al. (2019)
Simulated	†0.7	†3.9	Distribution ID 0
	†0.3	†8.2	Distribution ID 2

Table 8.3: *Sensitivity of bite force to masseter meta-unit anatomical variations.*

ID	CDI	F^k_{LR}/N	F^k_{PA}/N	F^k_{CC}/N	F^k_{M}/N	θ^k_{V}/deg.	θ^k_{H}/deg.
0	0.86	-12	-5	148	149	85	-114
1	0.69	-13	-2	148	148	85	-98
2	0.39	-16	3	144	144	83	-79
3	0.59	-14	1	147	148	85	-86
4	0.44	-12	3	145	145	85	-75
5	0.05	-15	5	143	144	84	-72
6	0.16	-18	4	142	144	83	-78
7	0.89	-15	33	162	166	77	-24
8	0.86	-17	-25	138	142	78	-145
9	0.90	-17	17	138	140	80	-45
10	0.79	-19	18	142	144	80	-48
mean	0.60	-15	5	145	147	82	-79
SD	0.29	2.4	14	6.3	6.6	2.8	32
range	0.86	8	58	24	26	8	121

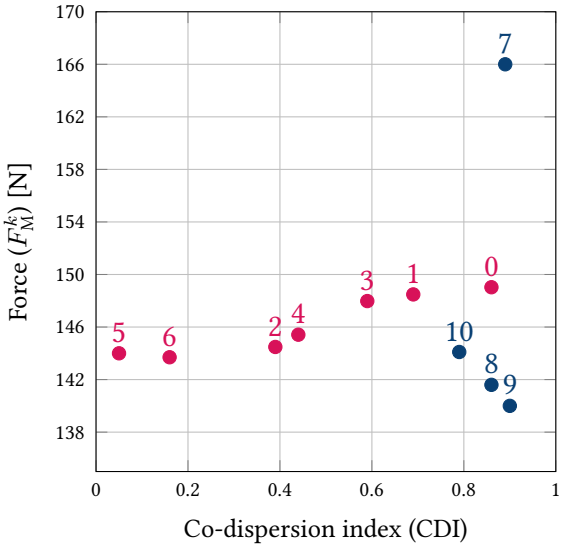

Figure 8.4: *Variation of peak force magnitude with fibre dispersion, as measured by the co-dispersion index. The marks in red are distributions with varying dispersion parameters but the same territory positions. The marks in blue have the same dispersion parameters but varying territory positions. The distribution parameter IDs are indicated directly above the marks.*

8.1.3 Discussion

The force component that was most sensitive to changes in meta-unit anatomy was the posterior-anterior component (F_{PA}), followed by the left-right (F_{LR}) and caudal-cranial (F_{CC}) components (Figure 8.2). These differences in force sensitivity can be explained by the architecture of the masseters. If the muscle had an approximately uniform fibre orientation and uniform geometry, the particular region in charge of force production would have little impact on the resultant force vector, e.g., this was seen with idealised geometry in Section 6.4. On the other hand, the greater the variance in fibre orientation within the muscle, the larger the variation in the resultant force vector when the α-motor-neuron innervation is altered. Since the greatest variation of fibre orientation in the masseter was along the posterior-anterior axis, i.e., fibres in the superior head face posteriorly and anteriorly in the deep head, F_{PA} was impacted the most by changes in meta-unit territory.

Motor-unit territory confinement and innervation-ratio

The force component sensitivity reveals the link between the neural organisation of the muscle, its structural organisation and motor-output. That is, it would make sense that a muscle with a complex and varying internal architecture had many locally confined territories. Only then could the neuromuscular system exploit each region of the muscle effectively.

This has been observed in the masseter, which have smaller, more confined territories as compared to muscles of the limbs—*"suggest[ing] a more localized organisation of motor control in masticatory muscles"* (van Eijden et al., 2001). This enables such a muscle to produce a variety of force vectors, e.g., the rabbit masseter produced *"lines of action ...at least as large as the variation in fibre directions"* (Turkawski et al., 1998). Additionally, Schindler et al. (2014) found that small "sub-volumes" of the masseter were recruited under particular tasks via the recruitment of adjacent motor-units. Ogawa et al. (2006) found motor-units of the masseter that had a preferred "firing range", meaning that certain units only contributed to certain bite force directions.

These studies, among others, suggest that the masseter has both a highly specialised internal architecture *and* small enough territories that these regional differences can be exploited. This is reflected in the sensitivity study by the fact that altering the *position* of highly confined territories had a much larger impact on bite force than did the amount of overlap. That is, distributions 7–10 had a much larger influence than did 1–6.

In fact, given that only a fraction of the motor-unit pool is active, changes in overlap also alter the (mean) position of the active territories. This can be seen in Figure 8.4, where larger changes in force magnitude are observed for distributions 2, 4, 5 and 6 compared to 1 and 3, since a more mixed distribution (co-dispersion index closer to 0) effectively repositions the *mean location* of the territory. In other words, it appears that the effective center of activity influences bite force to a higher degree than the overlap of the territories.

Furthermore, when highly confined distributions (co-dispersion index closer to 1) are repositioned, large changes in force magnitude are seen. This suggests that the relationship between motor-unit anatomy and force output is likely:

$$\text{territory overlap} \;\rightarrow\; \text{mean territory location} \;\rightarrow\; \text{force output.}$$

As mean territory location shifts posteriorly, the force-magnitude decreases. This occurs for

distributions 2, 4 and 6 and much more drastically for distributions confined territories: 8, 9 and 10. This reduction in bite force could be due to (i) changes in the force-length relationship of skeletal muscles, (ii) force transmission through the muscle cross-section, (iii) muscle architectural changes and (iv) modelling errors and the interplay between these factors.

First, the posterior region of the masseter is less confined by surrounding tissue as is the deep region of the muscle. Since a large part of the deep region is attached to the mandible, this may limit the stretch of this region (staying close to optimal length) as it is activated. Furthermore, the model lacks connective tissues surrounding the muscle, i.e., the epimysium, which may act to resist muscle contraction. Therefore, sarcomere lengths may undergo greater changes when posteriorly located and thus cause the masseter to fall below its optimal length and lead to reduced force production.

Second, force transmission occurs both along the fibres and transversely between fibres via shearing effects (e.g. Huijing, 1999b). When the contraction occurs superficially in the masseter, this laterally transmitted force may be "dissipated" (by elastic deformation of neighbouring regions) leading to a lower force transmission at the tendons.

Third, the fibre orientation in the superior head may redistribute force away from the cranial caudal component. This can be seen in the F_{LR} force component, which in fact is higher for distribution 9 than distribution 7, which has the highest overall magnitude.

Fourth, despite best efforts to model the jaw musculoskeletal system accurately, modelling assumptions and errors will inevitably influence simulation results. In this case, the abrupt changes in the geometry of the caudal end of the masseters may alter force transmission to the mandible, which would otherwise be more efficiently transmitted given a smoother curvature of the muscle.

8.1.4 Conclusion

Variation of motor-unit territory distributions in the masseters had a significant impact on the bite force at the molars, both in terms of magnitude and orientation. The sensitivity of the bite force components was closely linked to the masseter architecture. The posterior-anterior force (and horizontal angle) was most sensitive to changes in territory location, which corresponds to the large variety of posterior-anterior fibre orientation within the superior and deep heads. This indicates that in muscles which have locally confined territories, individualistic motor-unit territory distributions should be taken into account as this can impact joint force predictions, especially at low to medium force levels. The results showed that territory location outweighs territory overlap in governing overall muscle force output. And that changes in force elicited by territory overlap could in fact be due to their influence on the effective territory location.

8.2 Compartmental Activity and Intramuscular Pressure in the Masseters

A popular approach to infer muscle activity is intramuscular pressure, which measures the hydrostatic fluid pressure in skeletal muscle as it contracts, and shows good agreement with muscle force (e.g. Aratow et al., 1993; Ateş et al., 2018). Mechanically speaking, according to the Law of Laplace, when curved fibres contract they exert pressures inwards proportional to their tension and curvature. Given its mechanical nature, intramuscular pressure is further

used to predict the stress-state in the muscle (Ward et al., 2007; Sadeghi et al., 2019).

However, this technique faces some challenges. For example, during dynamic contractions the correlation to muscle stress breaks down (Ward et al., 2007), or that pressure measurements are sensitive to catheter depth (Nakhostine et al., 1993). A more fundamental issue is that pressure arises due to both active and passive muscle deformations. To circumvent this, pressure measurements are typically supplemented with electromyography (e.g. Styf et al., 1995; Ateş et al., 2018).

This situation becomes more complicated for sub-maximal contractions, especially for muscles that show regional contraction (e.g. Holtermann et al., 2009; Schindler et al., 2014). Under these conditions, portions of the muscle remain inactive. These regions, while not generating electromyographic signals, would experience passive deformation, due to lateral force transmission via connective tissues (e.g. Purslow, 2010). The ability of pressure in these inactive regions to predict joint force remains unclear.

In order to address this, the prototype masticatory model was used to perform sub-maximal contractions and the pressures in the active and passive regions were correlated to bite force. Since intramuscular pressure measurements are (minimally) invasive, typically a single sensor is used intramuscularly. The benefit of a simulation model is that intramuscular pressure can be measured at any number of points throughout the muscle (a virtual high-density intramuscular pressure measurement). Therefore, the correlation between the temporal-evolution of pressure and bite force was performed at each spatial-point within the muscle, enabling statistical analysis of the resulting correlation coefficients. Furthermore, to test the robustness of the correlations between the active and passive pressures and bite force, the statistical analyses were repeated for a variety of masseters, each with a unique meta-unit architecture.

8.2.1 Methods

The sub-maximal contractions and meta-unit architecture variations were identical to those described in Section 8.1. Briefly, $33/50$ meta-units in each of the left and right masseters were recruited to simulate a sub-maximal static bite over the period $t = [0, 0.6\,\text{s}]$. The bite force was measured over the molar occlusal surface.

Whereas the previous study involved variations on both territory overlap and position; this analysis is restricted to the former, i.e., distributions 0–6 (Table 8.1). Furthermore, pressures in the right masseter are taken as representative of both masseters. Lastly, the pressures are only correlated to the bite force magnitude $F_{\text{M}}(t)$, i.e., not the individual components.

Statistical Analysis

For clarity, the superscript $(\cdot)^k$, which denotes the distribution ID, is omitted (keeping in mind that the analysis outlined below is performed for each distribution separately). To determine the ability of intramuscular pressure in the active and passive regions to predict musculoskeletal motor-output, the pressures in each region were correlated with the bite force. The main steps in this analysis were:

1. Intramuscular pressures $\sigma_{\text{IMP}}(t, \boldsymbol{\xi}_p)$ (Equation 3.37) were extracted at all Gauß points, $p = 1, \ldots, N_{\text{GP}}$. This results in N_{GP} pressure traces, over $t = [0, 0.6\,\text{s}]$.
2. Muscle activities $\alpha_{\text{M}}(t, \boldsymbol{\xi}_p)$ were also extracted at all Gauß points. This results in N_{GP} activity traces over $t = [0, 0.6\,\text{s}]$.

3. Bite force magnitude $F_{\mathrm{M}}(t)$ at the molars was extracted. This results in a single force trace over $t = [0, 0.6\,\mathrm{s}]$.

The pressure traces at each Gauß point were then correlated with the bite force to determine the Spearman correlation coefficient, i.e.,

$$r(\boldsymbol{\xi}_p) = r_p = \mathrm{corr}\left(\sigma_{\mathrm{IMP}}(t, \boldsymbol{\xi}_p), F_{\mathrm{M}}(t)\right), \tag{8.1}$$

for $p = 1, \ldots, N_{\mathrm{GP}}$ and where $r = [-1, 1]$ with values closer to 0 implying a weaker correlation. Then statistical analyses were performed on these coefficients, e.g., the mean $r_{\mathrm{avg}} = \mathrm{mean}(r_1, r_2, \ldots, r_{N_{\mathrm{GP}}})$ and standard deviation $r_{\mathrm{sd}} = \mathrm{std}(r_1, r_2, \ldots, r_{N_{\mathrm{GP}}})$.

Based on the activity traces in the masseter $\alpha_{\mathrm{M}}(t, \boldsymbol{\xi}_p)$, each point was classified as either "active" or "passive". This was done by computing the mean activity $\tilde{\alpha}_{\mathrm{M}}(\boldsymbol{\xi}_p)$ over $t = [0, 0.6\,\mathrm{s}]$, and if this value was 0, the corresponding r_p was classified as passive: $r_p \to r_p^{\mathrm{pass}} \mid \tilde{\alpha}_{\mathrm{M},p} = 0$, and as active otherwise: $r_p \to r_p^{\mathrm{act}} \mid \tilde{\alpha}_{\mathrm{M},p} > 0$.

The mean active pressure correlation-coefficients were computed *within* a distribution (k) by $\tilde{r}^{\mathrm{act},k} = \mathrm{mean}(r_p^{\mathrm{act},k})$. Then, the mean correlation across *all* distributions can be computed by $\tilde{\tilde{r}}^{\mathrm{act}} = \mathrm{mean}(\tilde{r}^{\mathrm{act},k})$. Similarly for the passive pressures.

In other words, $\tilde{r}^{\mathrm{act},k}$ and $\tilde{r}^{\mathrm{pass},k}$, are scalar values that represent the mean-pressure to bite force correlation in the active and passive regions of a single right masseter, respectively. Whereas $\tilde{\tilde{r}}^{\mathrm{act}}$ and $\tilde{\tilde{r}}^{\mathrm{pass}}$ represent the mean-pressure to bite force correlation across the active and passive regions of *all* right masseters (each with a unique meta-unit architecture).

Lastly, to isolate the *relative* predictive ability of the passive pressures, the mean passive correlation-factors per masseter were divided by the active pressure correlations, i.e.,

$$\tau^k = \frac{\tilde{r}^{\mathrm{pass},k}}{\tilde{r}^{\mathrm{act},k}}. \tag{8.2}$$

8.2.2 Results

Across all distributions, intramuscular pressure in the right masseter had a mean and standard-deviation of 53 ± 10 kPa and 6 ± 1.7 kPa in the active and passive regions, respectively. The descriptive statistics of the correlation coefficients for each meta-unit territory distribution are shown via box-plots in Figure 8.5a. Intramuscular pressure within the active regions of the masseter showed, on average, strong to very strong correlations to bite force across all motor-unit distributions. The mean pressure-force correlations in the passive regions were not correlated as strongly, and showed double the spread. The mean and standard-deviation of the correlation coefficients for the active and passive pressures, across all distributions, were $\tilde{\tilde{r}}^{\mathrm{act}} = 0.86 \pm 0.13$ and $\tilde{\tilde{r}}^{\mathrm{pass}} = 0.78 \pm 0.22$, respectively.

Fibre-type distribution was taken as a marker for meta-unit overlap and quantified by the co-dispersion index (Section 8.1.1). The *relative* ability of the passive pressures to predict bite force was then plotted against the co-dispersion index in Figure 8.5b.

8.2.3 Discussion

The statistical analysis of the pressure-force correlation factors showed that not only are the passive regions less strongly correlated than the active regions, on average, but also produce a much wider spread in their force prediction ability. This implies that placing the intramuscular

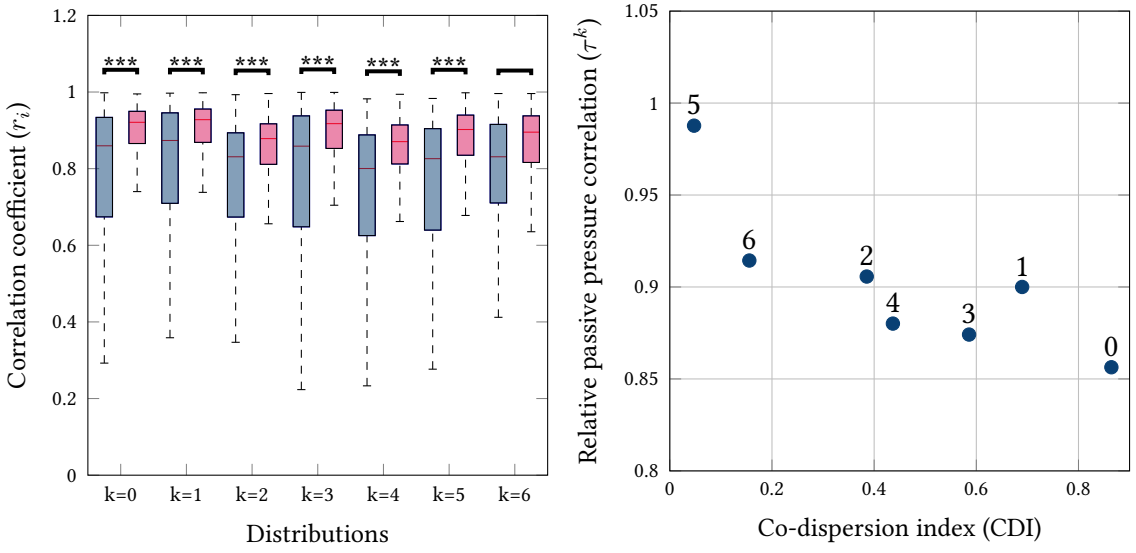

(a) *Spread of correlation coeff.* ***(b)*** *Relative predictive ability of passive pressure.*

Figure 8.5: *Correlations of active and passive compartmental pressures with bite force. (a) blue and red boxes represent passive and active regions. Statistical significant shown with asterisks ($p < 1 \times 10^{-3}$). (b) The distribution parameter IDs are indicated directly above the marks.*

pressure sensor within an active muscular region would increase the chances of measuring pressure which correlates well with joint force.

Passive or lateral force transmission in muscles seems to be the main mechanism that allows passive muscle regions to exhibit pressures which correlate well with overall muscle force output. Connective tissues within the muscle, such as the perimysium and endomysium, enable the transmission of force from active fibres, laterally, to neighbouring passive fibres. Therefore, the passive deformation of these neighbouring fibres, and the pressure developed therein, is closely coupled to the active behaviour of the muscle. The characteristics of force transmission may be influenced by factors such as the material behaviour of the connective tissues and muscle architecture such as geometry, aponeuroses, and fibre orientation.

The results showed that as the motor-unit territories become more evenly distributed, the relative ability of pressures in the passive regions to predict bite force increased. At a very low co-dispersion index, i.e., highly mixed fibres and highly overlapped motor-unit territories, passive pressures performed as well as the active pressures in predicting bite force. As territory overlap increases, the probability of a passive fibre to lie next to an active fibre increases and thus via the lateral force transmission, deformation in the muscle becomes more uniform. Note that the current modelling approach applies a homogenisation step between the discrete fibre distributions and the mechanical simulation. This means that subtle changes in co-dispersion index may not be captured since shearing between individual fibres is not captured.

The masseter showed drastic differences in the passive and active regions. Such regional differences in pressure may be used to investigate muscle fatigue. For example, intramuscular pressure seems to interact with arterial pressure and drive blood perfusion in the muscle (e.g. Kirkebø et al., 1982; Sjøgaard et al., 1986). This may play an important role in regulating motor-output during fatigue (e.g. Sjøgaard et al., 1988; Murthy et al., 2001).

8.2.4 Conclusion

The difference of the force prediction capability between active and passive regions was reduced when the fibre mixing was increased—even when a portion of the muscle was contracting. Such fibre-type mixing is observed for young and healthy individuals. For these cases intramuscular pressures sensor placement may not influence predictive ability. Conversely, for muscles with confined motor-unit anatomy—such as that occurring during ageing and neuromuscular disorders—sensor placement becomes more critical.

8.3 Determining Motor-Unit Twitch Properties in the Masticatory System

Motor-unit twitch properties, such as contraction time and peak force, are commonly measured via the spike-triggered-averaging technique (e.g. Stein et al., 1972; William et al., 1978; Roatta et al., 2008), which involves simultaneously recording intramuscular electrical activity and joint force and using motor-unit discharge times or "spikes", as a trigger to average the joint the force signal. While this technique provides a convenient way to measure in vivo twitch properties, there are certain complications. Several of the shortcomings of spike-triggered-averaging have already been investigated by experimental, simulation, and theoretical approaches (e.g. Troiani et al., 1999; Taylor et al., 2002; Negro et al., 2014; Dideriksen et al., 2018). For example, animal experiments on the non-linearity of twitch force summation (Troiani et al., 1999) or the theoretical analysis of motor-unit synchronisation (during voluntary contractions) (Negro et al., 2014). These, and other limitations, lead to mismatches even under ideal conditions (Negro et al., 2014; Dideriksen et al., 2018). More recently, alternative methods have been proposed to measure in vivo twitch properties. For example, Negro et al. (2017) use a deconvolution approach on sub-populations of motor-units to determine the average twitch response.

Independent of the method to characterise in vivo twitch forces, measurements occur at some point other than the muscle, i.e., at some point connected via biomechanical linkage to the muscle. For example, in masticatory muscles, bite force is typically used as an indirect measurement of their twitch properties (Yemm, 1977; McMillan et al., 1990). While moment arms may be used to account for this; such analytical methods typically oversimplify the anatomy. For example, the geometry is typically treated as two-dimensional, or the biomechanical linkage is treated as rigid, or that motor-unit location within the muscle is not taken into account.

The aim of this case-study is to use the prototype masticatory model to address these issues and investigate the role of biomechanical linkage in the attenuation of the twitch response, in an anatomically realistic three-dimensional model of the masticatory system. This is done by stimulating individual motor-units in the masseter and comparing the twitch forces at the muscle and over the molar. Additionally, the validity of the linear summation of twitches measured at the molar is investigated by comparing algebraically summed twitches to equivalent compound-twitches.

8.3.1 Methods

The geometries, material properties and boundary conditions of the masticatory system model described in the Section 7.2 were used in the present investigation. The territory distribution was described by the distribution parameters with ID 0 in Table 8.1 and is visualised in Figures

7.4a and 7.4b.

To recap, the masseters were populated by 50 meta-units each, whose sizes were governed by an exponential relationship (Equation 5.16). The numbering of the units proceeds from smallest to largest. The twitch properties were spread continuously throughout the pool, with the smallest units being those with the slowest and weakest twitch responses.

In the left masseter, four meta-units—number 10, 20, 30 and 40—were stimulated individually. Forces (all in N) were recorded at a frequency of 2 kHz over the masseter origin (attachment with the zygomatric arch) in the left-right, posterior-anterior and caudal-cranial directions and are denoted: $F^{\text{LR}}_{\text{tw,origin}}$, $F^{\text{PA}}_{\text{tw,origin}}$ and $F^{\text{CC}}_{\text{tw,origin}}$, respectively. Peak twitch force is taken as the maximum value of the magnitude of these components and is denoted $F_{\text{tw,origin}}$. Twitch forces were similarly measured at the molar occlusal surface and are differentiated by the subscript $(\cdot)_{\text{molar}}$.

The twitch force for a particular unit is specified via a superscript, e.g., $F^{10}_{\text{tw,origin}}$ refers to the peak twitch force of unit 10, measured at the masseter origin. By comparing the forces from each measurement site, the effect of the biomechanical linkage between the masseter and tooth was quantified along each axis. The difference in the force components was computed by

$$F^{j}_{\text{tw,error}} = F^{j}_{\text{tw,molar}} - F^{j}_{\text{tw,origin}}, \tag{8.3}$$

where $j = \{\text{LR}, \text{PA}, \text{CC}\}$. The relative error $\bar{F}^{j}_{\text{tw,error}}$ is computed by dividing the above equation with the maximum force of the respective force component.

To verify the linear twitch forces summation, meta-units were stimulated together. The particular combination of meta-units that are simultaneously stimulated are denoted with a plus sign. The particular combination of stimulations were: $10 + 20$, $10 + 20 + 30$ and $10 + 20 + 30 + 40$ and are referred to as *compound* twitches. By comparing the compound-twitch forces (now measured only at the molars) to algebraic summations of the individual twitch forces, discrepancies between the two can be quantified in all three directions.

To investigate impact of the linear summation on the local stress behaviour of the muscle, the shear stresses (in Voigt notation) σ_{13} (in MPa), where the 1-direction is the local fibre-direction, were compared between the two cases. However, since an overwhelming part of the muscle is inactive during these simulations, the mean or standard deviation of σ_{13} would obscure the differences. Alternatively, the skewness of the *difference* between the compound and algebraically summed shear distributions was used. The differences in the shear stresses were computed as follows:

1. For individual twitches, the shear stresses at the point of maximum twitch force (the time-to-peak or TTP), throughout the masseter was recorded:

$$\sigma^{10}_{13}(\text{TTP}, \boldsymbol{\xi}_p),\ \sigma^{20}_{13},\ \sigma^{30}_{13} \text{ and } \sigma^{40}_{13}, \quad p = 1, \ldots, N_{\text{GP}}.$$

2. The individual shear stresses were added together to compute the "summed shear":

$$\tilde{\sigma}_{13}(t = \text{TTP}, \boldsymbol{\xi}_p)^{10+20+30+40} = \sigma^{10}_{13} + \sigma^{20}_{13} + \sigma^{30}_{13} + \sigma^{40}_{13}.$$

3. For the compound-twitch, the shear stresses at the point of maximum twitch

force, throughout the masseter were recorded:

$$\sigma_{13}^{10+20+30+40}(\mathrm{TTP}, \boldsymbol{\xi}_p).$$

4. The difference between the summed and compound shear was computed:

$$\sigma_{13}^{\mathrm{diff}}(\mathrm{TTP}, \boldsymbol{\xi}_p) = \tilde{\sigma}_{13}^{10+20+30+40}(\mathrm{TTP}, \boldsymbol{\xi}_p) - \sigma_{13}^{10+20+30+40}(\mathrm{TTP}, \boldsymbol{\xi}_p).$$

8.3.2 Results

Influence of twitch force measurement location

The range of peak-twitch forces, measured at the molar, predicted by the simulation was between 0.62–6.2 N for meta-unit 10 and 40 (of 50), respectively. The corresponding twitch forces measured over the masseter origin were between 0.69–8.7 N. The time-to-peak differences were in the sub-millisecond range. The peak twitch forces and time-to-peak values for each motor-unit at both measurement locations are plotted in Figure 8.8a.

The relative error in twitch force components, across all units, was between 20-40 %, barring a couple of exceptions (Figure 8.6). For the left-right components, the molar twitch force was higher than the masseter insertion twitch force; whereas for the caudal-cranial component, the bite twitch always underpredicted insertion twitch. The posterior-anterior component showed mixed results, with some units (10 & 30) producing higher twitch forces, while the others were drastically lower (20 & 40).

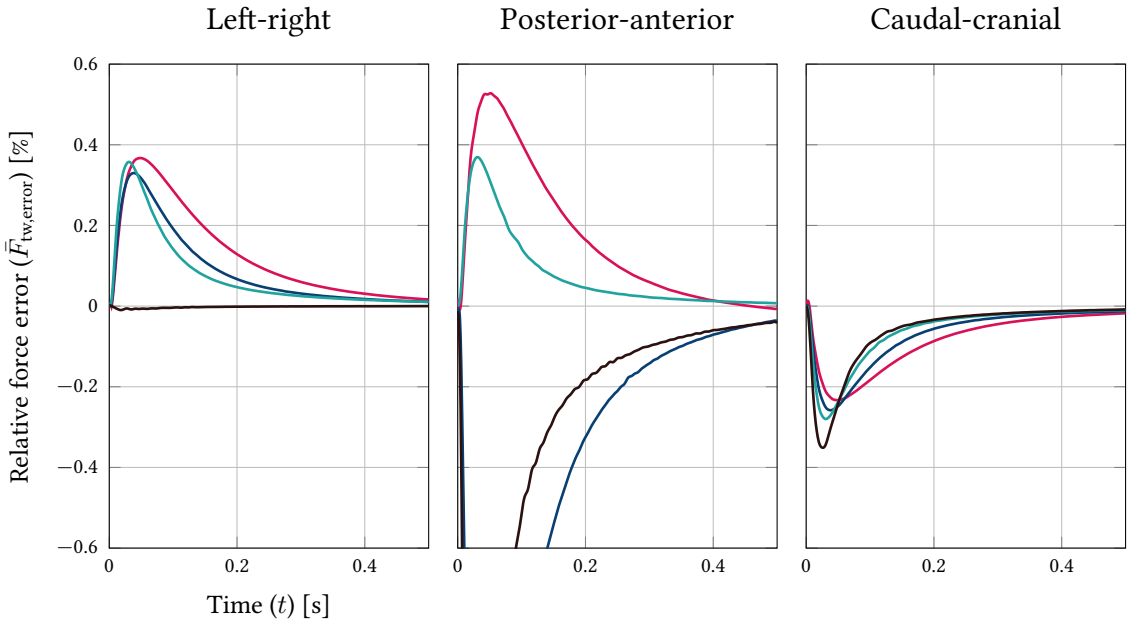

Figure 8.6: *Relative error in twitch force components between measurements at the masseter insertion and at the occlusal surface for independently stimulated meta-units. Where, maroon: meta-unit 10, dark blue: meta-unit 20, green: meta-unit 30 and black: meta-unit 40.*

Difference in summed and compound-twitches

The linearly summed twitch forces generally underpredicted the actual compound-twitch force (Figure 8.7). With the peak compound-twitch forces $10 + 20$, $10 + 20 + 30$ and $10 + 20 + 30 + 40$ being 25 %, 26 %, and 31 % higher than their linearly summed counterparts. This holds for all combinations in the caudal-cranial direction, but not for the other directions. In fact, some compound-twitch forces were not only weaker than their linearly summed counterparts, but were also oriented in opposite directions.

The summed shear stresses σ_{13}, at the point of maximum contraction, were higher than the shear in the compound-twitches. This was evidenced by the fact that the differences (summed shear minus compound shear) in the shear were skewed right—the skewness of $\sigma_{13}^{\text{diff}}$ is computed as -2.7 (Figure 8.8b).

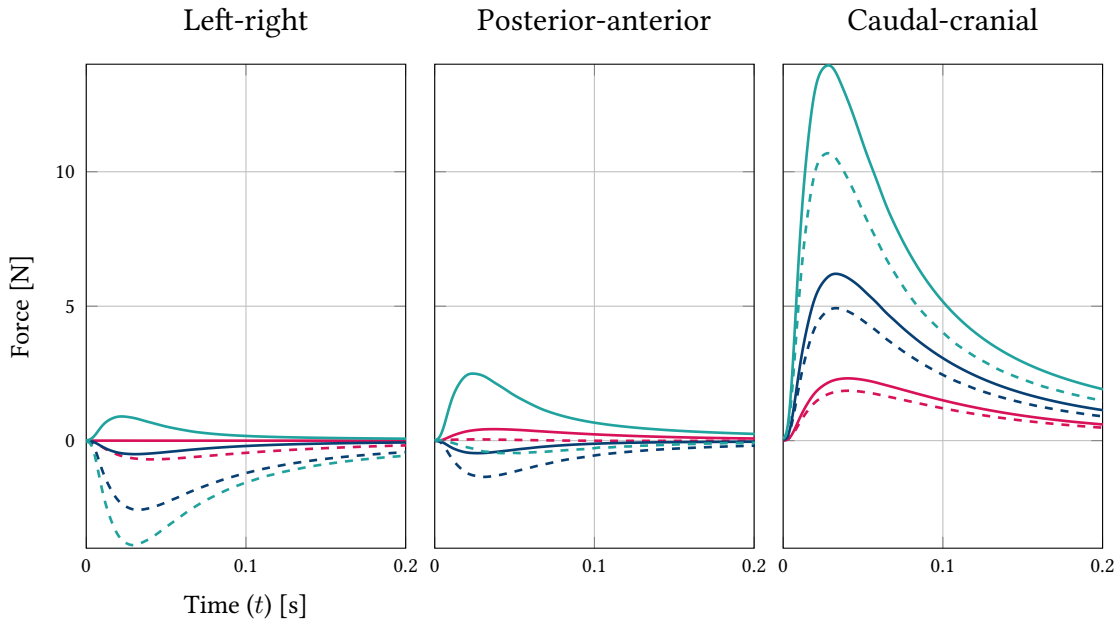

Figure 8.7: *Linearly summed (dashed) and compound (solid) twitch forces. Where maroon: meta-unit 10+20, dark blue: meta-unit 10+20+30 and green: meta-unit 10+20+30+40.*

8.3.3 Discussions

Influence of twitch force measurement location

Joint and muscle forces are typically linked via moment arms (e.g. An et al., 1984; McMillan et al., 1990; Challis et al., 1994; Blemker et al., 2007; Miller et al., 2015). For example, when muscles are modelled as line segments, the moment arms between insertion and origin points and the joint-center are used to relate forces and moments. Similarly, when a region of a three-dimensional muscle model contracts, the "center of force transmission" at the tendon may also be slightly shifted, effectively altering the moment arm to the joint.

Since spike-triggered-averaging typically does not measure twitch force at the muscle directly, moment arms are used to infer muscle twitch force (e.g. McMillan et al., 1990). Such approaches, however, typically treat the mechanical linkages between the two points as rigid, enabling a straight forward mathematical analysis. The advantage of computer simulations in solving the

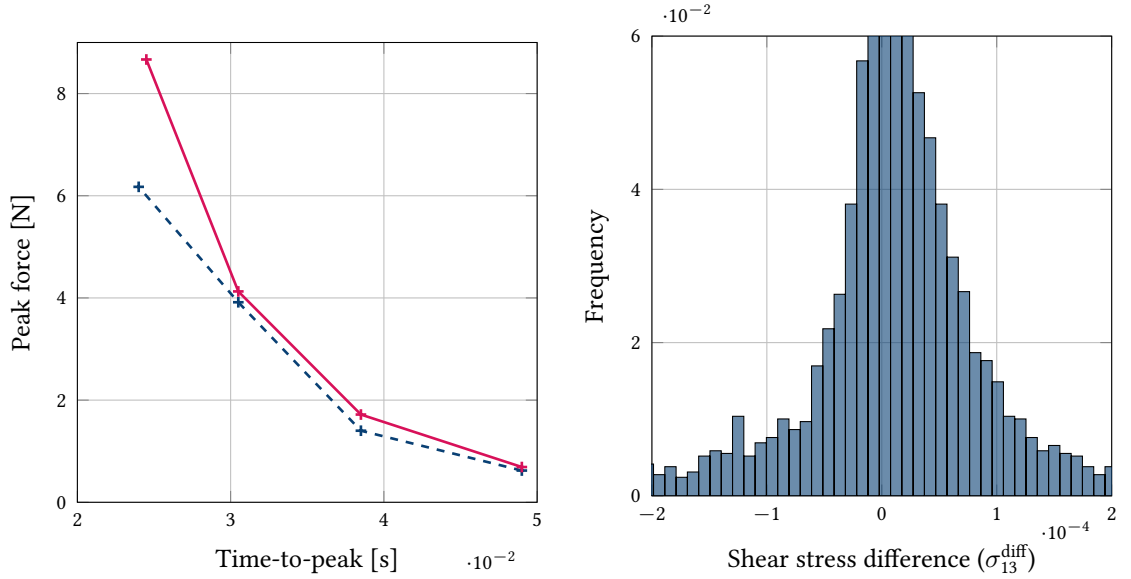

(a) *Insertion vs. molar comparison.* ***(b)*** *Summed vs. compound difference.*

Figure 8.8: *(a) Peak twitch force and TTP measured at the molar: dark-blue, and at the muscle origin: red (b) distribution of shear stress differences obtained by: linearly-summed-twitch-shear minus compound-twitch-shear.*

mechanical problem is that this same principle (balance of momentum) can be applied at a much higher resolution, and also account for the deformation of the components forming the mechanical linkage.

Twitch forces at the molar do not match those at the muscle insertion and this mismatch is not uniform between the twitch force components, i.e., there is a mismatch of the direction of the twitch force. The contraction of the left masseter pulls on the mandible at the attachment area, whose movement is resisted by both the left and right condyles and the right molar. Passive stretching of the right masseter would also occur due to the movement of the mandible. The direction, the mandible is pulled towards, depends on the local fibre orientation of the motor-unit in the left masseter and the exact location of the unit within the masseter cross-sectional area. For example, meta-unit 10 is located anteriorly and deep whereas meta-unit 40 is more posterior and superficial. The interplay of these factors means that, not only is the resistive force distributed differently between the condyles and molar, but also that each force component is affected differently.

These results suggest that, when measuring twitch force magnitude only, the bite twitch seems to predict the muscle twitch quite well, albeit underpredicting the magnitude, with mismatches becoming greater for larger units. Yet, when the twitch force direction is of interest, it is unlikely that measurements at the tooth predict those at the muscle.

Difference in summed and compound-twitches

In the caudal-cranial direction, larger twitch forces were observed for compound stimulation compared to isolated stimulation and linear summation (“greater than linear summation”). This trend was not as clear-cut for the other components. Such mixed behaviour, i.e., greater and less than linear summation, has been observed for twitch force magnitudes for various

combinations of motor-units (e.g. Troiani et al., 1999).

For a compound-twitch, a larger volume of muscle contracts simultaneously when compared to an isolated twitch. Meaning that there is less relative movement of different regions in the muscle, i.e., less shearing within the muscle. Indeed, linearly summing the twitches lead to a higher shear stress in the muscle compared to the compound-twitch. This may reduce the lateral dispersion of energy in the muscle, and lead to more efficient force transfer towards the tendons, resulting in a higher twitch force at the molars for the compound-twitch.

Certain combinations of the left-right and posterior-anterior directions showed less than linear summation. This may also be explained in terms of the shear stress behaviour. The flip-side of more efficient transfer of force towards the tendons may mean that the other components receive a lower contribution. In other words, not only is the force magnitude larger for a compound-twitch, but the distribution of force favours the dominant fibre direction, which for the masseter is along the caudal-cranial direction (CC), then the posterior-anterior direction (PA) and lastly the left-right direction (LR). This can be seen in the reduction of the $10 + 20 + 30 + 40$ compound-twitch force in relation to the equivalent summed twitch, decreasing from the CC to the PA to the LR components.

8.3.4 Conclusion

The relationship between masseter twitch forces and those measured at the molar revealed that the latter underpredicted peak twitch magnitude. Mismatches between the components was related to the position of the motor-unit within the muscle cross-section and also on the local fibre direction. The interplay of these factors makes it difficult to predict twitch force direction from measurements carried out at some biomechanically linked point.

The compound-twitches elicited a higher twitch force than the linearly summed counter parts. This was partly due to more efficient transfer of forces along the fibres towards the tendons. This, additionally, acted to redistribute the force towards the dominant fibre direction of the muscle, leading to some components being overpredicted by linear summation. Therefore, models which linearly sum twitch force magnitudes may underpredict muscle forces. Linear summation to predict twitch force direction should be approached with caution due to the redistribution effects of the compound-twitches.

9 Extended Case-Study: Ageing and Neuromuscular Disorders

The neuromuscular system is continually changing, due to, for example: healthy ageing (Lexell et al., 1988), exercise (Howald, 1982; Messi et al., 2016), or neuromuscular disorders such as Parkinson's disease (Kelly et al., 2018), amyotrophic lateral sclerosis (ALS) (Morris, 1969), or cerebral palsy (CP) (Rose et al., 1998). There is a tremendous variety in the degree, type, and rapidity of the neuromuscular changes that occur during these processes, and are beyond the scope of this thesis, for further details, see Shefner (2001), Mitchell et al. (2012), Henderson et al. (2017) and Larsson et al. (2018). The remodelling of motor-unit anatomy is but one of these changes, and is the focus of this chapter.

The dominant mechanism that facilitates motor-unit remodelling is the successive denervation and reinnervation of muscle fibres. Motor-neuron death causes the denervation of the fibres it innervates, which are (gradually) reinnervated by α-motor-neurons of neighbouring fibres (e.g. Engel, 1965; McComas et al., 1973). The reinnervation may, however, be incomplete, leading to atrophy of these dormant fibres. The atrophied fibres in the muscle are replaced by fat and connective tissue, for example, Lexell et al. (1988) reported that *"for the younger individuals approx.* 70 % *of the muscle area is composed of muscle fibres, while for the older individuals this value is approx.* 50 %*"*. This is synonymous with motor-unit loss, which either begins gradually after age 20 or occurs more abruptly in the latter decades of life, reaching at least 50 % unit loss by the age of seventy (Shefner, 2001, and references therein). Furthermore, type-I fibres (type-S motor-units) appear to be slightly spared with age, with the average fraction of this fibre-type increasing from 50% to 55% between the second and eighth decades of life (Lexell et al., 1988).

Similar neuromuscular changes occur in disease, and may be more drastic than in healthy ageing. For example, in amyotrophic lateral sclerosis (ALS), between 50–70 % motor-unit loss can occur within 10–12 months (Arasaki et al., 1998; van Dijk et al., 2010b). Again, type-I fibres appear to be spared in neuromuscular disorders, with fractions of these fibres increasing to 64% in ALS, 71% in alcoholic neuropathy, and up to 93% in carcinomatous neuropathy (Morris, 1969, Table 1). For some disorders, however, motor-unit remodelling is non-differentiable from healthy ageing, for example, rates of age related motor-unit loss were similar to patients with Charcot-Marie-Tooth disease (van Dijk et al., 2010a).

Muscle fibre atrophy is accompanied by, or leads to, an increase in fibre-type grouping (e.g. Morris, 1969; Lexell et al., 1991). The distribution of fibre-types within young, healthy human skeletal muscle appears to be close to random or even exhibit a slight checker-board pattern (Willison et al., 1980; Lester et al., 1983; Lexell et al., 1991). During the cyclic denervation/reinnervation, fibres become less uniformly distributed and begin to cluster together by type (e.g. Johnson et al., 1973b; Lester et al., 1983; Lexell et al., 1991).

The impact of muscle fibre atrophy and motor-unit remodelling is difficult to quantify via experimental techniques, especially under in vivo conditions in humans. This is because motor-unit remodelling is often accompanied by changes in fibre morphology, biochemistry, and

recruitment strategies. For example, the exact degree to which the motor-unit fibre clustering and muscle atrophy, in isolation, account for force loss is unclear (Mitchell et al., 2012).

The aims of this section are therefore two-fold. First, to extend the motor-unit architecture algorithm to account for cycles of denervation and partial or complete reinnervation and thereby account for motor-unit anatomy in healthy and pathological states (Section 9.1). Second, to apply this process to the prototype masticatory model to compare the function (maximal static bite) of healthy (young/old) and pathological masseters, where the only difference is motor-unit remodelling (Section 9.2). By keeping all other aspects identical in the prototype models, the sole impact of motor-unit remodelling can be quantified.

9.1 Modelling Denervation and Reinnervation

To model aged and pathological states of innervation, a reference motor-unit distribution is subjected to cycles of denervation and reinnervation. The algorithm is based on Lester et al. (1993) and is described briefly in the following.

The starting point is set of fibre-scaffolds $\mathcal{F}_k$ ($k = 1, \ldots, N_{\text{FS}}$), which are innervated by N_{MU} α-motor-neurons. An innervated fibre-scaffold is indicated by the superscript $(\cdot)^i$, i.e., $\mathcal{F} \rightarrow \mathcal{F}^i$. The set of innervated fibre-scaffolds forms a certain motor-unit distribution in the muscle (Section 5.2). Then, at a given time-instance, a denervation event takes place: a certain number n_{dener} of α-motor-neurons degenerate. This severs the connection between the α-motor-neuron and the fibres that they previously innervated, i.e., $\mathcal{F}^i \rightarrow \mathcal{F}$. The denervation events occur regularly, with a frequency of f_{denir}. The units of f_{denir} are 1/T, where T is an arbitrary time unit, e.g., days, months, or years. The denervation process continues till some final time t_{fin} (in T).

Reinnervation occurs between the denervation events, during which, nerve sprouts from α-motor-neuron of neighbouring fibre-scaffolds grow towards the denervated fibres. Nerve sprout growth is governed by sprout growth rates: g_{I} and g_{II} (in mm/T) for type-S and -F α-motor-neurons, respectively. After sufficient time has passed, a sprout of a neighbouring α-motor-neuron reaches and innervates the previously denervated fibre-scaffold. At this point, the fibre-scaffold is innervated by the neighbouring α-motor-neuron and is incorporated into the motor-unit. If however, a neuromuscular-junction remains uninnervated or dormant for a certain amount of time t_{dorm} (in T), it atrophies and cannot be subsequently reinnervated. This occurs since reinnervation proceeds only from immediate neighbours of denervated fibre; thus for a cluster of atrophied fibres, those in the middle may lie dormant for several time instances.

The selective nature of denervation/innervation for type-S and -F neurons is considered by setting a probability of type-S α-motor-neuron denervation at each time instance $\rho_{\text{k}}^{\text{I}}$, and using various sprout growth rates for type-S and -F α-motor-neurons. For example, setting a low likelihood that type-S α-motor-neurons are denervated ($\rho_{\text{k}}^{\text{I}} = 20\,\%$) and doubling their sprout growth rate ($g_{\text{I}} = 2\,g_{\text{II}}$) would result in a "take-over" of the muscle by type-I fibres.

Constitutive modelling considerations

To account for atrophied fibres in the musculotendon complex constitutive relation, they are assigned to a dummy *atrophy* motor-unit, which exists outside the pool of active units. This is achieved by numbering the atrophy motor-unit as $N_{\text{MU}} + 1$. Since the $N_{\text{MU}} + 1^{\text{th}}$ unit does not, by definition (Equation 6.3), receive any activation, the fibres in the atrophy motor-unit

remain inactive during the contraction. By expanding the pool of motor-units in such a way, atrophied fibres are accounted for in a simple manner. The homogenisation is blind to the fact that these fibres are atrophied and proceeds "as usual", but now for $N_{\mathrm{MU}} + 1$ units. Again, the only difference with the atrophy motor-unit is that it cannot be activated.

In summary, the set of parameters t_{fin}, f_{denir}, t_{dorm}, n_{dener}, $g_{\mathrm{r}}^{\mathrm{I}}$, $g_{\mathrm{r}}^{\mathrm{II}}$ and $\rho_{\mathrm{k}}^{\mathrm{I}}$ characterises the ageing/disease process. The cyclic denervation/reinnervation procedure is integrated into the workflow prior to the homogenisation step. Restating Equation 6.34 with an additional subscript $(\cdot)_{\mathrm{rm}}$ to denote the aged/pathological motor-unit architecture:

$$\underbrace{\mathcal{B}_0,\ \boldsymbol{f}(\boldsymbol{Y})}_{\substack{\text{muscle}\\ \text{architecture}}} \rightarrow \underbrace{\{\mathcal{S},\mathcal{F}\}}_{\substack{\text{reconstructed}\\ \text{microstructure}}} \rightarrow \underbrace{\{\tilde{\mathcal{S}},\tilde{\mathcal{F}}\}}_{\substack{\text{reference}\\ \text{distribution}}} \rightarrow \underbrace{\{\tilde{\mathcal{S}}_{\mathrm{rm}},\tilde{\mathcal{F}}_{\mathrm{rm}}\}}_{\substack{\text{reinnervated}\\ \text{distribution}}} \rightarrow \kappa_{\mathrm{p},i}(\boldsymbol{X}^{\mathrm{micro}}) \rightarrow \hat{\kappa}_{\mathrm{p},i}(\boldsymbol{\xi}) \rightarrow \mathbf{k_m}, \tag{9.1}$$

where $i = 1, \ldots, N_{\mathrm{MU}} + 1$, including the atrophy motor-unit.

Demonstration of aged and diseased fibre distributions

The idealised model as described in Section 5.3.5 was used to demonstrate the denervation/reinnervation model. Except, the number of fibres was reduced from approximately 12,000 to 3000. Variations were taken on the type of denervation/reinnervation, for example, slow sprout growth rates or denervation of more than one motor-unit at once; the characterisation parameters are given in Table 9.1. The parameters were chosen manually to elicit differing motor-unit remodelling.

In addition to visualising fibre distributions over the cross-section at evenly spaced time intervals, several common diagnostic statistics were recorded at the end of the process, namely: co-dispersion index, fraction of atrophied fibres, fraction of remaining type-I fibres, and the total number of denervated motor-units.

Table 9.1: *Cyclic denervation/reinnervation parameters for the idealised geometry. Variables are explained in Section 9.1.*

ID	$t_{\mathrm{fin}}/\mathrm{T}$	$f_{\mathrm{denir}}/\mathrm{T}^{-1}$	$t_{\mathrm{dorm}}/\mathrm{T}$	n_{dener}	$g_{\mathrm{r}}^{\mathrm{I}}/\mathrm{mm}\cdot\mathrm{T}^{-1}$	$g_{\mathrm{r}}^{\mathrm{II}}/\mathrm{mm}\cdot\mathrm{T}^{-1}$	$\rho_{\mathrm{k}}^{\mathrm{I}}$
A	124	2	3	1	1	1	0.3
B	170	4	30	2	0.125	0.125	0.4
C	170	2	25	1	0.025	0.025	0.4

Results

Snapshots of the fibres in the muscle cross-section, at various time instances during the denervation/reinnervation process, for the different parameter-sets, are shown in Figure 9.1. The segregation or clustering of type-I and type-II fibres can be seen for parameter-set A and B, respectively, and is quantified by the corresponding increase in co-dispersion index from 0.0 to $+0.14$ and $+0.45$, respectively. Furthermore, given the slow growth rate, the atrophy of fibres was observed for parameter-set C.

At the end of the denervation and reinnervation process, diagnostic measures were computed and are summarised in Table 9.2. The clustering of the fibres is reflected with increases in co-

dispersion index. Reducing the sprout growth rate and increasing denervation frequency lead to a 23 % fibre atrophy (parameter-set C). The slightly lower probability to denervate type-I fibres lead to an increase of 17 % of this fibre-type (parameter-set B).

Table 9.2: *Fibre distribution statistics at the end of the denervation/reinnervation cycles. Where atroph.: atrophied, MUs: motor-units, and denerv.: denervated. The parameter sets are indicated via the IDs A-C (see Table 9.1).*

ID	CDI	%-atroph.	%-type-I	MUs denerv.
-	0.00	0%	75%	0
A	0.14	0%	92%	53
B	0.45	0%	63%	19
C	0.50	23%	82%	30

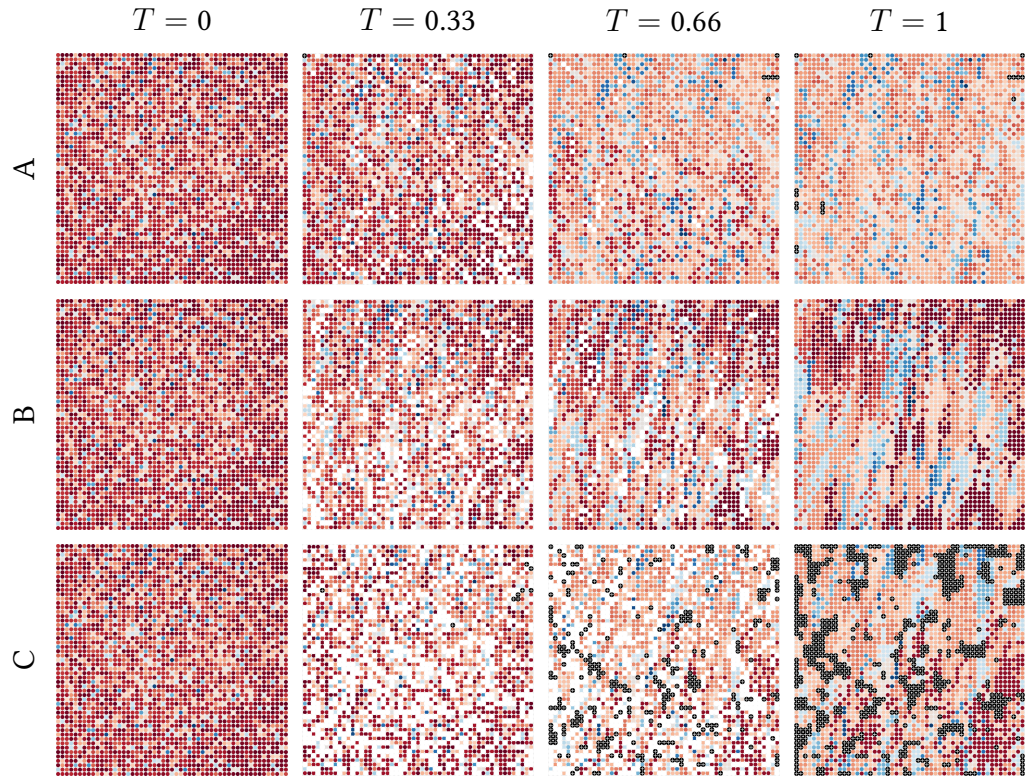

Figure 9.1: *Evolution of fibre distribution during denervation/reinnervation cycles, viewed in the cross-section of the idealised muscle geometry, with fibres oriented out of the page. Fibres belonging to the smallest and largest motor-units are colour-coded from dark-blue (to cream) to maroon, respectively. Additionally, white and black coloured fibres indicate denervated and atrophied fibres, respectively. Each rectangular cross-section is* 40×40 mm.

9.2 Changes in Bite Force during Ageing and Disease

Proper and healthy functioning of the masticatory system significantly impacts the quality of life of individuals (Gerritsen et al., 2010). Bite force is often used to diagnose healthy ageing (e.g. Palinkas et al., 2010) and can also be used to diagnose neuromuscular disorders (e.g. Guimaraes et al., 2007; Ueki et al., 2007; Riera-Punet et al., 2018). However, the atrophy that accompanies ageing (and neuromuscular disorders) typically underpredicts the amount of force loss. For example, for patients above 75 years of age, Dey et al. (2009) found a drop in grip-strength of 18 %, even though fat-free tissue loss was only about 3 %. Further examples include a loss of 16 % of knee-extensor strength despite only a 5 % loss of thigh muscle mass (Mitchell et al., 2012, and references therein).

To determine the effect of neuromuscular reorganisation *alone* on motor-output; the prototype model is used to simulate a unilateral maximal bite with healthy and reinnervated masseters. The healthy masseter has a non-clustered, non-atrophied motor-unit architecture. Then, other prototype models with varying degrees of fibre clustering and atrophy were generated by subjecting the healthy masseter to cycles of denervation and reinnervation. The twitch properties, muscle geometries, recruitment strategies and excitatory drive were kept identical between the models. Therefore, any changes in bite force arise solely due to the changes in masseter architecture, including the degree of muscle atrophy.

9.2.1 Methods

The control (or healthy) model was generated by populating the right masseter with $\breve{N}_{\text{MU}} = 50$ meta-units, whose innervation-ratios are described in Section 7.3.1. Using the results of the motor-unit distribution study (Section 5.3), the motor-unit distribution was characterised by $\{R,\, D\} >> \text{CSA}^{\text{R}}$, to ensure the maximal amount of fibre-type mixing. That is, the selection spaces for central and peripheral axons were greater than the muscle's cross-sectional area, thus the motor-units were randomly distributed throughout the muscle. This yielded a co-dispersion index of 0, which is observed in healthy, young adult muscle (Brenner et al., 1987).

Aged/disordered protoype models

The masseter of the healthy model was subjected to 3 types of denervation/innervation cycles to produce a variety of fibre-type dispersion, atrophy, and proportional type-I fibres. All cycles were run for $t_{\text{fin}} = 100$ time intervals with varying parameters: frequency of denervation events, period of dormancy prior to fibre atrophy, and growth-rate of neighbouring α-motor-neuron-axons (Table 9.3). This yielded 4 prototype models, including the model with healthy muscles.

The remaining parameters governing the denervation/innervation cycles were constant for all cycle types: (i) per denervation event, a single α-motor-neuron was denervated $n_{\text{dener}} = 1$, (ii) the growth rate of the type-F α-motor-neuron spouts was identical to those of the type-S neurons $g_{\text{r}}^{\text{II}} = g_{\text{r}}^{\text{I}}$, and (iii) the denervation was slightly biased to preserve type-S α-motor-neurons $\rho_{\text{k}}^{\text{I}} = 0.4$.

It was assumed that initially the smallest $37/50$ of meta-units were type-S, i.e., contained type-I muscle fibres. Note that this classification is to facilitate the calculation of the co-dispersion index only, and does not affect the twitch properties of the motor-units (which vary continuously between the smallest to largest motor-unit). The innervation-ratio follows an

Table 9.3: *Cyclic denervation/reinnervation parameters and fibre distribution statistics in the masseter model. Where CDI: co-dispersion index, atroph.: atrophied, MUs: motor-units, denerv.: denervated, and the remaining variables are explained in Section 9.1.*

ID	t_{fin}/T	$f_{\text{denir}}/\text{T}^{-1}$	t_{dorm}/T	$g_{\text{r}}^{\text{I}}/\text{mm}\cdot\text{T}^{-1}$	CDI	%-atroph.	%-type-I	MUs denerv.
-	-	-	-	-	0.00	0%	75%	0
A	100	3	4	0.27	0.08	3%	56%	6
B	100	4	5	0.17	0.51	38%	84%	12
C	100	2	7	0.09	0.64	54%	84%	25

exponential distribution, with many small units and a few large units. Therefore, although 75 % of the meta-unit are type-S, this translates to about 50 % type-I fibres. This is similar to Enoka et al. (2001).

Bite force simulation

A unilateral maximal bite was performed with each of the healthy, aged, and disordered prototype models. All modes were supplied with identical excitatory drive: the meta-unit pool of the right masseter was recruited (left masseter remains passive) via an excitatory drive $E(t)$ increasing from 0 to 1.1 over $\Delta t = 0.7s$ and held constant afterwards. For all models, the recruitment and twitch properties were kept identical.

9.2.2 Results

All simulations were performed with `Abaqus/Explicit` (v6.14-3, Dassault Systèmes, France), using an `AMD Opteron 6373` (2.3 GHz, 32 cores) with 24 GB memory[1] with computation times of approximately 10–15 h. The force components along the left-right F_{LR}, posterior-anterior F_{PA} and caudal-cranial F_{CC} axes, together with the force magnitude F_{M}, and angles (in the horizontal plane θ_{H} and elevation θ_{V}) at maximum contraction are listed in Table 9.4. Forces are in N and angles in degree.

Table 9.4: *Influence of ageing and pathology on peak bite force.*

	F_{LR}/N	F_{PA}/N	F_{CC}/N	F_{M}/N	$\theta_{\text{H}}/\text{degree}$	$\theta_{\text{V}}/\text{degree}$
-	65	11	376	382	80	83
A	63	12	363	368	79	83
B	30	7	185	187	79	83
C	16	7	113	114	68	85

As expected, force loss was positively correlated with masseter atrophy, however, atrophy amount underpredicted the amount of force loss. Force magnitude dropped by 4 %, 51 % and

[1] Part of the `LEAD` cluster at the University of Stuttgart.

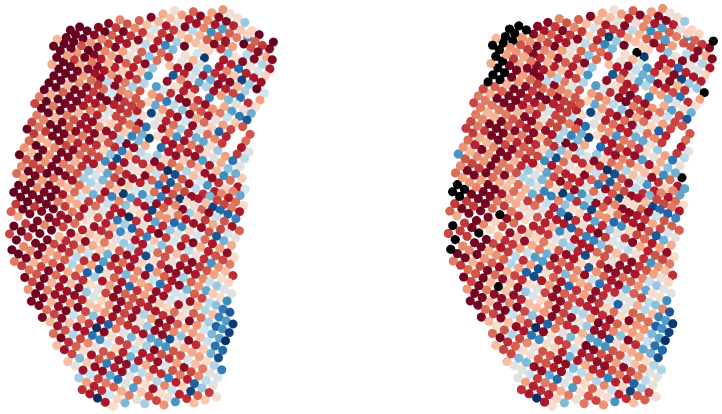

(a) *Healthy.* ***(b)*** *ID A.*

(c) *ID B.* ***(d)*** *ID C.*

Figure 9.2: *Fibre distributions of the right masseter after cycles of denervation/reinnervation. Motor-unit fibres are colour coded from smallest: blue to largest: maroon, with black coloured fibres indicating atrophied fibres. The cross-sectional area of the masseter is approximately* 630 cm^2.

70 % for atrophy amounts of 3 %, 38 % and 54 %, respectively. Force components F_{LR} and F_{CC} showed similar trends, however F_{PA} was less affected: 37 % at 54 % atrophy.

Bite force angles were less sensitive to the fibre redistribution and atrophy: both horizontal and elevation angles showing virtually no change for parameter-sets A and B. For parameter-set C, a slight change in θ_{V} of 2 % and a moderate change in θ_{H} of 15 % were observed.

Normalised bite forces, per parameter-set, were computed by:

$$\bar{F}_{\mathrm{M}}^{j}(t) = \frac{F_{\mathrm{M}}^{j}(t)}{\max(F_{\mathrm{M}}^{j})}, \tag{9.2}$$

where $j = \{\mathrm{A,B,C,D}\}$ are the different parameter-sets, and are shown in Figure 9.3a. The orientation of the bite force, in terms of its angle in the sagittal plane θ_{H}^{j}, for each parameter-set is shown in Figure 9.3b.

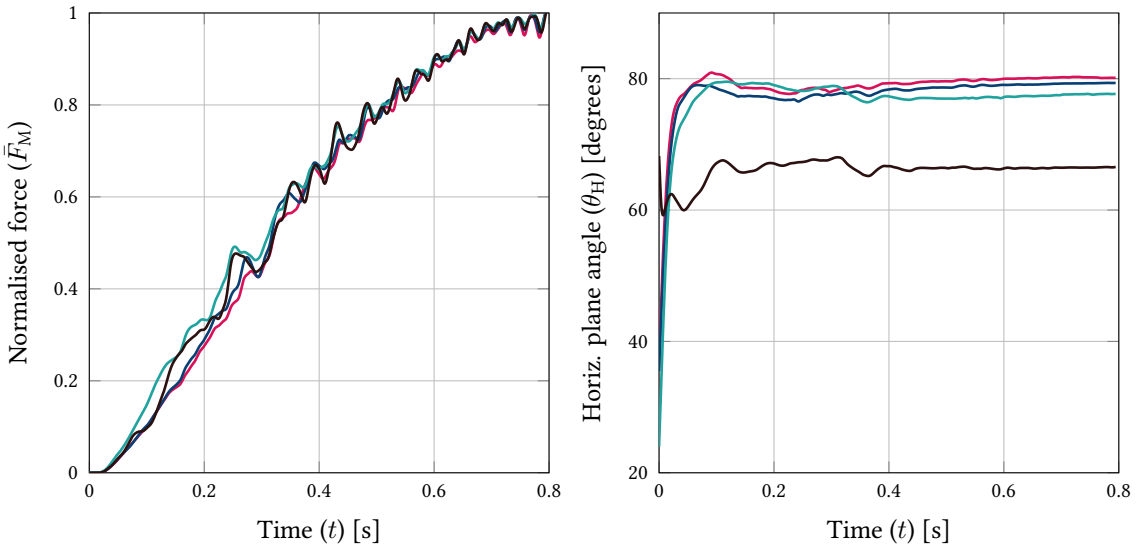

(a) *Magnitude.* ***(b)*** *Orientation.*

Figure 9.3: *Influence of ageing and pathology on bite force, where maroon: healthy, dark-blue: ID A, green: ID B and black: ID C.*

9.3 Discussion

In this case-study, the effect of masseter fibre-redistribution and -atrophy on static bite force was investigated. The results show that, as expected, the amount of atrophy is positively correlated with the loss of peak bite force magnitude. Surprisingly, even though all other neuromuscular properties were unaltered, atrophy still could not explain the entire amount of force loss. For example, force magnitude dropped by 51 % for 38 % atrophy. Assuming that 38 out of 51 % of the force loss can be explained by the atrophy amount, the possible causes of the remaining 13 % are discussed below.

Since denervation of type-F motor-units was preferred; a larger portion of, weaker, type-I fibres survived as atrophy increased. This means that not only were there fewer total fibres in the muscle, but those that remained, produced a lower peak force. Another contributing factor is the shifting mean centre of activity within the masseter. As the sensitivity analysis revealed (Section 8.1), this has a substantial impact on bite force.

This means that the conversion of fibre-type and architectural changes in motor-unit may explain the remaining gap in the force loss. This is similar to the findings of Granger et al. (1999), who when measuring a 50 % lower bite force for patients suffering from spinal muscular atrophy (SMA) hypothesised that 10 % is due to changes in mechanical advantage, *"suggesting that the intrinsic jaw muscle strength is reduced by at least* 40 % *in SMA patients."*.

The normalised force shows that as the motor-unit reorganisation increases (atrophy and increase in type-I fibres), a less smooth force is observed. This is because of the conversion of the surviving fibres to smaller type-S motor-units, which means that these units grow in relative size. The recruitment of the, now relatively larger, type-S units cause larger jumps in the force magnitude. Since, the surviving (larger) type-F units are untouched; increases in force unsteadiness are observed mainly in the low to medium force range.

Bite force orientation was not affected to the same degree as the magnitude, which remained largely constant until more than half of the masseter was atrophied. The insensitivity of the

bite force orientation to atrophy could be due to the spatial distribution of the atrophied fibres. Consider an extreme case where all atrophied fibres are located in the deep head of the masseter; this would of course heavily affect the bite force orientation (mainly in the posterior-anterior axis). But the cross-sectional images of the fibre distribution (Figure 9.2) show that the atrophied fibres were spread approximately uniformly.

Bite force reorientation above 50 % atrophy may be due to the effect of atrophy on overall masseter contraction. For example, Hodges et al. (2003) observed marked changes in pennation angle, muscle thickness and fascicle length *below* 50 % of maximum voluntary contraction, above which these values stabilised. That is, when reducing force (or contraction amount) from 100 % to 50 %, the muscle structure remains largely steady, and begins to change once it falls below 50 % contraction. Here, this means that once overall force drops *below* 50 % of maximum voluntary bite force, changes in pennation angle could influence the bite force orientation. A 70 % force loss was observed for 54 % atrophy, and for this case, the bite force orientation was also drastically affected.

The mechanical behaviour of the musculotendon complex was unaltered, i.e., the passive response of the atrophied and healthy muscle was identical. However, ageing and neuromuscular disease often leads to alterations (stiffening) in skeletal muscle mechanical behaviour (e.g. Smith et al., 2011; Eby et al., 2015). These changes may be incorporated into the constitutive model via a phenomenological approach or via more advanced homogenistion techniques that account for microstructural changes in the muscle (collagen) ground matrix (e.g. Bleiler et al., 2019; Bleiler et al., 2021).

Despite the limitations of this case-study, the limited scope being one of them, it highlights the potential of investigating three-dimensional neuromuscular structure and musculoskeletal functional output in an integrated sense. Atrophy explains about 70-80 % of the force drop, the remaining 20-30 % stems from factors including fibre-type conversion and mean motor-unit position. Force orientation does not seem to change till more than half of the muscle is atrophied, although this may be due to the specific pattern of atrophied fibres considered in the current study.

10 Discussion and Outlook

This thesis developed a method and workflow to embed motor-unit activity and anatomy into three-dimensional, anatomically realistic, continuum-mechanical skeletal muscle models. The fundamental element of force production—the motor-unit—was thus allowed to exert its influence over musculoskeletal function at the joint-scale. A prototype masticatory system model was used to demonstrate the integrated neuro-musculoskeletal modelling approach, and was used to perform a variety of case-studies. The major contributions of the thesis were:

- A constitutive relation for the musculotendon complex, implemented in a `FORTRAN` user-material, integrating the microstructurally derived neural activity, anatomy, and allowing for atrophied fibres (Chapters 4 & 6).
- A method to compute motor-unit recruitment and twitch behaviour, implemented in `MATLAB` (Chapter 5).
- A method to approximate muscle microstructure in three-dimensions, for non-trivial geometries such as bipennate and multi-pennate muscles (Chapter 5).
- A method to generate motor-unit anatomy, implemented in `MATLAB`, able to reproduce typical features of mammalian motor-unit territories and undergo cycles of denervation and reinnervation (Chapters 5 & 9).
- A workflow implemented in `MATLAB` to homogenise and integrate neural information for use with finite element skeletal muscle models (Chapter 6).
- An anatomically realistic prototype, multi-muscle, neuro-musculoskeletal model of the masticatory system, implemented in the commercial finite element software `Abaqus` (Chapter 7).

The key results, including those from the case studies, were:

- The assumption of instantaneous action-potential propagation minimally affects the mechanical response. For a 40 cm musculotendon complex (2.5 muscle-to-tendon ratio) the force response reached the same magnitude but was advanced by 17 ms compared to the case with action-potential propagation (Section 6.1).
- Neglecting motor-unit structure and activity drastically impacts bite force at low to medium activation levels. The impact was greater in force orientation (60° difference at 50% MU-pool recruitment) than in force magnitude (12% difference at 50% MU-pool recruitment) (Chapter 7).
- The "centre of activity" of a motor-unit territory affects bite force more than territory overlap. The dispersion of fibres had a smaller impact on bite force magnitude and direction. Altering territory-overlap and territory-position resulted force-magnitude ranges of 5.5 N and 26 N, respectively (Section 8.1).
- Intramuscular pressure in active compartments better predicts bite force than in passive regions. Mean correlation coefficients, between intramuscular pressure

and bite force, in the active and passive regions were $r = 0.86 \pm 0.13$ and $r = 0.78 \pm 0.22$, respectively (Section 8.2).

- The higher the motor-unit territory overlap the better the correlations of pressure in passive regions to bite force.
- Twitch force measured at the tooth under-predicts the force measured at the muscle insertion. For the masseter, a 10% difference in force magnitude was seen for MU 10 (of 50); and 20 % for unit 40 (Section 8.3).
- Linearly summed twitch forces under-predict compound twitches, by between 6-10% (both taken at the tooth).
- The greater the number of co-contracting motor-units, the lower the shear-stress in the muscle, compared to the equivalent linearly summed case.
- Motor-unit atrophy explains about 80 % of the force reduction (Chapter 9).
- Fibre-remodelling during ageing/disease affects force orientation after about 50 % of the muscle has atrophied.
- Growth and atrophy of certain motor-units during ageing/disease causes less steady force below about 80 % force.

These findings should be interpreted with care given the limitations of the models, case-studies, and methods. While specific drawbacks were covered in their respective chapters, the general limitations of the thesis, such as the limited scope and model idealisations, are covered here (Section 10.1).

Despite these limitations, there were several key implications of the thesis. Again, the specific implications of the methods and case-studies are covered in their respective chapters. The focus here is on the general implications of the thesis in the field of musculoskeletal simulation, and are discussed in Section 10.2. Lastly, a broader view is taken and future research directions including augmenting experimental techniques and informing medical interventions are highlighted, ending with concluding remarks (Section 10.3).

10.1 General Limitations and Proposed Solutions

10.1.1 Limited scope

A single joint-system—the masticatory system—with a single geometry and fixed fibre architecture was used for both the modelling comparisons and the case-studies. The latter were proof-of-concept investigations that were limited in scope from the outset. Modelling comparisons highlighted the importance of including motor-unit activity and anatomy in three-dimensional finite element simulations of motor-output. The generalisability of these findings rests on the uniqueness of the masseter and the masticatory system. Masseters show task-dependence or selective activation, for example, different regions of the masseter are differently active during various jaw movements (Blanksma et al., 1997; Schindler et al., 2005; Ogawa et al., 2006; Schindler et al., 2014). This was reflected in the prototype model by the dependence of bite force on the particular subset of recruited motor-units.

Other joints and muscles that exhibit task-dependence, then, would also show altered motor-output when regionally activated. Muscles which display such task-specificity include the: lateral pterygoid (Schindler et al., 2005), biceps brachii (Holtermann et al., 2005), and triceps

surae (Csapo et al., 2015) (other examples are given in Chapter 1). In other words, using a model with three-dimensional motor-unit anatomy is crucial to understanding nuances in the contractile function of these muscles, at low to medium activation ranges.

Furthermore, from an anatomical perspective, heterogeneous fibre-type distribution across the muscle cross-sectional area may indicate functional heterogeneity. Since fast and slow motor-units are, in turn, composed of fast and slow fibres, fibre-type can be used as a rough marker for territory distribution. Such preferential location of fibre-types within regions of muscle cross-sectional area is fairly common in human muscles. For example, this has been observed for the: temporalis (Korfage et al., 1999), biceps brachii, deltoid, rectus femoris (lat. head), vastus medialis (Johnson et al., 1973a), tibialis anterior (Johnson et al., 1973a; Henriksson-Larsén, 1984), and vastus lateralis (Johnson et al., 1973a; Lexell et al., 1983). Further examples can be found in Johnson et al. (1973a, Table 5).

The experimental evidence suggests that the functional heterogeneity of the masseter is not unique. Therefore, the inclusion of such information in continuum-mechanical musculoskeletal models is paramount in understanding their function, especially during sub-maximal contractions, which include day-to-day tasks and posture maintenance.

10.1.2 Number of motor-units and mesh size

In the prototype masticatory system model, motor-units were not individually modelled, but instead were grouped into so-called meta-units. Recruiting a meta-unit thus recruited all motor-units that it contained, effectively synchronising their activities. Furthermore, meta-units also overestimate the size of motor-unit territories. For example, consider a meta-unit territory formed from two motor-units that span the superior and deep heads of the masseter. If recruited individually, the motor-units would produce forces aligned with their local fibre directions. When recruited together, via the meta-unit, the (larger) force magnitude would be directed along the averaged direction of the two motor-units.

Both temporal and spatial synchronisation of motor-units reduces the granularity of motor-output within the muscle. Synchronisation of motor-units has been shown to reduce force steadiness (e.g. Yao et al., 2000) and is typically observed during fatigue (e.g. Contessa et al., 2009), rather than normal conditions. Additionally, using a low number of motor-units in a multiscale model resulted in both a less steady force and a reduction in force magnitude (Röhrle et al., 2012).

Therefore, peak forces predicted by the prototype model were likely less steady and lower in magnitude than would be expected if a larger number of meta-units were considered. Regarding the modelling comparison, however, the same number of meta-units were used to derive the activation for both the motor-unit driven and status-quo models. Therefore, the relative, rather than absolute bite force (and motor-output in general) was of primary concern.

The maximum number of motor-units that can be simultaneously considered in the model is not an inherent limitation of the method itself, but is constrained by computational time. For any finite element simulation, a finer mesh results in increased computational cost. For a fixed muscle volume, as the number of meta-units increases, so does the spatial resolution required to resolve them. Basically, the same (cross-sectional) area is being divided up into smaller and smaller pieces. This means that a finer finite element mesh is required, since the element dictates the area over which a motor-unit can transmit a (contractile) force. Such a finer mesh would be required along the length of the muscle.

Adaptive meshing is one way to mitigate the increased costs of mesh refinement, by setting mesh size proportional to motor-unit size. This can be combined with model-order-reduction or highly-parallel computing techniques (e.g. Mordhorst et al., 2017; Maier et al., 2019) to reduce overall computational time.

10.2 General Findings and Implications

When compared to a traditional macroscopic model, the prototype model showed marked changes in bite force and in masseter intramuscular pressure, especially at low to medium activation levels. For example, as the motor-units in the deep region were active at lower contraction levels, the bite force was directed posteriorly. As larger, more superior, motor-units were recruited, the bite force was directed anteriorly. No such reversal was observed when the masseters were uniformly activated, i.e., the status-quo modelling approach. Furthermore, intramuscular pressure was drastically different between the two models. The status-quo model not only underpredicted the mean pressure, but also distributed the pressure differently within the masseter. The pressures in the prototype model clearly reflected the active motor-units.

As the muscle approached full activation, the entire population of motor-units were recruited and the differences in motor-output between the two models vanished. The agreement between the two approaches at maximal contraction would not hold, however, if the history of compartmental activation is taken into account. For example, blood perfusion between compartments, which is influenced by intramuscular pressure (e.g. Sjøgaard et al., 1986), would likely reach a different end-state given different histories of regional pressure.

The integrated neuro-musculoskeletal prototype masticatory model appears to be the first time that the activity and distribution of individual motor-units was treated in the context of joint-system function, in a three-dimensional finite element model. Given that the proposed method shares similarities with both traditional macroscopic and multiscale models, it has implications for both.

10.2.1 Implications for traditional macroscopic models

Motor-unit activities, along with their spatial distributions (motor-unit anatomy) are combined to compute the muscle's heterogeneous activity. Since this computation occurs during an offline phase, the added computational cost during run-time, in comparison to traditional macroscopic models, is minimal.

The nature of the proposed method to calculate neural information as a *pre-computation* means that it could be incorporated into traditional macroscopic constitutive relations of muscles in a relatively straight-forward manner. More specifically, in those relations where the active stress is additively split—the activation parameter provides a convenient entry point, for example, those of Gielen et al. (2000), Oomens et al. (2003), Blemker et al. (2005b), Röhrle et al. (2007), Wu et al. (2014), Röhrle et al. (2017) and Ramasamy et al. (2018).

Computing skeletal muscle motor-output from motor-unit distribution and activity may lead to more accurate predictions of local stresses and strains. This may improve, for example; damage modelling, which is based on critical strains in the muscle (Ramasamy et al., 2018); strain inhomogeneity within the muscle (Blemker et al., 2005b; Rehorn et al., 2010); contact pressure between muscle and bone (Röhrle et al., 2017); muscle deformation and shape change (Wu et al., 2014; Fan et al., 2017); and movement predictions for wide muscles with broad

attachment areas (Péan et al., 2019). Selected examples are detailed below.

First, consider the model of the shoulder joint (Péan et al., 2019), where 23 muscles span the shoulder joint. Certain muscles, such as the upper trapezius show task-dependence (e.g. Jensen et al., 1997; Samani et al., 2010) and thus movement predictions may be improved by taking individual motor-unit anatomy and activity into account.

Second, consider the static bite force simulation (Weickenmeier et al., 2017), which treats the masseter as a single contracting unit. This, however, does not reflect the well documented functional heterogeneity of the masseter (e.g. Hannam et al., 1994; Blanksma et al., 1995; Blanksma et al., 1997; Schindler et al., 2005; Ogawa et al., 2006; Schindler et al., 2014) which was highlighted by the prototype masticatory model.

Third, consider the case of muscle strains in the biceps (Blemker et al., 2005b). It has been shown that supination/pronation activates task-specific motor-units in the biceps (e.g. van Zuylen et al., 1988; Holtermann et al., 2005). Therefore, for such complex movements, the modelling of individual motor-unit anatomy and activity may improve local strain predictions.

The results of the thesis showed that the impact of the motor-unit driven modelling approach was more pronounced for certain muscle structures, motor-unit anatomy, and contraction levels. As mentioned, in cases where maximal force is of interest, compartmental activation seems to have little impact. Furthermore, simpler muscle geometries are less impacted in their force generation by regional activation. For example, the compartmental activation of the idealised geometry had virtually no impact on force-output—intramuscular pressure was affected however. The anatomy of the motor-units plays a crucial role as well. As the motor-units fibre distribution becomes uniformly spread throughout the muscle, they generate uniform contractile stresses within the muscle when recruited. However, as discussed in Section 10.1.1, this is atypical for several human skeletal muscles.

10.2.2 Implications for multiscale models

In addition to muscle geometry, multiscale models require the coordinates of individual muscle fibres in three-dimensional space. To simulate physiologically realistic muscle activation, these virtual fibres are typically grouped into motor-units and stimulated at their neuromuscular-junctions (e.g. Davidson et al., 2006; Röhrle et al., 2008; Röhrle et al., 2012; Heidlauf et al., 2014; Mordhorst et al., 2014). The fibre geometries, their grouping into anatomically realistic motor-units and virtual neuromuscular-junctions can be provided by the method proposed in this thesis, both for healthy (young/old) and neuromuscular-disordered states.

10.2.3 Implications for other models

Tongue modelling. The tongue is a muscular hydrostat, being composed of several interlaced muscle fibre groups. The selective activation of these groups allows the hydrostat to perform complex movements. From a macroscopic modelling perspective, this means that each point within the hydrostat contains various fractions of muscles.

This is analogous to the way in which motor-units are treated in the current approach. The difference being that while motor-units always transmit force in the same direction, i.e., the fibre orientation of the muscle, in a hydrostat this direction can vary depending on the combination of muscles active at a point. Similar to the approach by Wang et al. (2013), muscle fibre groups may be modelled via superposition of the structural tensor, with each tensor directing the

active stress along a certain direction.

Simulation of electromyographic signals. Several motor-unit anatomy models are used solely for the simulation of electromyography signals within a two-dimensional slice of the muscle (taken perpendicular to the muscle fibres) (e.g. Stashuk, 1993; Schnetzer et al., 2001; Carriou et al., 2016; Robertson et al., 2017). The motor-unit anatomy algorithm developed in this thesis may directly provide these simulations with anatomically realistic muscle cross-sections, with the possibility of extending it readily into three-dimensions.

Recently, Klotz et al. (2020), developed a (multi-domain) approach to model the electrophysiological behaviour of skeletal muscle tissue in three-dimensional, macroscopic continuum-mechanical models. The model uses volume-fractions of the intracellular phases as weighting of a modified bi-domain model. By using the motor-unit distribution factors, i.e., the homogenised motor-unit anatomy in 3D, to characterise these intracellular phases, electromyography may be simulated within realistic muscle geometries. However, in order to model electrophysiology and muscle contraction simulatenously, the assumption (made in this thesis) of instantaneous action-potential propagation would no longer hold. In other words, the propagating potential determined via the multi-domain approach would need to govern (local) muscle contraction.

10.3 Conclusion and Outlook

The prototype model and proof-of-concept case-studies, despite their limited scope, revealed the potential of three-dimensional modelling of motor-unit driven musculoskeletal system modelling. The linking of neural anatomy with musculoskeletal function opens up several avenues of future research. Having looked at the more direct implications in the previous section, a wider perspective is now taken to consider applications that require further development and planning.

10.3.1 Decoding experimental data

The integrated neuromuscular model developed within this thesis, provides a controlled and transparent environment to augment the development and calibration of techniques that use mechanical quantities to infer neural activity. For example, the integrated neuromuscular model can predict regional changes in muscle velocity, pressure, etc., while knowing the exact α-motor-neuron firing pattern and motor-unit distribution within this region.

Besides intramuscular pressure considered in a case-study, specific examples of these quantities include: muscle thickness or tissue velocity for ultrasound (Peolsson et al., 2008; Dieterich et al., 2014; Rohlén et al., 2020) and velocity-encoded magnetic resonance imaging (MRI) (Csapo et al., 2015); strain for strain-tensor MRI (Englund et al., 2011); muscle vibrations for mechanomyography (Farina et al., 2008); or muscle surface pressure for force-myography (Radmand et al., 2016).

10.3.2 Augmenting control of human-machine-interaction devices

Human interaction with robotic devices is on the rise, from robot-human collaborative environments, to powered exoskeletons, orthoses, and prostheses; technological advances are enabling a wide variety of human-machine-interaction applications (Tsarouchi et al., 2016). The coming

together of human movement with robotic devices poses complex challenges. Human-machine-interface devices need to decipher movement intent to improve their performance and ensure the user's safety. For example, with foreknowledge of a user's movement, powered orthoses can provide optimal assistive forces.

Towards this end, one of main challenges is to infer movement intent based on bio-signals (primarily) from skeletal muscles. These raw signals need to be decoded to extract movement intent and to inform control algorithms of human-machine-interaction devices. Muscle bio-signals can be classified into two types: biomechanical and electromyographic. While electromyographic signals remain the dominant method to classify movements (e.g. Dwivedi et al., 2020; Lara et al., 2020), biomechanical signals have been gaining popularity in recent decades. For example: ultrasound (Zheng et al., 2006), mechanomyography (Silva et al., 2005; Antonelli et al., 2009), and high-density force-myography (Radmand et al., 2016).

Integrated neuro-musculoskeletal models at the joint-scale can shed light on the relationships between neural activity and muscle function and aid the design of control algorithms for human-machine-interaction devices. For example, high-density force-myography can be replicated by confining the muscle circumferentially and recording the pressure development as individual motor-units are recruited. Robust contact mechanics algorithms are in place within the commercial finite element software package, enabling such an analysis in a relatively straight-forward manner.

Techniques such as mechanomyography, which measure muscle "sound" between 5–100 Hz, require simulation data at a high temporal resolution. By its nature, the explicit finite element solver (used in the current implementation) requires sub-millisecond incrementation steps. This means that muscle displacement can be computed with a fine temporal resolution at virtually no additional computational cost. Enabling, for example, frequency analysis of muscle deformations in response to varying motor-unit activity.

A foreseeable limitation in applying the current model to such applications is the lack of tissues surrounding the muscle, e.g., connective tissues, fat and skin. Non-invasive techniques, as the name suggests, lie on the skin surface rather than directly on the muscle. This intermediate tissue layer may attenuate the simulated mechanical quantities such as pressure and frequency. The development of an anatomically realistic, three-dimensional finite element musculoskeletal model, with independently modelled connective tissue, fat and skin layers remains a challenge in the field of musculoskeletal simulations.

10.3.3 Improving motor-output predictions during fatigue

Fatigue affects the ability of a muscle to maintain desired force. Important factors contributing to fatigue include alterations in metabolism caused by decreases in blood flow and muscle oxygenation (e.g. Murthy et al., 2001, and references therein). Intramuscular pressure is thought to impede blood flow once it rises above arterial pressure (e.g. Sjøgaard et al., 1988; van Donkelaar et al., 2001). Furthermore, at lower levels of sustained contraction, some muscles appear to vary motor-unit recruitment to shunt blood to different regions of the muscle, reinvigorating fatiguing regions and allowing the muscle to sustain force (e.g. Sjøgaard et al., 1986). This recruitment variation may occur via motor-unit *substitution*, where a motor-unit becomes derecruited and another takes its place. If subsequently, they switch again, this is described as motor-unit *rotation* (Bawa et al., 2009). Not only is motor-unit recruitment altered during fatigue, but motor-unit discharge rates are also affected (Marsden et al., 1983).

Given the heterogeneous distribution of motor-unit fibres in the muscle, as motor-units are substituted or rotated and their discharge rates altered, the motor-output is also affected. To use the integrated neuro-musculoskeletal modelling approach developed in this thesis to analyse fatigue requires two major considerations. First, two-way coupling between muscle contraction and neural activity is required (addressed in Section 6.5.1). Second, a model is needed, which relates mechanical quantities (such as intramuscular pressure) to motor-unit recruitment and discharge rate whether based on blood perfusion or a phenomenological model. Such a model can shed light on the relationships between motor-unit recruitment strategies, discharge rate, motor-output and fatigue.

10.3.4 Improving applicability of the neuro-musculoskeletal model

The applicability of computational biomechanical models can be improved by either personalisation or by generating data for statistical analyses, or both. While there are a large variety of aspects within the current model that require such treatment, for example: joint geometry, material behaviour of biological tissues, skeletal muscle fibre direction and -type composition; the focus in this section is placed on the personalisation of motor-unit anatomy.

Histochemical staining techniques, where individual α-motor-neurons are stimulated to identify the fibres they innervate, cannot be used on humans because of ethical reasons. Therefore, most knowledge about fibre distributions within motor-unit territories comes from animal (mammal) studies. For human muscles, biopsies reveal fibre-type distribution *in general*, i.e., independent of the motor-unit they belong to. By combining both animal studies and human biopsy data, a rough picture can be formed about territory distribution in human muscles (as was done in this thesis). But the aim remains to identify whole muscle, individualised motor-unit territories.

Non-invasive imaging and electromyographic techniques may be able to meet this challenge. In the last decade or so, there have been several attempts to use these techniques to identify territory locations, including: ultrasound (Deffieux et al., 2008), magnetic resonance imaging (MRI) (Csapo et al., 2015), and (needle, bipolar, or high-density) electromyography (EMG) (Vieira et al., 2011; Gallina et al., 2015; van Dijk et al., 2016; Luu et al., 2017). The accuracy of these techniques varies; some identify "task groups" of motor-units while others demarcate individual units. The trade-off seems to be specificity, for example, scanning (needle) EMG yields high-resolution territory data, restricted to select muscle locations (e.g. van Dijk et al., 2016). Alternatively, velocity-encoded-MRI scans multiple muscles but "only" uncovers *"neuromuscular compartments or task groups of motor-units"* (Csapo et al., 2015).

More recently, Lapatki et al. (2019) used high-density EMG and advanced signal processing to extract the lengths of 8–40 units, up to a depth of approximately 70 %, of the masseter. This was during a voluntary bite force of approximately 20 % of maximal voluntary contraction. Using medical imaging, Rohlén et al. (2020) apply ultra-fast high-resolution ultrasound to identify motor-unit territories within a 4 cm $\times$ 4 cm cross-section of the biceps brachii. By analysing tissue velocity, areas of contracting motor-units were demarcated, and approximately 44% of the active territories were identified at 5% maximal voluntary contraction.

Also using medical imaging, Birkbeck et al. (2020) developed a novel "motor-unit MRI" technique that combines electrical stimulation with diffusion weighted MRI, to obtain high-resolution data of individual motor-unit territories in the muscles of the lower leg. Although only 1-3 motor-units were identified per muscle, high fidelity data about individual territory

shapes was obtained, enabling the classification of individual territory shapes.

These techniques show great potential in personalising motor-unit territory placement in three-dimensional skeletal muscle models. In the absence of such high-resolution data, the current method relied on a stochastic approach, supplemented by qualitative anatomical descriptions, to place territories in the muscle.

As experiments reveal more quantitative information about the neuromuscular structure, the stochastic element in the placement algorithms can be restricted. Motor-unit territories can instead be directly defined by the experimental measurements. For example, the territory depths in Lapatki et al. (2019) can be used to restrict the position of the territories, and the ultrasound data from Rohlén et al. (2020) informing territory size.

10.3.5 Virtual test-bed for medical interventions

There has been increasing interest in the use of computational modelling in the medical field. Programmes such as the AMSE V&V 40[1] and H2020 SC1-PM-16-2017[2] aim to standardise both computational modelling for medical devices and in-silico trials for biomedical products. Although these programmes focus on medical products and devices, they show promise for the future use of biomechanical simulations in medicine.

Prediction of surgery outcomes and planning of rehabilitation protocols are examples of the medical relevance of an integrated neuro-musculoskeletal limb-scale model. For example, in cerebral palsy, motor-unit anatomy, and recruitment strategies are altered (Rose et al., 1998). One approach to correct for pathological gait in cerebral palsy is to alter tendon length (e.g. Rutz et al., 2011). An integrated model enables the simultaneous treatment of these factors (motor-unit remodelling, changes in motor-unit recruitment and musculotendon complex structure) and the impact this has on motor-output. This may improve the predictive ability of a biomechanical model, compared with a traditional macroscopic modelling approach.

Functional electrical stimulation is another example of a medical intervention where motor-unit anatomy plays a crucial role. Functional electrical stimulation involves cutaneous stimulation of the muscle and is used to restore movement in paralysed or weak muscles, for example, due to stroke (e.g. Howlett et al., 2015; Miller et al., 2017, and references therein). The stimulation electrodes, when placed over the belly of the muscle, diffuse an electrical current into the muscle and *"recruit[] motor-units in a non-selective, spatially fixed, and temporally synchronous pattern"* (Bickel et al., 2011). Understanding the relationship between the local motor-unit recruitment in three-dimensional muscles and joint or limb movement, may help adjust parameters such as electrode size, placement, and stimulus strength.

10.3.6 Concluding remarks

This thesis developed a method to include motor-unit activity and anatomy in continuum-mechanical, macroscopic muscle models. This was applied to a prototype musculoskeletal model at the joint-scale to, for the first time, investigate the relationship between motor-unit properties, activity, anatomy, volumetric muscle contraction, and three-dimensional motor-output in an anatomically realistic model.

[1] American Society of Mechanical Engineers—Assessing credibility of computational modelling through verification and validation: application to medical devices.

[2] European Commission—In-silico trials for developing and assessing biomedical products.

By computing prototype model muscle activity as an ensemble of motor-unit anatomy and activity, significant differences in motor-output were observed at low to medium contraction levels when compared to a status-quo macroscopic model. Proof-of-concept case-studies revealed novel insights into the relationships between motor-unit anatomy and motor-output. For example, the contribution of motor-unit remodelling to the force loss that occurs during ageing and neuromuscular disorders.

Although certain microstructural features were idealised, and only one joint-system was considered, the prototype model and proof-of-concept case-studies show the potential of the virtual neuro-musculoskeletal environment. Such insights may aid the decoding of experimentally obtained data, for example, by ultrasound, intramuscular pressure, and mechanomyography and also augment control strategies for human-machine-interface devices. More broadly, such models can help understand muscle function, such as fatigue, and inform medical interventions, for example, by predicting surgery outcomes or planning (movement) rehabilitation protocols related to ageing, trauma, or neuromuscular disorders.

A Occlusal boundary conditions: case-study using implicit muscles

Note: Parts of this section have been previously published in **Saini** et al. (2020).

Computational modelling techniques can provide insights into the stresses and strains in the dental structures not practically obtainable via experimental techniques. Such analyses, however, require assumptions on boundary conditions such as the modelling of occlusal loads and mandibular movement. Typically, in such studies, the occlusal loads are assumed to be either single point forces (e.g. De Jager et al., 2005; Lanza et al., 2005; Baggi et al., 2008) or multiple point forces across the occlusal surface (e.g. Bahrami et al., 2014; Verri et al., 2016; Vootla et al., 2016) and the mandible is typically fixed in space (e.g. Verri et al., 2016; Vootla et al., 2016). On the one hand, it has been shown that stresses incurred in the teeth are sensitive to occlusal load direction and distribution (Rees, 2002; Eskitascioglu et al., 2004; Röhrle et al., 2018a) and on the other hand, the need for appropriate muscle driven masticatory models in producing realistic stress distributions has been highlighted (Röhrle et al., 2007).

It follows that even if appropriate and accurate mechanical models, i.e., geometrical and constitutive models of dental structures would be used, the choice of modelling the occlusal load as single or multiple point forces, would most likely lead to unrealistic stress predictions in the dental structures. This is mainly due to the choice of boundary conditions, the discretisation error or neglecting shear and compressive components. The sensitivity of the mechanical response of dental structures to the type of occlusal loading, both in terms of loading direction and distribution, remains poorly understood.

The aims of this section are therefore twofold: First, to predict the stress response of the first molar dental structures during mastication using a simplified form of the model presented in the preceding section. Second, to use this model to quantify the response of the dental structures when occlusal loading is modelled as; a continuous, variable load distributed across the occlusal surfaces; as a single point force; or as four point forces, i.e., representing occlusal load modelling in typical computational studies; and by loading the occlusal surface with a sphere, i.e., as in typical experimental testing scenarios in prosthodontic laboratories. Understanding the influence of occlusal load modelling on the internal loading of the dental structures can lead to better representation of masticatory states in both virtual and experimental dental analyses.

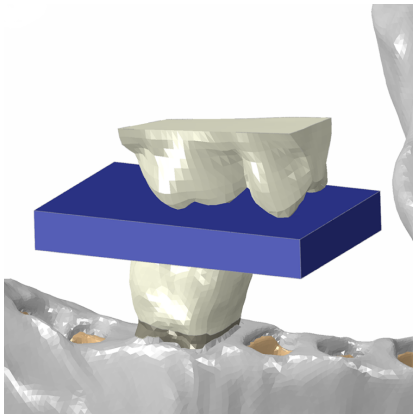

(a) *Rubber bite.*

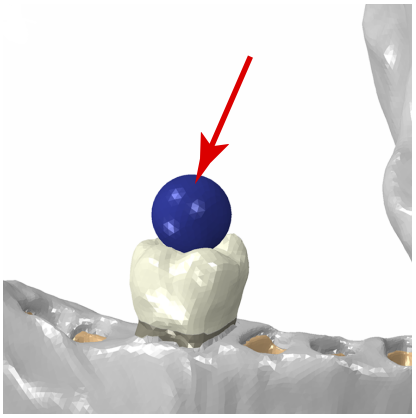

(b) *Sphere loading.*

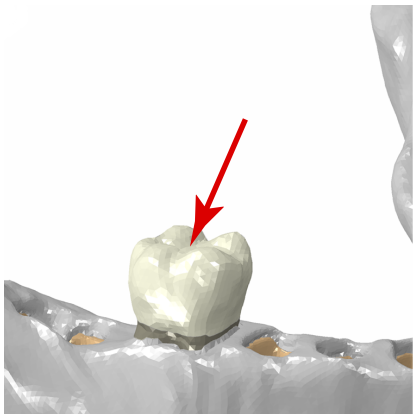

(c) *Single point force.*

(d) *Four point forces.*

Figure A.1: *Details of molar occlusal load case models.*

A.1 Methods

Computational model development

The model described in the Section 7.2 is used to compute the stress distributions within the dental structures during biting of a rubber sample (similar to Röhrle et al. (2018b)). The main difference being that the muscles were modelled implicitly as pressure boundary conditions, rather than as separate volumetric bodies.

Idealisation of masticatory muscles. Mandibular movement during biting of the rubber sample between the first right molars was driven by the combined action of four muscle groups, including the superior and deep masseter, the anterior, middle and posterior temporalis and the superior lateral, inferior lateral and medial pterygoid.

The action of each individual muscle upon the mandible was represented by a muscle force vector distributed over its entire area of mandibular attachment as previously described in van Essen et al. (2005) and Röhrle et al. (2007). All muscle force vectors were computed by multiplying unit vectors describing muscle directions by the corresponding muscle force magnitudes. The muscle force magnitudes were determined by multiplying maximum voluntary force muscle weights with scaling factors that represent the relative muscle activity during a unilateral bite between the molars on the right side. The muscle-weights, scaling factors and

unit vectors were based on literature (Nelson, 1986; Korioth et al., 1992; van Essen et al., 2005) and were chosen to represent a maximal voluntary bite between the first right molars (Table A.1).

Table A.1: *Summary of muscle weights, scaling factors and unit vectors used to compute muscle forces in the present study. Unit vectors of muscle forces are given for the right side of the jaw. For symbol definitions, see the text.*

Muscle group	Muscle weights/N	Scaling factors		Unit vector (right)		
		R-WS	L	x	y	z
AT	158	0.72	0.58	-0.15	-0.04	0.99
MT	95.6	0.66	0.67	-0.22	0.5	0.84
PT	75.6	0.59	0.39	-0.21	0.86	0.47
DM	81.6	0.72	0.60	-0.55	0.36	0.76
SM	190.4	0.72	0.60	-0.21	-0.42	0.89
ILP	66.9	0.30	0.65	0.63	-0.76	-0.17
SLP	28.7	0.50	0.50	0.76	-0.65	0.07
MP	174.8	0.84	0.60	0.49	-0.37	0.79

The rubber sample used in the biting simulations had dimensions $20 \times 20 \times 5$ mm. The material properties of the rubber sample were characterized by uniaxial compression testing (`Instron` Model 3521, Parker Hydraulics, USA) and described using a frist-order isotropic, hyperelastic and incompressible Ogden material law (Ogden et al., 1972), resulting in material parameters c_1 and c_2 as 0.6725 and 7.264, respectively.

Biting simulations. The rubber-biting was simulated at maximal voluntary bite force effort and is referred to as the gold-standard case (GS). The biting simulation was repeated by taking the computed occlusal force magnitude and direction from the GS simulation and applying it as: (i) an equivalent single concentrated force at the midcentral groove on the mandibular molar (CF1 case), (ii) four equally split forces applied at the molar cusps (CF2 case), and (iii) contact on the top of an 8 mm diameter sphere (in the range of experimentally used diameters, e.g., 6.4 mm (Linn et al., 1994) and 9.5mm (Jantarat et al., 2001) sitting centrally between the four cusps (SL case) (Figure 2). All simulations were performed using `Abaqus/Standard` (v6.14-3, Dassault Systèmes, France) using an `AMD Opteron 6373`[1] (2.3 GHz, 32 cores) with 24 GB memory.

A.2 Results

Computation times during simulations were approximately 7 h for the GS case, 1.5 h for the SL case and 1 h for both the CF1 and CF2 cases. The sum of all left- and right-side muscle forces was 511 N and 599 N, respectively. The resultant bite force on the rubber sample was 578 N, with components 34 N, 90 N and 570 N in the left, posterior and inferior directions, respectively.

[1]Part of the `LEAD` cluster at the University of Stuttgart.

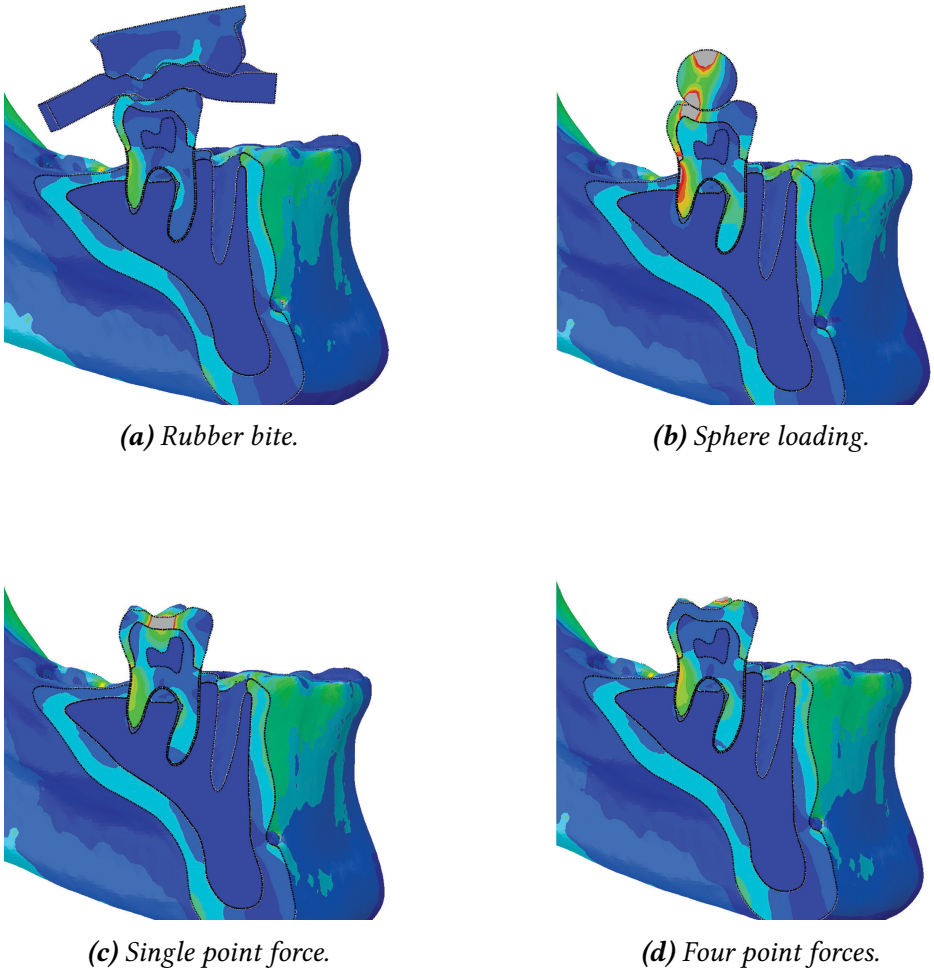

(a) Rubber bite.

(b) Sphere loading.

(c) Single point force.

(d) Four point forces.

Figure A.2: *Stress distribution in the molar and mandible for a loading force of* 578 N *in the sagittal plane cross-section. Stresses are scaled between* 0–50 MPa.

The peak enamel stress for the GS, CF1, CF2 and SL case was 110 MPa, 677 MPa, 270 MPa and 305 MPa, respectively (Figure A.2). The peak dentin stress for the GS, CF1, CF2 and SL cases was 44 MPa, 46 MPa, 50 MPa and 63 MPa, respectively. This stress was concentrated on the upper, lingual region of the dentin roots (Figure A.2). The CF1, CF2 and S cases produced peak stresses closer to the lingual side, whereas the loading for the GS case resulted in a peak stress located more distally.

A.3 Discussion

The prototype model of the masticatory system was driven by implicit muscles to predict the stress response of the first mandibular molar during biting, and to evaluate the influence of different occlusal load models on the resultant stress response. The peak simulated bite force is validated by comparison to previously published studies. The simulated bite force was 578 N, which is similar to experimentally measured values for unilateral biting on the second molar, determined using a force transducer (550 N) (Fastier-Wooller et al., 2016) and an optical sensor 635 N (Umesh et al., 2016).

The way in which occlusal load is modelled significantly influences the stress response of the underlying dental structures, which has been previously observed for point forces (e.g. Rees, 2002; Eskitascioglu et al., 2004) sphere contact loading (e.g. Röhrle et al., 2018a), and static clenching contact (e.g. Benazzi et al., 2014); however, occlusal load has not previously been modelled as a dynamic and variable load distributed over the occlusal surface during natural mastication. The use of point loads to model occlusal loading requires the definition of their number, location, magnitude and direction. Typically, a combination of literature values and assumptions are used for these definitions (e.g. Baggi et al., 2008; Vootla et al., 2016; Röhrle et al., 2018a), influencing the static equilibrium and stress distribution within the dental structures. The choice of loading conditions directly impacts the stress distributions within the tooth and may lead to stress concentrations due to the chosen discretisation and thus enamel loading should be analysed with caution.

The impact can be observed by comparison to the ultimate compressive strength of enamel, taken as 241 MPa (Stanford et al., 1960; Chun et al., 2014). At 50 % of bite force effort, stresses within the enamel were insufficient to cause yielding for the GS, CF2 and SL cases, while yielding was already predicted for the CF1 case. At 100 % of bite force, stresses within the enamel for the GS, CF1, CF2 and SL cases were 45 %, 281 %, 112 % and 126 % of its compressive yield strength, respectively. This suggests that the application of maximum bite force as a concentrated force, or even sphere contact, may ultimately lead to failure of the crown enamel unless the load contact area of the maximum force bite measurement is replicated. This finding is in agreement with previous studies that showed enamel incurs most of the occlusal stress and redistributes loading away from the crown towards the dentin roots and mandible (Yettram et al., 1976; Wang et al., 1997), due to the high stiffness of enamel.

There are a number of limitations of the present study that ought to be considered. First, bite force data were obtained from only one subject, i.e., one specific bite location and occlusal surface morphology; however, the main finding of the dependence of dental structures on the type of occlusal load may be generalized to other teeth and biting conditions. Second, masticatory muscle forces were not personalized to the subject. While muscle force patterns may vary between subjects, changes in the resultant bite force magnitude are unlikely to change the major conclusion of this study describing the influence of occlusal loading on stress distributions within the tooth and supporting structures.

A.4 Conclusion

The present study demonstrates that the magnitude, direction and distribution of forces on the occlusal surface play an important role in the stress response of enamel during mastication, while dentin was found to be relatively insensitive to the way in which occlusal loading was modelled. Modelling occlusal loading during maximum force bite conditions with up to four point forces, or using sphere contact, may result in yielding of enamel. The results may be useful in designing computational and experimental studies to evaluate dental materials, prosthodontic devices and teeth restorations, as well as in surgical planning.

B Simulated Motor-Unit Territories in the Prototype Masticatory Model

As described in Chapter 8, the motor-unit territories in the prototype model's left masseter for IDs 1 and 3-10 are given here. For each of the figures below, the cross-sections are oriented such that the following page-to-anatomical direction relations hold: left-superior, top-posterior, right-medial (or deep), and bottom-anterior. The cross-sectional area is approximately 630 mm^2. The motor-unit territories boundaries and virtual fibres are colour-coded from dark-blue (to cream) to maroon, corresponding to the smallest and largest motor-units, respectively. Additionally, extended statistics for the motor-unit territories are also given in Table B.1.

Table B.1: *Masseter motor-unit territory statistics for various distributions, where CSA: cross-sectional area, $\bar{l}$ is the territory span or length, and the subscripts $(\cdot)_{min}$, $(\cdot)_{max}$, $(\cdot)_{10}$ and $(\cdot)_{90}$ correspond to the minimum, maximum, 10^{th} and 90^{th} percentile, respectively.*

ID	%-CSA_{min}	%-CSA_{max}	%-CSA_{10}	%-CSA_{90}	$\bar{l}_{min}$/mm	$\bar{l}_{max}$/mm	$\bar{l}_{10}$	$\bar{l}_{90}$
0	0.4	19.0	0.8	6.0	2.0E-02	5.1	0.7	3.9
1	4.4	35.0	7.5	29.0	4.6E-03	13.0	0.2	4.3
2	0.1	42.0	1.1	13.0	4.6E-03	17.0	0.3	8.2
3	7.8	50.0	13.0	40.0	4.6E-03	8.7	0.2	6.4
4	0.3	36.0	0.9	11.0	6.8E-02	7.0	0.3	5.1
5	1.4	79.0	5.3	43.0	4.6E-03	20.0	0.2	8.5
6	2.1	49.0	3.8	24.0	1.8E-01	8.7	0.5	5.4
7	0.3	8.3	1.2	6.8	4.6E-03	5.5	0.2	3.1
8	0.4	10.0	0.6	6.2	4.4E-01	5.5	0.6	4.2
9	0.4	12.0	0.9	7.1	2.4E-01	12.0	0.5	4.2
10	0.5	67.0	0.9	6.9	9.1E-02	6.8	0.4	4.1

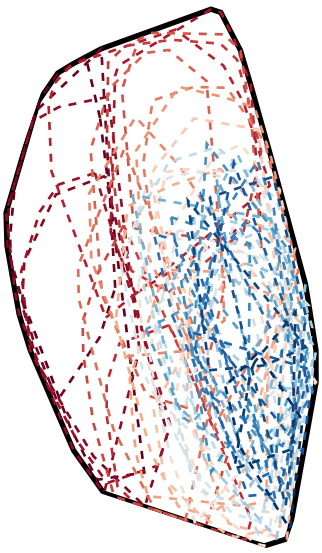

(a) *Meta-unit territories.*

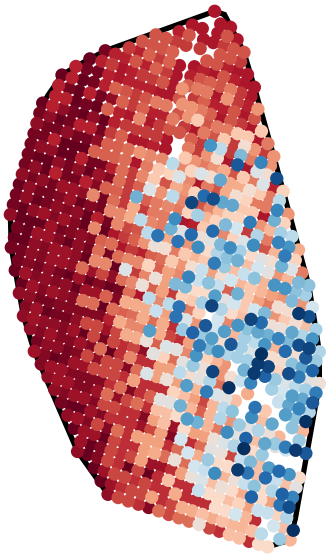

(b) *Meta-unit fibre distributions.*

Figure B.1: *Meta-unit territory distribution ID 1.*

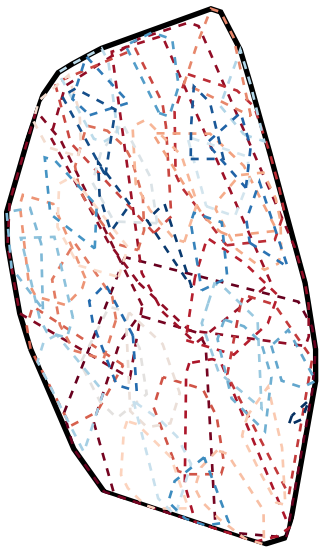

(a) *Meta-unit territories.*

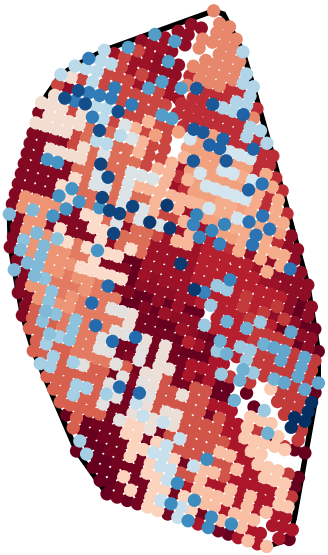

(b) *Meta-unit fibre distributions.*

Figure B.2: *Meta-unit territory distribution ID 3.*

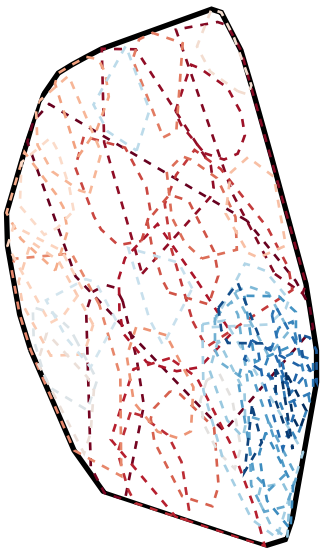

(a) *Meta-unit territories.*

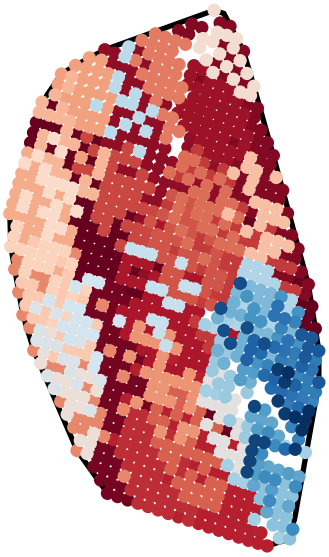

(b) *Meta-unit fibre distributions.*

Figure B.3: *Meta-unit territory distribution ID 4.*

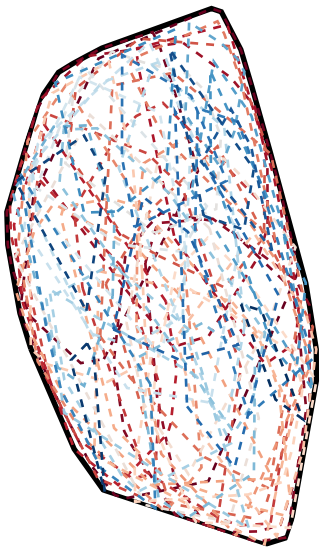

(a) *Meta-unit territories.*

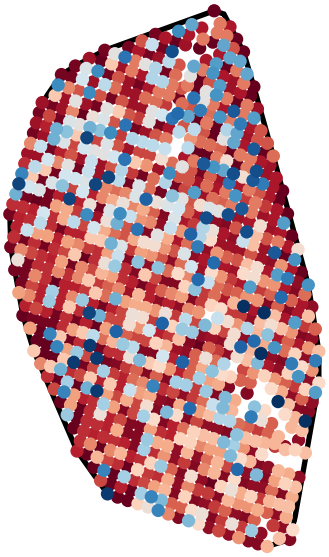

(b) *Meta-unit fibre distributions.*

Figure B.4: *Meta-unit territory distribution ID 5.*

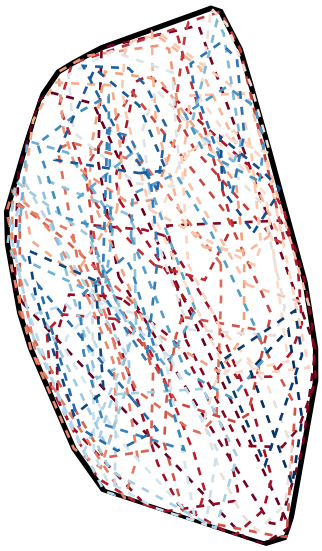

(a) *Meta-unit territories.*

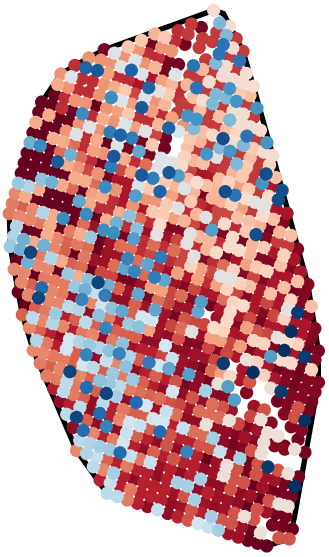

(b) *Meta-unit fibre distributions.*

Figure B.5: *Meta-unit territory distribution ID 6.*

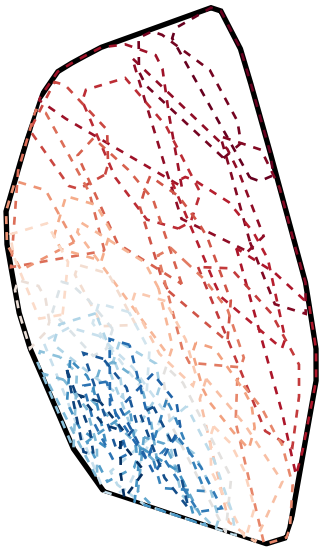

(a) *Meta-unit territories.*

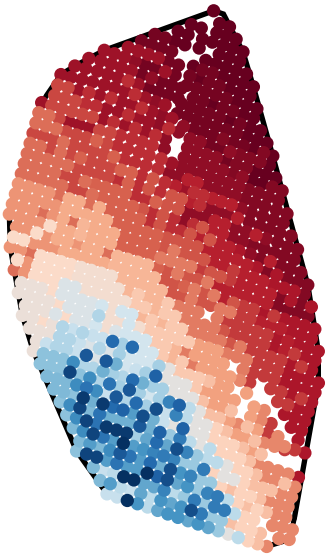

(b) *Meta-unit fibre distributions.*

Figure B.6: *Meta-unit territory distribution ID 7.*

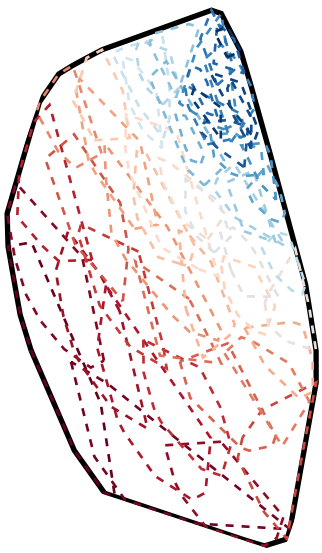

(a) *Meta-unit territories.*

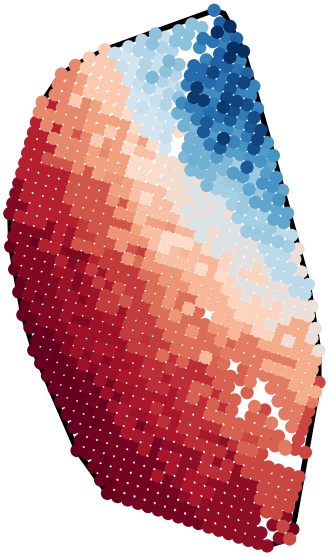

(b) *Meta-unit fibre distributions.*

Figure B.7: *Meta-unit territory distribution ID 8.*

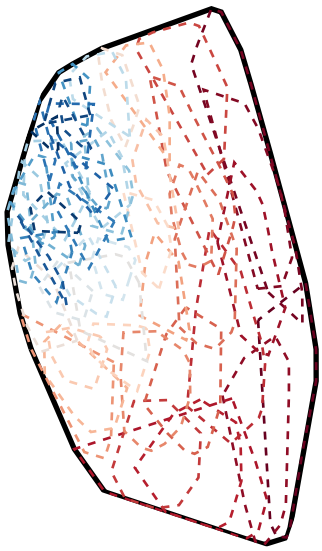

(a) *Meta-unit territories.*

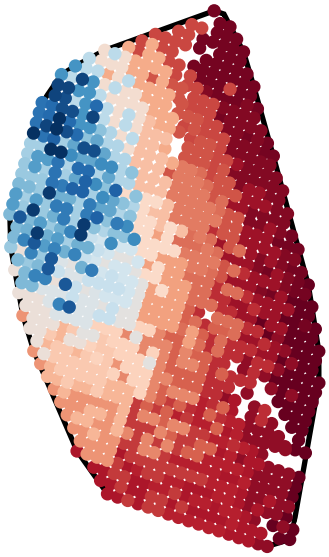

(b) *Meta-unit fibre distributions.*

Figure B.8: *Meta-unit territory distribution ID 9.*

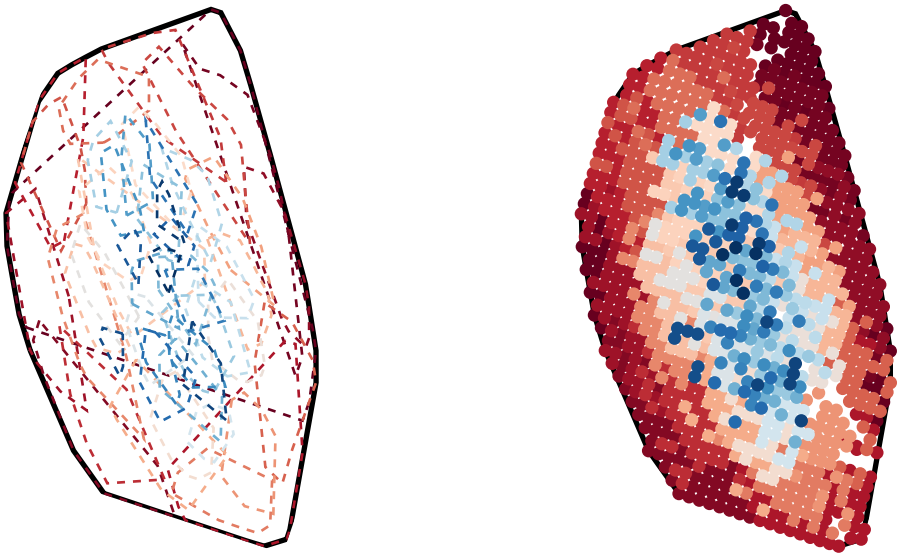

(a) *Meta-unit territories.* ***(b)*** *Meta-unit fibre distributions.*

Figure B.9: *Meta-unit territory distribution ID 10.*

Bibliography

[1] Ackland, D. C., Robinson, D., Redhead, M., Lee, P. V. S., Moskaljuk, A. and Dimitroulis, G. "A Personalized 3D-Printed Prosthetic Joint Replacement for the Human Temporomandibular Joint: From Implant Design to Implantation". *Journal of the Mechanical Behavior of Biomedical Materials* **69** (2017), pp. 404–411 (cit. on pp. 11, 132).

[2] Adrian, E. D. and Bronk, D. W. "The Discharge of Impulses in Motor Nerve Fibres". *The Journal of Physiology* **67**.2 (1929), pp. 9–151 (cit. on pp. 1, 23).

[3] Aitkenhead, A. H. "Mesh Voxelisation (Version 1.2)". *MATLAB Central File Exchange* (2013) (cit. on p. 103).

[4] Alcazar, J., Csapo, R., Ara, I. and Alegre, L. M. "On the Shape of the Force-Velocity Relationship in Skeletal Muscles: The Linear, the Hyperbolic, and the Double-Hyperbolic". *Frontiers in Physiology* **10** (2019), p. 769 (cit. on p. 19).

[5] Ali Khan, M. "Histochemical Characteristics of Vertebrate Striated Muscle: A Review". *Progress in Histochemistry and Cytochemistry* **8**.4 (1976), pp. III–47 (cit. on p. 19).

[6] Aliev, R. R. and Panfilov, A. V. "A Simple Two-Variable Model of Cardiac Excitation". *Chaos, Solitons & Fractals* **7**.3 (1996), pp. 293–301 (cit. on pp. 65, 66, 71, 92, 112, 130).

[7] Amabile, C., Moal, B., Chtara, O. A., Pillet, H., Raya, J. G., Iannessi, A., Skalli, W., Lafage, V. and Bronsard, N. "Estimation of Spinopelvic Muscles' Volumes in Young Asymptomatic Subjects: A Quantitative Analysis". *Surgical and Radiologic Anatomy* **39**.4 (2017), pp. 393–403 (cit. on p. 16).

[8] Ambrosi, D. and Pezzuto, S. "Active Stress vs. Active Strain in Mechanobiology: Constitutive Issues". *Journal of Elasticity* **107**.2 (2012), pp. 199–212 (cit. on pp. 3, 51).

[9] Ameredes, B. T. and Provenzano, M. A. "Regional Intramuscular Pressure Development and Fatigue in the Canine Gastrocnemius Muscle in Situ". *Journal of Applied Physiology* **83**.6 (1997), pp. 1867–1876 (cit. on p. 5).

[10] An, K. N., Takahashi, K., Harrigan, T. P. and Chao, E. Y. "Determination of Muscle Orientations and Moment Arms". *Journal of Biomechanical Engineering* **106**.3 (1984), pp. 280–282 (cit. on p. 159).

[11] Antonelli, M. G., Zobel, P. B. and Giacomin, J. "Use of MMG Signals for the Control of Powered Orthotic Devices: Development of a Rectus Femoris Measurement Protocol". *Assistive Technology* **21**.1 (2009), pp. 1–12 (cit. on p. 179).

[12] Arasaki, K. and Tamaki, M. "A Loss of Functional Spinal Alpha Motor Neurons in Amyotrophic Lateral Sclerosis". *Neurology* **51**.2 (1998), pp. 603–605 (cit. on p. 163).

[13] Aratow, M., Ballard, R. E., Crenshaw, A. G., Styf, J., Watenpaugh, D. E., Kahan, N. J. and Hargens, A. R. "Intramuscular Pressure and Electromyography as Indexes of Force during Isokinetic Exercise". *Journal of Applied Physiology* **74**.6 (1993), pp. 2634–2640 (cit. on pp. 11, 152).

[14] Ateş, F., Davies, B. L., Chopra, S., Coleman-Wood, K., Litchy, W. J. and Kaufman, K. R. "Intramuscular Pressure of Tibialis Anterior Reflects Ankle Torque but Does Not Follow Joint Angle-Torque Relationship". *Frontiers in Physiology* **9** (2018) (cit. on pp. 11, 152, 153).

[15] Baggi, L., Cappelloni, I., Di Girolamo, M., Maceri, F. and Vairo, G. "The Influence of Implant Diameter and Length on Stress Distribution of Osseointegrated Implants Related to Crestal Bone Geometry: A Three-Dimensional Finite Element Analysis". *The Journal of Prosthetic Dentistry* **100**.6 (2008), pp. 422–431 (cit. on pp. 183, 187).

[16] Bahrami, B., Shahrbaf, S., Mirzakouchaki, B., Ghalichi, F., Ashtiani, M. and Martin, N. "Effect of Surface Treatment on Stress Distribution in Immediately Loaded Dental Implants—A 3D Finite Element Analysis". *Dental Materials* **30**.4 (2014), e89–e97 (cit. on p. 183).

[17] Bakke, M. "Bite Force and Occlusion". *Seminars in Orthodontics* **12**.2 (2006), pp. 120–126 (cit. on p. 132).

[18] Balzani, D., Neff, P., Schröder, J. and Holzapfel, G. A. "A Polyconvex Framework for Soft Biological Tissues. Adjustment to Experimental Data". *International Journal of Solids and Structures* **43**.20 (2006), pp. 6052–6070 (cit. on p. 52).

[19] Barbenel, J. "The Biomechanics of the Temporomandibular Joint: A Theoretical Study". *Journal of Biomechanics* **5**.3 (1972), pp. 251–256 (cit. on p. 124).

[20] Basford, J. R. "The Law of Laplace and Its Relevance to Contemporary Medicine and Rehabilitation". *Archives of Physical Medicine and Rehabilitation* **83**.8 (2002), pp. 1165–1170 (cit. on pp. 5, 12).

[21] Bawa, P. and Murnaghan, C. "Motor Unit Rotation in a Variety of Human Muscles". *Journal of Neurophysiology* **102**.4 (2009), pp. 2265–2272 (cit. on p. 179).

[22] Bayer, J. D., Blake, R. C., Plank, G. and Trayanova, N. A. "A Novel Rule-Based Algorithm for Assigning Myocardial Fiber Orientation to Computational Heart Models". *Annals of Biomedical Engineering* **40**.10 (2012), pp. 2243–2254 (cit. on p. 93).

[23] Belavý, D. L., Miokovic, T., Rittweger, J. and Felsenberg, D. "Estimation of Changes in Volume of Individual Lower-Limb Muscles Using Magnetic Resonance Imaging (during Bed-Rest)". *Physiological Measurement* **32**.1 (2011), pp. 35–50 (cit. on p. 16).

[24] Belser, U. C. and Hannam, A. G. "The Contribution of the Deep Fibers of the Masseter Muscle to Selected Tooth-Clenching and Chewing Tasks". *The Journal of Prosthetic Dentistry* **56**.5 (1986), pp. 629–635 (cit. on pp. 78, 121, 142).

[25] Benazzi, S., Grosse, I. R., Gruppioni, G., Weber, G. W. and Kullmer, O. "Comparison of Occlusal Loading Conditions in a Lower Second Premolar Using Three-Dimensional Finite Element Analysis". *Clinical Oral Investigations* **18**.2 (2014), pp. 369–375 (cit. on p. 187).

[26] Bennett, M. R. "Development of Neuromuscular Synapses". *Physiological Reviews* **63**.3 (1983), pp. 915–1048 (cit. on p. 94).

[27] Beran, M. J. "Statistical Continuum Theories". *American Journal of Physics* **36**.10 (1968), pp. 923–923 (cit. on p. 98).

[28] Bickel, C. S., Gregory, C. M. and Dean, J. C. "Motor Unit Recruitment during Neuromuscular Electrical Stimulation: A Critical Appraisal". *European Journal of Applied Physiology* **111**.10 (2011), p. 2399 (cit. on p. 181).

[29] Birkbeck, M. G., Heskamp, L., Schofield, I. S., Blamire, A. M. and Whittaker, R. G. "Non-Invasive Imaging of Single Human Motor Units". *Clinical Neurophysiology* **131**.6 (2020), pp. 1399–1406 (cit. on pp. 9, 81, 124, 180).

[30] Biswas, B. K., Bag, S. and Pal, S. "Biomechanical Analysis of Normal and Implanted Tooth Using Biting Force Measurement". *International Journal of Engineering* **4**.2 (2013), pp. 17–23 (cit. on p. 132).

[31] Blackett, S., Bullivant, D., Stevens, C. and Hunter, P. "Open Source Software Infrastructure for Computational Biology and Visualization". *2005 IEEE Engineering in Medicine and Biology 27th Annual Conference*. 2005, pp. 6079–6080 (cit. on p. 78).

[32] Blanksma, N. and Eijden, T. van. "Electromyographic Heterogeneity in the Human Temporalis Muscle". *Journal of Dental Research* **69**.10 (1990), pp. 1686–1690 (cit. on p. 5).

[33] Blanksma, N. and van Eijden, T. "Electromyographic Heterogeneity in the Human Temporalis and Masseter Muscles during Static Biting, Open\Close Excursions, and Chewing". *Journal of Dental Research* **74**.6 (1995), pp. 1318–1327 (cit. on pp. 5, 177).

[34] Blanksma, N., van Eijden, T., van Ruijven, L. and Weijs, W. "Electromyographic Heterogeneity in the Human Temporalis and Masseter Muscles during Dynamic Tasks Guided by Visual Feedback". *Journal of Dental Research* **76**.1 (1997), pp. 542–551 (cit. on pp. 121, 141, 142, 174, 177).

[35] Bleiler, C., Ponte Castañeda, P. and Röhrle, O. "A Microstructurally-Based, Multi-Scale, Continuum-Mechanical Model for the Passive Behaviour of Skeletal Muscle Tissue". *Journal of the Mechanical Behavior of Biomedical Materials* **97** (2019), pp. 171–186 (cit. on p. 171).

[36] Bleiler, C., Ponte Castañeda, P. and Röhrle, O. "Tangent Second-Order Homogenisation Estimates for Incompressible Hyperelastic Composites with Fibrous Microstructures and Anisotropic Phases". *Journal of the Mechanics and Physics of Solids* **147** (2021), p. 104251 (cit. on p. 171).

[37] Blemker, S. S., Asakawa, D. S., Gold, G. E. and Delp, S. L. "Image-Based Musculoskeletal Modeling: Applications, Advances, and Future Opportunities". *Journal of Magnetic Resonance Imaging* **25**.2 (2007), pp. 441–451 (cit. on p. 159).

[38] Blemker, S. S. and Delp, S. L. "Three-Dimensional Representation of Complex Muscle Architectures and Geometries". *Annals of Biomedical Engineering* **33**.5 (2005), pp. 661–673 (cit. on p. 93).

[39] Blemker, S. S., Pinsky, P. M. and Delp, S. L. "A 3D Model of Muscle Reveals the Causes of Nonuniform Strains in the Biceps Brachii". *Journal of Biomechanics* **38**.4 (2005), pp. 657–665 (cit. on pp. 5, 46, 176, 177).

[40] Bodine, S. C., Garfinkel, A., Roy, R. R. and Edgerton, V. R. "Spatial Distribution of Motor Unit Fibers in the Cat Soleus and Tibialis Anterior Muscles: Local Interactions". *Journal of Neuroscience* **8**.6 (1988), pp. 2142–2152 (cit. on pp. 7, 94, 95).

[41] Bodine-Fowler, S. C., Garfinkel, A., Roy, R. R. and Edgerton, V. R. "Spatial Distribution of Muscle Fibers within the Territory of a Motor Unit". *Muscle & Nerve* **13**.12 (1990), pp. 1133–1145 (cit. on pp. 6, 7, 81, 94).

[42] Böl, M., Ehret, A. E., Leichsenring, K., Weichert, C. and Kruse, R. "On the Anisotropy of Skeletal Muscle Tissue under Compression". *Acta Biomaterialia* **10**.7 (2014), pp. 3225–3234 (cit. on pp. 46, 56, 119).

[43] Bonet, J. and Wood, R. D. *Nonlinear Continuum Mechanics for Finite Element Analysis*. Cambridge University Press, 1997 (cit. on p. 25).

[44] Bonjardim, L. R., Gaviao, M. B. D., Pereira, L. J. and Castelo, P. M. "Bite Force Determination in Adolescents with and without Temporomandibular Dysfunction". *Journal of Oral Rehabilitation* **32**.8 (2005), pp. 577–583 (cit. on p. 132).

[45] Bortel, E. L., Langer, M., Rack, A., Forien, J.-B., Duda, G. N., Fratzl, P. and Zaslansky, P. "Combining Coherent Hard X-Ray Tomographies with Phase Retrieval to Generate Three-Dimensional Models of Forming Bone". *Frontiers in Materials* **4** (2017) (cit. on p. 132).

[46] Borzelli, D., Gazzoni, M., Botter, A., Gastaldi, L., d'Avella, A. and Vieira, T. M. "Contraction Level, but Not Force Direction or Wrist Position, Affects the Spatial Distribution of Motor Unit Recruitment in the Biceps Brachii Muscle". *European Journal of Applied Physiology* **120**.4 (2020), pp. 853–860 (cit. on p. 63).

[47] Botelho, D. P., Curran, K. and Lowery, M. M. "Anatomically Accurate Model of EMG during Index Finger Flexion and Abduction Derived from Diffusion Tensor Imaging". *PLOS Computational Biology* **15**.8 (2019), e1007267 (cit. on pp. 10, 93).

[48] Bradley, C. P., Pullan, A. J. and Hunter, P. J. "Geometric Modeling of the Human Torso Using Cubic Hermite Elements". *Annals of Biomedical Engineering* **25**.1 (1997), pp. 96–111 (cit. on p. 78).

[49] Bradley, C., Bowery, A., Britten, R., Budelmann, V., Camara, O., Christie, R., Cookson, A., Frangi, A. F., Gamage, T. B., Heidlauf, T., Krittian, S., Ladd, D., Little, C., Mithraratne, K., Nash, M., Nickerson, D., Nielsen, P., Nordbø, Ø., Omholt, S., Pashaei, A., Paterson, D., Rajagopal, V., Reeve, A., Röhrle, O., Safaei, S., Sebastián, R., Steghöfer, M., Wu, T., Yu, T., Zhang, H. and Hunter, P. "OpenCMISS: A Multi-Physics & Multi-Scale Computational Infrastructure for the VPH/Physiome Project". *Progress in Biophysics and Molecular Biology* **107**.1 (2011), pp. 32–47 (cit. on p. 100).

[50] Bradley, C., Emamy, N., Ertl, T., Göddeke, D., Hessenthaler, A., Klotz, T., Krämer, A., Krone, M., Maier, B., Mehl, M., Rau, T. and Röhrle, O. "Towards Realistic HPC Models of the Neuromuscular System". *arXiv:1802.03211 [physics]* (2018). arXiv: 1802.03211 [physics] (cit. on p. 4).

[51] Bradley, C. P., Emamy, N., Ertl, T., Göddeke, D., Hessenthaler, A., Klotz, T., Krämer, A., Krone, M., Maier, B., Mehl, M., Rau, T. and Röhrle, O. "Enabling Detailed, Biophysics-Based Skeletal Muscle Models on HPC Systems". *Frontiers in Physiology* **9** (2018) (cit. on p. 4).

[52] Brenner, J. F., Zahniser, D. J., Ziegelmiller, D. W., Adelman, L. S., Munsat, T. L. and Bradley, W. G. "Automated System for the Analysis of Muscle and Nerve Biopsies". *Applied Optics* **26**.16 (1987), pp. 3398–3407 (cit. on pp. 94, 167).

[53] Buchthal, F., Erminio, F. and Rosenfalck, P. "Motor Unit Territory in Different Human Muscles". *Acta Physiologica Scandinavica* **45**.1 (1959), pp. 72–87 (cit. on p. 8).

[54] Burke, R. E. and Tsairis, P. "Anatomy and Innervation Ratios in Motor Units of Cat Gastrocnemius". *The Journal of Physiology* **234**.3 (1973), pp. 749–765 (cit. on pp. 6, 140).

[55] Campbell, K. B., Taheri, H., Kirkpatrick, R. D., Burton, T. and Hunter, W. C. "Similarities between Dynamic Elastance of Left Ventricular Chamber and Papillary Muscle of Rabbit Heart". *American Journal of Physiology - Heart and Circulatory Physiology* **264**.6 (1993), H1926–H1941 (cit. on pp. 71, 112, 130).

[56] Campbell, K. B., Razumova, M. V., Kirkpatrick, R. D. and Slinker, B. K. "Myofilament Kinetics in Isometric Twitch Dynamics". *Annals of Biomedical Engineering* **29**.5 (2001), pp. 384–405 (cit. on pp. 71, 112, 130).

[57] Carlsöö, S. "Motor Units and Action Potentials in Masticatory Muscles; an Electromyographic Study of the Form and Duration of the Action Potentials and an Anatomic Study of the Size of the Motor Units". *Acta Morphologica Neerlando-Scandinavica* **2**.1 (1958), pp. 13–19 (cit. on pp. 16, 129).

[58] Carriou, V., Boudaoud, S., Laforet, J. and Ayachi, F. S. "Fast Generation Model of High Density Surface EMG Signals in a Cylindrical Conductor Volume". *Computers in Biology and Medicine* **74** (2016), pp. 54–68 (cit. on pp. 10, 178).

[59] Cavanagh, P. R. and Komi, P. V. "Electromechanical Delay in Human Skeletal Muscle under Concentric and Eccentric Contractions". *European Journal of Applied Physiology and Occupational Physiology* **42**.3 (1979), pp. 159–163 (cit. on p. 116).

[60] Chagnon, G., Rebouah, M. and Favier, D. "Hyperelastic Energy Densities for Soft Biological Tissues: A Review". *Journal of Elasticity* **120**.2 (2015), pp. 129–160 (cit. on p. 51).

[61] Challis, J. H. and Kerwin, D. G. "Determining Individual Muscle Forces during Maximal Activity: Model Development, Parameter Determination, and Validation". *Human Movement Science* **13**.1 (1994), pp. 29–61 (cit. on p. 159).

[62] Chen, C. S., Hon, Y. C. and Schaback, R. A. *Scientific Computing with Radial Basis Functions*. Department of Mathematics, University of Southern Mississippi, Hattiesburg, MS, 2005 (cit. on p. 75).

[63] Chi, S.-W., Hodgson, J., Chen, J.-S., Reggie Edgerton, V., Shin, D. D., Roiz, R. A. and Sinha, S. "Finite Element Modeling Reveals Complex Strain Mechanics in the Aponeuroses of Contracting Skeletal Muscle". *Journal of Biomechanics* **43**.7 (2010), pp. 1243–1250 (cit. on p. 46).

[64] Chleboun, G. S., France, A. R., Crill, M. T., Braddock, H. K. and Howell, J. N. "In Vivo Measurement of Fascicle Length and Pennation Angle of the Human Biceps Femoris Muscle". *Cells Tissues Organs* **169**.4 (2001), pp. 401–409 (cit. on p. 15).

[65] Choi, H. F. and Blemker, S. S. "Skeletal Muscle Fascicle Arrangements Can Be Reconstructed Using a Laplacian Vector Field Simulation". *PLOS ONE* **8**.10 (2013) (cit. on pp. 75, 93).

[66] Chun, K., Choi, H. and Lee, J. "Comparison of Mechanical Property and Role between Enamel and Dentin in the Human Teeth". *Journal of Dental Biomechanics* **5**.0 (2014), pp. 1–7 (cit. on p. 187).

[67] Ciarlet, P. G. *Mathematical Elasticity Volume I: Three-Dimensional Elasticity*. Vol. 20. North Holland, Amsterdam: Elsevier, 1988 (cit. on p. 51).

[68] Cioffi, I., Gallo, L. M., Palla, S., Erni, S. and Farella, M. "Macroscopic Analysis of Human Masseter Compartments Assessed by Magnetic Resonance Imaging". *Cells Tissues Organs* **195**.5 (2012), pp. 465–472 (cit. on pp. 11, 16, 81, 122, 125, 141, 145).

[69] Cohen, M. H., Lester, J. M., Bradley, W. G., Brenner, J. F., Hirsch, R. P., Silber, D. I. and Ziegelmiller, D. "A Computer Model of Denervation-Reinnervation in Skeletal Muscle". *Muscle & Nerve* **10**.9 (1987), pp. 826–836 (cit. on pp. 93, 94).

[70] Colomo, F., Piroddi, N., Poggesi, C., Kronnie, G. te and Tesi, C. "Active and Passive Forces of Isolated Myofibrils from Cardiac and Fast Skeletal Muscle of the Frog." *The Journal of Physiology* **500**.2 (1997), pp. 535–548 (cit. on p. 17).

[71] Contessa, P., Adam, A. and De Luca, C. J. "Motor Unit Control and Force Fluctuation during Fatigue". *Journal of Applied Physiology* **107**.1 (2009), pp. 235–243 (cit. on p. 175).

[72] Cowin, S. C. *Continuum Mechanics of Anisotropic Materials*. New York: Springer-Verlag, 2013 (cit. on pp. 25, 32).

[73] Csapo, R., Malis, V., Sinha, U. and Sinha, S. "Mapping of Spatial and Temporal Heterogeneity of Plantar Flexor Muscle Activity during Isometric Contraction: Correlation of Velocity-Encoded MRI with EMG". *Journal of Applied Physiology* **119**.5 (2015), pp. 558–568 (cit. on pp. 5, 9, 175, 178, 180).

[74] Dahm, L. M. and Landmesser, L. T. "The Regulation of Intramuscular Nerve Branching during Normal Development and Following Activity Blockade". *Developmental Biology* **130**.2 (1988), pp. 621–644 (cit. on pp. 7, 94).

[75] Dao, T. T. and Tho, M.-C. H. B. "A Systematic Review of Continuum Modeling of Skeletal Muscles: Current Trends, Limitations, and Recommendations". *Applied Bionics and Biomechanics* **2018**.Article ID 7631818 (2018), pp. 1–17 (cit. on p. 46).

[76] Dassault Systèmes. *Abaqus Manual*. https://abaqus-docs.mit.edu/2017/English/SIMACAEEXCRefMap/simaexc-c-docproc.htm. 2017 (cit. on pp. 40, 104, 110, 118).

[77] Davidson, J., Kim, J., Cheng, L., Rohrle, O., Shorten, P., Soboleva, T., Clarke, R. and Pullan, A. "Mathematically Modeling the Effects of Electrically Stimulating Skeletal Muscle". *2006 International Conference of the IEEE Engineering in Medicine and Biology Society*. IEEE, 2006, pp. 4635–4638 (cit. on p. 177).

[78] De Jager, N., Pallav, P. and Feilzer, A. J. "The Influence of Design Parameters on the FEA-Determined Stress Distribution in CAD–CAM Produced All-Ceramic Dental Crowns". *Dental Materials* **21**.3 (2005), pp. 242–251 (cit. on p. 183).

[79] De Luca, C. J., LeFever, R. S., McCue, M. P. and Xenakis, A. P. "Behaviour of Human Motor Units in Different Muscles during Linearly Varying Contractions". *The Journal of Physiology* **329**.1 (1982), pp. 113–128 (cit. on pp. 23, 64).

[80] de Vlugt, E., de Groot, J. H., Wisman, W. H. J. and Meskers, C. G. M. "Clonus Is Explained from Increased Reflex Gain and Enlarged Tissue Viscoelasticity". *Journal of Biomechanics* **45**.1 (2012), pp. 148–155 (cit. on p. 118).

[81] Dechow, P. C., Nail, G. A., Schwartz-Dabney, C. L. and Ashman, R. B. "Elastic Properties of Human Supraorbital and Mandibular Bone". *American Journal of Physical Anthropology* **90**.3 (1993), pp. 291–306 (cit. on p. 132).

[82] Deffieux, T., Gennisson, J.-l., Tanter, M. and Fink, M. "Assessment of the Mechanical Properties of the Musculoskeletal System Using 2-D and 3-D Very High Frame Rate Ultrasound". *IEEE Transactions on Ultrasonics, Ferroelectrics, and Frequency Control* **55**.10 (2008), pp. 2177–2190 (cit. on pp. 9, 180).

[83] Delp, S. L. "Surgery Simulation: A Computer Graphics System to Analyze and Design Musculoskeletal Reconstructions of the Lower Limb". PhD thesis. Stanford University, 1990 (cit. on p. 2).

[84] Demer, L. L. and Yin, F. C. "Passive Biaxial Mechanical Properties of Isolated Canine Myocardium." *The Journal of Physiology* **339**.1 (1983), pp. 615–630 (cit. on p. 49).

[85] Dey, D. K., Bosaeus, I., Lissner, L. and Steen, B. "Changes in Body Composition and Its Relation to Muscle Strength in 75-Year-Old Men and Women: A 5-Year Prospective Follow-up Study of the NORA Cohort in Göteborg, Sweden". *Nutrition* **25**.6 (2009), pp. 613–619 (cit. on p. 167).

[86] Dideriksen, J. L. and Negro, F. "Spike-Triggered Averaging Provides Inaccurate Estimates of Motor Unit Twitch Properties under Optimal Conditions". *Journal of Electromyography and Kinesiology* **43** (2018), pp. 104–110 (cit. on pp. 12, 156).

[87] Dieterich, A. V., Pickard, C. M., Strauss, G. R., Deshon, L. E., Gibson, W. and McKay, J. "Muscle Thickness Measurements to Estimate Gluteus Medius and Minimus Activity Levels". *Manual Therapy* **19**.5 (2014), pp. 453–460 (cit. on p. 178).

[88] Dobrin, P. B. "Mechanical Properties of Arteries". *Physiological Reviews* **58**.2 (1978), pp. 397–460 (cit. on p. 49).

[89] Dwivedi, A., Lara, J., Cheng, L. K., Paskaranandavadivel, N. and Liarokapis, M. "High-Density Electromyography Based Control of Robotic Devices: On the Execution of Dexterous Manipulation Tasks". *2020 IEEE International Conference on Robotics and Automation (ICRA)*. IEEE, 2020, pp. 3825–3831 (cit. on p. 179).

[90] Ebrahimi, E. A. "Musculo-Aponeurotic Architecture of the Human Masseter Muscle: A Three-Dimensional Cadaveric Study". PhD Thesis. University of Toronto, 2015 (cit. on p. 78).

[91] Eby, S. F., Cloud, B. A., Brandenburg, J. E., Giambini, H., Song, P., Chen, S., LeBrasseur, N. K. and An, K.-N. "Shear Wave Elastography of Passive Skeletal Muscle Stiffness: Influences of Sex and Age throughout Adulthood". *Clinical Biomechanics* **30**.1 (2015), pp. 22–27 (cit. on p. 171).

[92] Edman, K. A. "Double-Hyperbolic Force-Velocity Relation in Frog Muscle Fibres." *The Journal of Physiology* **404**.1 (1988), pp. 301–321 (cit. on p. 19).

[93] Edström, L. and Kugelberg, E. "Histochemical Composition, Distribution of Fibres and Fatiguability of Single Motor Units. Anterior Tibial Muscle of the Rat." *Journal of Neurology, Neurosurgery, and Psychiatry* **31**.5 (1968), pp. 424–433 (cit. on pp. 6, 81, 140).

[94] Engel, W. K. "Histochemistry of Neuromuscular Disease—Significance of Muscle Fiber Types". *Proceedings of the 8th International Congress of Neurology*. Vol. 2. Vienna, Austria: Verlag der Wiener Medizinischen Akademie Vienna, 1965, pp. 67–101 (cit. on p. 163).

[95] English, A. W. and Letbetter, W. D. "Intramuscular 'compartmentalization' of the Cat Biceps Femoris and Semitendinosus Muscles: Anatomy and EMG Patterns". *Society Neuroscience Abstracts* **7** (1981), p. 557 (cit. on p. 5).

[96] Englund, E. K., Elder, C. P., Xu, Q., Ding, Z. and Damon, B. M. "Combined Diffusion and Strain Tensor MRI Reveals a Heterogeneous, Planar Pattern of Strain Development during Isometric Muscle Contraction". *American Journal of Physiology-Regulatory, Integrative and Comparative Physiology* **300**.5 (2011), R1079–R1090 (cit. on p. 178).

[97] Enoka, R. M. "Morphological Features and Activation Patterns of Motor Units:" *Journal of Clinical Neurophysiology* **12**.6 (1995), pp. 538–559 (cit. on pp. 16, 21–23).

[98] Enoka, R. M. and Fuglevand, A. J. "Motor Unit Physiology: Some Unresolved Issues". *Muscle & Nerve* **24**.1 (2001), pp. 4–17 (cit. on pp. 69, 168).

[99] Eriksson, P. O. and Thornell, L. E. "Histochemical and Morphological Muscle-Fibre Characteristics of the Human Masseter, the Medial Pterygoid and the Temporal Muscles". *Archives of Oral Biology* **28**.9 (1983), pp. 781–795 (cit. on pp. 9, 94, 123, 140).

[100] Eskitascioglu, G., Usumez, A., Sevimay, M., Soykan, E. and Unsal, E. "The Influence of Occlusal Loading Location on Stresses Transferred to Implant-Supported Prostheses and Supporting Bone: A Three-Dimensional Finite Element Study". *The Journal of Prosthetic Dentistry* **91**.2 (2004), pp. 144–150 (cit. on pp. 183, 187).

[101] Fan, A.-X., Dakpé, S., Dao, T. T., Pouletaut, P., Rachik, M. and Tho, M. C. H. B. "MRI-Based Finite Element Modeling of Facial Mimics: A Case Study on the Paired Zygomaticus Major Muscles". *Computer Methods in Biomechanics and Biomedical Engineering* **20**.9 (2017), pp. 919–928 (cit. on pp. 5, 176).

[102] Farina, D., Li, X. and Madeleine, P. "Motor Unit Acceleration Maps and Interference Mechanomyographic Distribution". *Journal of Biomechanics* **41**.13 (2008), pp. 2843–2849 (cit. on p. 178).

[103] Fastier-Wooller, J., Phan, H.-P., Dinh, T., Nguyen, T.-K., Cameron, A., Öchsner, A. and Dao, D. "Novel Low-Cost Sensor for Human Bite Force Measurement". *Sensors* **16**.8 (2016), p. 1244 (cit. on p. 186).

[104] Feinstein, B., Lindegård, B., Nyman, E. and Wohlfart, G. "Morphologic Studies of Motor Units in Normal Human Muscles". *Cells Tissues Organs* **23**.2 (1955), pp. 127–142 (cit. on p. 21).

[105] Fernandez, J. W. and Hunter, P. J. "An Anatomically Based Patient-Specific Finite Element Model of Patella Articulation: Towards a Diagnostic Tool". *Biomechanics and Modeling in Mechanobiology* **4**.1 (2005), pp. 20–38 (cit. on pp. 2, 5).

[106] FitzHugh, R. "Impulses and Physiological States in Theoretical Models of Nerve Membrane". *Biophysical Journal* **1**.6 (1961), pp. 445–466 (cit. on p. 66).

[107] FitzHugh, R. *Mathematical Models of Excitation and Propagation in Nerve*. Biomedical Engineering. New York: McGraw-Hill, 1969 (cit. on p. 66).

[108] Floyd, W. F. and Silver, P. H. S. "Electromyographic Study of Patterns of Activity of the Anterior Abdominal Wall Muscles in Man". *Journal of Anatomy* **84**.2 (1950), pp. 132–145 (cit. on p. 2).

[109] Fontijn-Tekamp, F., Slagter, A., Der Bilt, A. van, 'T Hof, M. van, Witter, D., Kalk, W. and Jansen, J. "Biting and Chewing in Overdentures, Full Dentures, and Natural Dentitions". *Journal of Dental Research* **79**.7 (2000), pp. 1519–1524 (cit. on pp. 121, 132).

[110] Fuglevand, A. J., Winter, D. A. and Patla, A. E. "Models of Recruitment and Rate Coding Organization in Motor-Unit Pools". *Journal of Neurophysiology* **70**.6 (1993), pp. 2470–2488 (cit. on pp. 64, 65, 69, 92).

[111] Fung, Y. C. *Biomechanics: Mechanical Properties of Living Tissues*. Second. New York: Springer-Verlag, 1993 (cit. on pp. 45, 46).

[112] Gallina, A. and Vieira, T. "Territory and Fiber Orientation of Vastus Medialis Motor Units: A Surface Electromyography Investigation". *Muscle & Nerve* **52**.6 (2015), pp. 1057–1065 (cit. on pp. 7, 8, 180).

[113] S. C. Gandevia, U. Proske and D. G. Stuart, eds. *Sensorimotor Control of Movement and Posture*. First. Vol. 508. Advances in Experimental Medicine and Biology. Boston: Springer Science & Business Media, 2002 (cit. on p. 21).

[114] Gans, C. "Fibre Architecture and Muscle Function". *Exercise and Sport Sciences Reviews* **10**.1 (1982), pp. 160–207 (cit. on p. 15).

[115] Garland, S. J. and Gossen, E. R. "The Muscular Wisdom Hypothesis in Human Muscle Fatigue". *Exercise and Sport Sciences Reviews* **30**.1 (2002), pp. 45–49 (cit. on p. 117).

[116] Gerritsen, A. E., Allen, P. F., Witter, D. J., Bronkhorst, E. M. and Creugers, N. H. "Tooth Loss and Oral Health-Related Quality of Life: A Systematic Review and Meta-Analysis". *Health and Quality of Life Outcomes* **8**.1 (2010), p. 126 (cit. on p. 167).

[117] Gielen, A. W. J., Oomens, C. W. J., Bovendeerd, P. H. M., Arts, T. and Janssen, J. D. "A Finite Element Approach for Skeletal Muscle Using a Distributed Moment Model of Contraction". *Computer Methods in Biomechanics and Biomedical Engineering* **3**.3 (2000), pp. 231–244 (cit. on pp. 5, 63, 176).

[118] Gollapudi, S. K. and Lin, D. C. "Experimental Determination of Sarcomere Force–Length Relationship in Type-I Human Skeletal Muscle Fibers". *Journal of Biomechanics* **42**.13 (2009), pp. 2011–2016 (cit. on pp. 56, 58, 59, 141).

[119] Gordon, A. M., Huxley, A. F. and Julian, F. J. "The Variation in Isometric Tension with Sarcomere Length in Vertebrate Muscle Fibres". *The Journal of Physiology* **184**.1 (1966), pp. 170–192 (cit. on pp. 3, 18, 19, 56, 58, 60).

[120] Granger, M. W., Buschang, P. H., Throckmorton, G. S. and Iannaccone, S. T. "Masticatory Muscle Function in Patients with Spinal Muscular Atrophy". *American Journal of Orthodontics and Dentofacial Orthopedics* **115**.6 (1999), pp. 697–702 (cit. on p. 170).

[121] Guimaraes, A. S., Carlsson, G. E. and Marie, S. K. N. "Bite Force and Handgrip Force in Patients with Molecular Diagnosis of Myotonic Dystrophy". *Journal of Oral Rehabilitation* **34**.3 (2007), pp. 195–200 (cit. on p. 167).

[122] Guzmán-Venegas, R. A., Picand, J. L. B. and de la Rosa, F. J. B. "Functional Compartmentalization of the Human Superficial Masseter Muscle". *PLOS ONE* **10**.2 (2015), e0116923 (cit. on pp. 5, 11).

[123] Handsfield, G. G., Bolsterlee, B., Inouye, J. M., Herbert, R. D., Besier, T. F. and Fernandez, J. W. "Determining Skeletal Muscle Architecture with Laplacian Simulations: A Comparison with Diffusion Tensor Imaging". *Biomechanics and Modeling in Mechanobiology* **16**.6 (2017), pp. 1845–1855 (cit. on pp. 75, 93).

[124] Hannam, A. G. and McMillan, A. S. "Internal Organization in the Human Jaw Muscles". *Critical Reviews in Oral Biology & Medicine* **5**.1 (1994), pp. 55–89 (cit. on pp. 121, 122, 124, 142, 177).

[125] Hasan, I., Madarlis, C., Keilig, L., Dirk, C., Weber, A., Bourauel, C. and Heinemann, F. "Changes in Biting Forces with Implant-Supported Overdenture in the Lower Jaw: A Comparison between Conventional and Mini Implants in a Pilot Study". *Annals of Anatomy - Anatomischer Anzeiger* **208** (2016), pp. 116–122 (cit. on pp. 121, 132).

[126] Heckman, C. and Enoka, R. M. "Motor Unit". *Comprehensive Physiology*. Hoboken, NJ, USA: John Wiley & Sons, Inc., 2012 (cit. on p. 70).

[127] Hegarty, P. V. and Hooper, A. C. "Sarcomere Length and Fibre Diameter Distributions in Four Different Mouse Skeletal Muscles." *Journal of Anatomy* **110**.2 (1971), pp. 249–257 (cit. on p. 117).

[128] Heidlauf, T. "Chemo-Electro-Mechanical Modelling of the Neuromuscular System". Ph.D. Thesis. University of Stuttgart, 2016 (cit. on pp. 71, 99).

[129] Heidlauf, T., Klotz, T., Rode, C., Siebert, T. and Röhrle, O. "A Continuum-Mechanical Skeletal Muscle Model Including Actin-Titin Interaction Predicts Stable Contractions on the Descending Limb of the Force-Length Relation". *PLOS Computational Biology* **13**.10 (2017), e1005773 (cit. on pp. 4, 65, 67).

[130] Heidlauf, T. and Röhrle, O. "A Multiscale Chemo-Electro-Mechanical Skeletal Muscle Model to Analyze Muscle Contraction and Force Generation for Different Muscle Fiber Arrangements". *Frontiers in Physiology* **5** (2014) (cit. on pp. 4, 99, 177).

[131] Henderson, R. D. and McCombe, P. A. "Assessment of Motor Units in Neuromuscular Disease". *Neurotherapeutics* **14** (2017), pp. 69–77 (cit. on p. 163).

[132] Henneman, E. "Relation between Size of Neurons and Their Susceptibility to Discharge". *Science* **126**.3287 (1957), pp. 1345–1347 (cit. on pp. 1, 22, 64).

[133] Henriksson-Larsén, K., Friden, J. and Wretling, M.-L. "Distribution of Fibre Sizes in Human Skeletal Muscle. An Enzyme Histochemical Study in m Tibialis Anterior". *Acta Physiologica Scandinavica* **123**.2 (1985), pp. 171–177 (cit. on pp. 9, 93).

[134] Henriksson-Larsén, K. "Distribution, Total Number and Size of Different Types of Fibres in Male and Female Skeletal Muscles: An Enzyme Histochemical Study of Whole Muscle Cross-Sections". PhD Thesis. Umeå University, 1984 (cit. on p. 175).

[135] Hernández-Gascón, B., Grasa, J., Calvo, B. and Rodríguez, J. F. "A 3D Electro-Mechanical Continuum Model for Simulating Skeletal Muscle Contraction". *Journal of Theoretical Biology* **335** (2013), pp. 108–118 (cit. on p. 3).

[136] Herring, S. W., Anapol, F. C. and Wineski, L. E. "Motor-Unit Territories in the Masseter Muscle of Infant Pigs". *Archives of Oral Biology* **36**.12 (1991), pp. 867–873 (cit. on pp. 7, 124, 140).

[137] Herring, S. W., Grimm, A. F. and Grimm, B. R. "Functional Heterogeneity in a Multipinnate Muscle". *American Journal of Anatomy* **154**.4 (1979), pp. 563–575 (cit. on pp. 1, 5, 9).

[138] Hill, A. V. "The Heat of Shortening and the Dynamic Constants of Muscle". *Proceedings of the Royal Society of London, B - Biological Sciences* **126**.843 (1938), pp. 136–195 (cit. on pp. 3, 18).

[139] Hirose, M., Tanaka, E., Tanaka, M., Fujita, R., Kuroda, Y., Yamano, E., Eijden, T. M. G. J. van and Tanne, K. "Three-Dimensional Finite-Element Model of the Human Temporomandibular Joint Disc during Prolonged Clenching". *European Journal of Oral Sciences* **114**.5 (2006), pp. 441–448 (cit. on p. 132).

[140] Hodges, P. W., Pengel, L. H. M., Herbert, R. D. and Gandevia, S. C. "Measurement of Muscle Contraction with Ultrasound Imaging". *Muscle & Nerve* **27**.6 (2003), pp. 682–692 (cit. on p. 171).

[141] Hodgkin, A. L. and Huxley, A. F. "A Quantitative Description of Membrane Current and Its Application to Conduction and Excitation in Nerve". *The Journal of Physiology* **117**.4 (1952), pp. 500–544 (cit. on p. 66).

[142] Holtermann, A., Roeleveld, K., Mork, P. J., Grönlund, C., Karlsson, J. S., Andersen, L. L., Olsen, H. B., Zebis, M. K., Sjøgaard, G. and Søgaard, K. "Selective Activation of Neuromuscular Compartments within the Human Trapezius Muscle". *Journal of Electromyography and Kinesiology* **19**.5 (2009), pp. 896–902 (cit. on pp. 5, 6, 121, 153).

[143] Holtermann, A., Roeleveld, K. and Karlsson, J. S. "Inhomogeneities in Muscle Activation Reveal Motor Unit Recruitment". *Journal of Electromyography and Kinesiology* **15**.2 (2005), pp. 131–137 (cit. on pp. 5, 121, 174, 177).

[144] Holzapfel, G. A. *Nonlinear Solid Mechanics: A Continuum Approach for Engineering*. West Sussex: John Wiley & Sons Ltd, 2000 (cit. on pp. 25, 32, 34, 35, 46, 50, 51).

[145] Holzbaur, K. R. S., Murray, W. M., Gold, G. E. and Delp, S. L. "Upper Limb Muscle Volumes in Adult Subjects". *Journal of Biomechanics* **40**.4 (2007), pp. 742–749 (cit. on p. 16).

[146] Hooke, R. and Jeeves, T. A. "" Direct Search" Solution of Numerical and Statistical Problems". *Journal of the Association for Computing Machinery* **8**.2 (1961), pp. 212–229 (cit. on p. 57).

[147] Hopkins, J., Feland, J. and Hunter, I. "A Comparison of Voluntary and Involuntary Measures of Electromechanical Delay". *International Journal of Neuroscience* **117**.5 (2007), pp. 597–604 (cit. on p. 116).

[148] Howald, H. "Training-Induced Morphological and Functional Changes in Skeletal Muscle". *International Journal of Sports Medicine* **3**.1 (1982), pp. 1–12 (cit. on pp. 145, 163).

[149] Howlett, O. A., Lannin, N. A., Ada, L. and McKinstry, C. "Functional Electrical Stimulation Improves Activity After Stroke: A Systematic Review With Meta-Analysis". *Archives of Physical Medicine and Rehabilitation* **96**.5 (2015), pp. 934–943 (cit. on p. 181).

[150] Huijing, P. A. "Muscular Force Transmission: A Unified, Dual or Multiple System? A Review and Some Explorative Experimental Results". *Archives of Physiology and Biochemistry* **107**.4 (1999), pp. 292–311 (cit. on p. 20).

[151] Huijing, P. A. "Muscle as a Collagen Fiber Reinforced Composite: A Review of Force Transmission in Muscle and Whole Limb". *Journal of Biomechanics* **32**.4 (1999), pp. 329–345 (cit. on p. 152).

[152] Huwaldt, J. A. *Plot Digitizer*. http://plotdigitizer.sourceforge.net/. 2015 (cit. on pp. 18, 56).

[153] Huxley, A. F. and Niedergerke, R. "Structural Changes in Muscle During Contraction: Interference Microscopy of Living Muscle Fibres". *Nature* **173**.4412 (1954), pp. 971–973 (cit. on p. 17).

[154] Huxley, H. and Hanson, J. "Changes in the Cross-Striations of Muscle during Contraction and Stretch and Their Structural Interpretation". *Nature* **173**.4412 (1954), pp. 973–976 (cit. on p. 17).

[155] Jantarat, J., Palamara, J. E. A. and Messer, H. H. "An Investigation of Cuspal Deformation and Delayed Recovery after Occlusal Loading". *Journal of Dentistry* **29**.5 (2001), pp. 363–370 (cit. on p. 185).

[156] Jaworowski, Å., Porter, M. M., Holmbäck, A. M., Downham, D. and Lexell, J. "Enzyme Activities in the Tibialis Anterior Muscle of Young Moderately Active Men and Women: Relationship with Body Composition, Muscle Cross-Sectional Area and Fibre Type Composition". *Acta Physiologica Scandinavica* **176**.3 (2002), pp. 215–225 (cit. on p. 145).

[157] Jennekens, F. G. I., Tomlinson, B. E. and Walton, J. N. "Data on the Distribution of Fibre Types in Five Human Limb Muscles An Autopsy Study". *Journal of the Neurological Sciences* **14**.3 (1971), pp. 245–257 (cit. on p. 95).

[158] Jensen, C. and Westgaard, R. H. "Functional Subdivision of the Upper Trapezius Muscle during Low-Level Activation". *European Journal of Applied Physiology and Occupational Physiology* **76**.4 (1997), pp. 335–339 (cit. on pp. 6, 177).

[159] Johansson, T., Meier, P. and Blickhan, R. "A Finite-Element Model for the Mechanical Analysis of Skeletal Muscles". *Journal of Theoretical Biology* **206**.1 (2000), pp. 131–149 (cit. on pp. 2, 5, 46).

[160] Johnson, M. A., Polgar, J., Weightman, D. and Appleton, D. "Data on the Distribution of Fibre Types in Thirty-Six Human Muscles: An Autopsy Study". *Journal of the Neurological Sciences* **18**.1 (1973), pp. 111–129 (cit. on p. 175).

[161] Johnson, M. A., Sideri, G., Weightman, D. and Appleton, D. "A Comparison of Fibre Size, Fibre Type Constitution and Spatial Fibre Type Distribution in Normal Human Muscle and in Muscle from Cases of Spinal Muscular Atrophy and from Other Neuromuscular Disorders". *Journal of the Neurological Sciences* **20**.4 (1973), pp. 345–361 (cit. on pp. 7, 146, 163).

[162] Kanda, K. and Hashizume, K. "Factors Causing Difference in Force Output among Motor Units in the Rat Medial Gastrocnemius Muscle." *The Journal of Physiology* **448**.1 (1992), pp. 677–695 (cit. on pp. 7, 22, 95, 117, 118).

[163] Kandel, E. R., Schwartz, J. H., Jessell, T. M., Biochemistry, D. of, Jessell, M. B. T., Siegelbaum, S. and Hudspeth, A. J. *Principles of Neural Science*. Vol. 4. New York, NY: McGraw-hill, 2000 (cit. on pp. 15, 17, 18, 21, 121).

[164] Kawakami, Y., Abe, T., Kanehisa, H. and Fukunaga, T. "Human Skeletal Muscle Size and Architecture: Variability and Interdependence". *American Journal of Human Biology* **18**.6 (2006), pp. 845–848 (cit. on p. 15).

[165] Keener, J. and Sneyd, J. *Mathematical Physiology: II: Systems Physiology*. Second. Interdisciplinary Applied Mathematics. New York, NY: Springer-Verlag, 2009 (cit. on p. 66).

[166] Kellis, E., Galanis, N., Natsis, K. and Kapetanos, G. "In Vivo and in Vitro Examination of the Tendinous Inscription of the Human Semitendinosus Muscle". *Cells Tissues Organs* **195**.4 (2012), pp. 365–376 (cit. on p. 21).

[167] Kelly, N. A., Hammond, K. G., Bickel, C. S., Windham, S. T., Tuggle, S. C. and Bamman, M. M. "Effects of Aging and Parkinson's Disease on Motor Unit Remodeling: Influence of Resistance Exercise Training". *Journal of Applied Physiology* **124**.4 (2018), pp. 888–898 (cit. on pp. 7, 63, 163).

[168] Kent-Braun, J. A. and Ng, A. V. "Specific Strength and Voluntary Muscle Activation in Young and Elderly Women and Men". *Journal of Applied Physiology* **87**.1 (1999), pp. 22–29 (cit. on p. 141).

[169] Kernell, D. "High-Frequency Repetitive Firing of Cat Lumbosacral Motoneurones Stimulated by Long-Lasting Injected Currents". *Acta Physiologica Scandinavica* **65**.1-2 (1965), pp. 74–86 (cit. on p. 23).

[170] Kirkebø, A. and Wisnes, A. "Regional Tissue Fluid Pressure in Rat Calf Muscle during Sustained Contraction or Stretch". *Acta Physiologica Scandinavica* **114**.4 (1982), pp. 551–556 (cit. on p. 155).

[171] Klotz, T., Gizzi, L., Yavuz, U. Ş. and Röhrle, O. "Modelling the Electrical Activity of Skeletal Muscle Tissue Using a Multi-Domain Approach". *Biomechanics and Modeling in Mechanobiology* **19**.1 (2020), pp. 335–349 (cit. on p. 178).

[172] Kogawa, E. M., Calderon, P. S., Lauris, J. R. P., Araujo, C. R. P. and Conti, P. C. R. "Evaluation of Maximal Bite Force in Temporomandibular Disorders Patients". *Journal of Oral Rehabilitation* **33**.8 (2006), pp. 559–565 (cit. on pp. 121, 132).

[173] Kolz, C. W., Suter, T. and Henninger, H. B. "Regional Mechanical Properties of the Long Head of the Biceps Tendon". *Clinical Biomechanics* **30**.9 (2015), pp. 940–945 (cit. on pp. 49, 56–59).

[174] Koolstra, J. H., Eijden, T. M. G. J. van, Weijs, W. A. and Naeije, M. "A Three-Dimensional Mathematical Model of the Human Masticatory System Predicting Maximum Possible Bite Forces". *Journal of biomechanics* **21**.7 (1988), pp. 563–576 (cit. on p. 125).

[175] Koolstra, J. H. and van Eijden, T. M. G. J. "Application and Validation of a Three-Dimensional Mathematical Model of the Human Masticatory System in Vivo". *Journal of Biomechanics* **25**.2 (1992), pp. 175–187 (cit. on pp. 121, 125).

[176] Korfage, J. a. M. and Eijden, T. M. G. J. van. "Regional Differences in Fibre Type Composition in the Human Temporalis Muscle". *The Journal of Anatomy* **194**.3 (1999), pp. 355–362 (cit. on p. 175).

[177] Korioth, T. W. P., Romilly, D. P. and Hannam, A. G. "Three-Dimensional Finite Element Stress Analysis of the Dentate Human Mandible". *American Journal of Physical Anthropology* **88**.1 (1992), pp. 69–96 (cit. on pp. 121, 125, 132, 185).

[178] Korsawe, J. "In Triangulation (Version 1.5)". *MATLAB Central File Exchange* (2016) (cit. on p. 103).

[179] Korthuis, R. J. *Skeletal Muscle Circulation*. Integrated Systems Physiology: From Molecule to Function to Disease. San Rafael, CA: Morgan & Claypool Life Sciences, 2011 (cit. on p. 15).

[180] Kröner, E. *Statistical Continuum Mechanics*. Vienna: Springer-Verlag, 1972 (cit. on p. 98).

[181] Kshirsagar, R., Jaggi, N. and Halli, R. "Bite Force Measurement in Mandibular Parasymphyseal Fractures: A Preliminary Clinical Study". *Craniomaxillofacial Trauma and Reconstruction* **4**.04 (2011), pp. 241–244 (cit. on pp. 121, 132).

[182] Kugelberg, E., Edström, L. and Abbruzzese, M. "Mapping of Motor Units in Experimentally Reinnervated Rat Muscle: Interpretation of Histochemical and Atrophic Fibre Patterns in Neurogenic Lesions". *Journal of Neurology, Neurosurgery & Psychiatry* **33**.3 (1970), pp. 319–329 (cit. on pp. 7, 95).

[183] Kupczik, K., Stark, H., Mundry, R., Neininger, F. T., Heidlauf, T. and Röhrle, O. "Reconstruction of Muscle Fascicle Architecture from Iodine-Enhanced microCT Images: A Combined Texture Mapping and Streamline Approach". *Journal of Theoretical Biology* **382** (2015), pp. 34–43 (cit. on pp. 74, 75).

[184] Kwa, S., Weijs, W. and van Eijden, T. M. G. J. "Effects of Activation Rate on Contractile Properties of Rabbit Masseter Motor Units". *Experimental Brain Research* **142**.2 (2002), pp. 221–226 (cit. on p. 123).

[185] Kwa, S. H., Weijs, W. A. and Juch, P. J. "Contraction Characteristics and Myosin Heavy Chain Composition of Rabbit Masseter Motor Units". *Journal of Neurophysiology* **73**.2 (1995), pp. 538–549 (cit. on p. 123).

[186] Kwa, S., Korfage, J. and Weijs, W. "Function-Dependent Anatomical Parameters of Rabbit Masseter Motor Units". *Journal of Dental Research* **74**.10 (1995), pp. 1649–1657 (cit. on p. 7).

[187] Lanza, A., Aversa, R., Rengo, S., Apicella, D. and Apicella, A. "3D FEA of Cemented Steel, Glass and Carbon Posts in a Maxillary Incisor". *Dental Materials* **21**.8 (2005), pp. 709–715 (cit. on p. 183).

[188] Lapatki, B. G., Eiglsperger, U., Schindler, H. J., Radeke, J., Holobar, A. and van Dijk, J. P. "Three-Dimensional Amplitude Characteristics of Masseter Motor Units and Representativeness of Extracted Motor Unit Samples". *Clinical Neurophysiology* **130**.3 (2019), pp. 388–395 (cit. on pp. 7, 9, 81, 94, 124, 140, 149, 180, 181).

[189] Lara, J., Paskaranandavadivel, N. and Cheng, L. K. "HD-EMG Electrode Count and Feature Selection Influence on Pattern-Based Movement Classification Accuracy". *2020 42nd Annual International Conference of the IEEE Engineering in Medicine Biology Society (EMBC)*. IEEE, 2020, pp. 4787–4790 (cit. on p. 179).

[190] Larsson, L., Edstrom, L., Lindegren, B., Gorza, L. and Schiaffino, S. "MHC Composition and Enzyme-Histochemical and Physiological Properties of a Novel Fast-Twitch Motor Unit Type". *American Journal of Physiology - Cell Physiology* **261**.1 (1991), pp. C93–C101 (cit. on pp. 7, 95).

[191] Larsson, L., Degens, H., Li, M., Salviati, L., Lee, Y. il, Thompson, W., Kirkland, J. L. and Sandri, M. "Sarcopenia: Aging-Related Loss of Muscle Mass and Function". *Physiological Reviews* **99**.1 (2018), pp. 427–511 (cit. on pp. 12, 92, 163).

[192] Lateva, Z. C., McGill, K. C. and Johanson, M. E. "The Innervation and Organization of Motor Units in a Series-Fibered Human Muscle: The Brachioradialis". *Journal of Applied Physiology* **108**.6 (2010), pp. 1530–1541 (cit. on pp. 20, 93).

[193] Laursen, T. A. *Computational Contact and Impact Mechanics: Fundamentals of Modeling Interfacial Phenomena in Nonlinear Finite Element Analysis*. Berlin Heidelberg: Springer-Verlag, 2003 (cit. on p. 41).

[194] Lemos, R., Epstein, M., Herzog, W. and Wyvill, B. "Realistic Skeletal Muscle Deformation Using Finite Element Analysis". *Proceedings XIV Brazilian Symposium on Computer Graphics and Image Processing*. Florianopolis, Brazil: IEEE, 2001, pp. 192–199 (cit. on p. 5).

[195] Lester, J. M., Silber, D. I., Cohen, M. H., Hirsch, R. P., Bradley, W. G. and Brenner, J. F. "The Co-Dispersion Index for the Measurement of Fiber Type Distribution Patterns". *Muscle & Nerve* **6**.8 (1983), pp. 581–587 (cit. on pp. 2, 7, 8, 85, 94, 146, 163).

[196] Lester, J. M., Soule, N. W., Bradley, W. G. and Brenner, J. F. "An Augmented Computer Model of Motor Unit Reorganization in Neurogenic Diseases of Skeletal Muscle". *Muscle & Nerve* **16**.1 (1993), pp. 43–56 (cit. on p. 164).

[197] Lexell, J. and Downham, D. Y. "The Occurrence of Fibre-Type Grouping in Healthy Human Muscle: A Quantitative Study of Cross-Sections of Whole Vastus Lateralis from Men between 15 and 83 Years". *Acta Neuropathologica* **81**.4 (1991), pp. 377–381 (cit. on pp. 7, 81, 145, 163).

[198] Lexell, J., Henriksson-Larsén, K. and Sjöström, M. "Distribution of Different Fibre Types in Human Skeletal Muscles 2. A Study of Cross-Sections of Whole m. Vastus Lateralis". *Acta Physiologica Scandinavica* **117**.1 (1983), pp. 115–122 (cit. on p. 175).

[199] Lexell, J., Taylor, C. C. and Sjöström, M. "What Is the Cause of the Ageing Atrophy?: Total Number, Size and Proportion of Different Fiber Types Studied in Whole Vastus Lateralis Muscle from 15- to 83-Year-Old Men". *Journal of the Neurological Sciences* **84**.2 (1988), pp. 275–294 (cit. on pp. 2, 7, 8, 63, 163).

[200] Li, N., Fang, H., Zhang, C., Gutowski, M., Palta, E. and Wang, Q. "A Numerical Study of Occupant Responses and Injuries in Vehicular Crashes into Roadside Barriers Based on Finite Element Simulations". *Advances in Engineering Software* **90** (2015), pp. 22–40 (cit. on p. 40).

[201] Liddell, E. G. T. and Sherrington, C. S. "Recruitment and Some Other Features of Reflex Inhibition". *Proceedings of the Royal Society of London, B - Biological Sciences* **97**.686 (1925), pp. 488–518 (cit. on p. 21).

[202] Linn, J. and Messer, H. H. "Effect of Restorative Procedures on the Strength of Endodontically Treated Molars". *Journal of Endodontics* **20**.10 (1994), pp. 479–485 (cit. on p. 185).

[203] Loeb, G. E. "Motoneurone Task Groups: Coping with Kinematic Heterogeneity". *Journal of Experimental Biology* **115**.1 (1985), pp. 137–146 (cit. on p. 1).

[204] Lund, J. "Mastication and Its Control by the Brain Stem". *Critical Reviews in Oral Biology & Medicine* **2**.1 (1991), pp. 33–64 (cit. on p. 122).

[205] Luu, B. L., Muceli, S., Saboisky, J. P., Farina, D., Héroux, M. E., Bilston, L. E., Gandevia, S. C. and Butler, J. E. "Motor Unit Territories in Human Genioglossus Estimated with Multichannel Intramuscular Electrodes". *Journal of Applied Physiology* **124**.3 (2017), pp. 664–671 (cit. on pp. 7, 8, 180).

[206] Lynch, H. A., Johannessen, W., Wu, J. P., Jawa, A. and Elliott, D. M. "Effect of Fiber Orientation and Strain Rate on the Nonlinear Uniaxial Tensile Material Properties of Tendon". *Journal of Biomechanical Engineering* **125**.5 (2003), pp. 726–731 (cit. on p. 54).

[207] MacIntosh, B., Gardiner, P. and McComas, A. *Skeletal Muscle: Form and Function*. 2nd Edition. Champaign, IL: Human Kinetics, 2005 (cit. on pp. 15, 16).

[208] Maganaris, C. N., Baltzopoulos, V., Ball, D. and Sargeant, A. J. "In Vivo Specific Tension of Human Skeletal Muscle". *Journal of Applied Physiology* **90**.3 (2001), pp. 865–872 (cit. on p. 141).

[209] Maier, B., Emamy, N., Krämer, A. and Mehl, M. "Highly Parallel Multi-Physics Simulation of Muscular Activation and EMG". *Proceedings of VIII International Conference on Computational Methods for Coupled Problems in Science and Engineering*. CIMNE, 2019, pp. 610–621 (cit. on pp. 4, 176).

[210] Manly, R. S., Hodge, H. C. and Ange, L. E. "Density and Refractive Index Studies of Dental Hard Tissues: II. Density Distribution Curves". *Journal of Dental Research* **18**.3 (1939), pp. 203–211 (cit. on p. 132).

[211] Marsden, C. D., Meadows, J. C. and Merton, P. A. ""Muscular Wisdom" That Minimizes Fatigue during Prolonged Effort in Man: Peak Rates of Motoneuron Discharge and Slowing of Discharge during Fatigue". *Advances in Neurology* **39** (1983), pp. 169–211 (cit. on pp. 117, 179).

[212] Maughan, R. J., Watson, J. S. and Weir, J. "Strength and Cross-Sectional Area of Human Skeletal Muscle." *The Journal of Physiology* **338**.1 (1983), pp. 37–49 (cit. on p. 141).

[213] McComas, A. J., Upton, A. R. M. and Sica, R. E. P. "Motorneurone Disease and Ageing". *The Lancet*. Originally Published as Volume 2, Issue 7844 **302**.7844 (1973), pp. 1477–1480 (cit. on pp. 7, 163).

[214] McMillan, A. S. and Hannam, A. G. "Motor-Unit Territory in the Human Masseter Muscle". *Archives of Oral Biology* **36**.6 (1991), pp. 435–441 (cit. on pp. 7, 8, 123, 124, 140, 149).

[215] McMillan, A. S., Sasaki, K. and Hannam, A. G. "The Estimation of Motor Unit Twitch Tensions in the Human Masseter Muscle by Spike-Triggered Averaging". *Muscle & Nerve* **13**.8 (1990), pp. 697–703 (cit. on pp. 12, 156, 159).

[216] Merkher, Y., Sivan, S., Etsion, I., Maroudas, A., Halperin, G. and Yosef, A. "A Rational Human Joint Friction Test Using a Human Cartilage-on-Cartilage Arrangement". *Tribology Letters* **22**.1 (2006), pp. 29–36 (cit. on p. 44).

[217] Mesin, L., Merlo, E., Merletti, R. and Orizio, C. "Investigation of Motor Unit Recruitment during Stimulated Contractions of Tibialis Anterior Muscle". *Journal of Electromyography and Kinesiology* **20**.4 (2010), pp. 580–589 (cit. on pp. 9, 81, 93).

[218] Messi, M. L., Li, T., Wang, Z.-M., Marsh, A. P., Nicklas, B. and Delbono, O. "Resistance Training Enhances Skeletal Muscle Innervation Without Modifying the Number of Satellite Cells or Their Myofiber Association in Obese Older Adults". *The Journals of Gerontology: Series A* **71**.10 (2016), pp. 1273–1280 (cit. on pp. 81, 145, 163).

[219] Miller, L., McFadyen, A., Lord, A. C., Hunter, R., Paul, L., Rafferty, D., Bowers, R. and Mattison, P. "Functional Electrical Stimulation for Foot Drop in Multiple Sclerosis: A Systematic Review and Meta-Analysis of the Effect on Gait Speed". *Archives of Physical Medicine and Rehabilitation* **98**.7 (2017), pp. 1435–1452 (cit. on p. 181).

[220] Miller, S. C., Korff, T., Waugh, C., Fath, F. and Blazevich, A. J. "Tibialis Anterior Moment Arm: Effects of Measurement Errors and Assumptions:" *Medicine & Science in Sports & Exercise* **47**.2 (2015), pp. 428–439 (cit. on p. 159).

[221] Mitchell, W. K., Atherton, P. J., Williams, J., Larvin, M., Lund, J. N. and Narici, M. "Sarcopenia, Dynapenia, and the Impact of Advancing Age on Human Skeletal Muscle Size and Strength; a Quantitative Review". *Frontiers in Physiology* **3** (2012) (cit. on pp. 163, 164, 167).

[222] Miyamoto, N., Wakahara, T. and Kawakami, Y. "Task-Dependent Inhomogeneous Muscle Activities within the Bi-Articular Human Rectus Femoris Muscle". *PLOS ONE* **7**.3 (2012) (cit. on pp. 5, 121).

[223] Miyaura, K., Matsuka, Y., Morita, M., Yamashita, A. and Watanabe, T. "Comparison of Biting Forces in Different Age and Sex Groups: A Study of Biting Efficiency with Mobile and Non-Mobile Teeth". *Journal of Oral Rehabilitation* **26**.3 (1999), pp. 223–227 (cit. on p. 132).

[224] Moga, R. A. and Chiorean, C. G. "Strain Analysis of a Human Tooth with Support Tissues Resorption". *Proceedings of the World Congress on Engineering*. Vol. 2. London, U.K.: Newswood Limited, 2013, pp. 1374–1379 (cit. on p. 132).

[225] Mohammadkhah, M. "Tension and Compression Stress-Strain Asymmetry in Passive Skeletal Muscle". PhD Thesis. Trinity College Dublin, 2017 (cit. on p. 56).

[226] Monti, R. J., Roy, R. R. and Edgerton, V. R. "Role of Motor Unit Structure in Defining Function". *Muscle & Nerve* **24**.7 (2001), pp. 848–866 (cit. on pp. 7, 20, 21).

[227] Mooney, M. "A Theory of Large Elastic Deformation". *Journal of Applied Physics* **11**.9 (1940), pp. 582–592 (cit. on p. 46).

[228] Mordhorst, M., Strecker, T., Wirtz, D., Heidlauf, T. and Röhrle, O. "POD-DEIM Reduction of Computational EMG Models". *Journal of Computational Science* **19** (2017), pp. 86–96 (cit. on pp. 4, 176).

[229] Mordhorst, M., Heidlauf, T. and Röhrle, O. "Mathematically Modelling Surface EMG Signals: Mathematically Modelling Surface EMG Signals". *Proceedings in Applied Mathematics and Mechanics* **14**.1 (2014), pp. 123–124 (cit. on pp. 4, 177).

[230] Mordhorst, M., Heidlauf, T. and Röhrle, O. "Predicting Electromyographic Signals under Realistic Conditions Using a Multiscale Chemo–Electro–Mechanical Finite Element Model". *Interface Focus* **5**.2 (2015), p. 20140076 (cit. on p. 4).

[231] Mörl, F., Siebert, T., Schmitt, S., Blickhan, R. and Günther, M. "Electro-Mechanical Delay in Hill-Type Muscle Models". *Journal of Mechanics in Medicine and Biology* **12**.05 (2012), p. 1250085 (cit. on p. 100).

[232] Morris, C. J. "Human Skeletal Muscle Fibre Type Grouping and Collateral Re-Innervation." *Journal of Neurology, Neurosurgery, and Psychiatry* **32**.5 (1969), pp. 440–444 (cit. on pp. 2, 7, 63, 81, 163).

[233] Mugge, W., Munts, A. G., Schouten, A. C. and van der Helm, F. C. T. "Modeling Movement Disorders—CRPS-Related Dystonia Explained by Abnormal Proprioceptive Reflexes". *Journal of Biomechanics* **45**.1 (2012), pp. 90–98 (cit. on p. 118).

[234] Murray, G. M., Phanachet, I. and Klineberg, I. J. "Electromyographic Evidence for Functional Heterogeneity in the Inferior Head of the Human Lateral Pterygoid Muscle: A Preliminary Multi-Unit Study". *Clinical Neurophysiology* **110**.5 (1999), pp. 944–950 (cit. on p. 5).

[235] Murthy, G., Hargens, A. R., Lehman, S. and Rempel, D. M. "Ischemia Causes Muscle Fatigue". *Journal of Orthopaedic Research* **19**.3 (2001), pp. 436–440 (cit. on pp. 117, 143, 155, 179).

[236] Nagumo, J., Arimoto, S. and Yoshizawa, S. "An Active Pulse Transmission Line Simulating Nerve Axon". *Proceedings of the IRE* **50**.10 (1962), pp. 2061–2070 (cit. on p. 66).

[237] Naito, A., Shindo, M., Miyasaka, T., Sun, Y.-J. and Morita, H. "Inhibitory Projection from Brachioradialis to Biceps Brachii Motoneurones in Human". *Experimental Brain Research* **111**.3 (1996), pp. 483–486 (cit. on p. 118).

[238] Nakhostine, M., Styf, J. R., van Leuven, S., Hargens, A. R. and Gershuni, D. H. "Intramuscular Pressure Varies with Depth: The Tibialis Anterior Muscle Studied in 12 Volunteers". *Acta Orthopaedica Scandinavica* **64**.3 (1993), pp. 377–381 (cit. on pp. 143, 153).

[239] Navallas, J., Malanda, A., Gila, L., Rodríguez, J. and Rodríguez, I. "A Muscle Architecture Model Offering Control over Motor Unit Fiber Density Distributions". *Medical & Biological Engineering & Computing* **48**.9 (2010), pp. 875–886 (cit. on pp. 10, 81, 93).

[240] Negro, F. and Orizio, C. "Robust Estimation of Average Twitch Contraction Forces of Populations of Motor Units in Humans". *Journal of Electromyography and Kinesiology* **37** (2017), pp. 132–140 (cit. on pp. 12, 156).

[241] Negro, F., Yavuz, U. Ş. and Farina, D. "Limitations of the Spike-Triggered Averaging for Estimating Motor Unit Twitch Force: A Theoretical Analysis". *PLOS ONE* **9**.3 (2014), e92390 (cit. on pp. 12, 156).

[242] Nelson, G. J. "Three Dimensional Computer Modeling of Human Mandibular Biomechanics". Ph.D. Thesis. University of British Columbia, 1986 (cit. on p. 185).

[243] Nishigawa, K., Bando, E. and Nakano, M. "Quantitative Study of Bite Force during Sleep Associated Bruxism". *Journal of Oral Rehabilitation* **28**.5 (2001), pp. 485–491 (cit. on p. 142).

[244] Nolan, D., Lally, C. and McGarry, P. *Understanding the Deformation Gradient in Abaqus and Key Guidelines for Anisotropic Hyperelastic User Material Subroutines (UMATs).* https://engrxiv.org/4ryu2/. 2019 (cit. on p. 105).

[245] Nordez, A., Gallot, T., Catheline, S., Guével, A., Cornu, C. and Hug, F. "Electromechanical Delay Revisited Using Very High Frame Rate Ultrasound". *Journal of Applied Physiology* **106**.6 (2009), pp. 1970–1975 (cit. on p. 116).

[246] Nordstrom, M. A., Miles, T. S. and Veale, J. L. "Effect of Motor Unit Firing Pattern on Twitches Obtained by Spike-Triggered Averaging". *Muscle & Nerve* **12**.7 (1989), pp. 556–567 (cit. on p. 123).

[247] O'Mahony, A. M., Williams, J. L., Katz, J. O. and Spencer, P. "Anisotropic Elastic Properties of Cancellous Bone from a Human Edentulous Mandible". *Clinical Oral Implants Research* **11**.5 (2000), pp. 415–421 (cit. on p. 132).

[248] Odegard, G. M., Haut Donahue, T. L., Morrow, D. A. and Kaufman, K. R. "Constitutive Modeling of Skeletal Muscle Tissue With an Explicit Strain-Energy Function". *Journal of Biomechanical Engineering* **130**.6 (2008) (cit. on p. 50).

[249] Oden, J. T. "A Theory of Penalty Methods for Finite Element Approximations of Highly Nonlinear Problems in Continuum Mechanics". *Computers & Structures* **8**.3 (1978), pp. 445–449 (cit. on p. 48).

[250] Ogawa, T., Kawata, T., Tsuboi, A., Hattori, Y., Watanabe, M. and Sasaki, K. "Functional Properties and Regional Differences of Human Masseter Motor Units Related to Three-Dimensional Bite Force". *Journal of Oral Rehabilitation* **33**.10 (2006), pp. 729–740 (cit. on pp. 5, 6, 11, 121, 140, 142, 145, 151, 174, 177).

[251] Ogden, R. W. and Hill, R. "Large Deformation Isotropic Elasticity – on the Correlation of Theory and Experiment for Incompressible Rubberlike Solids". *Proceedings of the Royal Society of London, A - Mathematical and Physical Sciences* **326**.1567 (1972), pp. 565–584 (cit. on p. 185).

[252] Al-Omiri, M. K., Sghaireen, M. G., Alhijawi, M. M., Alzoubi, I. A., Lynch, C. D. and Lynch, E. "Maximum Bite Force Following Unilateral Implant-Supported Prosthetic Treatment: Within-Subject Comparison to Opposite Dentate Side". *Journal of Oral Rehabilitation* **41**.8 (2014), pp. 624–629 (cit. on p. 132).

[253] Oomens, C. W. J., Maenhout, M., van Oijen, C. H., Drost, M. R. and Baaijens, F. P. "Finite Element Modelling of Contracting Skeletal Muscle". *Philosophical Transactions of the Royal Society B: Biological Sciences* **358**.1437 (2003), pp. 1453–1460 (cit. on pp. 5, 63, 176).

[254] OpenStax. *Axial Muscles of the Head, Neck, and Back - Anatomy and Physiology*. https://openstax.org/books/anatomy-and-physiology/pages/11-3-axial-muscles-of-the-head-neck-and-back. 2020 (cit. on p. 123).

[255] Osborn, J. and Baragar, F. "Predicted Pattern of Human Muscle Activity during Clenching Derived from a Computer Assisted Model: Symmetric Vertical Bite Forces". *Journal of Biomechanics* **18**.8 (1985), pp. 599–612 (cit. on p. 125).

[256] Palinkas, M., Nassar, M. S. P., Cecílio, F. A., Siéssere, S., Semprini, M., Machado-de-Sousa, J. P., Hallak, J. E. C. and Regalo, S. C. H. "Age and Gender Influence on Maximal Bite Force and Masticatory Muscles Thickness". *Archives of Oral Biology* **55**.10 (2010), pp. 797–802 (cit. on p. 167).

[257] Péan, F., Tanner, C., Gerber, C., Fürnstahl, P. and Goksel, O. "A Comprehensive and Volumetric Musculoskeletal Model for the Dynamic Simulation of the Shoulder Function". *Computer Methods in Biomechanics and Biomedical Engineering* **22**.7 (2019), pp. 740–751 (cit. on pp. 4–6, 63, 177).

[258] Peolsson, M., Larsson, B., Brodin, L.-Å. and Gerdle, B. "A Pilot Study Using Tissue Velocity Ultrasound Imaging (TVI) to Assess Muscle Activity Pattern in Patients with Chronic Trapezius Myalgia". *BMC Musculoskeletal Disorders* **9**.1 (2008), p. 127 (cit. on p. 178).

[259] Pérot, C., André, L., Dupont, L. and Vanhoutte, C. "Relative Contributions of the Long and Short Heads of the Biceps Brachii during Single or Dual Isometric Tasks". *Journal of Electromyography and Kinesiology* **6**.1 (1996), pp. 3–11 (cit. on p. 5).

[260] Peyron, M.-A., Blanc, O., Lund, J. P. and Woda, A. "Influence of Age on Adaptability of Human Mastication". *Journal of neurophysiology* **92**.2 (2004), pp. 773–779 (cit. on p. 132).

[261] Pfeiffer, G. and Friede, R. L. "The Localization of Axon Branchings in Two Muscle Nerves of the Rat". *Anatomy and Embryology* **172**.2 (1985), pp. 177–182 (cit. on pp. 7, 94).

[262] Phanachet, I., Whittle, T., Wanigaratne, K., Klineberg, I., Sessle, B. and Murray, G. "Functional Heterogeneity in the Superior Head of the Human Lateral Pterygoid". *Journal of Dental Research* **82**.2 (2003), pp. 106–111 (cit. on pp. 5, 141).

[263] Polgar, J., Johnson, M. A., Weightman, D. and Appleton, D. "Data on Fibre Size in Thirty-Six Human Muscles: An Autopsy Study". *Journal of the Neurological Sciences* **19**.3 (1973), pp. 307–318 (cit. on p. 117).

[264] Pratt, C. A., Chanaud, C. M. and Loeb, G. E. "Functionally Complex Muscles of the Cat Hindlimb". *Experimental Brain Research* **85**.2 (1991), pp. 281–299 (cit. on pp. 5, 121).

[265] Purslow, P. P. "Muscle Fascia and Force Transmission". *Journal of Bodywork and Movement Therapies* **14**.4 (2010), pp. 411–417 (cit. on pp. 16, 153).

[266] Radmand, A., Scheme, E. and Englehart, K. "High-Density Force Myography: A Possible Alternative for Upper-Limb Prosthetic Control". *Journal of Rehabilitation Research and Development* **53**.4 (2016), pp. 443–456 (cit. on pp. 178, 179).

[267] Rafuse, V. F. and Gordon, T. "Self-Reinnervated Cat Medial Gastrocnemius Muscles. I. Comparisons of the Capacity for Regenerating Nerves to Form Enlarged Motor Units after Extensive Peripheral Nerve Injuries". *Journal of Neurophysiology* **75**.1 (1996), pp. 268–281 (cit. on p. 95).

[268] Ramasamy, E., Avci, O., Dorow, B., Chong, S.-Y., Gizzi, L., Steidle, G., Schick, F. and Röhrle, O. "An Efficient Modelling-Simulation-Analysis Workflow to Investigate Stump-Socket Interaction Using Patient-Specific, Three-Dimensional, Continuum-Mechanical, Finite Element Residual Limb Models". *Frontiers in Bioengineering and Biotechnology* **6** (2018) (cit. on pp. 4, 5, 63, 176).

[269] Ramírez, A., Grasa, J., Alonso, A., Soteras, F., Osta, R., Muñoz, M. and Calvo, B. "Active Response of Skeletal Muscle: In Vivo Experimental Results and Model Formulation". *Journal of Theoretical Biology* **267**.4 (2010), pp. 546–553 (cit. on pp. 92, 118).

[270] Razumova, M. V., Bukatina, A. E. and Campbell, K. B. "Stiffness-Distortion Sarcomere Model for Muscle Simulation". *Journal of Applied Physiology* **87**.5 (1999), pp. 1861–1876 (cit. on pp. 65, 67, 92).

[271] Rees, J. S. "The Effect of Variation in Occlusal Loading on the Development of Abfraction Lesions: A Finite Element Study". *Journal of Oral Rehabilitation* **29**.2 (2002), pp. 188–193 (cit. on pp. 183, 187).

[272] Rehorn, M. R. and Blemker, S. S. "The Effects of Aponeurosis Geometry on Strain Injury Susceptibility Explored with a 3D Muscle Model". *Journal of Biomechanics* **43**.13 (2010), pp. 2574–2581 (cit. on p. 176).

[273] Riera-Punet, N., Martinez-Gomis, J., Paipa, A., Povedano, M. and Peraire, M. "Alterations in the Masticatory System in Patients with Amyotrophic Lateral Sclerosis". *Journal of Oral & Facial Pain and Headache* **32**.1 (2018), pp. 84–90 (cit. on p. 167).

[274] Rismanchian, M., Bajoghli, F., Mostajeran, Z., Fazel, A. and Eshkevari, P. "Effect of Implants on Maximum Bite Force in Edentulous Patients". *Journal of Oral Implantology* **35**.4 (2009), pp. 196–200 (cit. on p. 132).

[275] Roatta, S., Arendt-Nielsen, L. and Farina, D. "Sympathetic-Induced Changes in Discharge Rate and Spike-Triggered Average Twitch Torque of Low-Threshold Motor Units in Humans". *The Journal of Physiology* **586**.22 (2008), pp. 5561–5574 (cit. on p. 156).

[276] Robertson, J. W. and Johnston, J. A. "Modifying Motor Unit Territory Placement in the Fuglevand Model". *Medical & Biological Engineering & Computing* **55**.11 (2017), pp. 2015–2025 (cit. on pp. 10, 93, 178).

[277] Rohlén, R., Stålberg, E., Stöverud, K.-H., Yu, J. and Grönlund, C. "A Method for Identification of Mechanical Response of Motor Units in Skeletal Muscle Voluntary Contractions Using Ultrafast Ultrasound Imaging—Simulations and Experimental Tests". *IEEE Access* **8** (2020), pp. 50299–50311 (cit. on pp. 9, 178, 180, 181).

[278] Röhrle, O., Davidson, J. B. and Pullan, A. J. "A Physiologically Based, Multi-Scale Model of Skeletal Muscle Structure and Function". *Frontiers in Physiology* **3** (2012) (cit. on pp. 4, 10, 81, 93, 175, 177).

[279] Röhrle, O., Sprenger, M. and Schmitt, S. "A Two-Muscle, Continuum-Mechanical Forward Simulation of the Upper Limb". *Biomechanics and Modeling in Mechanobiology* **16**.3 (2017), pp. 743–762 (cit. on pp. 4, 5, 46, 50, 63, 78, 176).

[280] Röhrle, O., Davidson, J. B. and Pullan, A. J. "Bridging Scales: A Three-Dimensional Electromechanical Finite Element Model of Skeletal Muscle". *SIAM Journal on Scientific Computing* **30**.6 (2008), pp. 2882–2904 (cit. on pp. 2, 4, 177).

[281] Röhrle, O., Neumann, V. and Heidlauf, T. "The Role of Parvalbumin, Sarcoplasmatic Reticulum Calcium Pump Rate, Rates of Cross-Bridge Dynamics, and Ryanodine Receptor Calcium Current on Peripheral Muscle Fatigue: A Simulation Study". *Computational and Mathematical Methods in Medicine* **2016** (2016), pp. 1–14 (cit. on p. 4).

[282] Röhrle, O. and Pullan, A. J. "Three-Dimensional Finite Element Modelling of Muscle Forces during Mastication". *Journal of Biomechanics* **40**.15 (2007), pp. 3363–3372 (cit. on pp. 5, 11, 121, 125, 126, 132, 176, 183, 184).

[283] Röhrle, O., **Saini**, H. and Ackland, D. C. "Occlusal Loading during Biting from an Experimental and Simulation Point of View". *Dental Materials* **34**.1 (2018), pp. 58–68 (cit. on pp. 11, 14, 141, 183, 187).

[284] Röhrle, O., **Saini**, H., Lee, P. V. S. and Ackland, D. C. "A Novel Computational Method to Determine Subject-Specific Bite Force and Occlusal Loading during Mastication". *Computer Methods in Biomechanics and Biomedical Engineering* **21**.6 (2018), pp. 453–460 (cit. on pp. 14, 40, 125, 184).

[285] Röhrle, O., Yavuz, U. Ş., Klotz, T., Negro, F. and Heidlauf, T. "Multiscale Modeling of the Neuromuscular System: Coupling Neurophysiology and Skeletal Muscle Mechanics". *Wiley Interdisciplinary Reviews: Systems Biology and Medicine* **11**.6 (2019), e1457 (cit. on pp. 46, 92).

[286] Romaiguère, P., Vedel, J.-P. and Pagni, S. "Fluctuations in Motor Unit Recruitment Threshold during Slow Isometric Contractions of Wrist Extensor Muscles in Man". *Neuroscience Letters* **103**.1 (1989), pp. 50–55 (cit. on p. 140).

[287] Rose, J. and McGill, K. C. "The Motor Unit in Cerebral Palsy". *Developmental Medicine and Child Neurology* **40**.4 (1998), pp. 270–277 (cit. on pp. 2, 3, 63, 163, 181).

[288] Roy, R. R., Garfinkel, A., Ounjian, M., Payne, J., Hirahara, A., Hsu, E. and Edgerton, V. R. "Three-Dimensional Structure of Cat Tibialis Anterior Motor Units". *Muscle & Nerve* **18**.10 (1995), pp. 1187–1195 (cit. on pp. 81, 93, 94).

[289] Rutherford, O. M. and Jones, D. A. "Measurement of Fibre Pennation Using Ultrasound in the Human Quadriceps in Vivo". *European Journal of Applied Physiology and Occupational Physiology* **65**.5 (1992), pp. 433–437 (cit. on p. 2).

[290] Rutz, E., Baker, R., Tirosh, O., Romkes, J., Haase, C. and Brunner, R. "Tibialis Anterior Tendon Shortening in Combination with Achilles Tendon Lengthening in Spastic Equinus in Cerebral Palsy". *Gait & Posture* **33**.2 (2011), pp. 152–157 (cit. on pp. 3, 181).

[291] Sadeghi, S., Johnson, M., Bader, D. A. and Cortes, D. H. "The Shear Modulus of Lower-Leg Muscles Correlates to Intramuscular Pressure". *Journal of Biomechanics* **83** (2019), pp. 190–196 (cit. on p. 153).

[292] **Saini**, H., Ackland, D. C., Gong, L., Cheng, L. K. and Röhrle, O. "Occlusal Load Modelling Significantly Impacts the Predicted Tooth Stress Response during Biting: A Simulation Study". *Computer Methods in Biomechanics and Biomedical Engineering* **23**.7 (2020), pp. 261–270 (cit. on pp. 14, 125, 183).

[293] **Saini**, H., Altan, E., Ramasamy, E., Klotz, T., Gizzi, L. and Röhrle, O. "Predicting Skeletal Muscle Force from Motor-Unit Activity Using a 3D FE Model". *Proceedings in Applied Mathematics and Mechanics* **18**.1 (2018), e201800035 (cit. on pp. 14, 93, 94).

[294] Samani, A., Holtermann, A., Søgaard, K. and Madeleine, P. "Active Biofeedback Changes the Spatial Distribution of Upper Trapezius Muscle Activity during Computer Work". *European Journal of Applied Physiology* **110**.2 (2010), pp. 415–423 (cit. on pp. 6, 177).

[295] Sathar, S., Trew, M. L., OGrady, G. and Cheng, L. K. "A Multiscale Tridomain Model for Simulating Bioelectric Gastric Pacing". *IEEE transactions on bio-medical engineering* **62**.11 (2015), pp. 2685–2692 (cit. on p. 93).

[296] Schindler, H. J., Hellmann, D., Giannakopoulos, N. N., Eiglsperger, U., van Dijk, J. P. and Lapatki, B. G. "Localised Task-Dependent Motor-Unit Recruitment in the Masseter". *Journal of Oral Rehabilitation* **41**.7 (2014), pp. 477–485 (cit. on pp. 5, 6, 11, 63, 121, 140, 145, 151, 153, 174, 177).

[297] Schindler, H. J., Rues, S., Türp, J. C., Schweizerhof, K. and Lenz, J. "Activity Patterns of the Masticatory Muscles during Feedback-Controlled Simulated Clenching Activities". *European Journal of Oral Sciences* **113**.6 (2005), pp. 469–478 (cit. on pp. 5, 6, 121, 141, 174, 177).

[298] Schmid, L., Klotz, T., Siebert, T. and Röhrle, O. "Characterization of Electromechanical Delay Based on a Biophysical Multi-Scale Skeletal Muscle Model". *Frontiers in Physiology* **10** (2019) (cit. on pp. 67, 99, 100, 116).

[299] Schnetzer, M.-A., Ruegg, D., Baltensperger, R. and Gabriel, J.-P. "Three-Dimensional Model of a Muscle and Simulation of Its Surface EMG". *2001 Conference Proceedings of the 23rd Annual International Conference of the IEEE Engineering in Medicine and Biology Society*. Vol. 2. IEEE, 2001, pp. 1038–1043 (cit. on pp. 81, 93, 178).

[300] Schröder, J., Balzani, D. and Brands, D. "Approximation of Random Microstructures by Periodic Statistically Similar Representative Volume Elements Based on Lineal-Path Functions". *Archive of Applied Mechanics* **81**.7 (2011), pp. 975–997 (cit. on p. 98).

[301] Schröder, J. and Neff, P. "Invariant Formulation of Hyperelastic Transverse Isotropy Based on Polyconvex Free Energy Functions". *International Journal of Solids and Structures* **40**.2 (2003), pp. 401–445 (cit. on p. 50).

[302] Scott, W., Stevens, J. and Binder–Macleod, S. A. "Human Skeletal Muscle Fiber Type Classifications". *Physical Therapy* **81**.11 (2001), pp. 1810–1816 (cit. on pp. 19, 70).

[303] Scutter, S. D. and Türker, K. S. "Recruitment Stability in Masseter Motor Units during Isometric Voluntary Contractions". *Muscle & Nerve* **21**.10 (1998), pp. 1290–1298 (cit. on pp. 64, 123).

[304] Segal, R. L. "Neuromuscular Compartments in the Human Biceps Brachii Muscle". *Neuroscience letters* **140**.1 (1992), pp. 98–102 (cit. on p. 5).

[305] Sejersted, O. M. and Hargens, A. R. "Intramuscular Pressures for Monitoring Different Tasks and Muscle Conditions". *Fatigue: Neural and Muscular Mechanisms*. Ed. by S. C. Gandevia, R. M. Enoka, A. J. McComas, D. G. Stuart, C. K. Thomas and P. A. Pierce. Advances in Experimental Medicine and Biology. Boston, MA: Springer US, 1995, pp. 339–350 (cit. on p. 117).

[306] Sejersted, O. M., Hargens, A. R., Kardel, K. R., Blom, P., Jensen, O. and Hermansen, L. "Intramuscular Fluid Pressure during Isometric Contraction of Human Skeletal Muscle". *Journal of Applied Physiology* **56**.2 (1984), pp. 287–295 (cit. on p. 2).

[307] Shefner, J. M. "Motor Unit Number Estimation in Human Neurological Diseases and Animal Models". *Clinical Neurophysiology* **112**.6 (2001), pp. 955–964 (cit. on p. 163).

[308] Shenhav, R. and Gath, I. "Simulation of the Spatial Distribution of Muscle Fibres in Human Muscles". *Computer Methods and Programs in Biomedicine* **23**.1 (1986), pp. 3–9 (cit. on pp. 93, 94).

[309] Sherrington, C. S. "Remarks on Some Aspects of Reflex Inhibition". *Proceedings of the Royal Society of London, B - Biological Sciences* **97**.686 (1925), pp. 519–545 (cit. on p. 21).

[310] Sherrington, C. S. "Ferrier Lecture.—Some Functional Problems Attaching to Convergence". *Proceedings of the Royal Society of London, B - Biological Sciences* **105**.737 (1929), pp. 332–362 (cit. on p. 1).

[311] Shiau, Y. Y., Wang, J. S. and Carlsson, G. E. "The Effects of Dental Condition on Hand Strength and Maximum Bite Force". *CRANIO* **11**.1 (1993), pp. 48–54 (cit. on p. 132).

[312] Shinogaya, T., Bakke, M., Thomsen, C. E., Vilmann, A., Sodeyama, A. and Matsumoto, M. "Effects of Ethnicity, Gender and Age on Clenching Force and Load Distribution". *Clinical Oral Investigations* **5**.1 (2001), pp. 63–68 (cit. on p. 132).

[313] Silva, J., Heim, W. and Chau, T. "A Self-Contained, Mechanomyography-Driven Externally Powered Prosthesis". *Archives of Physical Medicine and Rehabilitation* **86**.10 (2005), pp. 2066–2070 (cit. on p. 179).

[314] Simo, J. C. and Taylor, R. L. "Penalty Function Formulations for Incompressible Nonlinear Elastostatics". *Computer Methods in Applied Mechanics and Engineering* **35**.1 (1982), pp. 107–118 (cit. on pp. 48, 51).

[315] Sjøgaard, G., Kiens, B., Jørgensen, K. and Saltin, B. "Intramuscular Pressure, EMG and Blood Flow during Low-Level Prolonged Static Contraction in Man". *Acta Physiologica Scandinavica* **128**.3 (1986), pp. 475–484 (cit. on pp. 5, 63, 155, 176, 179).

[316] Sjøgaard, G., Savard, G. and Juel, C. "Muscle Blood Flow during Isometric Activity and Its Relation to Muscle Fatigue". *European Journal of Applied Physiology and Occupational Physiology* **57**.3 (1988), pp. 327–335 (cit. on pp. 5, 63, 117, 143, 155, 179).

[317] Sjöström, M., Lexell, J. and Downham, D. Y. "Differences in Fiber Number and Fiber Type Proportion within Fascicles. A Quantitative Morphological Study of Whole Vastus Lateralis Muscle from Childhood to Old Age". *The Anatomical Record* **234**.2 (1992), pp. 183–189 (cit. on p. 95).

[318] Smith, L. R., Lee, K. S., Ward, S. R., Chambers, H. G. and Lieber, R. L. "Hamstring Contractures in Children with Spastic Cerebral Palsy Result from a Stiffer Extracellular Matrix and Increased in Vivo Sarcomere Length". *The Journal of Physiology* **589**.10 (2011), pp. 2625–2639 (cit. on p. 171).

[319] Spitzer, V., Ackerman, M. J., Scherzinger, A. L. and Whitlock, D. "The Visible Human Male: A Technical Report". *Journal of the American Medical Informatics Association* **3**.2 (1996), pp. 118–130 (cit. on pp. 78, 125).

[320] Sprenger, M. "A 3D Continuum-Mechanical Model for Forward-Dynamics Simulations of the Upper Limb". Ph.D. Thesis. University of Stuttgart, 2016 (cit. on p. 78).

[321] Stålberg, E., Eriksson, P. O., Antoni, L. and Thornell, L. E. "Electrophysiological Study of Size and Fibre Distribution of Motor Units in the Human Masseter and Temporal Muscles". *Archives of Oral Biology* **31**.8 (1986), pp. 521–527 (cit. on p. 124).

[322] Stanford, J. W., Weigel, K. V., Paffenbarger, G. C. and Sweeney, W. "Compressive Properties of Hard Tooth Tissues and Some Restorative Materials". *The Journal of the American Dental Association* **60**.6 (1960), pp. 746–756 (cit. on p. 187).

[323] Stansfield, E., Parker, J. and O'Higgins, P. "A Sensitivity Study of Human Mandibular Biting Simulations Using Finite Element Analysis". *Journal of Archaeological Science: Reports* **22** (2018), pp. 420–432 (cit. on pp. 11, 132).

[324] Stashuk, D. W. "Simulation of Electromyographic Signals". *Journal of Electromyography and Kinesiology* **3**.3 (1993), pp. 157–173 (cit. on pp. 93, 178).

[325] Staudenmann, D., Kingma, I., Daffertshofer, A., Stegeman, D. F. and van Dieën, J. H. "Heterogeneity of Muscle Activation in Relation to Force Direction: A Multi-Channel Surface Electromyography Study on the Triceps Surae Muscle". *Journal of Electromyography and Kinesiology* **19**.5 (2009), pp. 882–895 (cit. on p. 5).

[326] Stein, R. B., French, A. S., Mannard, A. and Yemm, R. "New Methods for Analysing Motor Function in Man and Animals". *Brain Research* **40**.1 (1972), pp. 187–192 (cit. on p. 156).

[327] Styf, J., Ballard, R., Aratow, M., Crenshaw, A., Watenpaugh, D. and Hargens, A. R. "Intramuscular Pressure and Torque during Isometric, Concentric and Eccentric Muscular Activity". *Scandinavian Journal of Medicine & Science in Sports* **5**.5 (1995), pp. 291–296 (cit. on p. 153).

[328] Takaza, M., Moerman, K. M., Gindre, J., Lyons, G. and Simms, C. K. "The Anisotropic Mechanical Behaviour of Passive Skeletal Muscle Tissue Subjected to Large Tensile Strain". *Journal of the Mechanical Behavior of Biomedical Materials* **17** (2013), pp. 209–220 (cit. on pp. 46, 56, 58, 59).

[329] Tang, C., Zhang, G. and Tsui, C. "A 3D Skeletal Muscle Model Coupled with Active Contraction of Muscle Fibres and Hyperelastic Behaviour". *Journal of Biomechanics* **42**.7 (2009), pp. 865–872 (cit. on p. 46).

[330] Taylor, A. M., Steege, J. W. and Enoka, R. M. "Motor-Unit Synchronization Alters Spike-Triggered Average Force in Simulated Contractions". *Journal of Neurophysiology* **88**.1 (2002), pp. 265–276 (cit. on pp. 92, 156).

[331] ter Haar Romeny, B. M., Denier van der Gon, J. J. and Gielen, C. C. A. M. "Relation between Location of a Motor Unit in the Human Biceps Brachii and Its Critical Firing Levels for Different Tasks". *Experimental Neurology* **85**.3 (1984), pp. 631–650 (cit. on pp. 5, 63).

[332] Testa, M., Geri, T., Pitance, L., Lentz, P., Gizzi, L., Erlenwein, J., Petkze, F. and Falla, D. "Alterations in Jaw Clenching Force Control in People with Myogenic Temporomandibular Disorders". *Journal of Electromyography and Kinesiology* **43** (2018), pp. 111–117 (cit. on p. 132).

[333] Thai, D.-K. and Kim, S.-E. "Safety Assessment of a Nuclear Power Plant Building Subjected to an Aircraft Crash". *Nuclear Engineering and Design* **293** (2015), pp. 38–52 (cit. on p. 40).

[334] Tian, M., Hoang, P. D., Gandevia, S. C., Herbert, R. D. and Bilston, L. E. "Viscous Elements Have Little Impact on Measured Passive Length–Tension Properties of Human Gastrocnemius Muscle–Tendon Units in Vivo". *Journal of Biomechanics* **44**.7 (2011), pp. 1334–1339 (cit. on p. 46).

[335] Tonndorf, M. L. and Hannam, A. G. "Motor Unit Territory in Relation to Tendons in the Human Masseter Muscle". *Muscle & Nerve* **17**.4 (1994), pp. 436–443 (cit. on pp. 7–9, 11, 94, 124, 140, 145, 149).

[336] Troiani, D., Filippi, G. M. and Bassi, F. A. "Nonlinear Tension Summation of Different Combinations of Motor Units in the Anesthetized Cat Peroneus Longus Muscle". *Journal of Neurophysiology* **81**.2 (1999), pp. 771–780 (cit. on pp. 156, 161).

[337] Trotter, J. A. "Functional Morphology of Force Transmission in Skeletal Muscle". *Cells Tissues Organs* **146**.4 (1993), pp. 205–222 (cit. on pp. 20, 93).

[338] Trotter, J. A. and Purslow, P. P. "Functional Morphology of the Endomysium in Series Fibered Muscles". *Journal of Morphology* **212**.2 (1992), pp. 109–122 (cit. on p. 20).

[339] Trotter, J. A. "Interfiber Tension Transmission in Series-Fibered Muscles of the Cat Hindlimb". *Journal of Morphology* **206**.3 (1990), pp. 351–361 (cit. on p. 20).

[340] Truesdell, C. and Noll, W. *The Non-Linear Field Theories of Mechanics*. Ed. by S. S. Antman. Third. Berlin Heidelberg: Springer-Verlag, 2004 (cit. on p. 25).

[341] Tsarouchi, P., Makris, S. and Chryssolouris, G. "Human–Robot Interaction Review and Challenges on Task Planning and Programming". *International Journal of Computer Integrated Manufacturing* **29**.8 (2016), pp. 916–931 (cit. on p. 178).

[342] Turkawski, S., Eijden, T. van and Weijs, W. "Force Vectors of Single Motor Units in a Multipennate Muscle". *Journal of Dental Research* **77**.10 (1998), pp. 1823–1831 (cit. on pp. 5, 9, 151).

[343] Turrina, A., Martínez-González, M. A. and Stecco, C. "The Muscular Force Transmission System: Role of the Intramuscular Connective Tissue". *Journal of Bodywork and Movement Therapies* **17**.1 (2013), pp. 95–102 (cit. on pp. 12, 16).

[344] Ueki, K., Nakagawa, K. and Yamamoto, E. "Bite Force and Maxillofacial Morphology in Patients With Duchenne-Type Muscular Dystrophy". *Journal of Oral and Maxillofacial Surgery* **65**.1 (2007), pp. 34–39 (cit. on p. 167).

[345] Umesh, S., Padma, S., Asokan, S. and Srinivas, T. "Fiber Bragg Grating Based Bite Force Measurement". *Journal of Biomechanics* **49**.13 (2016), pp. 2877–2881 (cit. on p. 186).

[346] van Cutsem, M., Feiereisen, P., Duchateau, J. and Hainaut, K. "Mechanical Properties and Behaviour of Motor Units in the Tibialis Anterior during Voluntary Contractions". *Canadian Journal of Applied Physiology* **22**.6 (1997), pp. 585–597 (cit. on p. 22).

[347] van Dijk, J. P., Eiglsperger, U., Hellmann, D., Giannakopoulos, N. N., McGill, K. C., Schindler, H. J. and Lapatki, B. G. "Motor Unit Activity within the Depth of the Masseter Characterized by an Adapted Scanning EMG Technique". *Clinical Neurophysiology* **127**.9 (2016), pp. 3198–3204 (cit. on pp. 7–9, 81, 94, 124, 140, 149, 180).

[348] van Dijk, J. P., Verhamme, C., van Schaik, I. N., Schelhaas, H. J., Mans, E., Bour, L. J., Stegeman, D. F. and Zwarts, M. J. "Age-Related Changes in Motor Unit Number Estimates in Adult Patients with Charcot–Marie–Tooth Type 1A". *European Journal of Neurology* **17**.8 (2010), pp. 1098–1104 (cit. on p. 163).

[349] van Dijk, J. P., Schelhaas, H. J., van Schaik, I. N., Janssen, H. M. H. A., Stegeman, D. F. and Zwarts, M. J. "Monitoring Disease Progression Using High-Density Motor Unit Number Estimation in Amyotrophic Lateral Sclerosis". *Muscle & Nerve* **42**.2 (2010), pp. 239–244 (cit. on p. 163).

[350] van Donkelaar, C. C., Huyghe, J. M., Vankan, W. J. and Drost, M. R. "Spatial Interaction between Tissue Pressure and Skeletal Muscle Perfusion during Contraction". *Journal of Biomechanics* **34**.5 (2001), pp. 631–637 (cit. on p. 179).

[351] van Eijden, T., Brugman, P., Weijs, W. A. and Oosting, J. "Coactivation of Jaw Muscles: Recruitment Order and Level as a Function of Bite Force Direction and Magnitude". *Journal of Biomechanics* **23**.5 (1990), pp. 475–485 (cit. on p. 141).

[352] van Eijden, T. and Turkawski, S. "Morphology and Physiology of Masticatory Muscle Motor Units". *Critical Reviews in Oral Biology & Medicine* **12**.1 (2001), pp. 76–91 (cit. on pp. 122, 123, 140, 145, 151).

[353] van Essen, N. L., Anderson, I. A., Hunter, P. J., Carman, J., Clarke, R. D. and Pullan, A. J. "Anatomically Based Modelling of the Human Skull and Jaw". *Cells Tissues Organs* **180**.1 (2005), pp. 44–53 (cit. on pp. 78, 126, 184, 185).

[354] van Loocke, M., Lyons, C. G. and Simms, C. K. "A Validated Model of Passive Muscle in Compression". *Journal of Biomechanics* **39**.16 (2006), pp. 2999–3009 (cit. on p. 56).

[355] van Zuylen, E. J., Gielen, C. C. and Denier van der Gon, J. J. "Coordination and Inhomogeneous Activation of Human Arm Muscles during Isometric Torques". *Journal of Neurophysiology* **60**.5 (1988), pp. 1523–1548 (cit. on p. 177).

[356] Venema, H. W. "Spatial Distribution of Fiber Types in Skeletal Muscle: Test for a Random Distribution". *Muscle & Nerve* **11**.4 (1988), pp. 301–311 (cit. on p. 95).

[357] Verri, F. R., Cruz, R. S., Batista, V. E. d. S., Almeida, D. A. d. F., Verri, A. C. G., Lemos, C. A. d. A., Júnior, J. F. S. and Pellizzer, E. P. "Can the Modeling for Simplification of a Dental Implant Surface Affect the Accuracy of 3D Finite Element Analysis?" *Computer Methods in Biomechanics and Biomedical Engineering* **19**.15 (2016), pp. 1665–1672 (cit. on p. 183).

[358] Vieira, T. M. M., Loram, I. D., Muceli, S., Merletti, R. and Farina, D. "Postural Activation of the Human Medial Gastrocnemius Muscle: Are the Muscle Units Spatially Localised?: Localisation of Gastrocnemius Muscle Units". *The Journal of Physiology* **589**.2 (2011), pp. 431–443 (cit. on pp. 8, 180).

[359] Vootla, N. R., Barla, S. C., Kumar, V.-H.-C., Surapaneni, H., Balusu, S. and Kalyanam, S. "An Evaluation of the Stress Distribution in Screw Retained Implants of Different Crown Implant Ratios in Different Bone Densities Under Various Loads-A FEM Study". *Journal of Clinical and Diagnostic Research* **10**.6 (2016), ZC96–ZC101 (cit. on pp. 183, 187).

[360] Wakeling, J. M. "The Recruitment of Different Compartments within a Muscle Depends on the Mechanics of the Movement". *Biology Letters* **5**.1 (2009), pp. 30–34 (cit. on p. 5).

[361] Walter, J. R., **Saini**, H., Maier, B., Mostashiri, N., Aguayo, J. L., Zarshenas, H., Hinze, C., Shuva, S., Köhler, J., Sahrmann, A. S., Chang, C.-m., Csiszar, A., Galliani, S., Cheng, L. K. and Röhrle, O. "Comparative Study of a Biomechanical Model-Based and Black-Box Approach for Subject-Specific Movement Prediction". *International Conference of the IEEE Engineering in Medicine & Biology Society (EMBC)*. IEEE, 2020, pp. 4775–4778 (cit. on p. 14).

[362] Wang, C., Fu, G. and Deng, F. "Difference of Natural Teeth and Implant-Supported Restoration: A Comparison of Bone Remodeling Simulations". *Journal of Dental Sciences* **10**.2 (2015), pp. 190–200 (cit. on p. 132).

[363] Wang, R. Z. and Weiner, S. "Strain–Structure Relations in Human Teeth Using Moiré Fringes". *Journal of Biomechanics* **31**.2 (1997), pp. 135–141 (cit. on p. 187).

[364] Wang, Y. K., Nash, M. P., Pullan, A. J., Kieser, J. A. and Röhrle, O. "Model-Based Identification of Motion Sensor Placement for Tracking Retraction and Elongation of the Tongue". *Biomechanics and Modeling in Mechanobiology* **12**.2 (2013), pp. 383–399 (cit. on p. 177).

[365] Ward, S. R., Davis, J., Kaufman, K. R. and Lieber, R. L. "Relationship between Muscle Stress and Intramuscular Pressure during Dynamic Muscle Contractions". *Muscle & Nerve* **36**.3 (2007), pp. 313–319 (cit. on p. 153).

[366] Ward, S. R. and Lieber, R. L. "Density and Hydration of Fresh and Fixed Human Skeletal Muscle". *Journal of Biomechanics* **38**.11 (2005), pp. 2317–2320 (cit. on p. 58).

[367] Weickenmeier, J., Jabareen, M., Le Révérend, B. J. D., Ramaioli, M. and Mazza, E. "Experimental and Numerical Characterization of the Mechanical Masseter Muscle Response During Biting". *Journal of Biomechanical Engineering* **139**.12 (2017), p. 121007 (cit. on pp. 4–6, 11, 63, 121, 125, 132, 177).

[368] Wheatley, B. B., Odegard, G. M., Kaufman, K. R. and Haut Donahue, T. L. "A Validated Model of Passive Skeletal Muscle to Predict Force and Intramuscular Pressure". *Biomechanics and Modeling in Mechanobiology* **16**.3 (2017), pp. 1011–1022 (cit. on p. 46).

[369] William, R., Luschei, E. S. and Hoffman, D. S. "Recruitment Order, Contractile Characteristics, and Firing Patterns of Motor Units in the Temporalis Muscle of Monkeys". *Experimental Neurology* **61**.1 (1978), pp. 31–52 (cit. on p. 156).

[370] Willison, R. G., Waylonis, G. W., Ochoa, J., Vignos, P. J. and Kirby, A. C. "Arrangement of Muscle Fibers of a Single Motor Unit in Mammalian Muscles". *Muscle & Nerve* **3**.4 (1980), pp. 360–362 (cit. on pp. 94, 163).

[371] Wriggers, P. *Computational Contact Mechanics*. Second. Berlin Heidelberg: Springer-Verlag, 2006 (cit. on pp. 25, 41, 44).

[372] Wu, T., Hung, A. and Mithraratne, K. "Generating Facial Expressions Using an Anatomically Accurate Biomechanical Model". *IEEE Transactions on Visualization and Computer Graphics* **20**.11 (2014), pp. 1519–1529 (cit. on pp. 4, 5, 176).

[373] Yao, W., Fuglevand, R. J. and Enoka, R. M. "Motor-Unit Synchronization Increases EMG Amplitude and Decreases Force Steadiness of Simulated Contractions". *Journal of Neurophysiology* **83**.1 (2000), pp. 441–452 (cit. on p. 175).

[374] Yemm, R. "The Orderly Recruitment of Motor Units of the Masseter and Temporal Muscles during Voluntary Isometric Contraction in Man." *The Journal of Physiology* **265**.1 (1977), pp. 163–174 (cit. on p. 156).

[375] Yettram, A., Wright, K. and Pickard, H. "Finite Element Stress Analysis of the Crowns of Normal and Restored Teeth". *Journal of Dental Research* **55**.6 (1976), pp. 1004–1011 (cit. on p. 187).

[376] Zajac, F. E. "Muscle and Tendon: Properties, Models, Scaling, and Application to Biomechanics and Motor Control". *Critical Reviews in Biomedical Engineering* **17**.4 (1989), pp. 359–411 (cit. on pp. 2–4, 45).

[377] Zhang, C. and Gao, Y. "Finite Element Analysis of Mechanics of Lateral Transmission of Force in Single Muscle Fiber". *Journal of Biomechanics* **45**.11 (2012), pp. 2001–2006 (cit. on p. 20).

[378] Zheng, Y. P., Chan, M. M. F., Shi, J., Chen, X. and Huang, Q. H. "Sonomyography: Monitoring Morphological Changes of Forearm Muscles in Actions with the Feasibility for the Control of Powered Prosthesis". *Medical Engineering & Physics* **28**.5 (2006), pp. 405–415 (cit. on p. 179).

[379] Zienkiewicz, O. C., Taylor, R. L. and Zhu, J. Z. *The Finite Element Method: Its Basis and Fundamentals*. Elsevier, 2005 (cit. on p. 25).

Released Report Series

CBM-01 Heidlauf, T. “Chemo-Electro-Mechanical Modelling of the Neuromuscular System”. September 2015.

CBM-02 Sprenger, M. “A 3D Continuum-Mechanical Model for Forward-Dynamics Simulations of the Upper Limb”. October 2015.

CBM-03 Ramasamy E. “A Modelling-Simulation-Analysis Workflow for Investigating Socket-Stump Interaction”. April 2019.

CBM-04 Hessenthaler, A. “Multilevel Convergence Analysis: Parallel-in-Time Integration for Fluid-Structure Interaction Problems with Applications in Cardiac Flow Modeling”. February 2020.

CBM-05 Mordhorst, M. “Towards a Stable and Fast Dynamic Skeletal Muscle Model”. April 2020.

CBM-06 Asgharzadeh, P. “Image-based Analysis of Biological Network Structures using Machine Learning and Continuum Mechanics”. May 2020.

CBM-07 Bleiler, C. “Continuum-Mechanical Modelling Across Scales: Homogenisation Methods and Their Application to Microstructurally-Based Skeletal Muscle Modelling”. April 2021.